

**GEOMETRY ESTIMATION AND ADAPTIVE ACTUATION FOR
CENTERING PREPROCESSING AND PRECISION
MEASUREMENT**

A Dissertation
Presented to
The Academic Faculty

by

M. Laine Mears

In Partial Fulfillment
of the Requirements for the Degree
Doctor of Philosophy in the
School of Mechanical Engineering

Georgia Institute of Technology
May 2006

**GEOMETRY ESTIMATION AND ADAPTIVE ACTUATION FOR
CENTERING PREPROCESSING AND PRECISION
MEASUREMENT**

Approved by:

Dr. Thomas R. Kurfess, Advisor
Department of Mechanical Engineering
Clemson University

Dr. Shreyes N. Melkote
School of Mechanical Engineering
Georgia Institute of Technology

Dr. Jane C. Ammons
School of Industrial and Systems Engineering
Georgia Institute of Technology

Dr. Richard F. Salant
School of Mechanical Engineering
Georgia Institute of Technology

Dr. Francis M. Kolarits
Senior Development Specialist
The Timken Company

Date Approved: March 17, 2006

ACKNOWLEDGEMENTS

A number of people contributed to my completion of this work, and it would not be a reality without every one of them. I would first like to thank my advisor, Dr. Thomas Kurfess for his patient guidance and direction these past years not only on this project, but also on refining my attitude toward research, and giving me my own research vision for the future.

My thanks go to Joe Pack, Mike Thompson and Dr. Francis Kolarits of The Timken Company both for their sponsorship of and input on this project, including not only funding, but also equipment and excellent review of all successes and missteps along the way. I also specifically thank Lance Ferguson and Darren Averett of The Timken Company for allowing use of the Manufacturing Development Center facility and resources to perform my research, as well as Greg Lister and Dan Schertz of The Timken Company for their almost daily technical help on the project.

My thanks go also to Dr. Jeannie Falcon of National Instruments Corporation, not only for funding and equipment donations, but also for her positive support, excellent suggestions and detailed feedback on my work.

I thank my additional Reading Committee members: Dr. Jane Ammons of the Industrial and Systems Engineering School, and Drs. Shreyes Melkote and Richard Salant of the Mechanical Engineering School. They have given me valuable direction and helped me to think in new ways about many different aspects of the project.

Thanks to all the members of my research group, specifically Austin Chen, Dr. Kristian Krüger and Meghan Shilling, not only for their review of my work, but also for their ideas, encouragement and friendship through the entire research process.

I gratefully acknowledge the direct financial support of both the American Society for Quality and General Motors Corporation through scholarships that softened the financial blow of my returning to school full-time.

Finally, I would like to thank my family: Mom and Dad for the great life they gave me, instilling intelligence and tenacity, and to my wife Kristina for her unwavering support since my return to graduate school almost 10 years ago, both in leaving me alone when I needed and being there for me when I needed that too. Thank you.

Any opinions, findings and conclusions or recommendations are those of the authors and do not necessarily reflect the views of The Timken Company or National Instruments.

TABLE OF CONTENTS

ACKNOWLEDGEMENTS	III
LIST OF TABLES	XIII
LIST OF FIGURES	XIV
LIST OF ABBREVIATIONS	XXIII
LIST OF SYMBOLS	XXIV
SUMMARY	XXXI
CHAPTER 1 INTRODUCTION	1
Center-Based Manufacturing Methods	1
Centering Methods.....	2
Manually Actuated Centering.....	2
Jaw-Type Fixturing.....	3
Axis Offset Systems.....	4
Motivation.....	5
Solution Path and Metrics.....	6
Research Purpose and Objectives	6
Important Research Questions	7

Organizational Overview	7
CHAPTER 2 BACKGROUND AND PREVIOUS WORK	9
Centering System Research	9
Traditional Centering Approaches	9
Impact-Based Positioning Approaches	10
Friction Modeling.....	10
Control of Frictional Systems	14
Position Control	15
Pushing Actuation.....	15
Impulsive Actuation.....	16
Inverse Sliding Problem.....	16
Impact Problem.....	17
Additional Treatments of Impulsive Actuation	17
System Identification	18
A Note on Manual Actuation Capability and Cost in the Application	20
Manual Centering.....	20
Centering Using Alternative Methods	20
CHAPTER 3 SYSTEM DESIGN	24
Design Constraints and Targets	24
Equipment	26

Hardware.....	26
General Control Architecture.....	27
Prioritization	28
Parallel Loop Structure	29
User Interface and Memory Management	31
Additional System Design Considerations.....	32
Sensing Requirements.....	32
General.....	32
Minimum Stroke Distance	32
Selection.....	34
Spindle Velocity Requirement.....	35
Stiffness Determination	37
Restitution Determination.....	37
System Plant Identification and Response.....	38
System Simulation.....	40
Following Control Design.....	41
Following Controller Validation.....	42
Actuation Control Design.....	44
Actuation Controller Validation	45
CHAPTER 4 OPTIMAL GEOMETRY ESTIMATION	49
Data Collection	49
Part Geometry Estimation	49

Data Representation	51
Modeling Error.....	53
Error Correction.....	54
Validation of Error Correction.....	59
Data Fitting Algorithms	60
Definitions.....	60
Least Squares Fitting (LSQ)	60
Kalman Recursive Filtering	61
Recursive Least Squares (RLS)	64
Least Squares Using Partial Revolution Estimation (PRLS).....	65
Fitting Algorithm Simulation.....	66
Error Convergence	69
Computational Complexity - Simulation.....	71
Convergence of Estimated Parameter Values.....	72
Off-Center Amplitude.....	72
Off-Center Distance Angle	73
Validation and Comparison	74
Achievable Accuracy	75
Computational Complexity.....	76
Confidence-Based Data Validity.....	76
Simulation Validation.....	79
Validation Result	82
 CHAPTER 5 TRAJECTORY PLANNING AND LINEAR TIME-INVARIANT CONTROL	 85

Actuation Distance	85
Actuation Input	88
Trajectory Plan	88
Lead Angle Calculation	88
Lead Angle Validation	90
Actuation Velocity Energy Balance Model	91
Actuation Planning by Energy Balance Model.....	93
Validation of Actuation Planning by Energy Balance Model	94
Reaction Model.....	99
Validation of Reaction Model.....	104
Applicability of Reaction Model to Actuation.....	107
Distance Augmentation.....	107
Velocity Augmentation.....	107
Validation of Actuation Planning by Reaction Model.....	108
System Performance Results	110
Assumption of Data Normality	115
Stiction Resonance and Control	119
Resonance of Stiction	119
Stiction Resonance Frequency Invariance to Velocity	120
Input Signal Filtering and Actuation.....	122
Actuation Simulation Results	124
Validation Results.....	127
Validation of Lower Mass Part.....	129
Applicability of Input Signal Filtering.....	131

CHAPTER 6 OPTIMAL ESTIMATION AND SYSTEM ADAPTABILITY 133

Continuous Real-Time Estimation 133

Friction Model Parameter Estimation..... 133

 Direct Force Measurement..... 133

 Friction Parameter Derivation from Sliding Distance 139

 Predictor Validation 143

 Case 1 – Dry..... 143

 Case 2 – Lubricated 143

Discrete Adaptability and Estimation..... 146

 Discrete Actuation Error Compensation..... 147

 Validation of Discrete Adaptability 148

Feedforward Process Information..... 149

 Rapid Feed Protection..... 150

 Roundness Estimation..... 151

 Roundness Representation 153

 Benefits 154

 Limitations 155

 Required Geometry Signal Processing 155

 Loss of High-Frequency Information 157

 Validation..... 158

CHAPTER 7 CONCLUSIONS AND FUTURE WORK 165

Conclusions..... 165

Research Objectives..... 166

Important Research Questions	167
Contribution List	169
Contribution Details	170
1 Automated Centering System	170
2 Distributed Control Hierarchy	171
3 Optimal State Estimation Algorithm Validation.....	171
4 Roundness Information Derivation.....	172
5 Confidence-Based Data Modeling.....	172
6 Correction Function for Geometry Estimation	173
7 Energy Balance Method for Free-Sliding Control.....	173
8 Free-Sliding Distance Augmentation to Impulsive Actuation.....	173
9 Real-Time Iterative Friction Model Parameter Estimation	174
10 Frequency-Based Anti-Resonance Actuation.....	175
Recommendations for Future Work.....	175
Trajectory Planning.....	175
Controller Design.....	176
Multivariable Control.....	176
Environment Estimation Tracking.....	176
Distributed Network Information Sharing.....	177
Final Comments	178
APPENDIX A HOST CODE AND DESCRIPTION.....	179
APPENDIX B REAL-TIME CODE AND DESCRIPTION	184

APPENDIX C POSITION SIMULATION RESULTS.....	187
APPENDIX D FORCE SIMULATION RESULTS.....	193
APPENDIX E BANDLIMITED VELOCITY ACTUATION FORCE	199
APPENDIX F BANDLIMITED VELOCITY ACTUATION POSITION	205
REFERENCES.....	212
VITA.....	218

LIST OF TABLES

	Page
Table 3.1 - System Stiffness Data.....	37
Table 3.2 - Maximum Following Error by Actuation Velocity	47
Table 4.1 - Uncorrected vs. Corrected Radius Estimates, $R_{act}=61.9$ mm	59
Table 4.2 - Summary of Computational Requirements for Curve Fitting	71
Table 4.3 - Data Fitting Validation Part Information	74
Table 4.4 - Summary of Computational Accuracy for Curve Fitting.....	75
Table 4.5 - Summary of Computational Requirements for Curve Fitting to Part Data	76
Table 4.6 - Simulation Result for Variance-Based Validity.....	81
Table 4.7 - Validation Result for Variance-Based Validity.....	84
Table 5.1 - System Model Validation, $m=18.9$ kg.....	106
Table 5.2 - Validation Results for Free-Sliding Compensation ($n=10$ trials/level).....	110
Table 5.3 - Descriptions of Parts Under Test.....	111
Table 5.4 - Summary of System Performance Results	114
Table 6.1 - Peak Force Modeling Error	135
Table 6.2 - Results of Friction Prediction Experiment	144
Table 6.3 - Validation Data of Combined Friction Estimator, $v=5000$ mm/min.....	146
Table 6.4 - Roundness Validation Part Information	158
Table 6.5 - Peak Magnitude Reading Obtained by Rondcom 30C.....	160

LIST OF FIGURES

	Page
Figure 1.1 - Mitutoyo RA-100 Roundness Measuring Machine [Mitutoyo 2006].....	1
Figure 1.2 - Manual Centering Process.....	3
Figure 1.3 - Three-Jaw Precision Chuck for Measurement Machine	4
Figure 1.4 - Manual Axis Offset Adjustment [Mitutoyo 2005].....	5
Figure 2.1 - Linear Viscous Coulomb Friction (undefined at $v=0$)	11
Figure 2.2 - Stribeck Model of Force vs. Velocity	13
Figure 2.3 - Stick-Slip Motion Depiction of Spring y Pulling Sliding Mass x [Åström 1998]	13
Figure 2.4 - Three-Blade Iris Centering Device [Taylor 2003]	21
Figure 2.5 - Six-Jaw Centering Chuck [Taylor 2003]	22
Figure 2.6 - Three-Jaw Chucking of Four-Lobe Part Causing Center Misalignment	22
Figure 2.7 - Precision Chuck for Roundness Measurement	23
Figure 3.1 - Prototype System: Spindle, Linear Slide, Measurement Probe, Pusher Tip.	26
Figure 3.2 – Flowchart of Program Operation.....	28
Figure 3.3 - User Interface of Centering System	31
Figure 3.4 - Part Offset Geometry	33
Figure 3.5 - Bode Plot of Linear Slide System	39
Figure 3.6 - Block Diagram of Prototype Plant	40
Figure 3.7 - System Simulation Output	41
Figure 3.8 - Response Plot of PI Performance Objective	42
Figure 3.9 - Linear Slide Following Control Step Response	43
Figure 3.10 – Linear Slide Following Control Dynamic Response (setpoint=7928 μm).	44
Figure 3.11 - Following Error During Actuation of 0.8 kg Part at 3000 mm/min.....	46

Figure 3.12 - Following Error During Actuation of 18.9 kg Part.....	47
Figure 4.1 - Parameters for Part Velocity Derivation.....	49
Figure 4.2 - Radial Deviation of Data at Large Offset (expansion point shown).....	50
Figure 4.3 - Cosine Fitting of Circular Data at Large Offset (Limaçon Projection)	52
Figure 4.4 - Percent Estimation Error Using Limaçon Approximation.....	53
Figure 4.5 - Relation of Geometry to Rotation.....	55
Figure 4.6 - Numerical Solution of Radius Estimate Corrector.....	56
Figure 4.7 - Error in Correction Factor Model	57
Figure 4.8 - Error-Corrected Data of Limaçon Approximation.....	58
Figure 4.9 – Kalman Filtering of Simulated Data.....	67
Figure 4.10 - Recursive Least Squares (RLS) Fitting of Simulated Data.....	68
Figure 4.11 - Partial Revolution Least Squares Fitting of Simulated Data	68
Figure 4.12 - Fitting Error vs. Size of Data Set for Kalman Filtering.....	69
Figure 4.13 - Error vs. Size of Data Set for Recursive Least Squares Fitting	70
Figure 4.14 - Error vs. Size of Data Set for Partial Revolution Least Squares Fitting.....	70
Figure 4.15 - Error in Estimation of Off-Center Distance vs. Data Set Size.....	72
Figure 4.16 - Error in Estimation of Off-Center Angle vs. Data Set Size	73
Figure 4.17 - Raw Data of Part Sampled on Ring Centering Prototype.....	74
Figure 4.18 - Example MSE Requirement for J=99.9% confidence and $\epsilon=0.03$	79
Figure 4.19 - Simulation of Variance-Based Validity, $A=20000$	80
Figure 4.20 - Simulation of Variance-Based Validity, $A=1000$	80
Figure 4.21 - Simulation of Variance-Based Validity, $A=100$	81
Figure 4.22 - Validation of Variance-Based Validity, $A=20220 \mu\text{m}$	82
Figure 4.23 - Validation of Variance-Based Validity, $A=1043 \mu\text{m}$	83
Figure 4.24 - Validation of Variance-Based Validity, $A=246 \mu\text{m}$	83
Figure 5.1 - Part Positional Geometry	85

Figure 5.2 - Part Lead Geometry	87
Figure 5.3 - Velocity Idealized Profile of Actuation Move	88
Figure 5.4 - Angular Actuation Error by Offset Distance	91
Figure 5.5 - Actuation Velocity Plan, $m=0.8$ kg, $e=0.85$	94
Figure 5.6 - Polar Plot of $v=500$ mm/min Actuation.....	95
Figure 5.7 - Off-Center Distance over Number of Actuations, $v=500$ mm/min	96
Figure 5.8 - Polar Plot of $v=1000$ mm/min Actuation.....	96
Figure 5.9 - Polar Plot of $v=2000$ mm/min Actuation.....	97
Figure 5.10 - Off-Center Distance over Number of Actuations, $v=1000$ mm/min.....	97
Figure 5.11 - Off-Center Distance over Number of Actuations, $v=2000$ mm/min.....	98
Figure 5.12 - Polar Plot with Actuation Velocity Determined by Energy Balance Method	98
Figure 5.13 - Off-Center Distance over Number of Actuations, v by Energy Balance Method.....	99
Figure 5.14 - Idealized Relative Motion System	100
Figure 5.15 - Simulated Idealized System Position Response to Ramp Input.....	100
Figure 5.16 - Simulated Idealized System Velocity Response to Ramp Input.....	101
Figure 5.17 - Simulated Idealized System Force Response to Ramp Input.....	101
Figure 5.18 - Limit Cycle of Actuation Across Tolerance Zone	102
Figure 5.19 - System Response to Constant Velocity Input	104
Figure 5.20 - Modeled Position Data vs. Observed for $m=18.9$ kg, $v=600$ mm/min	105
Figure 5.21 - Position Data Normalized to Command Input ($m=18.9$ kg, $v=600$ mm/min)	105
Figure 5.22 - Sample Cycle Push-by-Push Results (Free Sliding Compensation OFF). 108	
Figure 5.23 - Sample Cycle Push-by-Push Results (Free Sliding Compensation ON) .. 109	
Figure 5.24 - Run Chart for Centering Time and Number of Actuations, Part 1	112

Figure 5.25 - Run Chart for Centering Time and Number of Actuations, Part 2	112
Figure 5.26 - Run Chart for Centering Time and Number of Actuations, Part 3	113
Figure 5.27 - Run Chart for Centering Time and Number of Actuations, Part 4	113
Figure 5.28 - Normal Probability Plot of Ring Model Residual Values, Part 1	116
Figure 5.29 - Normal Probability Plot of Ring Model Residual Values, Part 2	116
Figure 5.30 - Normal Probability Plot of Ring Model Residual Values, Part 3	117
Figure 5.31 - Normal Probability Plot of Ring Model Residual Values, Part 4	117
Figure 5.32 – Normal Probability Plot of Randomly-Distributed Data.....	118
Figure 5.33 - Modeled Force Data vs. Observed for $m=18.9$ kg, $v=600$ mm/min	120
Figure 5.34 - Resonance of Stiction in Constant Velocity Actuation.....	121
Figure 5.35 - Magnitude Transfer Function of Bandstop Filter.....	122
Figure 5.36 - Bandlimited Velocity Signal (20 Hz - 40 Hz removed).....	123
Figure 5.37 - Position Contour of Constant and Bandlimited Velocity Command Profiles	123
Figure 5.38 - Simulated Command Position Normalized to Constant Velocity Input ...	124
Figure 5.39 - Simulated Force Response with Constant and Bandlimited Velocity Inputs	125
Figure 5.40 – Simulated Position Response with Constant and Bandlimited Velocity Inputs.....	126
Figure 5.41 - Simulated Normalized Position Response with Constant and Bandlimited Velocity Inputs.....	126
Figure 5.42 - Force Data for Constant Velocity and Bandlimited Velocity Actuation, $m=18.9$ kg	127
Figure 5.43 – Experimental Position Data for Constant Velocity and Bandlimited Velocity Actuation, $m=18.9$ kg, $v=600$ mm/min.....	128

Figure 5.44 – Normalized Experimental Position Data for Constant Velocity and Bandlimited Velocity Actuation, $m=18.9$ kg, $v=600$ mm/min	129
Figure 5.45 - Force Response Data for Constant Velocity Actuation, $m=0.8$ kg	130
Figure 5.46 - Velocity Command Profile, Constant and [10 Hz, 100 Hz] Filtered, $v=2500$ mm/min	130
Figure 5.47 - Force Data for Constant Velocity and Bandlimited Velocity Actuation, $m=0.8$ kg	131
Figure 6.1 - Force Readings from Centering Cycle	134
Figure 6.2 - Modeled Force vs. Data, $m=18.9$ kg, $v=600$ mm/min	134
Figure 6.3 – Modeled Force Variation with μ_s over Velocity Range, $m=0.8$ kg	136
Figure 6.4 - Modeled Force Variation with μ_s over Velocity Range, $m=18.9$ kg	137
Figure 6.5 - Force Estimate Coefficients vs. Velocity	138
Figure 6.6 - Modeled Free-Sliding Distance vs. Velocity, $m=0.8$ kg	139
Figure 6.7 - Modeled Free-Sliding Distance vs. Velocity, $m=18.9$ kg	140
Figure 6.8 - Friction Relationship to Free Sliding Distance	142
Figure 6.9 - Cycle Operation with Discrete Adaptability OFF	148
Figure 6.10 - Cycle Operation with Discrete Adaptability ON	149
Figure 6.11 - Typical Grinding Cycle with Roughing, Finishing and Sparkout Stages [Malkin 1989]	150
Figure 6.12 - Roundness Measurement Standards based on ISO 4291-1985(E) [Dagnall 1996]	153
Figure 6.13 - Roundness Plot Generated by Centering System	154
Figure 6.14 - Frequency Spectra of Part Surface	154
Figure 6.15 - Measuring Probe Roller Tip [Heidenhain 2005]	155
Figure 6.16 - Part Geometry at 5 μ m Offset Amplitude	156
Figure 6.17 - Small vs. Large Measurement Tip, Bridging Effect [Dagnall 1996]	157

Figure 6.18 - Roundness Plot Obtained by Rondcom 30C Measuring Machine (0.2 $\mu\text{m}/\text{div}$).....	159
Figure 6.19 - Frequency Magnitude Plot Obtained by Rondcom 30C	160
Figure 6.20 - Roundness Plot of Subject Part on Centering Machine	161
Figure 6.21 - Frequency Magnitude Plot of Subject Part on Centering Machine.....	162
Figure 6.22 - Frequency Magnitude Chart of Rough-Turned Part	163
Figure 6.23 - Frequency Magnitude Chart of 2-Point Out of Round Part	163
Figure A-1 - User Interface Front Panel	179
Figure A-2 - Host Program Controls and Indicators.....	180
Figure A-3 - Host Subprogram Listing.....	181
Figure B-1 - Real-Time Program Controls and Indicators	184
Figure B-2 - Real-Time Subprogram Listing.....	185
Figure C-1 - Normalized Position Response Plots with Model Values (v=100 mm/min)	187
Figure C-2 - Normalized Position Response Plots with Model Values (v=200 mm/min)	187
Figure C-3 - Normalized Position Response Plots with Model Values (v=300 mm/min)	188
Figure C-4 - Normalized Position Response Plots with Model Values (v=400 mm/min)	188
Figure C-5 - Normalized Position Response Plots with Model Values (v=500 mm/min)	189
Figure C-6 - Normalized Position Response Plots with Model Values (v=700 mm/min)	189
Figure C-7 - Normalized Position Response Plots with Model Values (v=800 mm/min)	190

Figure C-8 - Normalized Position Response Plots with Model Values (v=900 mm/min)	190
Figure C-9 - Normalized Position Response Plots with Model Values (v=1000 mm/min)	191
Figure C-10 - Normalized Position Response Plots with Model Values (v=1200 mm/min)	191
Figure C-11 - Normalized Position Response Plots with Model Values (v=1500 mm/min)	192
Figure C-12 - Normalized Position Response Plots with Model Values (v=2000 mm/min)	192
Figure D-1 – Force Response Plots with Model Values (v=100 mm/min)	193
Figure D-2 – Force Response Plots with Model Values (v=200 mm/min)	193
Figure D-3 – Force Response Plots with Model Values (v=300 mm/min)	194
Figure D-4 – Force Response Plots with Model Values (v=400 mm/min)	194
Figure D-5 – Force Response Plots with Model Values (v=500 mm/min)	195
Figure D-6 – Force Response Plots with Model Values (v=700 mm/min)	195
Figure D-7 – Force Response Plots with Model Values (v=800 mm/min)	196
Figure D-8 – Force Response Plots with Model Values (v=900 mm/min)	196
Figure D-9 – Force Response Plots with Model Values (v=1000 mm/min)	197
Figure D-10 – Force Response Plots with Model Values (v=1200 mm/min)	197
Figure D-11 – Force Response Plots with Model Values (v=1500 mm/min)	198
Figure D-12 – Force Response Plots with Model Values (v=2000 mm/min)	198
Figure E-1 - Constant Velocity Pushing vs. Bandlimited Pushing Force, m=18.9 kg, v=100 mm/min	199
Figure E-2 - Constant Velocity Pushing vs. Bandlimited Pushing Force, m=18.9 kg, v=200 mm/min	199

Figure E-3 - Constant Velocity Pushing vs. Bandlimited Pushing Force, $m=18.9$ kg, v=300 mm/min.....	200
Figure E-4 - Constant Velocity Pushing vs. Bandlimited Pushing Force, $m=18.9$ kg, v=400 mm/min.....	200
Figure E-5 - Constant Velocity Pushing vs. Bandlimited Pushing Force, $m=18.9$ kg, v=500 mm/min.....	201
Figure E-6 - Constant Velocity Pushing vs. Bandlimited Pushing Force, $m=18.9$ kg, v=700 mm/min.....	201
Figure E-7 - Constant Velocity Pushing vs. Bandlimited Pushing Force, $m=18.9$ kg, v=800 mm/min.....	202
Figure E-8 - Constant Velocity Pushing vs. Bandlimited Pushing Force, $m=18.9$ kg, v=900 mm/min.....	202
Figure E-9 - Constant Velocity Pushing vs. Bandlimited Pushing Force, $m=18.9$ kg, v=1000 mm/min.....	203
Figure E-10 - Constant Velocity Pushing vs. Bandlimited Pushing Force, $m=18.9$ kg, v=1200 mm/min.....	203
Figure E-11 - Constant Velocity Pushing vs. Bandlimited Pushing Force, $m=18.9$ kg, v=1500 mm/min.....	204
Figure E-12 - Constant Velocity Pushing vs. Bandlimited Pushing Force, $m=18.9$ kg, v=2000 mm/min.....	204
Figure F-1 - Constant Velocity Pushing vs. Bandlimited Pushing Position, $m=18.9$ kg, v=100 mm/min.....	205
Figure F-2 - Constant Velocity Pushing vs. Bandlimited Pushing Position, $m=18.9$ kg, v=200 mm/min.....	206
Figure F-3 - Constant Velocity Pushing vs. Bandlimited Pushing Position, $m=18.9$ kg, v=300 mm/min.....	206

Figure F-4 - Constant Velocity Pushing vs. Bandlimited Pushing Position, m=18.9 kg, v=400 mm/min.....	207
Figure F-5 - Constant Velocity Pushing vs. Bandlimited Pushing Position, m=18.9 kg, v=500 mm/min.....	207
Figure F-6 - Constant Velocity Pushing vs. Bandlimited Pushing Position, m=18.9 kg, v=700 mm/min.....	208
Figure F-7 - Constant Velocity Pushing vs. Bandlimited Pushing Position, m=18.9 kg, v=800 mm/min.....	208
Figure F-8 - Constant Velocity Pushing vs. Bandlimited Pushing Position, m=18.9 kg, v=900 mm/min.....	209
Figure F-9 - Constant Velocity Pushing vs. Bandlimited Pushing Position, m=18.9 kg, v=1000 mm/min.....	209
Figure F-10 - Constant Velocity Pushing vs. Bandlimited Pushing Position, m=18.9 kg, v=1200 mm/min.....	210
Figure F-11 - Constant Velocity Pushing vs. Bandlimited Pushing Position, m=18.9 kg, v=1500 mm/min.....	210
Figure F-12 - Constant Velocity Pushing vs. Bandlimited Pushing Position, m=18.9 kg, v=2000 mm/min.....	211

LIST OF ABBREVIATIONS

ISO	International Standards Organization
LSQ	Least Squares curve fitting routine
MAX	National Instruments' Measurement and Automation Explorer
MLE	Maximum likelihood estimator
NPP	Normal probability plot
PC	Personal computer
PID	Proportional-Integral-Derivative controller design
ppr	Points per rotation
PRLS	Partial Revolution Least Squares curve fitting routine
PXI	Peripheral Component Interconnect bus with eXtensions for Instrumentation
RLS	Recursive Least Squares curve fitting routine
SFB	Standard Flexible Body
SRB	Standard Rigid Body
TCP	Transmission Control Protocol
T.I.R.	Total indicated runout
upr	Undulations per rotation
VI	Virtual Instrument

LIST OF SYMBOLS

\mathbf{a}	Matrix of basis coefficients for LSQ curve fitting
a_{\max}	Maximum slide acceleration
A	Off-center distance
A	Friction estimation scaling factor
A	Resampling intermediate variable
\mathbf{A}	State matrix (state space representation)
b_j	Basis function weighting coefficients
\mathbf{B}	Input matrix (state space representation)
$\hat{\mathbf{B}}_k$	Estimated RLS transformation matrix
C	Resampling intermediate variable
\mathbf{C}	Output matrix (state space representation)
C_1	Friction estimation power coefficient
C_2	Friction estimation power coefficient
d	Free sliding distance before rest
d_0	nominal free sliding distance
d_{ampl}	Distance from center of part geometry to center of rotation
\hat{d}_{ampl}	Estimated off-center distance
d_{gap}	Distance to close gap between probe and actuator
d_{lead}	Linear distance to compensate for leading the off-center angle

d_{\min}	Minimum measurement probe stroke distance
d_{probe}	Linear slide measurement probe relative position
$d_{\text{probe},p}$	Probe position at full closure
$d_{\text{probe},pt}$	Instantaneous probe position at end of actuation stroke
d_{remain}	Distance of open gap at end of actuation stroke
d_{slide}	Linear slide position
d_{stroke}	Residual distance error
d_{tip}	Linear slide measurement probe absolute position
df	Degrees of freedom
\mathbf{D}	Direct transformation matrix (state space representation)
E_{kinetic}	Kinetic energy of part in motion
E_{friction}	Dissipative energy of friction
F	Force
F_C	Coulomb friction force
F_e	Exerted force
F_f	Dynamic friction force
F_N	Normal force
F_S	Static friction force
F_p	Peak measured force

$F_{peak,corrected}$	Error-corrected peak force in single actuation
$F_{peak,observed}$	Observed peak force in single actuation
F_{centr}	Centrifugal force
g	Gravitational acceleration
$G(s)$	Transfer function matrix
H	Matrix of basis functions
I	Identity matrix
I_{lim}	Sample inclusion limit for PID integral calculation
J	Mass moment of inertia, required confidence level
k	System stiffness
k_v	Coulomb force / velocity proportionality constant
k_1	Friction estimation power exponent
k_2	Friction estimation power exponent
K_d	Controller derivative constant (PID gain)
K_i	Controller integral constant (PID gain)
K_k	Kalman filter optimal residual gain, RLS residual gain
K_p	Controller proportional constant (PID gain)
m	Mass
m	Number of data points
m_{part}	Mass of part
m_{slide}	Mass of linear slide knife (analogous to rotor)

MSE	Mean square error
n	Number of parameters estimated
$\%OV$	Percent system overshoot with step input
$\%OV_{nom}$	Nominal percent system overshoot with step input
P_k	Running integral offset at current discrete time step
\mathbf{P}_k	Covariance matrix of estimation error at current discrete time step
Q	Process covariance, Kalman filter
r	Circle radius, sample distance magnitude
R	Measurement covariance, Kalman filter
\hat{R}	Estimated part radius
SSE	Sum of squared error
t_0	Actuation start time
t_1	Actuation acceleration complete time
t_2	Actuation begin deceleration time
t_3	Actuation deceleration complete time
t_s	Settling time
$t_{s,nom}$	Nominal settling time
T_d	Derivative time, number of periods in derivative calculation (PID gain)
T_i	Integration time (PID gain)
\mathbf{u}	Matrix of system inputs (state space representation)
\mathbf{u}_k	System input state at current discrete time step

v	Velocity
v_0	Initial linear velocity
\mathbf{v}_k	Random measurement disturbance at current discrete time step
v_{\max}	Maximum interference velocity
$v_{part,a}$	Part velocity after impact
$v_{part,b}$	Part velocity before impact
$v_{ring,\max}$	Maximum part approach velocity
v_s	Constant actuation velocity, Stribeck velocity
$v_{slide,a}$	Linear slide velocity after impact
$v_{slide,b}$	Linear slide velocity before impact
$v_{slide,\max}$	Maximum slide velocity
\dot{v}	Linear acceleration
w_i	Individual objective weighting coefficient
\mathbf{w}_k	Random process disturbance at current discrete time step
x	Geometry calculation intermediate variable
\mathbf{x}	System state matrix (state space representation)
$\dot{\mathbf{x}}$	Time derivative of system state (state space representation)
(x_0, y_0)	Circle center point
x_f	Final object position
\mathbf{x}_k	System state at current discrete time step

$\hat{\mathbf{x}}_k$	Estimated system state at current discrete time step
\mathbf{y}	Matrix of system outputs (state space representation)
\mathbf{z}_k	Observed system value at current discrete time step
\mathbf{z}_{k+1}	Observed system value at next discrete time step
Z	Grand objective function
Z_i	Individual objective function
$Z_{\alpha/2}$	Normal distribution Z-value
α_L	Lead angle relative to off-center direction
β	Part geometric angle
β_1	Intermediate part angle variable
γ	Geometry calculation intermediate angle variable
δ_s	Stribeck exponent
ε	Coefficient of restitution, threshold error level
ε_k	RLS observation residual at current discrete time step
ϕ	Absolute direction from center of rotation to center of part geometry
$\hat{\phi}$	Estimated off-center direction
Φ	RLS model parameter matrix
μ	Coefficient of friction (general)
μ_0	Nominal coefficient of friction
μ_k	Kinetic coefficient of friction
μ_s	Static coefficient of friction

σ	Population standard deviation of a process
σ^2	Population variance
σ_i	Standard deviation of the random error of parameter i
σ_{b1}	Standard deviation of parameter b1
σ_{b2}	Standard deviation of parameter b2
θ	Spindle geometric angle
θ_f	Final object angle
ξ	Random disturbance variable
ω_0	Initial rotational velocity
$\dot{\omega}$	Rotational acceleration
ω_{\max}	Critical angular velocity

SUMMARY

Precise machining of bearing rings is integral to finished bearing assembly quality. The output accuracy of center-based machining systems such as lathes or magnetic chuck grinders relates directly to the accuracy of part centering before machining. Traditional tooling and methods for centering on such machines are subject to wear, dimensional inaccuracy, setup time (hard tooling) and human error (manual centering).

A flexible system for initial part centering is developed based on a single measurement system and actuator, whereby the part is placed by hand onto the machine table, rotated and measured to identify center of geometry offset from center of rotation, then moved by a series of controlled impacts or pushes to align the centers.

During data collection, the slide velocity is controlled by input from a measuring tip (digital probe) through a PID control scheme. Measurement tip position and spindle radial position are logged in real time. Raw data noise and frequencies higher than 1 undulation per revolution are removed through model estimation of a single-frequency basis function. Parameters derived from the modeled geometry are used to command a multi-step trapezoidal velocity motion profile to move the part to center within a 2.5 μm tolerance.

The prototype centering system is developed as a demonstration platform for research in a number of mechanical engineering areas, particularly:

- Characterization of optimal state estimators through analysis of accuracy and computational efficiency;

- Distributed communication and control, efficient transfer of information in a real-time environment, and information sharing between processes;
- Modeling of sliding dynamics and the interaction of friction with compliant body dynamic models;
- Motion path planning through both deterministic geometric transforms and through frequency domain command manipulation.

A vision is created for future work not only in the described areas, but also in the areas of advanced controller design incorporating multiple variables, derived machine diagnostic information, and application of the distributed communication architecture to information flow throughout the manufacturing organization. The guiding motivation for this research is reduction of manufacturing processing costs in the face of global competition. The technologies researched, developments made, and directions prescribed for future research aid in enabling this goal.

CHAPTER 1

INTRODUCTION

Center-Based Manufacturing Methods

Precise machining and measurement of circular manufactured parts is integral to final assembly quality and long-term performance. Applications of such parts cover all facets of manufacturing from large turbomachinery to miniature precision assemblies. The output accuracy of center-based machining systems such as lathes or magnetic chuck grinders, as well as measurement accuracy of center-based metrology equipment relates directly to the accuracy of part centering before machining. A typical roundness tester is shown in Figure 1.1.



Figure 1.1 - Mitutoyo RA-100 Roundness Measuring Machine [Mitutoyo 2006]

A number of methods are currently employed to ensure coincidence of geometric center with center of rotation prior to processing. Traditionally, center-based machines achieve initial centering through hard tooling into which the part is fixtured (e.g., chuck

jaws), axis offset compensation methods where an intermediate stage is adjusted between fixture and base (typical of roundness measurement machines), or through manual centering by a skilled operator using a hammer to tap the part as it is rotating and with a dial indicator as feedback. Each of these traditional methods presents a set of costs or penalties to the manufacturing organization as a whole.

Centering Methods

Centering methods range from simple manual actuations to fully automatic compensators, and are typically selected based on total cost analysis.

Manually Actuated Centering

This is the simplest of all the described methods. For example, precise sample measurement of finished bearing rings in manufacturing practice is conducted by placing the finished ground workpiece onto a table mounted to a precision spindle, then manually centering the part, rotating the table, and measuring the part roundness using an encoded glass scale, interferometer, or enclosed measurement probe. The resultant roundness measurement is carried out by calculating the deviation from a reference circle established in accordance with the ISO 4291-1985(E) standard [ISO 1985]. This centering method can be cumbersome and costly in practice, requiring skilled labor and extended cycle times due to manual actuation and limitations of the human machine.

The process is typically carried out manually using a brass hammer and the “touch” of the operator to bring the part within a given tolerance window before measurement (see Figure 1.2). The resulting cost is high in the form of extended centering time, leading to lower achievable part sampling frequency as well as the labor cost and skill involved in the process. The current centering process cycle time is approximately one minute for most parts in the range under study, but for very light or

heavy parts, the manual cycle can take longer, or not be achievable at all within the desired tolerance.

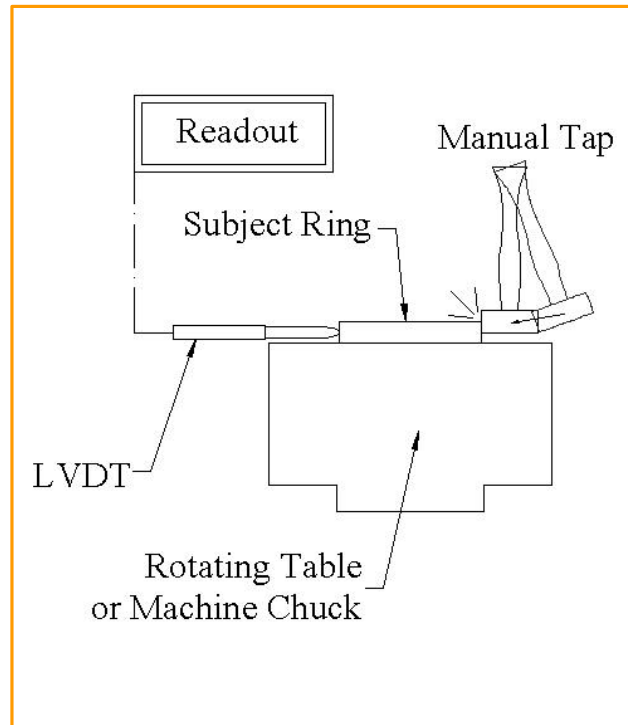


Figure 1.2 - Manual Centering Process

Manual centering methods are subject to human error, both in accuracy and repeatability, as well as concerns of operator safety since the part must be rotating in an unguarded state as the operator centers it.

Jaw-Type Fixturing

Another widely-used centering method in manufacturing is fixturing by chuck jaws or collets. In such a system, the part is placed into the fixture zone, and then the work holding mechanism is actuated to clamp the part in place (see Figure 1.3).

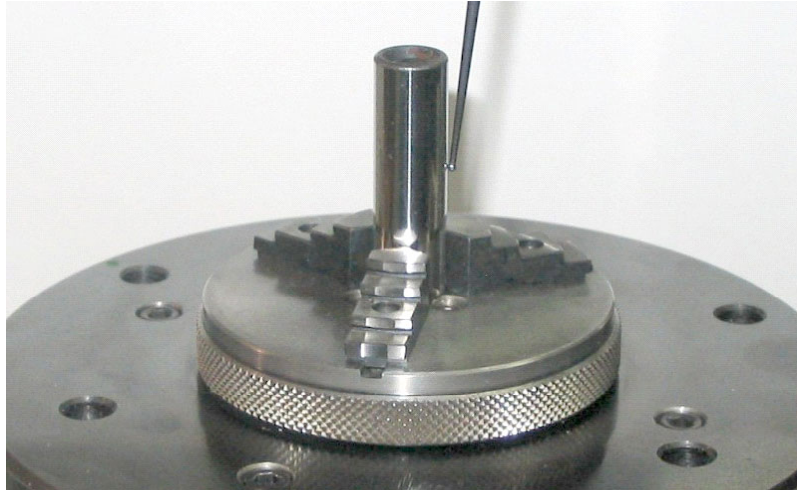


Figure 1.3 - Three-Jaw Precision Chuck for Measurement Machine

In addition to fixture wear and dimensional inaccuracy, a major drawback of the jaw-type system is part deflection introduced by the holding force itself. Although there has been good work concerning analysis of localized deformation due to fixturing forces and dynamic effects on stability, deflections can still be prohibitively large for very flexible rings [Li 2001, Malluck 2004, and Deng 2005]. Such a system is suboptimal in metrology operations, especially for flexible parts, as part geometry is significantly affected by the holding method.

In addition, jaw systems can require additional setup time and introduce an additional tooling requirement, both of which increase cost of use. A flexible system usable on a wide range of parts is a remedy for these shortcomings.

Axis Offset Systems

Axis offset systems are designed with an intermediate adjustable stage between the fixturing area and machine base. Initial measurements are taken to determine the offset vector, and then axis adjustments are made to center the workpiece (see Figure 1.4).

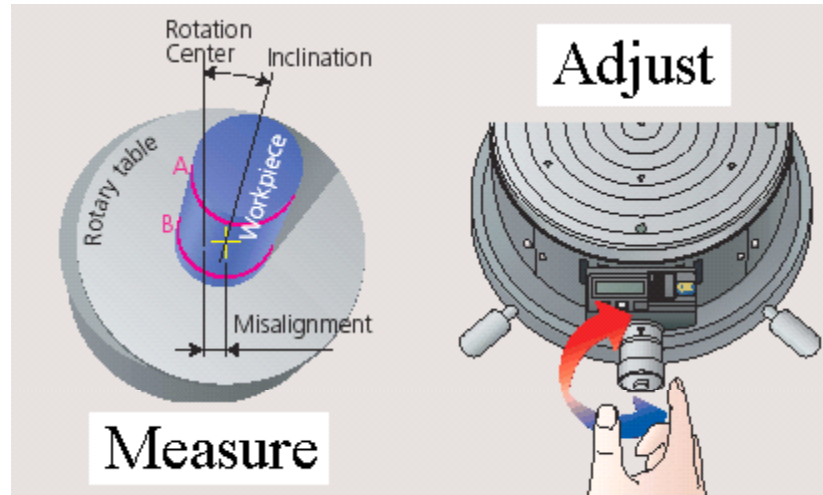


Figure 1.4 - Manual Axis Offset Adjustment [Mitutoyo 2005]

Due to extended cycle times, this centering method is typically used on sample inspection equipment such as roundness machines rather than on production equipment. Cycle time can be reduced by use of an automatic adjustment system incorporating small motor actuators, but with an increased investment cost. Automatic or manual systems are prohibitively expensive for use in production manufacturing equipment due to integration of precise servomechanisms.

Motivation

The traditional methods of part centering before processing or measurement leave room for improvement in the areas of safety, cost and time savings. Centering in magnetic chucking operations on production equipment is currently performed manually by the skilled operator. In today's domestic market, skilled manual labor is becoming increasingly expensive, so any reduction in the need for skilled labor reduces the operating cost proportionally. The target of this research is to reduce the overall centering time. This reduces operating cost by the elimination of skilled labor and fraction of the overhead cost applied to the centering cycle.

Solution Path and Metrics

In order to design a centering system for a family of bearing rings, a system model is developed by: estimating the known parameters, establishing relationships between physical workpiece characteristics and stiction / friction forces, and controlling the part position dynamically through a closed-loop feedback system of a measurement probe and one or more pushing or tapping actuators. This research builds upon previous work to develop an accurate two-dimensional parametric model of a rotating circular part which includes expected actuation forces due to friction and stiction. An actuator system is then designed and implemented to center the part in the minimal time, and within the target tolerance value of $2.5\ \mu\text{m}$ ($100\ \mu\text{in}$), a current manufacturing requirement.

Initial system design validation is executed through simulation, including robustness to noise and to variations in start position. The final design is implemented and tested through a full physical prototype in order to further validate the design across a range of input rings in the part family.

Research Purpose and Objectives

The broad purpose of this research is the design of a controlled actuation system for automatic centering of a family of bearing rings for the purpose of roundness measurement. The primary objectives are

1. Generation of a parametric system model that accurately incorporates frictional effects and required actuation input based on part geometry and operating conditions.
2. Development of a control algorithm, including workpiece position detection and feedback position control law. This includes an initial push with feedback and subsequent iterative actuations, as well as model refinement (adaptation) based on the system response to an input.

3. Development of overall system architecture for characterizing an unknown workpiece and actuating it to center, including prioritization levels applied to parallel processes.

Important Research Questions

The important questions to be addressed in this research are:

1. What is an appropriate cost function of performance for the centering problem and what is its response over ranges of design variables?
2. Can a single adaptive control algorithm be parameterized to account for a family of similar parts?
3. How robust is the system response over a variation of part and environment characteristics?
4. What is the economic viability of automated part centering as compared with the existing manual operation?
5. How can the resulting control methodology be extrapolated or enhanced to encompass different and larger part families?

Organizational Overview

The remainder of this paper is organized as follows:

- In Chapter 2, a review of previous work in germane domains is presented.
- Chapter 3 presents an overall description of the design constraints and proposed prototype system with a general explanation of system operation and simulation results.
- Chapter 4 discusses the data collection, filtering and analysis methods considered and used to best characterize the part geometry.
- In Chapter 5, the geometric model is used with system dynamic characteristics to plan trajectory path, distance and input energy to impart

to the workpiece for movement. An additional section in this chapter discusses varying the velocity input to the actuator through a frequency filtration scheme to avoid erratic part behavior due to the stick-slip effect.

- Chapter 6 gives a discussion of parameter estimation in real time, particularly deterministic estimation of friction parameters. Friction is estimated through both part positional behavior and through direct force measurement, and an optimal combined estimation is given. Additionally, a heuristic compensation scheme and information available to downstream processes are described.
- Finally in Chapter 7, statistical validation results are presented with directions for continuing work in the described areas.

CHAPTER 2

BACKGROUND AND PREVIOUS WORK

Centering System Research

Traditional Centering Approaches

The previously-described methods for centering in industrial use today have been augmented by numerous research improvements. As machine tool accuracy and speed improvements are implemented, workholding has lagged, often almost as an afterthought to machine tool developments [Destafani 2005]. Workpiece location error can arise from different sources, including

- Inaccurate part placement in the fixture
- Fixture geometric error
- Elastic deformation of the fixture by clamping force
- Elastic deformation of the workpiece by clamping force
- Fixturing on datum planes that contain surface errors

These effects have been successfully modeled and validated, showing that location error can be appreciable in fixtured systems [Salisbury 1998, Raghu 2005].

Dynamic effects are another source of inaccuracy. The latest chuck improvement research has been in dynamic force modeling and optimization in an effort to minimize inaccuracy from inelastic deflection by chuck jaw force. Research in this area prior to the last 10 years has mainly been in expert-systems approaches based in heuristics, and has just recently seen a turn toward true analytic modeling of machining force [Mishra 1991]. Siebenaler [2006] forgoes the typical assumption of rigid fixturing and explores finite element modeling of the entire workpiece-fixture system. Deng [2005] gives an extensive analytic treatment to general fixture modeling considering resonance effects.

Additionally, accuracy remains a consideration as cutting lathe chuck speeds increase over 10000 rpm to improve production output. Accuracy in these high-speed chucks is on the order of 10 μm , and improvement is desired beyond that [Waurzyniak 1999].

Impact-Based Positioning Approaches

A number of research efforts have been directed at positioning parts using impact actuation. Benefits are a more inexpensive and flexible actuation system that can be designed for very large or very small parts. Research in application of impact to positioning has mainly been focused on static initial and end conditions and single impact system input. That is, a part initially at translational and rotational rest is struck once to impart a velocity, and then allowed to come to rest under environmental conditions (typically friction).

Application of these concepts to impact-based static positioning systems is treated separately by Mendes et al. [1996] in the printed circuit board positioner, by Liu, Higuchi and Fung [2003] in their piezoelectric positioning table, as well as by Siebenhaar [2004] in electromechanical hammer control.

Friction Modeling

Friction is present in all mechanical systems, and contributes significantly to force analysis and control of motion systems. In this case, it is important to fully understand and accurately model friction when developing an idealistic model of the physical system.

There exists substantial research on modeling of static and dynamic friction, both in the idealized linear case and the nonlinear case. Both Olsson et. al. [1998] and Åström [1998] give a comprehensive overview of the major static and dynamic friction models

utilized in practice. These ideas are extended to the special case of low velocity friction compensation by Adams and Payandeh [1996].

The classical friction model was derived by Coulomb and is of the linearized form

$$F = F_C = \mu F_N \quad (2.1)$$

This model has been successfully applied in the literature, and is the basis for generalized idealistic friction modeling. It has been successfully augmented by adding a linear viscous component of the form

$$F_C = \mu F_N + k_v v \quad (2.2)$$

where k_v is the proportionally constant of force resistant to velocity. Simultaneous identification of μ and k_v through decrement analysis is treated by Feeny and Liang [1996].

These model forms only apply to moving objects $\left(\frac{dx}{dt} \neq 0\right)$. However, when velocity is at or near zero, there occurs distinct discontinuous and nonlinear behavior as shown in Figure 2.1.

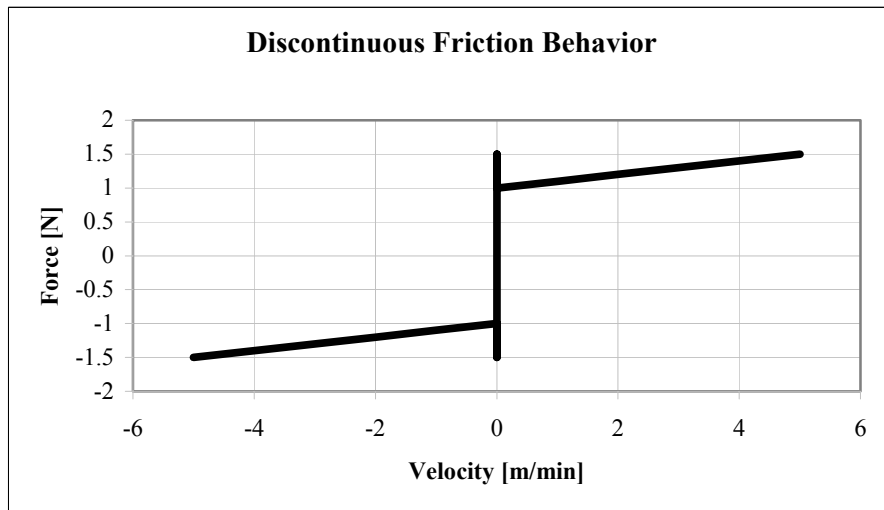


Figure 2.1 - Linear Viscous Coulomb Friction (undefined at $v=0$)

When a stationary object is excited by a force, it acts as a spring, resisting the force until the magnitude overcomes its static friction, a phenomenon known as stiction. After the static friction is overcome and the object begins to move, there is a decidedly nonlinear force-velocity relationship during the transient phase. One simple representation is to augment the Coulomb model with a specification at zero velocity:

$$\begin{aligned}
 F(0) &= F_e, \quad v = 0 \text{ and } |F_e| < F_s \\
 F_e &\equiv \text{applied force} \\
 F_s &\equiv \text{static friction force} = \mu F_N
 \end{aligned}
 \tag{2.3}$$

This model presents problems near $v = 0$ due to discontinuity and localized nonlinear behavior. Stribeck developed a model which separately defines the nonlinear portion of friction force in the neighborhood of $v = 0$:

$$F = \begin{cases} F(v), & v \neq 0 \\ F_e, & v = 0 \text{ and } |F_e| < F_s \\ F_s, & \text{otherwise} \end{cases}
 \tag{2.4}$$

where $F(v)$ is the force required to maintain a constant velocity. Stribeck [Åström 1998] empirically determined

$$\begin{aligned}
 F(v) &= F_C + (F_s - F_C) \exp \left[- \left| \frac{v}{v_s} \right|^{\delta_s} \right] + k_v v \\
 F_C &\equiv \mu_k F_N \\
 F_N &\equiv \text{normal force}
 \end{aligned}
 \tag{2.5}$$

Note that this is the augmented Coulomb model with a transient decay component to account for the discontinuity between definitions at $v=0$. This model is demonstrated in Figure 2.2.

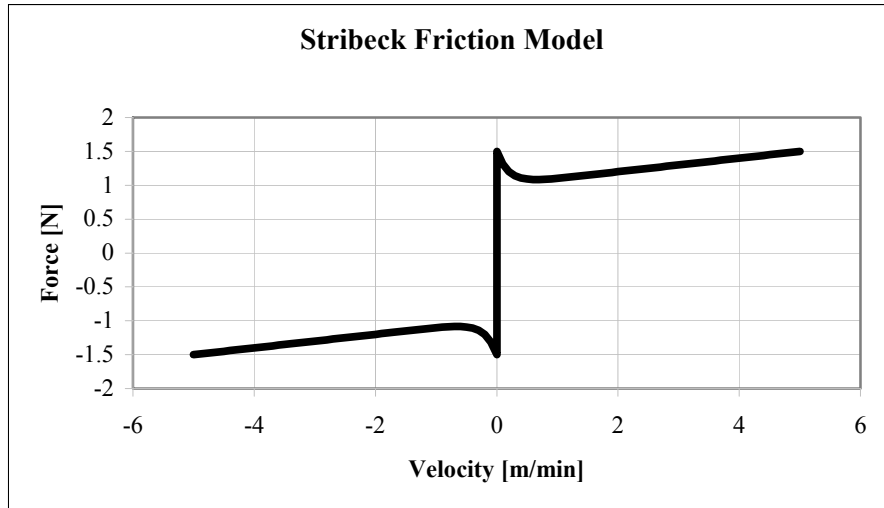


Figure 2.2 - Stribeck Model of Force vs. Velocity

At low velocity, the actuating force is less than the static friction force F_S (the force required to break static friction and begin movement). This disparity between the breakaway force and the force required to maintain velocity can lead to jerky movement or stick-slip motion, as described by Åström in Figure 2.3.

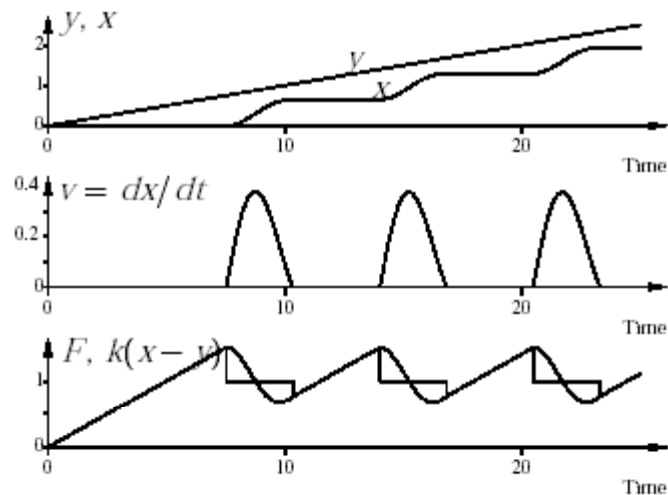


Figure 2.3 - Stick-Slip Motion Depiction of Spring y pulling Sliding Mass x [Åström 1998]

This nonlinear motion, if not properly controlled, can lead to limit cycles or nonconvergent behavior in fine positioning systems [Olsson 2001]. However, as explained by Hirschorn and Miller [1998], the more accurately and completely friction is modeled, the better performance achievable by the compensating controller.

A number of augmented friction models exist which provide accurate results in different application domains. Bliman and Sorine developed a group of dynamic friction models to account for velocity-dependent behavior [Åström 1998]. The LuGre model extends the model of Dahl to capture frictional properties such as stick-slip (known as stiction) and frictional time lag [Canudas de Wit et al. 1995]. Dupont et al. [2000] have developed a dynamic model that captures both stiction and observed presliding displacement. The model of de Wit et al. [1995] brings together most experimentally observed effects: the Stribeck effect, hysteresis, the spring-like behavior of stiction, and variation in the static friction force. The elasto-plastic friction model was developed to capture hysteretic and time-dependent frictional effects [Dupont et al. 2000, 2002, Avanzini et al. 2002]. Song, Kraus and Kumar [2001] analyze available rigid body dynamic models, and Kraus et al. [1998] propose a method for switching between rigid and compliant contact models in frictional systems to avoid discontinuities.

More recently, there has been work to capture frictional effects for small displacement actuation of rigid bodies. Ferrero and Barrau [1997] specifically study friction under small displacement and near-zero velocity. This is a highly nonlinear regime not modeled by Coulomb.

Control of Frictional Systems

The above models have been applied directly in control schemes for systems with appreciable friction. The model of Canudas de Wit et al. [1995] is explored to develop new control strategies for frictional systems, including observer-based control. Hirschorn and Miller [1997] presented a new continuous dynamic controller for application to

systems modeled on the dynamic nonlinear model of LuGre, and successfully applied it to a high-speed linear positioner. Alvarez et al. [1995] developed a control strategy based on accurate friction force estimation. Olsson and Åström [2001] as well as Dupont [1991] have developed friction control systems specifically targeted to avoid stiction-induced limit cycling behavior, a condition where stiction causes a system to continually overshoot its desired state.

Position Control

Several methods have been developed to control, compensate and mitigate frictional effects in precise positioning systems. Adams and Payandeh [1996] surveyed nonlinear friction compensation controller classes, both linear (PD and PID) and nonlinear. Xu and Yao [2000] proposed an adaptive controller based on a nonlinear friction model with unknown parameters.

There exists extensive work on automated fine positioning for the one-dimensional Standard Rigid Body (SRB) and Standard Flexible Body (SFB) idealized cases. Rathbun et al. [2005] have extended the Pulse Width Control (PWC) limiting cases of Yang and Tomizuka for SRBs to cases for SFBs.

Regarding actuation, Lynch and Mason [1999] examined stable (steady state) pushing in robotic applications as an alternative to grip and release. Zesch and Fearing [1998] have analyzed pushing using force control on a micropositioning scale. Wallace [2003] considered impact mechanism design in the centering application. Finally, Huang et al. [1995,1996,1998,2000] have considered a number of cases of impulsive manipulation, including tapper design considerations and modeling approaches.

Pushing Actuation

In addition to system stability and control, the ability to deterministically modify the system is important in frictional systems. One example is actuation of a sliding object

to a desired position. Peshkin and Sanderson [1988] described the motion of a sliding workpiece for all possible pressure distributions on the support surface. Zesch and Fearing [1998] explore force-controlled pushing for microparts with positional results in the 1 μ m range. Lynch and Mason [1992, 1993, 1995, 1996] have done extensive work on planning and control for stable pushing in the application of robotic manipulation as an alternative to pick-and-place positioning, including feasibility studies through both kinematic and force analyses. Lynch also explores friction estimation for pushed objects [1993] and open-loop control for pushing the general polygonal shape [1999], characterized by the “maneuverability” property.

Impulsive Actuation

Huang thoroughly examined manipulation by impulse for robotic applications, including path step planning, object translation and rotation modeling, and actuator design criteria. This research serves as an excellent base to apply to the part-centering problem. Huang and Mason [2000] break the impulsive positioning problems into two subparts: the Inverse Sliding Problem and the Impact Problem.

Inverse Sliding Problem

Given an initial position and orientation and a desired final position and orientation for the target object, what initial translational and rotational velocities need to be imparted to the object? Given the strongly coupled generalized equations of motion in one dimension (ignoring viscous frictional effect at low velocity),

$$m\dot{v} = -F(v, \omega), \quad v(0) = v_0, \quad F \equiv \text{force due to friction} \quad (2.6)$$

$$J\dot{\omega} = -T(v, \omega), \quad \omega(0) = \omega_0, \quad T \equiv \text{torque due to friction} \quad (2.7)$$

the final object positions are given by

$$x_f(v_0, \omega_0) = \int_0^{t_f} v(t) dt \quad (2.8)$$

$$\theta_f(v_0, \omega_0) = \int_0^{t_f} \omega(t) dt \quad (2.9)$$

where t_f = time object rests and $v(t)$, $\omega(t)$ are solutions to the equations of motion. Generally, the coupled system is solved numerically in $[v_0, \omega_0]$ space, and there is only one solution (v_0^*, ω_0^*) .

Impact Problem

Given the required initial translational and rotational velocities v_0^* and ω_0^* , how should these be generated by impact? Huang addresses this question by considering a free mass striker, the friction cone of possible impact vectors, then searching the boundary of the object for a valid impact point. An analytic search form exists for simple shapes such as a cylindrical bearing ring.

Actuator tip friction limits the available velocity ratio $\frac{\omega_0}{v_0}$, so in some cases multiple tap planning is required. Huang also addresses these methods.

Additional Treatments of Impulsive Actuation

Yamagata and Higuchi [1990,1995] treated impact using piezoelectric elements in the application of micropositioning. Huang and Mason [2000] have studied manipulation of sliding objects by imparting a momentum through impulsive actuation, then allowing the object to come to rest. Analysis of such actuation requires separate analysis of energy transfer during impact, then analysis of the free sliding motion with friction. Huang et al. [1995] gave a general solution to these problems (first the inverse sliding problem, then the impact problem) to a rotationally symmetric class of objects, and present limiting cases of this application in Huang and Mason [1996]. Yao et al. [2005] have recently explored an energy-based coefficient of restitution for the planar impact problem. Mirtich and Canny [1995] took a novel approach to impulsive actuation treatment by creating a dynamic simulation environment completely based on the impulse contact

model, where all forms of actuation (pushing, sliding, and impact) are modeled by a series of collisions. This has led to treatment of frictional analyses through time-stepping methods, whereby the integrals of modeled forces are applied over each time step, blurring the boundary between finite forces and impulses [Stewart 2000].

System Identification

The objective of system identification is to create an accurate model of system output given both deterministic (known) and noise or environmental (unknown) inputs. Not only will the base system need to be identified, but the system identification method should be explicitly contained within the algorithm in order to recalculate optimal system model parameters in the face of changing environmental conditions over time (different part conditions in different stages of the manufacturing process).

The generic state-space equation formulation of a system is

$$\begin{aligned}
 \dot{\mathbf{x}} &= \mathbf{A}\mathbf{x} + \mathbf{B}\mathbf{u} \\
 \mathbf{y} &= \mathbf{C}\mathbf{x} + \mathbf{D}\mathbf{u} \\
 x &\equiv \text{system state} \\
 y &\equiv \text{system output} \\
 u &\equiv \text{system input} \\
 A &\equiv \text{state matrix} \\
 B &\equiv \text{input matrix} \\
 C &\equiv \text{output matrix} \\
 D &\equiv \text{direct transmission matrix}
 \end{aligned} \tag{2.10}$$

The transfer function matrix $G(s)$ relating output to input [Ogata 2004] is

$$\mathbf{G}(s) = \mathbf{C}(s\mathbf{I} - \mathbf{A})^{-1} \mathbf{B} \tag{2.11}$$

or in scalar form with explicit Proportional-Integral-Derivative (PID) gains

$$G(s) = K_p \left(1 + \frac{1}{T_i s} + T_d s \right) \tag{2.12}$$

Optimal parameter values of the controller transfer function can be estimated by a number of experimental methods. Time response analysis, where the system is excited by a deterministic input (e.g., step, impulse or initial condition) and observed transient output can provide a low-order system approximation, but may not be accurate enough to control the system. Zeigler and Nichols proposed guiding rules for determining optimal PID gain values for a stable open-loop system based on transient response shape [Ogata 2004].

The above methods assume that the system is observable (all state variables are known). If this is not the case, as with systems where friction cannot be directly measured, an observer can be introduced. An observer-based control scheme relies on model or estimation of the unknown system state that is updated as the system updates.

Another unknown found in systems is noise. Random noise can improperly influence system observation and therefore control. Kalman suggested a filtering method for noise in linear system state variables [Kalman 1960]. According to the Kalman filter, state values for the next discrete time step are given by

$$\begin{aligned}
 \mathbf{x}_{k+1} &= \mathbf{C}\mathbf{x}_k + \mathbf{D}\mathbf{u}_k + \mathbf{w}_k \\
 \mathbf{z}_{k+1} &= \mathbf{H}\mathbf{x}_{k+1} + \mathbf{v}_{k+1} \\
 \mathbf{x} &\equiv \text{system state} \\
 \mathbf{u} &\equiv \text{system input} \\
 \mathbf{z} &\equiv \text{observed system state} \\
 \mathbf{w} &\equiv \text{random process disturbance} \\
 \mathbf{v} &\equiv \text{random measurement disturbance} \\
 \mathbf{H} &\equiv \text{basis function matrix (relates state to measurement)}
 \end{aligned} \tag{2.13}$$

The optimal state estimator with weighting matrix \mathbf{K} on the residual is

$$\hat{\mathbf{x}}_{k+1} = \hat{\mathbf{x}}_k + \mathbf{K}(\mathbf{z}_{k+1} - \mathbf{H}\hat{\mathbf{x}}_k) \tag{2.14}$$

The weighting matrix is used to correct error in the previous prediction to more closely estimate the true state. This method has been shown to be optimal for systems with Gaussian random noise, and is discussed further in Chapter 4.

A Note on Manual Actuation Capability and Cost in the Application

Following are the currently achievable cycle times and tolerances for conventional manual centering and for a traditional centering mechanism. Today the rings in this application are centered using the manual method with the given results.

Manual Centering

The part is placed by the operator and moved into place manually by tapping with visual feedback from the measuring probe digital readout. Current consistently achievable results are

- Cycle Time (centering after part placement) = 60 sec
- Positional accuracy = $2.5\mu\text{m}$ ($100\ \mu\text{in}$)
- Operation cost per part = \$0.42 (based on skilled operator rate of \$25/hr)

Centering Using Alternative Methods

The iris is a mechanism currently used in industrial practice for quick centering in measurement tables. The mechanism consists of three or more curved arms pinned at one end to a fixed reference and slotted at the other while fixed to a rotational disk. As the disk is rotated through a partial revolution, the arms collapse concentrically toward the center of the table (see Figure 2.4). This action essentially aligns any cylindrical object within the arms to the table center.



Figure 2.4 - Three-Blade Iris Centering Device [Taylor 2003]

The typical iris mechanism is able to actuate parts up to 4.5 kg and 150 mm OD with accuracy dependent on form error [Taylor 2003]. Though the cycle time is on the order of only one second, the accuracy is dependent on part form and is not adequate for manufacturing applications whose measurable precision depends on the initial centering state.

The precision chuck is another type of workholding device with three to six dependent jaws that move concurrently to grasp an object on the inner or outer diameter (see Figure 2.5).

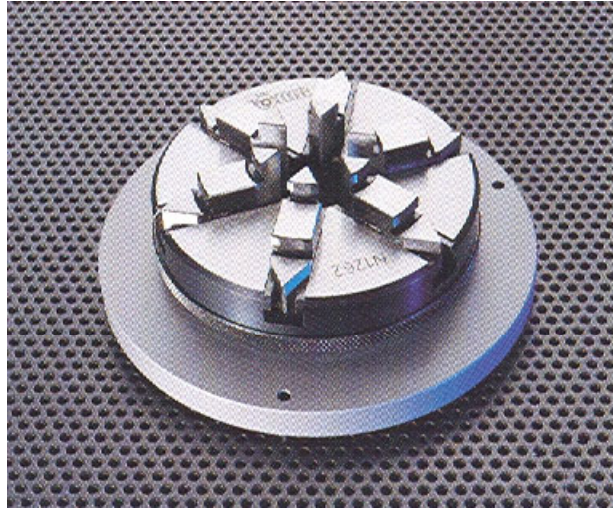


Figure 2.5 - Six-Jaw Centering Chuck [Taylor 2003]

Under light force, this type of workholding can be used to center a workpiece in the given measurement application. However, the chuck or collet mechanism has two drawbacks in the centering application.

First, there is no knowledge of the actual part geometry, specifically deviation from the idealized geometry (*i.e.*, circular form). Therefore, large deviations from the ideal form can cause an unwanted shift in the rotational center of the part. An exaggerated case is shown in Figure 2.6.

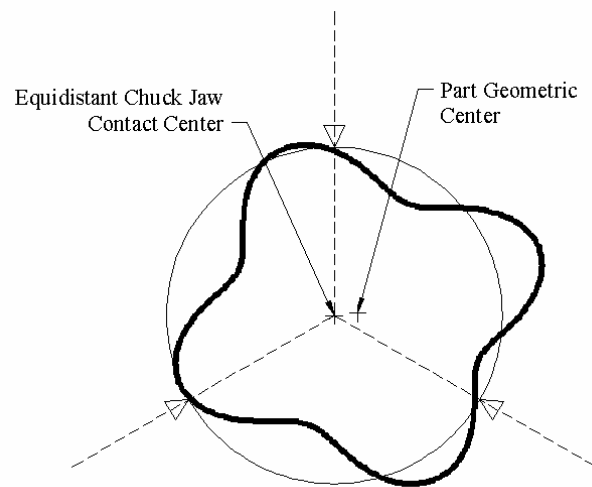


Figure 2.6 - Three-Jaw Chucking of Four-Lobe Part Causing Center Misalignment

Second, the chuck geometry can restrict the available part area for processing. For example, if an OD chuck is used for preprocess centering in a measurement application the lower part of the OD is inaccessible to the measurement probe without repositioning the part (see Figure 2.7).

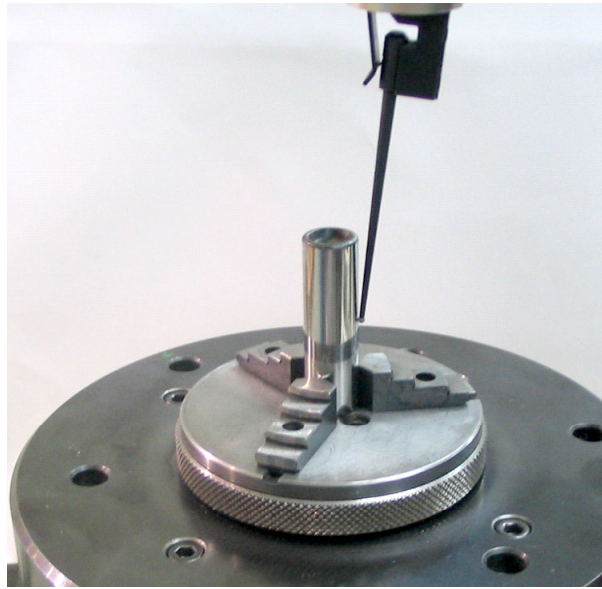


Figure 2.7 - Precision Chuck for Roundness Measurement

These shortcomings in traditional centering support the need for a more open and flexible automated system. This flexibility is a building block of the agile manufacturing organization [Mears 2005].

CHAPTER 3

SYSTEM DESIGN

Design Constraints and Targets

Design constraints for this system were first described in [Mears 2006]. The automatic part centering system is modeled upon the successful but resource-consuming manual centering operation, with the following key differences:

1. The dial indicator used by the operator is replaced with an electronic sensor having adequate resolution and bandwidth for measuring the part off-center distance.
2. The brass hammer is replaced with an actuation device capable of delivering controlled displacements of the part by pushing, tapping or a combination thereof.
3. The operator is replaced with a computer-controlled device and his skill and intelligence is transformed into a control algorithm that can be readily reproduced at low cost.
4. Data acquired from the sensor is synchronized with spindle rotation and processed more quickly for improved centering accuracy, repeatability and time.

In order to center a part, the proposed system:

- Prompts an operator or robot to load a workpiece onto a spindle mounted table. In this application, the spindle axis is vertical and work holding is the force due to gravity, but this concept can also be employed in other contexts (e.g., horizontal spindle and magnetic chuck) with proper modeling.
- Initiates the rotation of the spindle and part.

- Causes the sensor and actuator to approach the outside diameter of the part at a predefined height.
- Causes the sensor and actuator to follow the surface of the part during rotation using feedback from the sensor.
- Acquires sensor data on the part surface location relative to the spindle angle.
- Using the acquired data, computes the vector of the part geometric center with respect to the spindle center of rotation.
- Provides actuation to the part at a position and manner to move its geometrical center toward the center of spindle rotation.
- Uses the residual error of previous centering attempts to modify the actuation command for subsequent centering attempts.
- Identifies a successfully centered part based upon a predefined centering tolerance.
- Retracts the sensor and actuator upon completion of the centering cycle.
- Stops the spindle rotation and signals subsequent processes that the part has been centered.

Design targets for this system are:

- Ability to center rings consistently to an accuracy of $2.5\mu\text{m}$
- Ability to center rings from 0.5 to 70kg
- Minimization of centering error
- Minimization of centering time
- Minimization of implementation cost
- Minimization of operator skill requirement

Equipment

Hardware

The tooling system consists of an air-bearing spindle table upon which the subject part is placed, and a linear motor air-bearing slide that carries the measurement probe and pusher tip (see Figure 3.1). The probe used is a linear scale digital quadrature encoder with 50 nm resolution and 25 mm stroke. The slide encoder resolution is 20 nm and that of the spindle rotary encoder is 0.09° (equivalent to 4000 counts/revolution). The pusher tip is a 5 mm nylon button in an aluminum housing.



Figure 3.1 - Prototype System: Spindle, Linear Slide, Measurement Probe, Pusher Tip

The system is implemented on a National Instruments PXI-8176RT controller with a PXI-7350RT motion control board. PXI is an extension of the compact PCI bus architecture specific to instrumentation. This hardware allows for control loop rates up to 2 kHz with deterministic loop timing in a compact, rugged chassis.

General Control Architecture

The tooling control architecture is based on a real-time version of LabVIEW that allows deterministic loop time control. Determinism in programming is defined as ability to complete a given operation in a fixed, known time.

A flowchart of system operation is given as Figure 3.2. The part is first manually placed onto the machine table and the spindle is rotated. The spindle continues to rotate as the slide is advanced and commanded through a PID controller to follow the measurement probe signal. As the probe contacts the rotating part, the slide that carries the probe follows the periodic radial motion of the part. This is achieved by commanding the controller to maintain constant deflection of the probe. Once the target deflection has been achieved, the instantaneous position of the probe point of contact (neglecting probe tip radius) with the part outer diameter is determined by computing the sum of the probe and slide positions (r_i) and pairing that result with the spindle position (θ_i). Using a recursive least squares algorithm, the resulting data set is then fit to a cosine function having a period of one full spindle rotation. The fit model is used to determine the center of geometry relative to the center of rotation (i.e. the part off-center distance and direction) directly from the amplitude and phase of the cosine function. If the part is not centered to the required tolerance, it is subsequently moved by a rapid, controlled impact or push, initiated at the appropriate time, in an attempt to center the part. Upon completion of the part actuation motion control profile, the controller resumes measurement of the part as described above. This process loop continues until the part has been successfully centered or until an error occurs (e.g., timeout, collision, E-STOP, etc.).

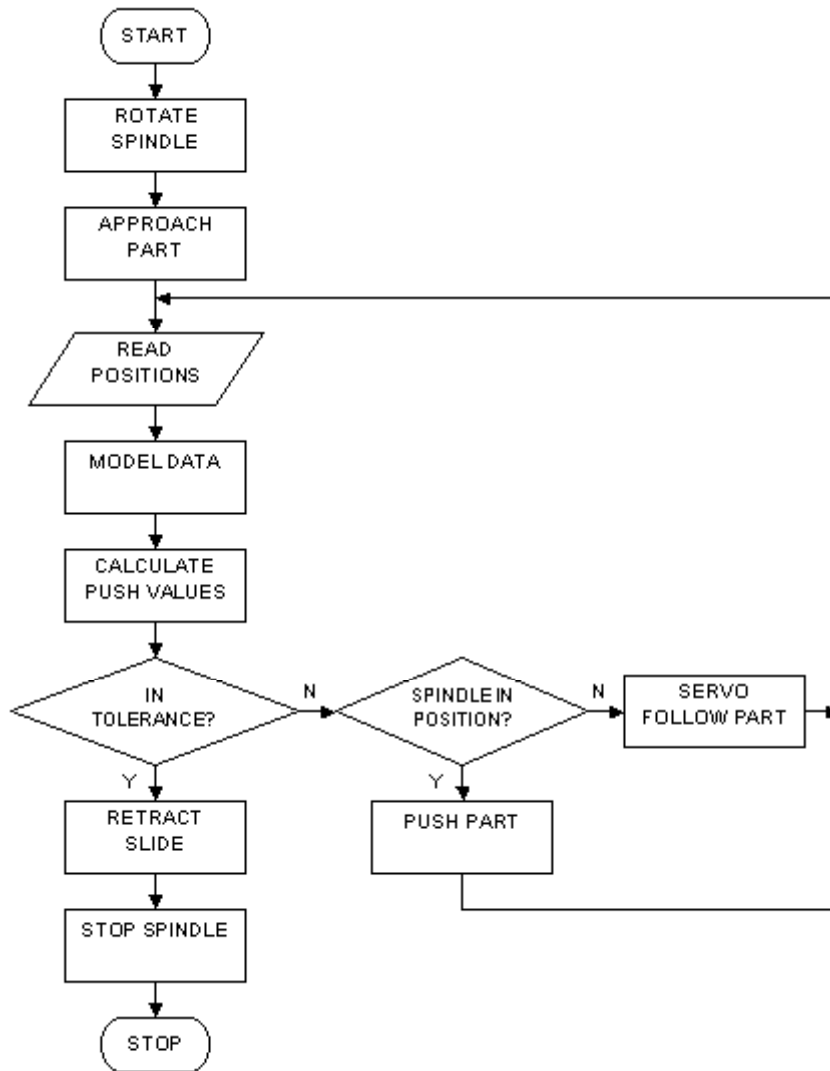


Figure 3.2 – Flowchart of Program Operation

Prioritization

A prioritization level is defined for each program function and used by the processor to schedule thread activity. If a lower priority process is running when a higher priority process requests processor time, the lower priority process is suspended while the higher priority process completes its tasks. After completion, control is returned to the lower priority process. This *preemption* of lower priority tasks by higher allows the

controller kernel to always apply the processor availability to the most important task.

Priority levels in the centering program are:

- Level 1 – Time Critical Priority. Preempts all other processes to maintain deterministic operation of activities.
- Level 2 – High Priority. Preempted by Level 1; runs above all lower priority tasks
- Level 3 – Normal Priority. Non-deterministic operations that can be suspended and restarted without ill effect.
- Level 4 – Low Priority. Preempted by all other tasks. Used mainly for nondeterministic communication between real-time system and host PC system.

Parallel Loop Structure

The algorithm is implemented through parallel loop architecture, with each thread scheduled according to its priority:

- Control Loop (Level 1 – Time Critical). This loop provides PID control during constant deflection servoing of the measurement probe. This loop also contains the pushing code that activates when all push conditions are met. The control loop occurs at a 100 Hz rate. During each following cycle, the probe position is read, the deviation from the target deflection is calculated, and the slide velocity is commanded through a PID control scheme. Superposition of acceleration and deceleration curves is internal to the motion control software. When the modeling is complete and the spindle is in correct position, the part following routine is suspended and the deterministic pushing profile is loaded into the motion controller.

After the push is complete, part following resumes. This loop executes at 100 Hz, or 300 times per revolution at 20 rpm.

- Data Collection Loop (Level 2 - High). This loop acquires measurement probe tip data in relation to spindle position. The data collection loop occurs at 100 Hz. During each pass, it acquires data from the probe, the slide, and the spindle encoders. It then computes the sum of the probe and slide positions. This result is paired with the acquired spindle position to create a raw data point representing the location of the point of contact between the probe and the part outer diameter surface. This loop executes at 100 Hz, or 300 times per revolution at 20 rpm.
- Data Modeling Loop (Level 3 – Normal). This loop fits the acquired signal to a single frequency model analogous to one rotation in order to determine the off-center vector. It becomes active after initial data collection has occurred over at least one full rotation of the part. The entire filtered data set is fitted by a linear least squares algorithm to a single period cosine wave function with a constant DC offset and a period of one spindle revolution. The program extracts from this function the parameters used in pushing, namely the off-center distance and direction. This loop executes every 5° of spindle rotation.
- Communication Loop (Level 4 – Low). This loop transfers user commands and input data from the PC to the real-time PXI controller, and transfers all pertinent output data from PXI memory to the PC user display using Ethernet protocol. Since this process is not time-critical, these actions can be preempted by any other loop, and then resumed after higher-priority activities are complete. This loop executes at 10 Hz, and is preempted by all other parallel loops.

User Interface and Memory Management

The control algorithm is implemented directly on PXI hardware and can run stand-alone. Consequently, a PC is not required, but one can be used for monitoring system performance. The user interface is shown in Figure 3.3. The Data plot displays raw data collected over a single spindle rotation as each point is acquired. The Model plot displays the least squares fit result of the last model loop cycle. The Polar plot tracks the last n (user-settable) models in r- θ form in order to show how the part progresses toward center. Due to the large dynamic range involved during part centering and importance of precision at small amplitudes, the polar plot is scaled logarithmically.

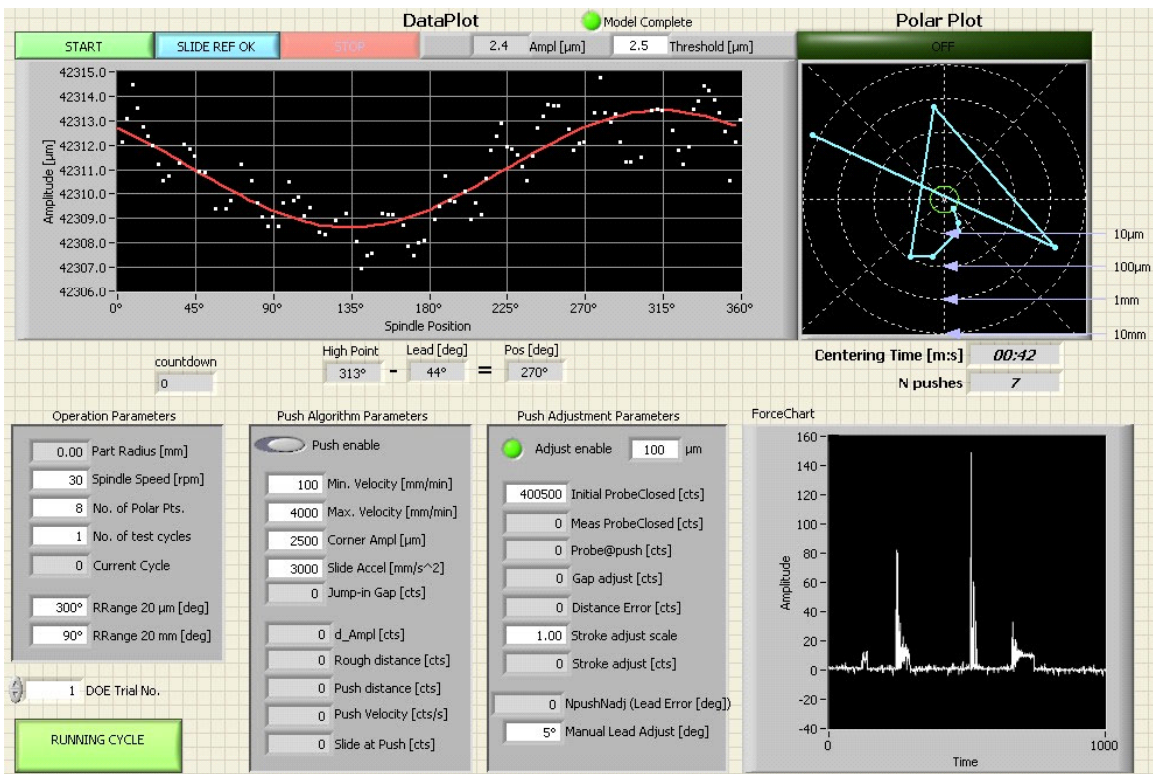


Figure 3.3 - User Interface of Centering System

Memory management of all loop activities and priorities is handled by the LabVIEW-RT runtime engine, which takes advantage of the PXI communication bus. This allows activities utilizing different hardware (e.g., data collection card, motion

control card) to operate deterministically with respect to each other. This management code is included at compilation. Code details for the host (PC) program are given in Appendix A, and code details for the target (Real-Time OS) program are given in Appendix B.

Additional System Design Considerations

Sensing Requirements

General

The design requirements of sensing in this application are:

- Resolve to $\leq 0.1\mu\text{m}$. The centering tolerance target is $2.5\mu\text{m}$ and should be discriminated at least 10X. Provision for lower tolerances in the future should be guaranteed by this design constraint.
- Minimize sensor cost while maintaining performance requirements.
- Minimize contact force. On lighter mass parts, sensor force can have an appreciable effect on actuation force and, in the worst case, sensor force alone can move the part undesirably. Ideally, the sensor would not contact the part being measured (i.e., zero force).
- Maximize sensor look-ahead capability. In order to initially approach the part at maximum slide velocity, sensor look-ahead should be maximized in order to provide adequate stopping distance after the part surface is detected.
- Sense parts of varying material, roughness, finish type, and color.

Minimum Stroke Distance

Sufficient sensor stroke is required to allow for stopping the slide after the probe encounters the part surface. The required stopping distance is a function of the approach

velocity, the initial part off-center distance, the spindle velocity, and the radius of the surface that will be contacted.

Referring to Figure 3.4, the instantaneous part position along the line of action of the probe is

$$r(d_{amp}, \omega, R, t) = d_{amp} \cos(\omega t) + \sqrt{R^2 - d_{amp}^2 \sin^2(\omega t)}$$

$$R \equiv \text{part radius [m]}$$

$$\omega \equiv \text{spindle angular velocity [rad/s]}$$
(3.1)

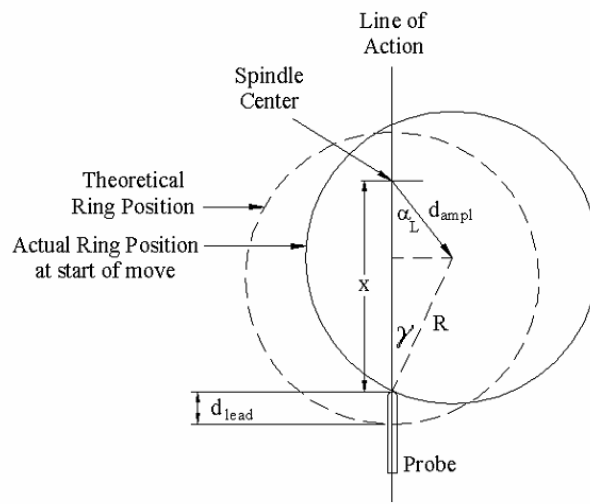


Figure 3.4 - Part Offset Geometry

This is the instantaneous measured radius of the part. The approach velocity of the part surface along the line of action of the probe is found by differentiating the position equation in time:

$$v_{ring}(t) = \frac{\partial}{\partial t} r(d_{amp}, \omega, R, t) = -d_{amp} \omega \sin(\omega t) - \frac{d_{amp}^2 \omega \sin(\omega t) \cos(\omega t)}{\sqrt{R^2 - d_{amp}^2 \sin^2(\omega t)}}$$
(3.2)

Assuming a maximum off-center distance of 25mm, a minimum part radius of 30mm and by (3.2),

$$v_{ringmax} = 154.3 \frac{mm}{s}$$
(3.3)

The maximum slide approach velocity is 120mm/s. The maximum interference velocity is given by

$$\begin{aligned} v_{\max} &= v_{ring,\max} + v_{slide,\max} \\ v_{\max} &= 274.3 \text{ mm/s} \end{aligned} \quad (3.4)$$

The maximum slide deceleration is 2560mm/s². Therefore the minimum stopping time at full deceleration is

$$\begin{aligned} d_{\min} &= \frac{a_{\max} t^2}{2} \\ t &= \frac{v_{\max}}{a_{\max}} = \frac{274.3}{2560} = 0.11\text{s} \end{aligned} \quad (3.5)$$

resulting in a stopping distance of

$$d_{\min} = 14.7 \text{ mm} \quad (3.6)$$

Since this stopping distance decreases as part radius increases, the assumed case is the limiting case. The sensor look-ahead should be maintained longer than this distance to avoid a crash (unintentional part contact) condition.

Selection

Laser and confocal sensors were initially considered due to their noncontacting nature, which would not impart force to the part being measured. However, these sensors were both cost-prohibitive and subject to reflectivity problems for differing part treatments and finishes.

The initial sensor used with the system was an analog signal linear variable differential transformer (LVDT) with 10mm range, 0.1μm resolution and 10V output. The LVDT is comprised of a ferritic core armature passing through three coils. The primary coil is excited by a voltage source, and the signal from the secondary coil on each side is read and summed, yielding a signal proportional to the armature distance from the null (center) position. This is a compact and high-resolution analog design. This

component was acceptable from a design constraint standpoint, but introduced noise into the analog measurement signal through induction of unwanted frequencies from the linear motor drive current.

The final sensor chosen is the Heidenhain MT2581 digital length gauge. This sensor incorporates a glass scale linear encoder, and minimizes noise through filtering during quadrature decoding. The sensor has 25 mm of stroke, 50 nm resolution, and imparts a maximum gauging force of 0.7 N at full stroke. Assuming a typical steel on carbide static friction coefficient of $\mu_s=0.15$, the minimum weight part able to be centered, assuming only gravity work holding, is 0.5 kg, which is at the minimum of the desired applicability domain for the tooling system.

Spindle Velocity Requirement

The angular velocity of the spindle is constrained by four limits:

1. The maximum angular velocity at which the part signal can be reliably sampled. This is determined both by the frequency response of the probe and the maximum data acquisition rate of the control system. Nyquist sampling rules apply.
2. The maximum servo following velocity and acceleration of the slide as it attempts to maintain constant probe deflection.
3. The maximum angular velocity at which a reliable push can be executed at the desired angular location.
4. The minimum centrifugal force that would overcome the work holding force. For a vertical spindle with gravity-based work holding, the work holding force is simply the static friction between the part and the worktable. The maximum angular velocity for this condition is derived from

$$\begin{aligned}
F_{centr} &= F_S \\
F_{centr} &\equiv \text{centrifugal force}[N] = m\omega_{max}^2 d_{ampl} \\
m &\equiv \text{part mass}[kg] \\
\omega_{max} &\equiv \text{critical angular velocity}[\frac{rad}{s}] \\
d_{ampl} &\equiv \text{off - center distance}[m] \\
F_S &\equiv \text{static friction force} = \mu_s mg \\
\mu_s &\equiv \text{static friction coefficient} \\
g &\equiv \text{gravitational acceleration}[\frac{m}{s^2}] = 9.807
\end{aligned} \tag{3.7}$$

Solving for angular velocity,

$$\omega_{max} [rpm] = \frac{60}{2\pi} \sqrt{\frac{\mu_s g}{d_{ampl}}} \tag{3.8}$$

Conservatively assuming $\mu_s=0.05$ and a 25mm maximum off-center distance,

$$\omega_{max} = 42.3 \text{ rpm} \tag{3.9}$$

The maximum angular velocity as limited by centrifugal force can be increased by increasing the work holding force through:

- Increased friction. The assumption of such a low value for μ_s is quite conservative. Actual measurements of different rings on the prototype setup are in the range 0.15-0.25.
- Supplementing with magnetic work holding force. This can come from electromagnetic chucking force as on a grinding machine or by the addition of small subsurface magnets installed below the table rails. Magnetic work holding cannot be used on nonferrous parts.
- Supplementing with some other form of work holding force such as Coulomb force or compliant adhesives in either fluid or gel form.
- Decreasing off-center distance of the part. As the part approaches center, off-center distance is decreased and the spindle speed can increase according to (3.8).

Stiffness Determination

The system stiffness is modeled as a simple spring according to Hooke's Law:

$$F = kx \quad (3.10)$$

The actual stiffness is determined through small actuations of the linear slide against a fixed object. The resultant force is measured using a piezoelectric force sensor and the stiffness k calculated according to (3.10). Results are shown in Table 3.1

Table 3.1 - System Stiffness Data

Actuation Distance [μm]	Measured Force [N]	System Stiffness [$\text{N}/\mu\text{m}$]
10	10.7	1.07
15	16.0	1.07
20	22.4	1.12
25	31.0	1.24
30	37.4	1.25
35	40.6	1.16

The average system stiffness is $1.15 \text{ N}/\mu\text{m}$ and stable over the range of offset distances tested, validating the underlying linear model. This stiffness value is used in subsequent simulations and modeling.

Restitution Determination

Restitution is a coefficient factor representing the fraction of energy transferred from one body to another in dynamic contact. The remaining fraction of energy is lost as heat or damped decay vibration within the bodies.

The restitution of the system is determined analysis of the impact process through Newton's Kinematic Impact Law:

$$\begin{aligned}
-\varepsilon(v_{slide,b} - v_{part,b}) &= v_{slide,a} - v_{part,a} \\
\varepsilon &\equiv \text{coefficient of restitution} \\
v_{part,b} &\equiv \text{part velocity before impact} = 0 \\
v_{part,a} &\equiv \text{part velocity after impact} \\
v_{slide,b} &\equiv \text{slide velocity before impact} \\
v_{slide,a} &\equiv \text{slide velocity after impact}
\end{aligned} \tag{3.11}$$

Setting initial part velocity to 0, restitution is calculated by

$$\varepsilon = \frac{v_{part,a} - v_{slide,a}}{v_{slide,b}} \tag{3.12}$$

The slide drive is disabled and the slide accelerated by hand and released to impact a stationary part. The measured velocities are

$$\begin{aligned}
v_{slide,b} &= 139 \frac{\mu\text{m}}{\text{ms}} \\
v_{slide,a} &= 104 \frac{\mu\text{m}}{\text{ms}} \\
v_{part,a} &= 222 \frac{\mu\text{m}}{\text{ms}}
\end{aligned} \tag{3.13}$$

resulting in a restitution value of

$$\varepsilon = 0.85 \tag{3.14}$$

This value is used in the energy modeling of Chapter 5.

System Plant Identification and Response

The plant model parameters (mass, stiffness, damping, motor characteristics) were initially selected from product literature and confirmed using stimulus-response testing, whereby the position and phase response to a sinusoidal input at varying frequencies is measured. The system gain and phase response is shown in Figure 3.5.

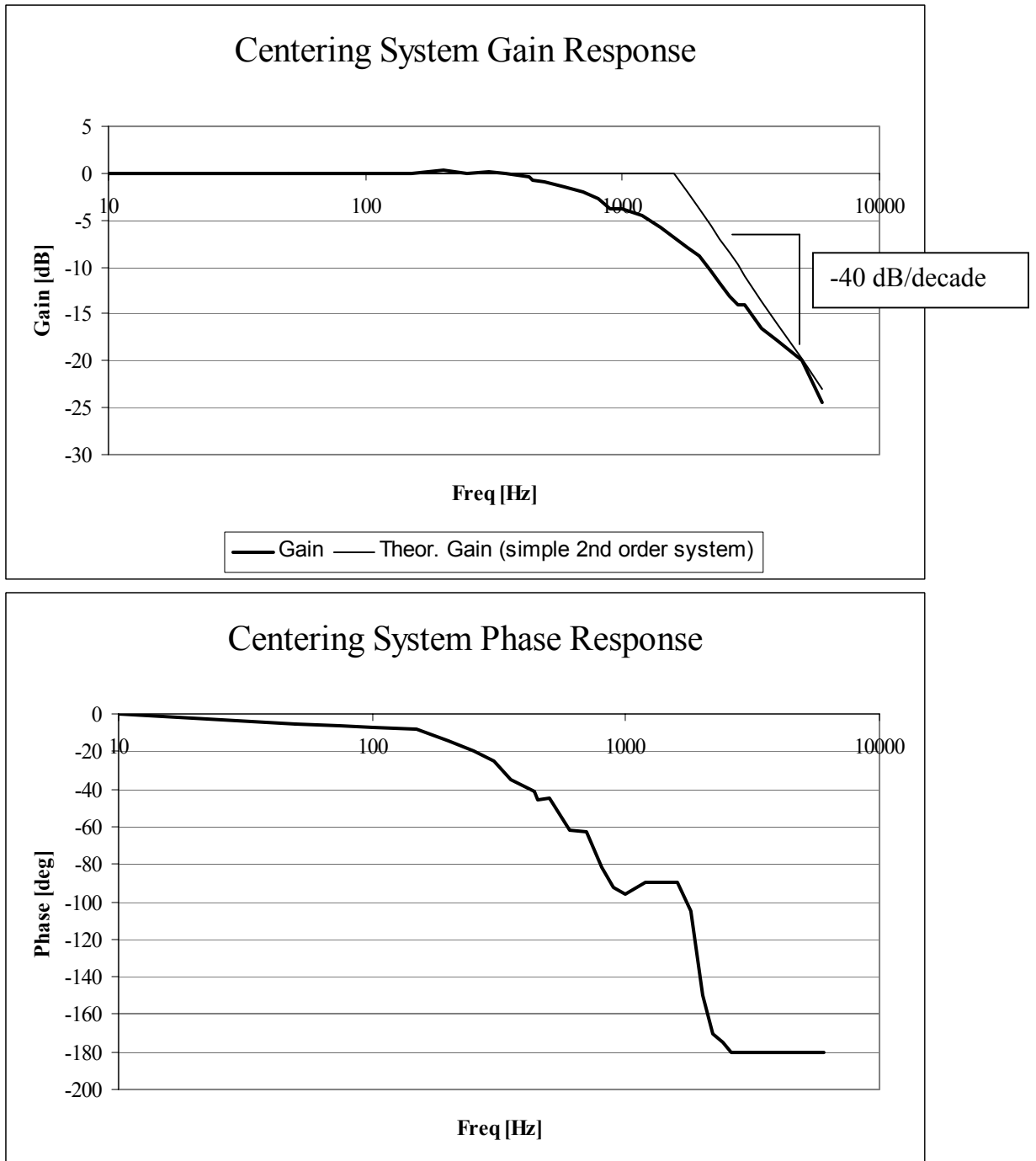


Figure 3.5 - Bode Plot of Linear Slide System

The system exhibits characteristics of a second order system, most notably a -40 dB/decade roll off attenuation above the corner frequency and phase shift not greater than

-180°. The system is therefore modeled as a simple second order system. The -3 dB response bandwidth of the system is 825 Hz.

System Simulation

In order to provide accurate feedback control and to enable virtual testing, the system is simulated using LabVIEW Simulation Toolkit 1.0. Using this software, a system control model is graphically developed and simulated (see Figure 3.6).

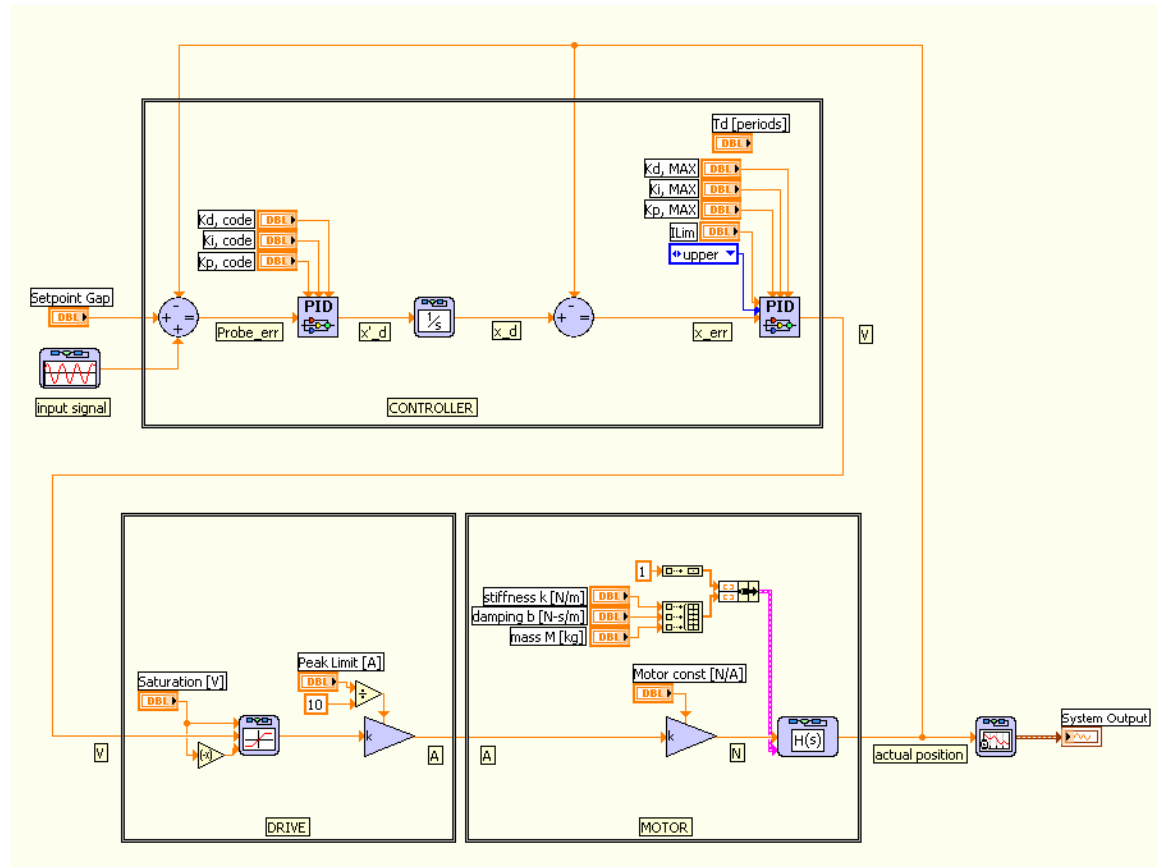


Figure 3.6 - Block Diagram of Prototype Plant

The controller consists of position and velocity Proportional-Integral-Derivative (PID) control loops that output a velocity command to the motor drive. The drive is simulated with saturation and an open-loop proportional gain to output a motor current command. The physical motor is simulated as a simple second order system with a

proportional $\frac{\text{force}}{\text{current}}$ motor constant. The force is applied to the second order system model to produce the simulated actual position for feedback.

The simulation output is given as Figure 3.7. The part location is simulated as a cosine function input with a static offset to represent the clearance between the pusher and part surfaces. The system output signal follows above the input at the commanded offset. The probe error is given as the difference between the simulated commanded and actual slide locations.

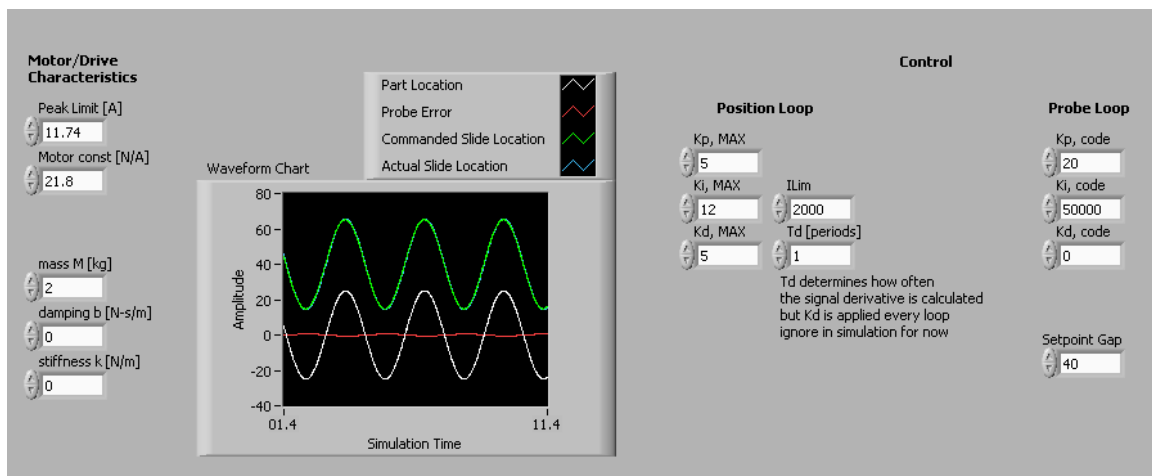


Figure 3.7 - System Simulation Output

Following Control Design

The control tuning parameters for the velocity loop were selected using an exploration of PI parameter space with a minimization objective function incorporating desired settling time and percent overshoot parameters:

$$Z = \frac{t_s}{t_{s,nom}} + \frac{\%OV}{\%OV_{nom}}$$

$t_s \equiv$ actual settling time
 $t_{s,nom} \equiv$ nominal settling time
 $\%OV \equiv$ percent overshoot (step input)
 $\%OV_{nom} \equiv$ nominal percent overshoot

(3.15)

The resultant objective function response surface is shown in Figure 3.8.

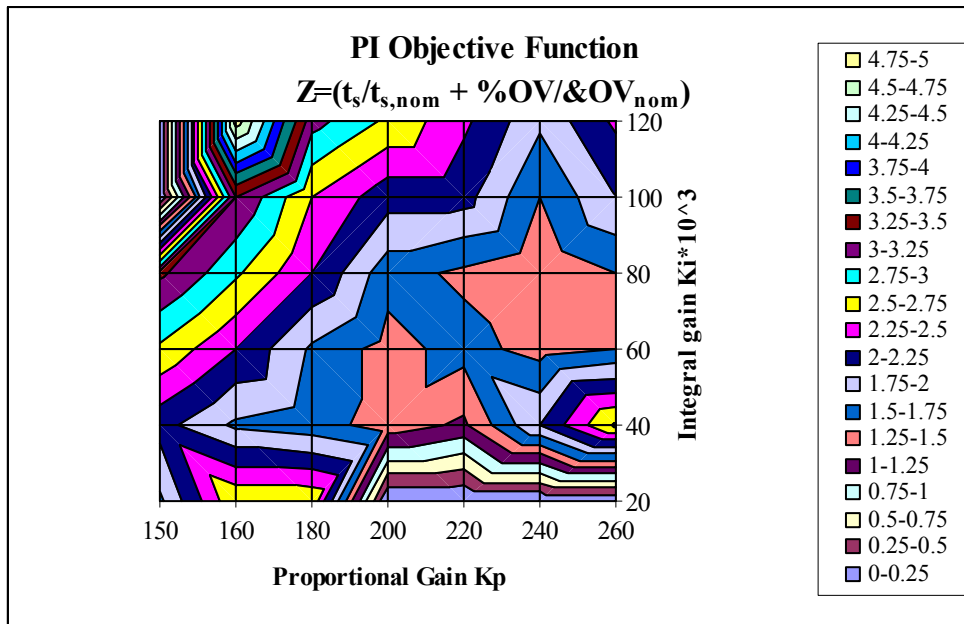


Figure 3.8 - Response Plot of PI Performance Objective

The function approaches a minimum in the local area near $(K_p, K_i) = (200, 50)$ and $(K_p, K_i) = (240, 70)$. The velocity loop settings selected are

$$\begin{aligned}
 K_p &= 200 \\
 K_i &= 50000
 \end{aligned}$$
(3.16)

Following Controller Validation

The designed controller is implemented in a servo following routine whereby the linear slide velocity command is given by deviation of the measurement probe position

for the set position (refer to the block diagram in Figure 3.6). The probe position is read and compared with the set point to determine an error signal. This signal is integrated and the original error signal and its integral are scaled by the gains in (3.16) to provide an output velocity command to the slide.

The system is first tested from an initial state of probe collapsed to the level of the actuator tip, then measured until the steady state following gap is reached. The system output for the static test is shown in Figure 3.9.

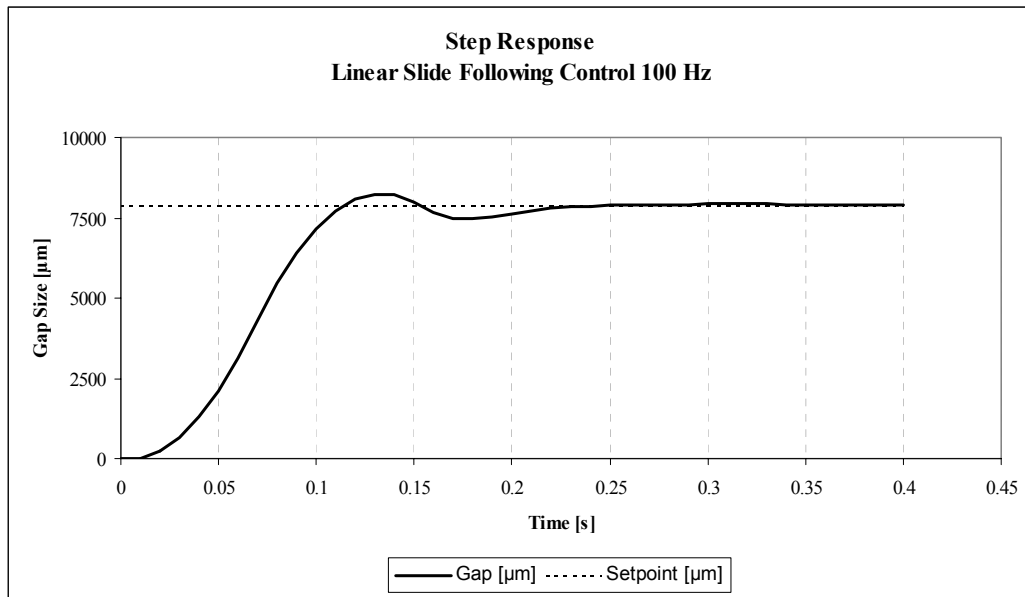


Figure 3.9 - Linear Slide Following Control Step Response

The system reaches the 99% steady state value in 0.11 seconds with a maximum overshoot of 4%. If the spindle were allowed to rotate at a maximum of 50 rpm during the centering cycle, the settling time corresponds to a swept angle of 33°. This is a small amount of lost data, and should not significantly increase the cycle time due to the fitting estimation algorithms described in Chapter 4.

The second system test is following an off-center part rotating at 20 rpm. The set point and following gap during steady state following are shown in Figure 3.10.

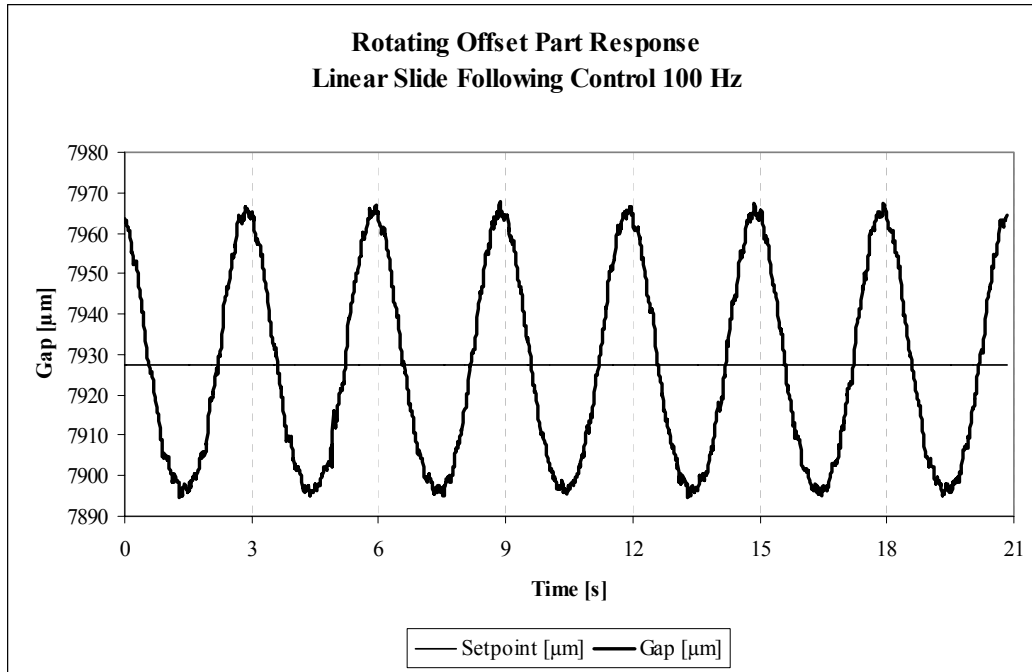


Figure 3.10 – Linear Slide Following Control Dynamic Response (setpoint=7928 μm)

The error is sinusoidal in nature with a frequency equivalent to the spindle rotation frequency and amplitude of 40 μm. This error does not directly affect the cycle since data measurements are taken as the sum of slide and probe positions according to

$$d_{tip} = d_{slide} + d_{probe} \quad (3.17)$$

For a fixed measurement point, as the slide value decreases (moves toward center), the probe value relative to the slide position will naturally increase by the same amount. Summing these to obtain the absolute tip position directly compensates for the following gap error.

Actuation Control Design

The position controller for actuation is specified as a PID control, initially tuned using the autotune feature of the support software, National Instruments' Measurement

and Automation Explorer (MAX). The controller is fine-tuned to eliminate undesirable vibration. The form of the designed PID controller with gains specified is

$$G_c(s) = \frac{K_d s^2 + K_p s + K_i}{s}$$

$$K_d = 15$$

$$K_p = 5$$

$$K_i = 12$$
(3.18)

Additional controller parameters are T_d , the number of periods used to determine the signal derivative, and I_{lim} , the maximum number of samples to be included in the integral error signal. These parameters are selected to be

$$T_d = 1$$

$$I_{lim} = 2000$$
(3.19)

Additionally, a gain schedule structure is included whereby separate controller gain sets can be specified for different parts to be actuated. It is expected that the controller designed for actuating a light part (e.g., 0.5 kg) may perform suboptimally when actuating a heavy part (e.g., 100 kg). In this work the controller is kept constant, but the adaptive nature is designed into the architecture.

Actuation Controller Validation

The designed controller is implemented for part actuation and tested for parts of different mass. Figure 3.11 shows the following error of the slide (i.e., difference between commanded and actual positions) for a part of 0.8 kg mass actuated at $v=3000$ mm/min.

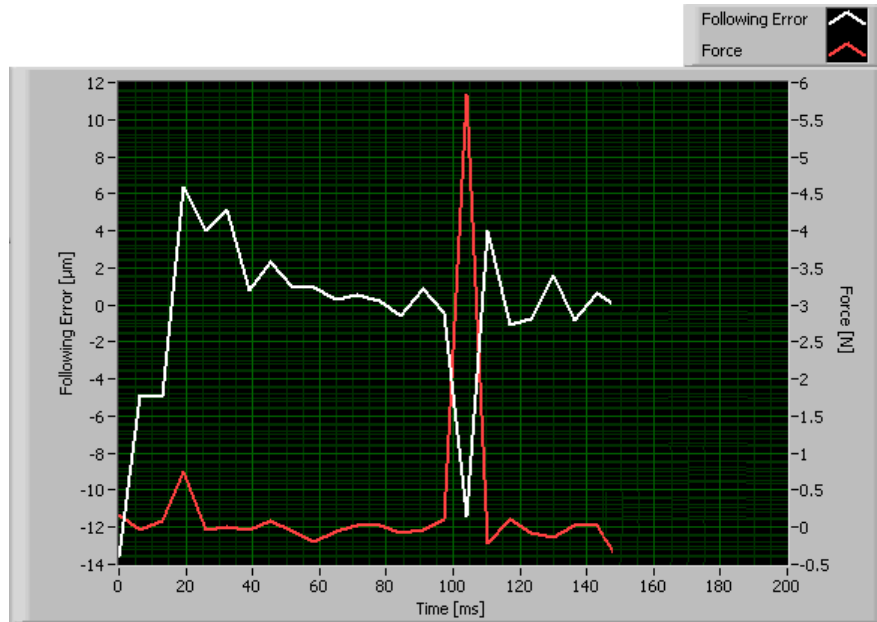


Figure 3.11 - Following Error During Actuation of 0.8 kg Part at 3000 mm/min

The initial following error is due to slide acceleration without part contact. When part contact does occur, the force rises to 6 N, and a slide following error of $-11.5 \mu\text{m}$ is induced. This error is corrected by the controller to within $2 \mu\text{m}$ in under 15 ms.

In Figure 3.12, the slide following error is shown for actuation of a part of 18.9 kg mass at $v=3000 \text{ mm/min}$.

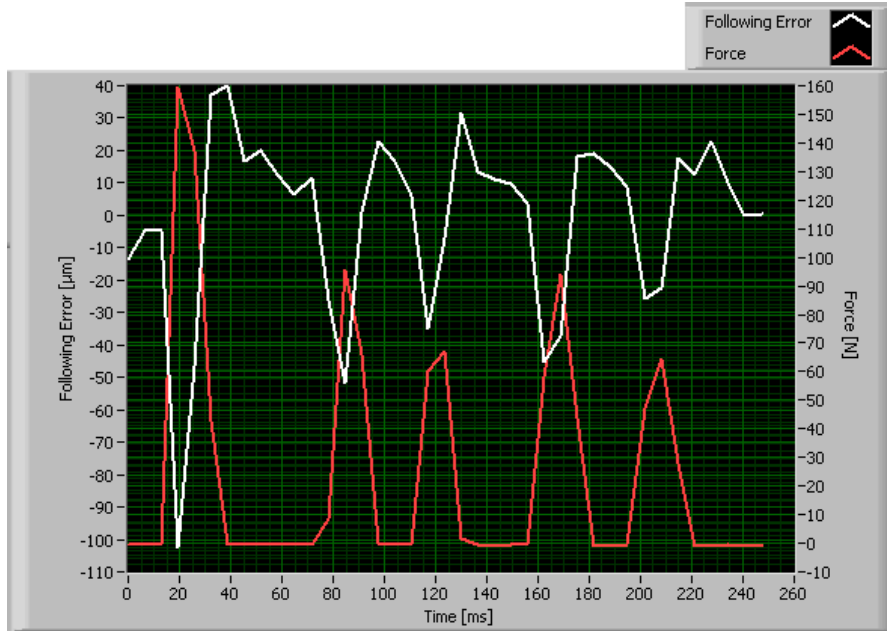


Figure 3.12 - Following Error During Actuation of 18.9 kg Part

In this case, the following error is greater (100 µm at initial contact) with a force rise of over 150 N. The maximum following errors for different actuation velocities for these parts are presented in Table 3.2.

Table 3.2 - Maximum Following Error by Actuation Velocity

Actuation Velocity [mm/min]	Following Error [µm]	
	m=0.8 kg	m=18.9 kg
100	2	10
500	8	26
1000	2	39
2000	14	76
3000	11	101
4000	14	158
5000	20	230

The following error generally increases with both increasing mass and increasing velocity. This is expected, since the controller overcomes a light force more easily than a heavy force, and inertial forces are greater at higher acceleration. Maximum following error for the light part is 20 μm at maximum actuation velocity, while maximum following error for the heavier part is 230 μm . Following error approaches zero at steady state (non-fluctuating force) pushing. However, the oscillatory nature of the error in the transient actuation phase shows room for improvement, either through the adaptive gain scheduling feature described above, the bandlimited velocity pushing described in Chapter 6, or through development of a more sophisticated controller, as described in Chapter 7.

CHAPTER 4

OPTIMAL GEOMETRY ESTIMATION

Data Collection

The measurement tip position is calculated from the linear slide and measurement probe encoder values. The slide convention is positive toward spindle center and the probe convention is positive away from spindle center. The tip position is given by

$$d_{tip} = d_{slide} + d_{probe} \quad (4.1)$$

Measuring tip data is collected relative to spindle radial position, so data pairs are in r - θ form (θ as shown in Figure 4.1).

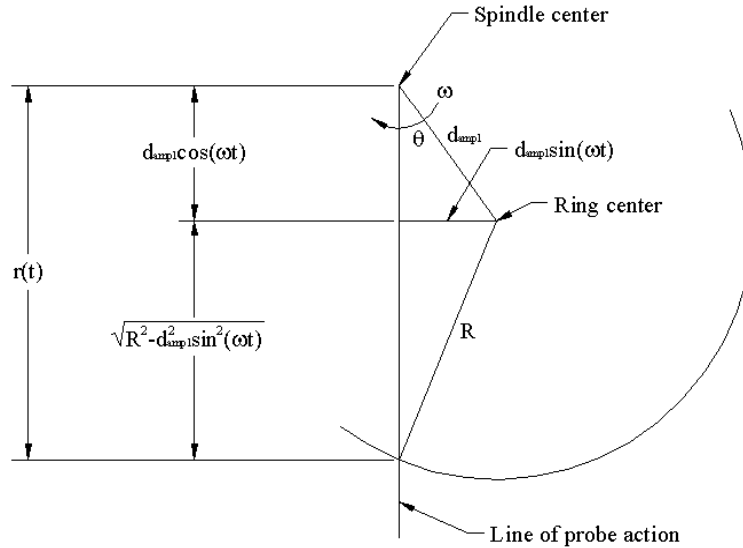


Figure 4.1 - Parameters for Part Velocity Derivation

Part Geometry Estimation

The idealized part geometry projected into two dimensions is circular. Therefore, the collected data in principle should ideally be fit to a model representation of the form

$$(x - x_0)^2 + (y - y_0)^2 = r^2$$

$$(x_0, y_0) \equiv \text{circle center point}$$

$$r \equiv \text{circle radius}$$
(4.2)

This representation is an implicit and nonlinear form that will be difficult or computationally intensive to fit especially in the presence of large random disturbances, a problem frequently studied in the literature [Zelniker 2005].

A logical approach to simplifying the circular representation is to transform into polar space, where the radius is represented as a function of angular offset:

$$r(\theta) = R + \xi$$

$$R \equiv \text{constant radial offset}$$

$$\xi \equiv \text{random disturbance variable}$$
(4.3)

However, the measurement system is fixed to a ground reference, not to the part itself. The result is departure from the constant offset assumption at larger off-center distances as shown in Figure 4.2.

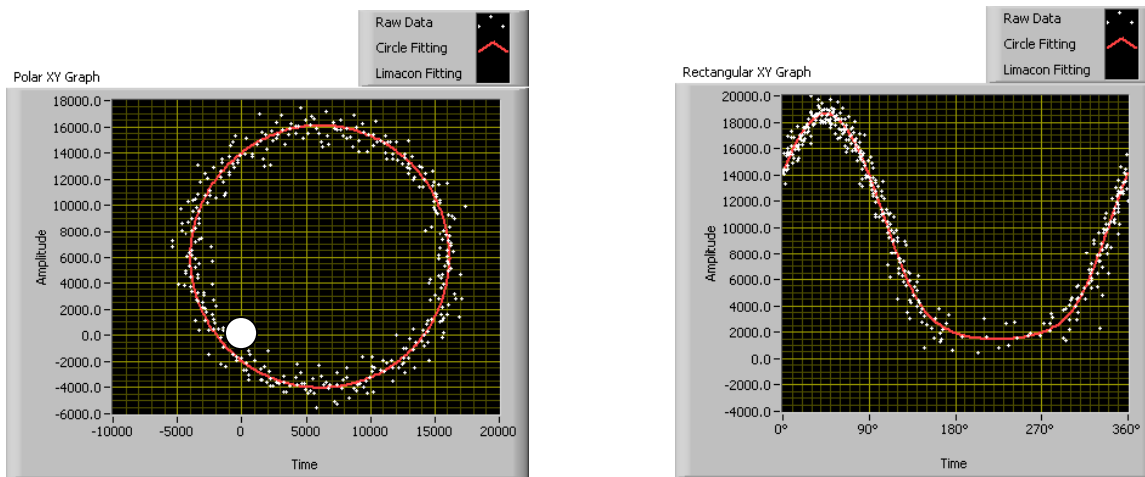


Figure 4.2 - Radial Deviation of Data at Large Offset (expansion point shown)

However, in the centering application, note that the needed model accuracy is not as great at larger offset amplitudes since the part will not be pushed directly to center

over such a distance due to unmodeled inaccuracies and nonlinearity. Therefore, it is possible to use an explicit representation with a single output point for each input. The explicit representation is computationally simple in a single variable and explicit in the independent variable θ . This form also lends itself well to data modeling techniques described later in this chapter.

Data Representation

The data are fitted to a cosine wave with a period equal to one spindle rotation. By introducing the off-center angle (ϕ) and assuming that $d_{amp} \ll R$, equation (4.3) is expanded to:

$$\begin{aligned}
 r(\theta) &= R + d_{amp} \cos(\theta - \phi) + \xi \\
 R &\equiv \textit{part radius [mm]} \\
 d_{amp} &\equiv \textit{off - center distance [mm]} \\
 \phi &\equiv \textit{off - center direction [rad]} \\
 \xi &\equiv \textit{random disturbance [mm]}
 \end{aligned} \tag{4.4}$$

This is explicitly expanded as a sum of scaled basis functions:

$$r = b_0 + b_1 \cos(\theta) + b_2 \sin(\theta) \tag{4.5}$$

where

$$\begin{aligned}
 b_0 &= \hat{R} \\
 b_1 &= \hat{d}_{amp} \cos(\phi) \\
 b_2 &= \hat{d}_{amp} \sin(\phi)
 \end{aligned} \tag{4.6}$$

The coefficients b_i are determined by minimizing the Chi-squared residual function

$$\chi^2 = \sum_{i=0}^{n-1} \left(\frac{r_i - \sum_{j=0}^2 b_j H_j(\theta_i)}{\sigma_i} \right)^2$$

$$H_0 \equiv 1$$

$$H_1 \equiv \sin(\theta)$$

$$H_2 \equiv \cos(\theta)$$

$$\sigma_i \equiv \text{std. deviation of the random error of } r$$

$$\text{assumed distributed } \sim N(0, \sigma^2)$$
(4.7)

From these coefficients, we can directly determine the off-center distance d_{ampl} and direction ϕ to be used in trajectory calculation and actuation path planning:

$$\hat{d}_{\text{ampl}} = \sqrt{b_1^2 + b_2^2}$$
(4.8)

$$\hat{\phi} = \tan^{-1} \left(\frac{b_2}{b_1} \right)$$
(4.9)

Fitting this model form to data taken from a fixed source on a circular object with large center-to-center offset results in a large departure from the circular assumption, as shown in Figure 4.3 using the same data of Figure 4.2:

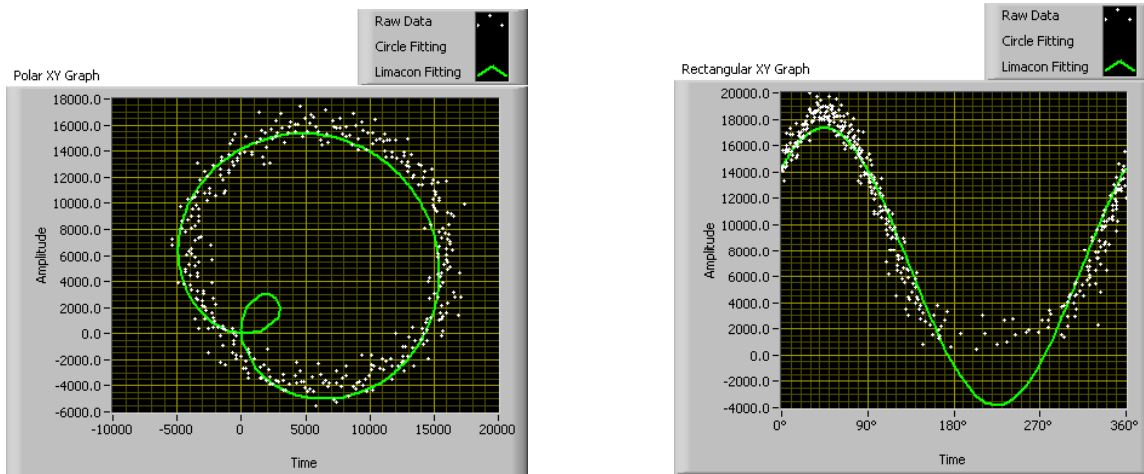


Figure 4.3 - Cosine Fitting of Circular Data at Large Offset (Limaçon Projection)

deviation). Ideally, the geometry estimation error falls below 1% at 20% offset, a large distance in comparison to the 2.5 μm tolerance target on an average-sized part. With typical process variation included this limit is also maintained.

The conclusion of this error analysis is that the error due to the limaçon approximation of a circular geometry increases as offset distance increases, but decreases exponentially as the part approaches center, ultimately yielding error values well within the required tolerance limits. This error situation lends itself well to the centering system, as accuracy is not as important at large offset distances. When actuating the part over a large distance, additional phenomena not included in the system model affect the actuation accuracy. Errors in the trajectory planning, sliding surface defects, tangential effects at the pusher tip, and unmodeled frictional effects are some examples. Because of this, the larger estimation error at longer distances can be tolerated, but as the part approaches center, improved accuracy is required. At this point, the limaçon approximation is sufficient.

Error Correction

Though the estimation error is tolerable in this application, it can be eliminated through correction to an error map of the theoretical case. For least squares, the data are fit to a cosine function through minimization of the chi-squared function of (4.7). Assuming constant variance, this reduces to an objective function of the form

$$\min Z = \sum_i (r_i - \hat{r}_i)^2 \quad (4.10)$$

The relationship of the observed r to part geometry is shown in Figure 4.8.

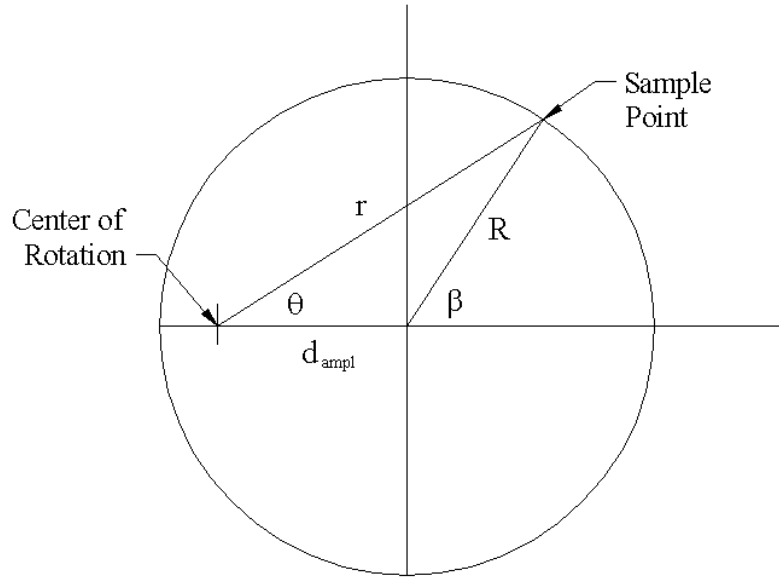


Figure 4.5 - Relation of Geometry to Rotation

The relationship is found by the law of cosines:

$$\begin{aligned}
 R^2 &= r^2 + d_{ampl}^2 - 2rd_{ampl} \cos \theta \\
 r^2 + r(-2d_{ampl} \cos \theta) + d_{ampl}^2 - R^2 &= 0 \\
 r &= d_{ampl} \cos \theta + \sqrt{R^2 - d_{ampl}^2 (1 - \cos^2 \theta)}
 \end{aligned} \tag{4.11}$$

Note that the lower quadratic root is negative when $d_{ampl} \ll R$ and is therefore the degenerate case. Substituting (4.5) and (4.11) into (4.10) gives

$$\min Z = \sum_i \left[d_{ampl} \cos \theta + \sqrt{R^2 - d_{ampl}^2 (1 - \cos^2 \theta)} - b_0 - b_1 \cos(\theta) - b_2 \sin(\theta) \right]^2 \tag{4.12}$$

Assuming zero phase angle, $E[b_0] = \hat{R}$, $E[b_1] = d_{ampl}$ and $E[b_2] = 0$ (i.e., $\phi = 0$), this simplifies to

$$\min Z = \sum_i \left[\sqrt{R^2 - d_{ampl}^2 (1 - \cos^2 \theta)} - \hat{R} \right]^2 \tag{4.13}$$

The continuous integral form of this expression is

$$\min Z = \oint \left[\sqrt{R^2 - d_{amp}^2 (1 - \cos^2 \theta)} - \hat{R} \right]^2 d\theta \quad (4.14)$$

The integral would ideally be solved as

$$Z = Z(R, \hat{R}, d_{amp}) \quad (4.15)$$

Minimization of Z is accomplished by

$$\frac{\partial Z}{\partial \hat{R}} = 0 = \frac{\partial Z(R, \hat{R}, d_{amp})}{\partial \hat{R}} \quad (4.16)$$

Since \hat{R} and \hat{d}_{amp} are estimated by the fitting routine and $\hat{d}_{amp} \approx d_{amp}$, this expression could be solved directly for

$$R = R(\hat{R}, \hat{d}_{amp}) \quad (4.17)$$

Normalizing to \hat{R} gives the general case applicable to any part size:

$$\frac{R}{\hat{R}} = f\left(\frac{\hat{d}_{amp}}{\hat{R}}\right) \quad (4.18)$$

Unfortunately, there is no closed form solution to the integral, so the system must be solved numerically. The solution is shown graphically in Figure 4.6.

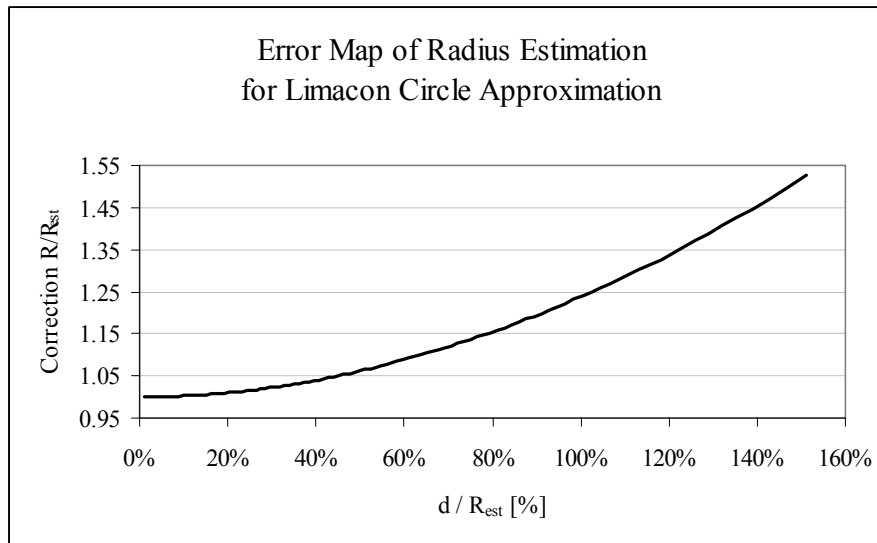


Figure 4.6 - Numerical Solution of Radius Estimate Corrector

The maximum domain value occurs at $d = R$. At this value, $R_{est} = R_{est,max}$. Therefore,

$$\frac{d}{R_{est}} = \frac{R}{R_{est,max}} \quad (4.19)$$

This equality is the state in Figure 4.6 where ordinate and abscissa values are equal, which occurs at $\frac{d}{R_{est,max}} = 151\%$. A second-order solution is assumed of the form

$$\frac{R}{\hat{R}} = c_0 \left(\frac{\hat{d}_{ampl}}{\hat{R}} \right)^2 + c_1 \left(\frac{\hat{d}_{ampl}}{\hat{R}} \right) + c_2 \quad (4.20)$$

A least squares fitting technique is used to find

$$\begin{aligned} c_0 &= 0.2346 \\ c_1 &= 0 \\ c_2 &= 1 \end{aligned} \quad (4.21)$$

The final form of the correction model is

$$\frac{R}{\hat{R}} = 0.2346 \left(\frac{\hat{d}_{ampl}}{\hat{R}} \right)^2 + 1 \quad (4.22)$$

Deviation of this model from the numerical solution is shown in Figure 4.7.

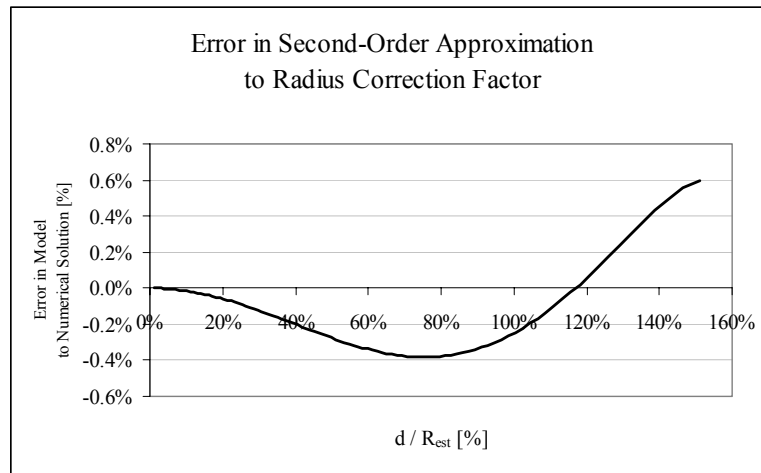


Figure 4.7 - Error in Correction Factor Model

The maximum error in $\frac{R}{\hat{R}}$ is 0.009, or 0.6% at maximum offset. The correction

of (4.22) is next applied to the data of Figure 4.4. The error corrected data of the simulation run average are shown in Figure 4.8 for each noise case.

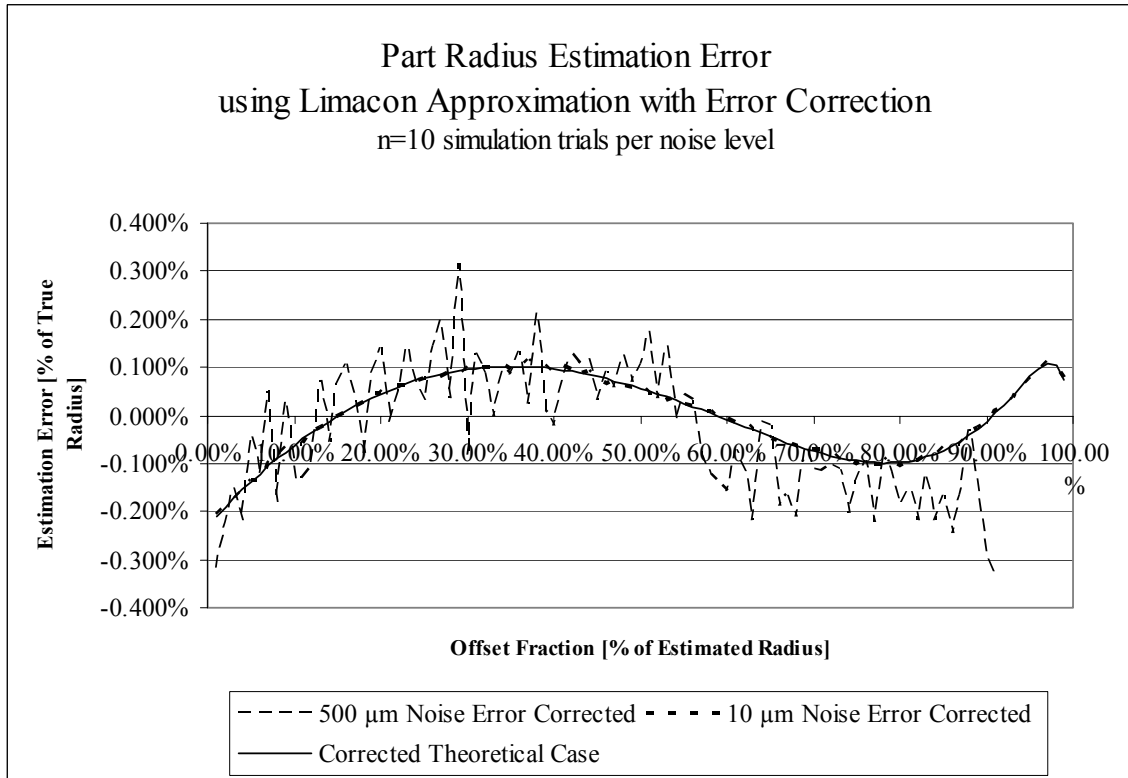


Figure 4.8 - Error-Corrected Data of Limaçon Approximation

The maximum error for the ideal case is -0.2% (due to modeling inaccuracy). In simulation, the maximum error in the 500 μm SD disturbance case is reduced from 26.7% to 0.3% and for the 10 μm SD case the maximum error is reduced from 34.5% to 0.2%.

Limaçon error correction of the radius estimate is implemented directly in the part centering algorithm. This results in an improvement of the push distance estimate and subsequent lead error calculation according to (5.6).

Validation of Error Correction

The error correction of (4.22) is applied to a ground part of 61.9 mm actual radius rotating at 30 rpm on the prototype system. The corrected and uncorrected radii are recorded for different offset distances. The results are shown in Table 4.1.

Table 4.1 - Uncorrected vs. Corrected Radius Estimates, $R_{act}=61.9$ mm

d_{ampl} [μm]	$R_{original}$ [mm]	$R_{corrected}$ [mm]	$d_{push,original}$ [μm]	$d_{push,corrected}$ [μm]	Push Distance Error [μm]
7	61.8	61.8	7973	7977	-4
6030	61.3	61.7	12716	12700	16
12480	60.3	61.7	17220	17200	20
18800	60.7	61.8	22500	22300	200
26400	58.9	61.9	28645	26500	145

The correction reduces the maximum error to the true value from 6.8% to 0.3%. The error in the push distance increases with increasing offset distance according to (5.6). The maximum observed error in the push distance is 200 μm at 18.8 mm offset. This value is compared with the expected result of (4.22). Since

$$\frac{d}{R_{est}} = \frac{26400}{58900} = 0.448 \quad (4.23)$$

Then by (4.22)

$$\frac{R}{\hat{R}} = 1.047 \quad (4.24)$$

This value is equivalent to an estimation error of

$$error = \frac{\hat{R} - R}{R} = \frac{1}{1.047} - 1 = -4.5\% \quad (4.25)$$

This is equivalent to the actual observed error

$$error = \frac{58900 - 61900}{61900} = -4.8\% \quad (4.26)$$

Observed error is as predicted by the error model. Generally, error increases with the noise level of the data set and with increasing rotational speed. This error is significant in the actuation path planning, but is corrected almost completely by the described error map.

Data Fitting Algorithms

Now that the underlying model equation for part geometry is validated, model estimation algorithms are explored. Geometry estimation methods for the collected data are considered based on achievable accuracy and computational requirement. Ideally, the data should be fit to a known set of basis functions in order to determine parameters for actuation. The presence of random system disturbances drives the need for accurate quantification of part geometry, and the system design goal of minimal cycle time requires that a fitting algorithm be computationally simple and quick to converge.

Definitions

Least Squares Fitting (LSQ)

The least squares algorithm fits a set of basis functions \mathbf{H} by adjusting the basis coefficients to minimize the squared residuals:

given $\mathbf{H} = [f_1, \dots, f_n]$ basis functions and data set \mathbf{z}
 find $a_1, \dots, a_n : a_1 f_1(x_i) + \dots + a_n f_n(x_i) \approx z_i$ by

$$\min \sum_{i=1}^m (a_1 f_1(x_i) + \dots + a_n f_n(x_i) - z_i)^2 \text{ or} \quad (4.27)$$

$$\min \|\mathbf{H}\mathbf{a} - \mathbf{z}\|^2$$

$$\therefore \mathbf{a} = (\mathbf{H}^T \mathbf{H})^{-1} (\mathbf{H}^T \mathbf{z})$$

For the limaçon estimation of circle fitting, the basis function matrix is

$$\mathbf{H} = [1 \quad \sin(x) \quad \cos(x)] \quad (4.28)$$

The method requires a data set representative of full circular part geometry for the calculation. The computational intensity increases as the square of the number of data points, and the error order is $O(n^3)$, where n is the number of estimation parameters (coefficients).

Kalman Recursive Filtering

The filter first presented by Kalman (1960) is an efficient recursive solution to optimally estimate the state of a process through the least-squares method given assumed values for the process and measurement variances. For a process state \mathbf{x} with input \mathbf{u} governed by the matrix equation

$$\mathbf{x}_k = \mathbf{A}\mathbf{x}_{k-1} + \mathbf{B}\mathbf{u}_{k-1} + \mathbf{w}_k \quad (4.29)$$

with an observed (measured) value of

$$\mathbf{z}_k = \mathbf{H}\mathbf{x}_k + \mathbf{v}_k \quad (4.30)$$

\mathbf{w}_k and \mathbf{v}_k are process and measurement noise, distributed respectfully as

$$\begin{aligned} p(\mathbf{w}) \text{ is } N(\mathbf{0}, \mathbf{Q}) \\ p(\mathbf{v}) \text{ is } N(\mathbf{0}, \mathbf{R}) \end{aligned} \quad (4.31)$$

where \mathbf{Q} and \mathbf{R} are covariances. The estimator for such a system is given by

$$\hat{\mathbf{x}}_k = \hat{\mathbf{x}}_k^- + \mathbf{K}(z_k - \mathbf{H}\hat{\mathbf{x}}_k^-) \quad (4.32)$$

The covariance of the estimate error is given by

$$\mathbf{P}_k \equiv E\left[(\mathbf{x}_k - \hat{\mathbf{x}}_k)(\mathbf{x}_k - \hat{\mathbf{x}}_k)^T\right] \quad (4.33)$$

The error covariance is minimized by substituting (4.32) into (4.33), differentiating with respect to \mathbf{K} , setting equal to zero and solving for \mathbf{K} . The residual weight \mathbf{K} known as the *Kalman gain* is that which minimizes the estimate error. Welch (2003) gives the derivation to be

$$\mathbf{K}_k = \frac{\mathbf{P}_k^- \mathbf{H}^T}{\mathbf{H}\mathbf{P}_k^- \mathbf{H}^T + \mathbf{R}} \quad (4.34)$$

The implementation of the Kalman filter is of predictor-corrector form. In the given centering application, a single-input, single-output (SISO) scalar system with unity transformation of state and measurement ($\mathbf{A}=1$, $\mathbf{H}=1$) and no input contribution ($\mathbf{B}=0$), the predictor step is

$$\hat{\mathbf{x}}_k^- = \hat{\mathbf{x}}_{k-1} \quad (4.35)$$

$$\mathbf{P}_k^- = \mathbf{P}_{k-1} + \mathbf{Q} \quad (4.36)$$

Note that the best estimator of the state at the next time step is the state value at the previous time step, and process noise is introduced directly to the estimate error. This estimation set now undergoes correction based on the observed value by

$$\mathbf{K}_k = \frac{\mathbf{P}_k^-}{\mathbf{P}_k^- + \mathbf{R}} \quad (4.37)$$

$$\hat{\mathbf{x}}_k = \hat{\mathbf{x}}_k^- + \mathbf{K}_k(z_k - \hat{\mathbf{x}}_k^-) \quad (4.38)$$

$$\mathbf{P}_k = (1 - \mathbf{K}_k)\mathbf{P}_k^- \quad (4.39)$$

This recursive predictor-corrector method marches forward in time as the system state updates and new measurements are taken. If the assumption that process and measurement covariances Q and R are constant is true, then the optimal gain converges to a constant value K .

This implementation is recursive, so does not depend on the number of data points in the set. The system state estimate is updated at each discrete time step given a single new data point. Error order associated with the Kalman filter implementation is $O(n^2)$, where n is the number of state coefficients to be estimated. Also, the method explicitly includes process and measurement variance information.

In the prototype setup, measurement noise covariance R was calculated from a data set taken by measuring a stationary object and found to be $(0.03\mu\text{m})^2$. Process noise covariance Q was tuned for good filter performance, and finally determined to be $(0.005\mu\text{m})^2$. This tuning gives beneficial smoothing of high-frequency physical noise (e.g., dust, part finish), while allowing for accurate representation of lower-frequency part manufacturing variation (e.g., multipoint lobe form from grinding) without appreciable phase lag.

As R is a property of the measurement device, it is assumed constant. Q is a property of not only the system setup, but also the specific workpiece being measured. However, after initial tuning it is held constant for all part types. This assumption may be relaxed in future work, where Q may become an input variable to the part-specific software setup.

One disadvantage of Kalman filtering for state estimation is lack of a defined a priori model underlying the data. Though the state estimate includes information about

process and measurement variance, it does not allow for explicit determination of underlying model parameters.

Recursive Least Squares (RLS)

A recursive form of the traditional least squares fitting algorithm has been developed in recent years. The motivation is to provide a continually updated state estimate that does not require an entire data set to be calculated. This method is similar to the Kalman implementation, but does not include process disturbance assumptions. However, underlying model basis functions are included, allowing optimal determination of model coefficients at each time step. The method is implemented by calculating a recursive transformation matrix \mathbf{B} that relates the system observation z to the optimal state estimate:

$$\begin{aligned}
 x_k &= \mathbf{B}\boldsymbol{\varphi}_{k-1} \\
 \mathbf{B} &\equiv \text{direct transformation and input matrix} \\
 \boldsymbol{\varphi} &\equiv \text{model parameter matrix} \\
 \hat{\mathbf{B}}_k &= \hat{\mathbf{B}}_{k-1} + \mathbf{K}_k \boldsymbol{\varepsilon}_k \\
 \boldsymbol{\varepsilon}_k &= z_k - \hat{\mathbf{B}}_{k-1} \boldsymbol{\varphi}_{k-1} \\
 \mathbf{K}_k &= \mathbf{P}_{k-1} \boldsymbol{\varphi}_k \left[\mathbf{I} + \boldsymbol{\varphi}_k^T \mathbf{P}_{k-1} \boldsymbol{\varphi}_k \right]^{-1} \\
 \mathbf{P}_k &= \left(\mathbf{I} - \mathbf{K}_k \boldsymbol{\varphi}_k^T \right) \mathbf{P}_{k-1}
 \end{aligned} \tag{4.40}$$

Similarly to the Kalman implementation, the RLS method updates the state estimate at each discrete time step, and the resultant error order is $O(n^2)$, where n is the number of state coefficients to be estimated. This method has been shown to be unstable in some situations, but stable variants have been developed such as the exponentially-decaying forgetting factor or the adaptive sliding window [Jiang 2004].

Implementing RLS in the context of the centering system allows part geometry definition through recursion. The system state is defined as

$$\begin{aligned}
x &= \mathbf{B}\boldsymbol{\varphi} \\
\mathbf{B} &\equiv \begin{bmatrix} b_1 \\ b_2 \end{bmatrix} \\
\boldsymbol{\varphi} &\equiv \begin{bmatrix} \sin \theta \\ \cos \theta \end{bmatrix} \\
\theta &\equiv \text{spindle angle}
\end{aligned} \tag{4.41}$$

The residual ε is calculated at time step k using the observed value z :

$$\varepsilon_k = z_k - \boldsymbol{\varphi}_k^T \hat{\mathbf{B}}_{k-1} \tag{4.42}$$

The residual gain matrix \mathbf{K} is calculated based on the parameter covariance matrix \mathbf{P} and parameter matrix $\boldsymbol{\varphi}$ as in (4.40) with \mathbf{P} defined by

$$\begin{aligned}
\mathbf{P} &\equiv \begin{bmatrix} \sigma_{b_1}^2 & \sigma_{b_1}\sigma_{b_2} \\ \sigma_{b_1}\sigma_{b_2} & \sigma_{b_2}^2 \end{bmatrix} \\
\sigma_{b_1} &\equiv \text{std. deviation of } b_1 \\
\sigma_{b_2} &\equiv \text{std. deviation of } b_2
\end{aligned} \tag{4.43}$$

The parameter coefficient matrix \mathbf{B} is found by (4.40). Finally, the system state estimate (excluding DC offset component) is determined by

$$x_k = \mathbf{B}\boldsymbol{\varphi}_{k-1} = b_1 \sin \theta + b_2 \cos \theta \tag{4.44}$$

and instantaneous part offset parameters are estimated by (4.8). These parameters are then passed to the centering algorithm for actuation determination.

Least Squares Using Partial Revolution Estimation (PRLS)

The general Least Squares fitting algorithm previously described is implemented using a full revolution of data. This type of analysis is counter to the design requirement of minimization of cycle time, as the system must wait for a full data set before parameters can be extracted for trajectory path planning. As an alternative, the general LSQ method is applied as each new data point is acquired. This implementation is formulated as

at time step $k+1$ find model data set $\mathbf{y}^{(k+1)}$:

given $\mathbf{H} = [f_1, \dots, f_n]$ basis functions and data set $\mathbf{z}^{(k)}$

find $a_1^{(k+1)}, \dots, a_n^{(k+1)} : a_1^{(k+1)} f_1(x_i^{(k)}) + \dots + a_n^{(k+1)} f_n(x_i^{(k)}) \approx z_i^{(k)}$ by

$$\min \|\mathbf{H}\mathbf{a}^{(k+1)} - \mathbf{z}^{(k)}\|^2 \quad (4.45)$$

$$\mathbf{a}^{(k+1)} = (\mathbf{H}^T \mathbf{H})^{-1} (\mathbf{H}^T \mathbf{z}^{(k)})$$

$$\mathbf{y}^{(k+1)} = \mathbf{y}^{(k)} + \mathbf{H}\mathbf{a}^{(k+1)}$$

and parameter estimation of amplitude and phase is made at each time step.

The LSQ algorithm can therefore be alternatively implemented at each time step to gain a refined LSQ model over the latest data range. Implementation in this fashion is beneficial because it can provide an immediate estimate rather than waiting for a full data set before any information is available. Note that this is not a recursive implementation; the data set is fully reevaluated at each time step. Since the computational complexity of the LSQ algorithm increases as m^2 (square of the number of data points), this method is prohibitively inefficient for real-time implementation on a large scale, but serves as a comparison alternative to the more efficient recursive methods.

Fitting Algorithm Simulation

Each of the described methods is employed to fit a curve to simulated sinusoidal data with randomly distributed Gaussian disturbance. Figure 4.9 shows a raw function of the form

$$y = A \cos(x - \phi) + \xi$$

$$A = 1$$

$$\phi = \frac{\pi}{2} \quad (4.46)$$

$$\xi \text{ is } N(0, 0.5^2)$$

Fit curves for Kalman Filtering, and Recursive Least Squares signal analysis techniques are given in Figure 4.9 and Figure 4.10 respectively. The Kalman filter uses the following parameters:

$$\begin{aligned} Q &= 0.0005 \quad (\text{process variance}) \\ R &= 0.03 \quad (\text{measurement variance}) \end{aligned} \quad (4.47)$$

Figure 4.11 shows results for the *Partial Revolution Least Squares (PRLS)* algorithm, whereby the entire data set is refit after each new point is taken. Each figure also shows the underlying generation function of the data set.

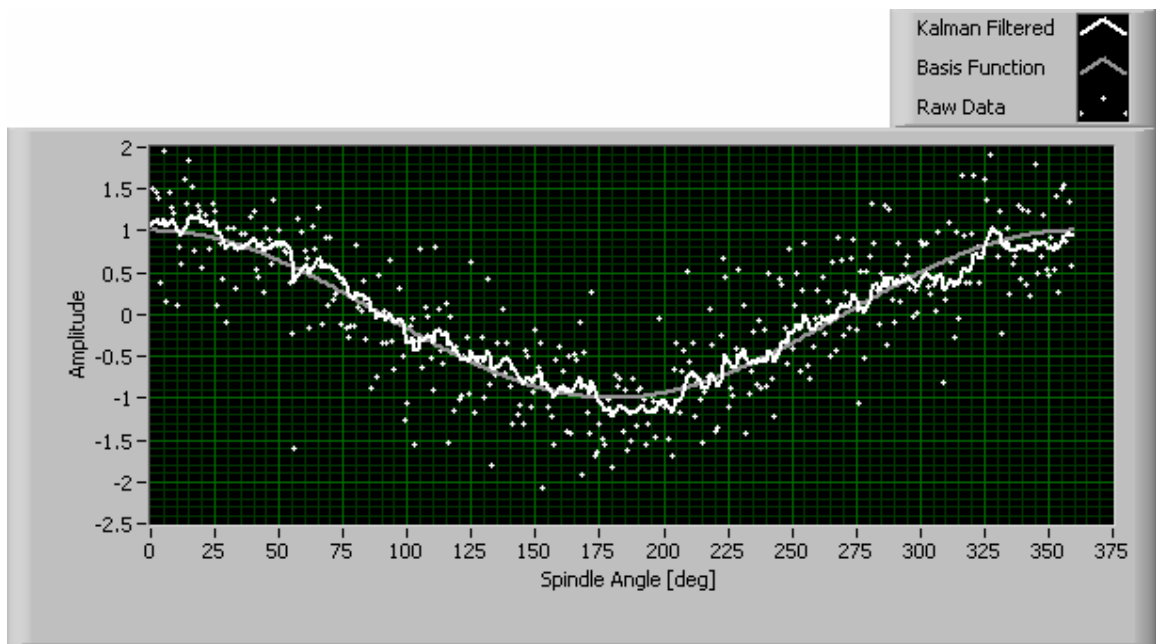


Figure 4.9 – Kalman Filtering of Simulated Data

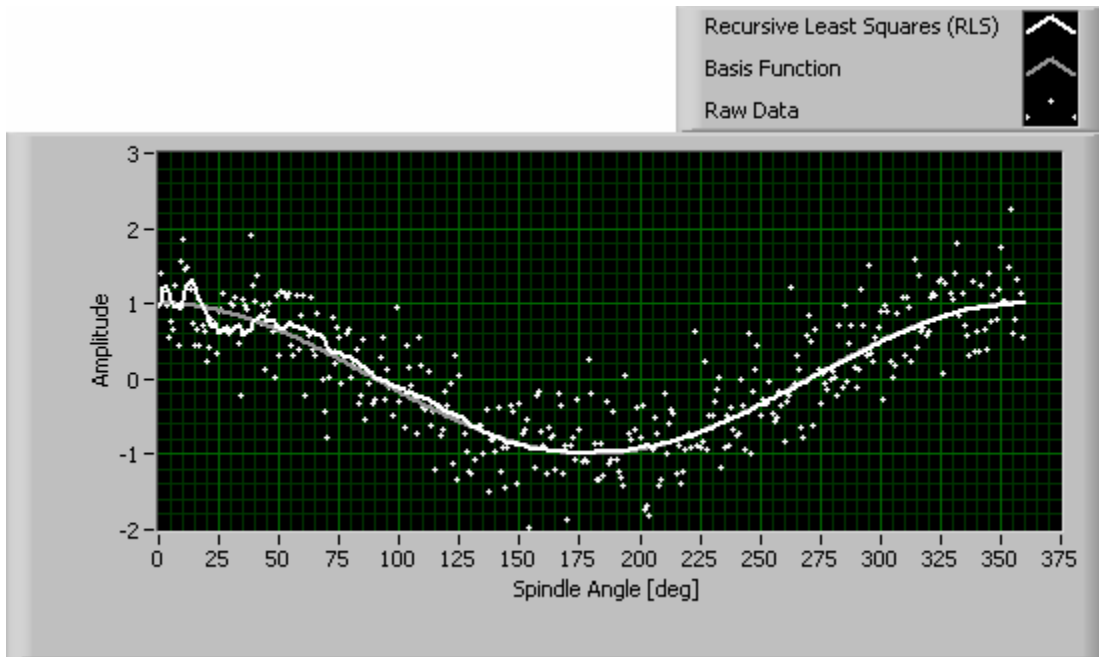


Figure 4.10 - Recursive Least Squares (RLS) Fitting of Simulated Data

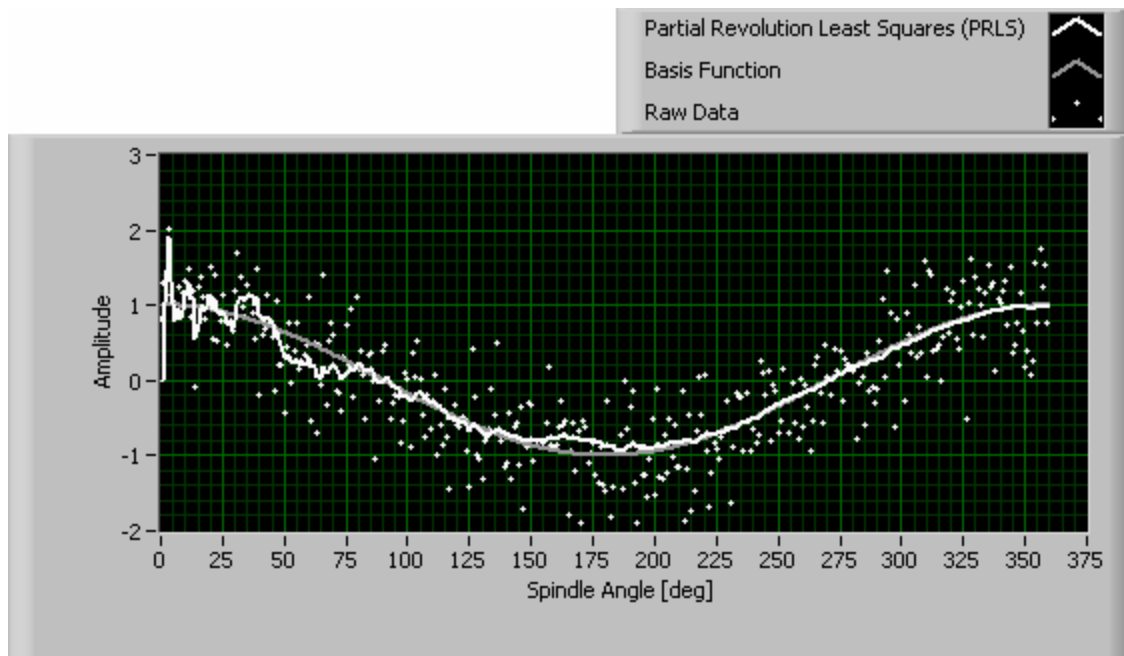


Figure 4.11 - Partial Revolution Least Squares Fitting of Simulated Data

Recursive methods (Kalman and RLS) and the PRLS method are evaluated at each time step. The RLS converges quickly to the basis function solution (less than $\frac{1}{2}$ spindle revolution), the PRLS converges, though less quickly and the Kalman estimator follows well from the start, but is continually affected by the assumed process variance and lack of knowledge of the underlying basis function.

Error Convergence

As more data of a single revolution are included in the estimation model, the Kalman filtering algorithm does not converge to the basis function value (see Figure 4.12), while the algorithms that include knowledge of the underlying signal in the form of basis functions (RLS, PRLS) tend to converge to the true geometric value of the function (see Figure 4.13 and Figure 4.14).

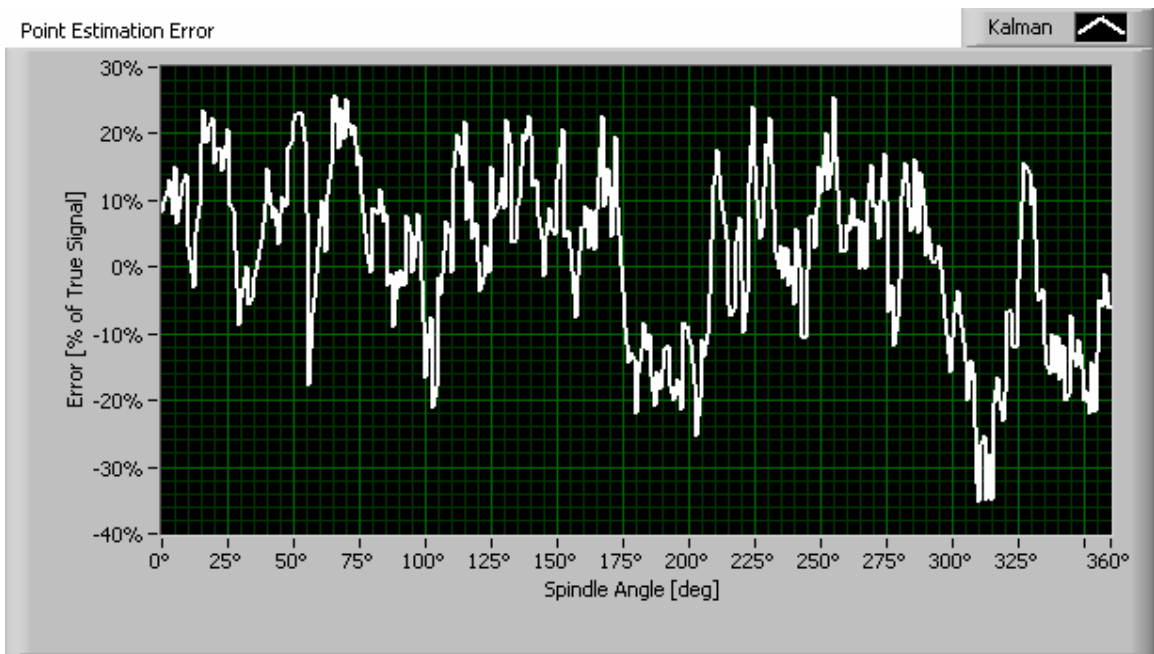


Figure 4.12 - Fitting Error vs. Size of Data Set for Kalman Filtering

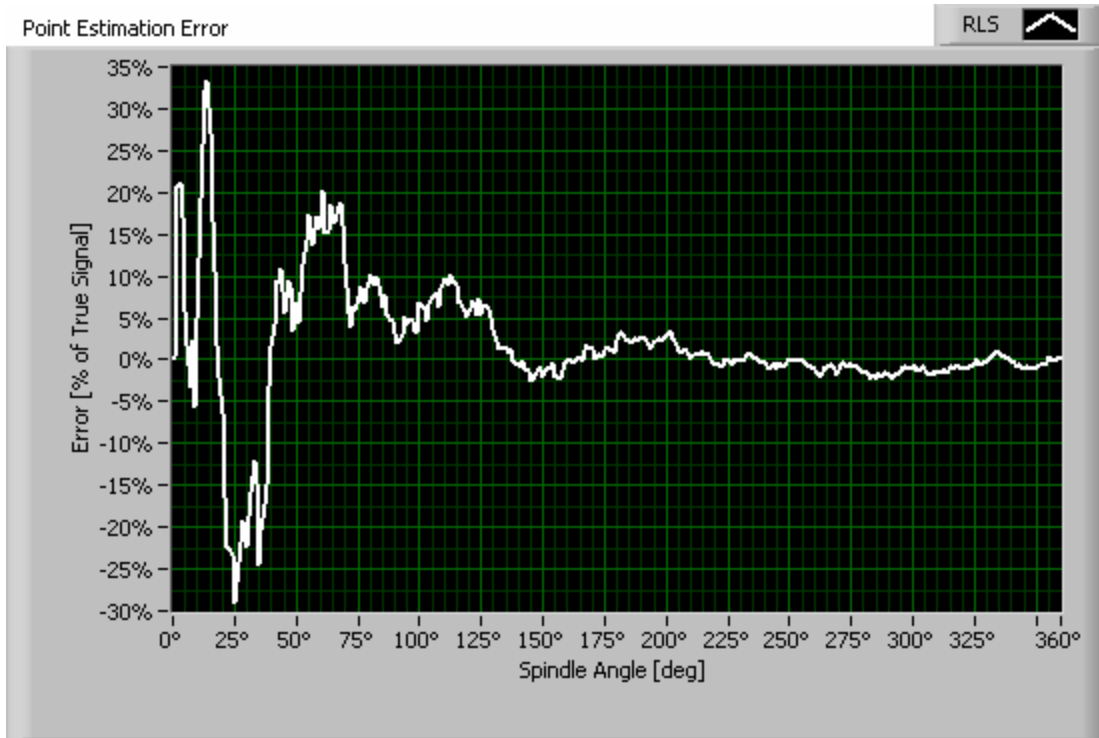


Figure 4.13 - Error vs. Size of Data Set for Recursive Least Squares Fitting

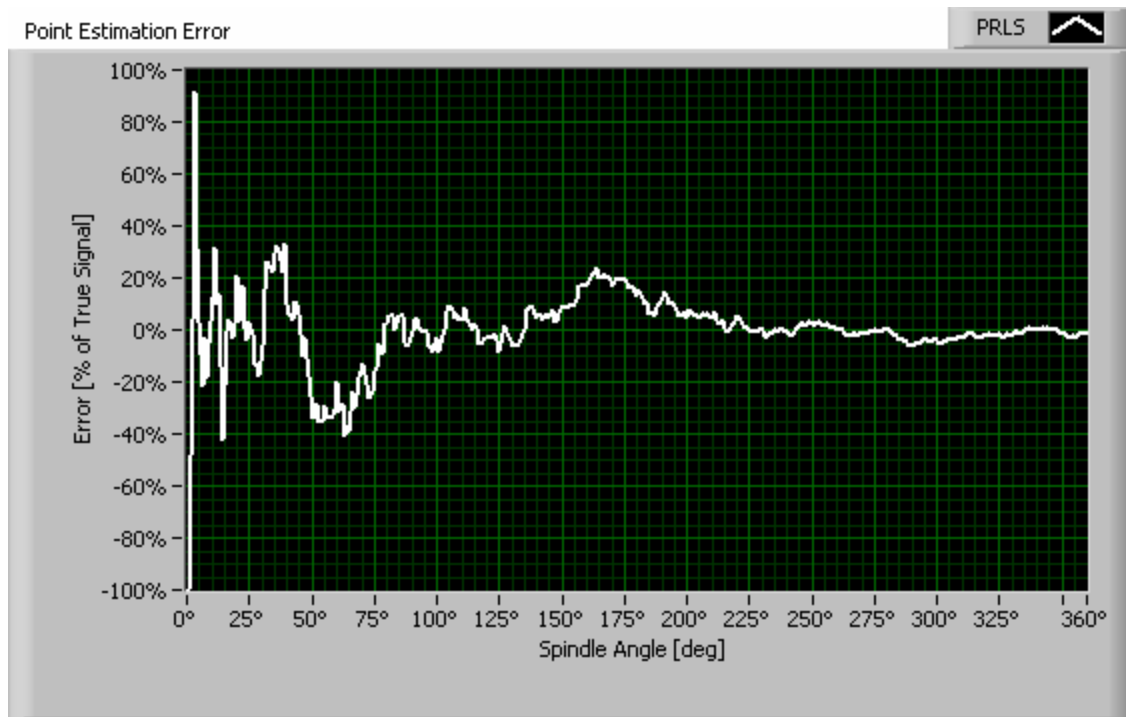


Figure 4.14 - Error vs. Size of Data Set for Partial Revolution Least Squares Fitting

Computational Complexity - Simulation

The computational requirements of each method are made by performing a recursive fit of the function in (4.46) and measuring the single cycle loop time. Results of number of operations and timing results are given in Table 4.2. Timing results are an average of 5 runs.

Table 4.2 - Summary of Computational Requirements for Curve Fitting

Fitting Algorithm	Number of Theoretical Operations per Step	Actual Computation Time [μs] (avg n=5)
Kalman Filtering	$3 + 2 - 2 * 2 /$	3.2
Recursive Least Squares (RLS)	$15 + 10 - 36 * 0 /$	9.0
Partial Revolution Least Squares (PRLS)	dependent on data set size and algorithm convergence rate	174.3*

* Computation time increases with increasing data set size. The reported computation time is over one full part revolution (first computation with 2 data points, last computation with 360 data points, average set size 180 data points).

The Kalman scheme calculates in less time than the RLS scheme as expected, due to fewer operations per iteration. Both recursive schemes execute on the order of 10 μ s. The nonrecursive PRLS algorithm takes considerably longer, averaging 174 μ s over one part revolution.

Convergence of Estimated Parameter Values

The purpose of estimating the function underlying the acquired data is to extract parameters used to plan the actuation path to center the part, namely the off-center amplitude and its vector angle with respect to the spindle.

Since the Kalman filter does not contain explicit information about the underlying data function, a separate fitting routine which includes basis functions would need to be fit to the Kalman filtered data. This additional computational step may warrant investigation in the future, however the Recursive Least Squares and Partial Revolution Least Squares state estimators are tested exclusively in this application since the underlying basis model is well defined.

Off-Center Amplitude

The estimated off-center amplitude is derived from the basis coefficients according to (4.8). The error in the amplitude estimate for the function described in (4.46) using both the recursive least squares and the partial revolution least squares techniques is given in Figure 4.15.

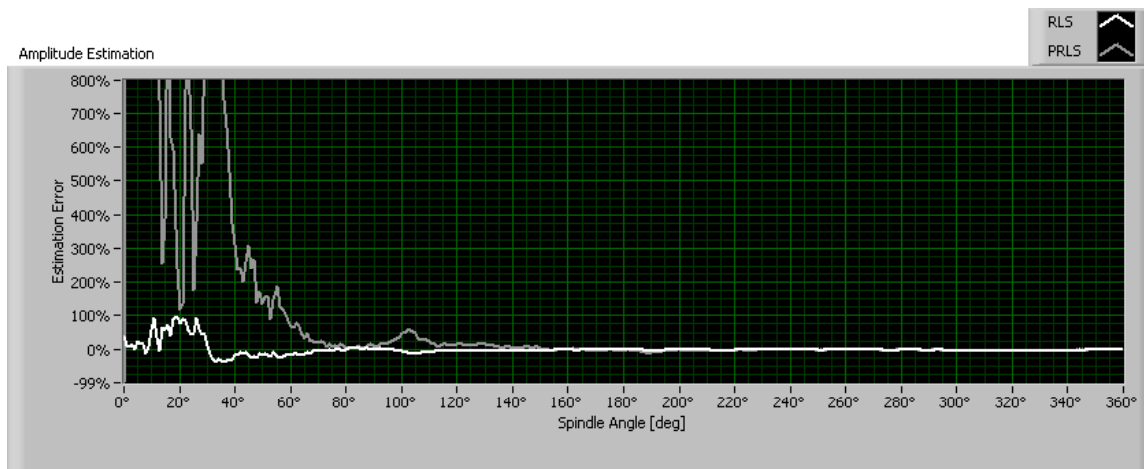


Figure 4.15 - Error in Estimation of Off-Center Distance vs. Data Set Size

The RLS algorithm converges to within 10% error of the estimate using 106° of collected data vs. 190° for the PRLS estimate. Also, the maximum error of the RLS algorithm never exceeds 100%, while the PRLS estimate takes 58° of data to completely drop below 100% error.

Off-Center Distance Angle

The estimated off-center angle is derived from the basis coefficients according to (4.9). The error in the angle (generating phase) estimate for the function described in (4.46) using both the recursive least squares and the partial revolution least squares techniques is given in Figure 4.16.

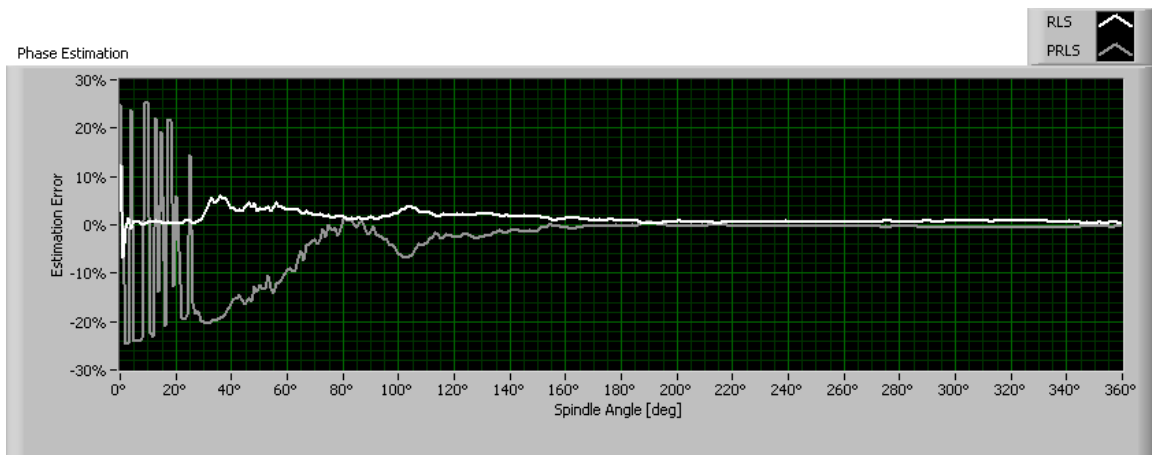


Figure 4.16 - Error in Estimation of Off-Center Angle vs. Data Set Size

Error using the RLS technique is consistently lower than with the PRLS method. Using RLS, error drops below 5% after 39° of data are collected vs. 110° of data required for PRLS. Maximum error for PRLS is 26%, while RLS error never exceeds 7%.

Validation and Comparison

Comparison of sampling methods is made against measurement taken on a roundness machine. The part described in Table 4.3 is independently measured, then estimated on the prototype equipment using each of the above-described techniques.

Table 4.3 - Data Fitting Validation Part Information

Material	1020 carbon steel round stock
Diameter [mm]	167.0
Finish type	Rough turned with rust
Roundness deviation, peak to peak [μm]	120 μm T.I.R.
Offset [μm]	3600

Given the single rotation of collected data shown in Figure 4.17, a fit is made using each of the described methods, and computation time is measured for each.

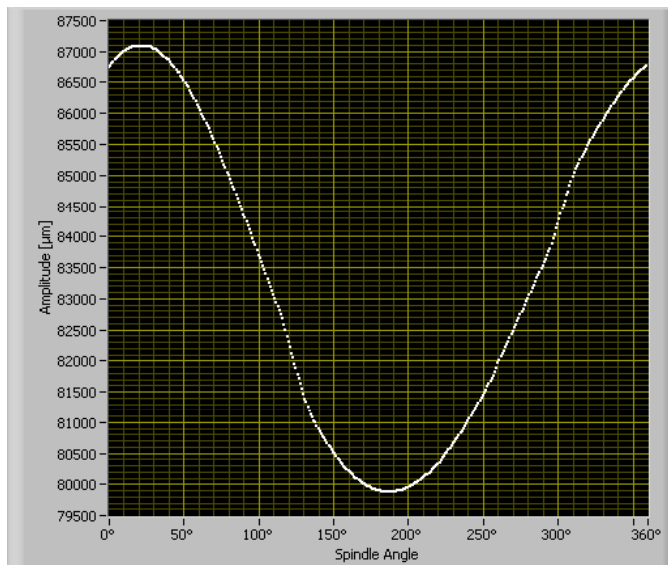


Figure 4.17 - Raw Data of Part Sampled on Ring Centering Prototype

Achievable Accuracy

The part is given a substantial offset, which is measured using a linear gauge by

$$d_{amp} = \frac{(x_{max} - x_{min})}{2} \quad (4.48)$$

and found to be 3606 μm . Data taken from this setup is processed on the real time controller to derive system geometric parameters. Accuracy results are given in Table 4.4. The estimation of off-center error is considered beyond 20° of data, an accepted minimum for circle estimation [Chernov 2005]. Also the estimate of off-center distance given fitting to the entire data set is shown. The Kalman filtering method has no running offset estimate.

Table 4.4 - Summary of Computational Accuracy for Curve Fitting

Fitting Algorithm	Maximum Absolute Estimation Error of Offset (>20° of data)	Final Estimation Error of Offset (360° of data)
Kalman	N/A	-0.9%
RLS	4.8%	0.7%
PRLS	53.7%	0.8%

The RLS method has a maximum error of under 5%, while the PRLS does not fall below 5% maximum error until 191° of data have been collected. The Kalman method is not conducive to a running offset estimate due to absence of basis functions. All methods converge to <1% given the entire data set. In this case, the Kalman amplitude estimator is found by (4.48).

Computational Complexity

Computational complexity is evaluated as in the simulated case by measuring single cycle loop time. Results are given in Table 4.5.

Table 4.5 - Summary of Computational Requirements for Curve Fitting to Part Data

Fitting Algorithm	Number of Theoretical Operations per Step	Actual Computation Time [μs]
Kalman Filtering	$3 + 2 - 2 * 2 /$	3.1
Recursive Least Squares (RLS)	$15 + 10 - 36 * 0 /$	8.3
Partial Revolution Least Squares (PRLS)	dependent on data set size and algorithm convergence rate	173.0*

* Computation time increases with increasing data set size. The reported computation time is over one full part revolution (first computation with 2 data points, last computation with 360 data points, average set size 180 data points).

These iteration times are on the order of the simulated calculation times. Again, the recursive Kalman and RLS scheme execute on the order of 10 μ s, while the nonrecursive PRLS scheme takes over 20 times longer, averaging 174 μ s over one part revolution due to recalculation of the entire data set.

Confidence-Based Data Validity

The aforementioned optimal routines are all able to provide an estimation of part geometry at each discrete time step, whether through recalculation of the data set or as part of their recursive nature. However, the question of data validity must be addressed;

it must be decided how many data points are required to provide the algorithm with enough information for making valid and effective trajectory decisions.

To this end, a confidence-based data validity approach is employed whereby the standard error of the mean is estimated with some degree of confidence and compared against an acceptance threshold value taken as a fraction of the required actuation distance. A confidence band is estimated for the mean state value, and when the width of this band falls below a fixed fraction of the actuation distance (*e.g.*, 3%), the uncertainty is considered low enough to validate the geometry estimate as a representation accurate enough to allow derivation of actuation parameters.

The data set variance is estimated from the Mean Squared Error (MSE):

$$\begin{aligned}
 MSE &= \frac{SSE}{df} \\
 SSE &= \sum_{i=1}^m (Y_i - \hat{Y}_i)^2 \\
 df &= m - 2 \\
 \sigma^2 &= E[MSE]
 \end{aligned} \tag{4.49}$$

The number of degrees of freedom of the data is the number of data points in the set m reduced by one dependent point and one point attributable to the error. The expected value of the MSE is the variance.

Since the off-center distance is related to the error of the mean of the data estimate, the error can be expressed as a function of the data and the number of data points collected:

$$\begin{aligned}
 \text{Std error of the mean} \equiv \sigma_M &= \frac{\sigma}{\sqrt{m}} \approx \sqrt{\frac{MSE}{m}} \\
 \sigma_M &\approx \sqrt{\frac{\sum_{i=1}^m (Y_i - \hat{Y}_i)^2}{m(m-2)}}
 \end{aligned} \tag{4.50}$$

A validity threshold for this variance in the estimate of the mean, or more properly a threshold for the confidence band (*i.e.*, the expected spread in the error of the mean) normalized to the off-center parameter estimate can be given. Using the off-center distance d_{ampl} with a mean error confidence level of $J\%$, a validity condition is imposed that the error normalized to the estimated off-center distance must be less than some threshold error level ε . A floor condition of $2 \mu\text{m}$ minimum error band size is also imposed:

$$\frac{\sigma_M Z_{\alpha/2=1-J\%}}{d_{\text{ampl}}} \leq \varepsilon$$

$$Z_{\alpha/2} \sqrt{\frac{\sum_{i=1}^m (Y_i - \hat{Y}_i)^2}{m(m-2)}} \leq \max(\varepsilon \cdot d_{\text{ampl}}, 2) \quad (4.51)$$

The resulting condition expressed in terms of the data set residual values is

$$\frac{\sum_{i=1}^m (Y_i - \hat{Y}_i)^2}{m(m-2)} \leq \left(\frac{\max(\varepsilon \cdot d_{\text{ampl}}, 2)}{Z_{1-J}} \right)^2 \quad (4.52)$$

An additional validity condition is imposed that a minimum of 30° of data must be collected before validation. At less than 30° , the possibility for an errant model is greater, and such a condition has little effect on the cycle time as compared to actuation based on a poor geometric model.

An example is given in Figure 4.18. Requiring $J = 99.9\%$ confidence with error level $\varepsilon=0.03$, and imposing a floor of $2 \mu\text{m}$ minimum required data spread results in the shown logarithmic relationship.

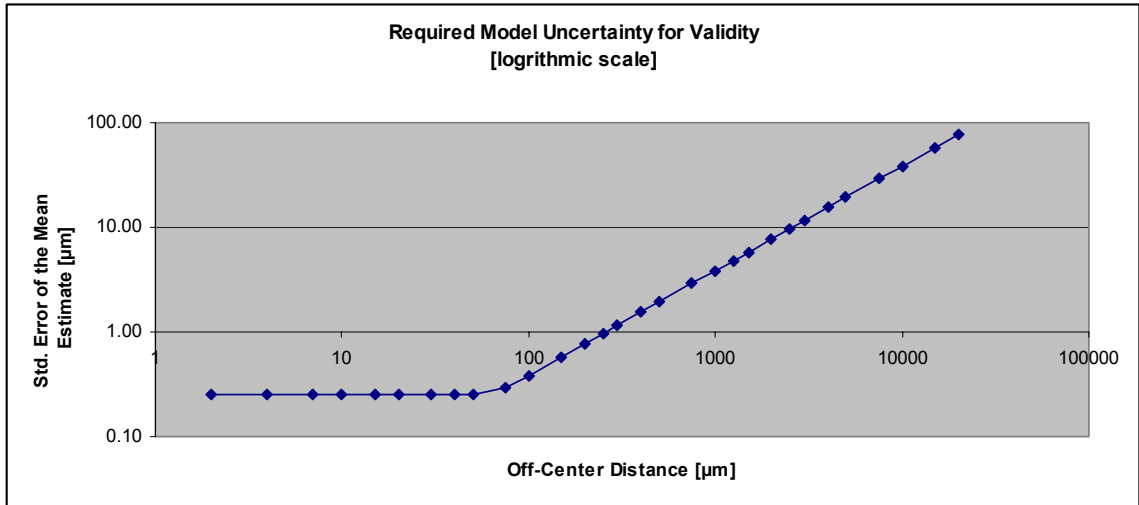


Figure 4.18 - Example MSE Requirement for J=99.9% confidence and $\epsilon=0.03$

As the off-center distance decreases, so does the standard error of the mean required for validity. Larger actuation distances allow validity at a wider confidence band in the mean estimate, as accuracy is not as great a concern. This situation requires fewer data points and allows the part to be actuated reasonably close to target in a short time. Conversely, smaller actuation distances require more data points to validate a model, resulting in higher accuracy for these actuations.

Simulation Validation

The variance-based validity approach is applied to simulated data of (4.46) with disturbance distributed as $N(0, 40^2)$ under 3 cases of amplitude:

- Case 1: $A=20000$ (typical starting position)
- Case 2: $A=1000$ (intermediate position)
- Case 3: $A=100$ (higher accuracy position)

Data are shown to the point of the first valid model meeting the criteria

- J=99.9% confidence
- $\epsilon = 0.03$

for Case 1 (Figure 4.19), Case 2 (Figure 4.20) and Case 3 (Figure 4.21).

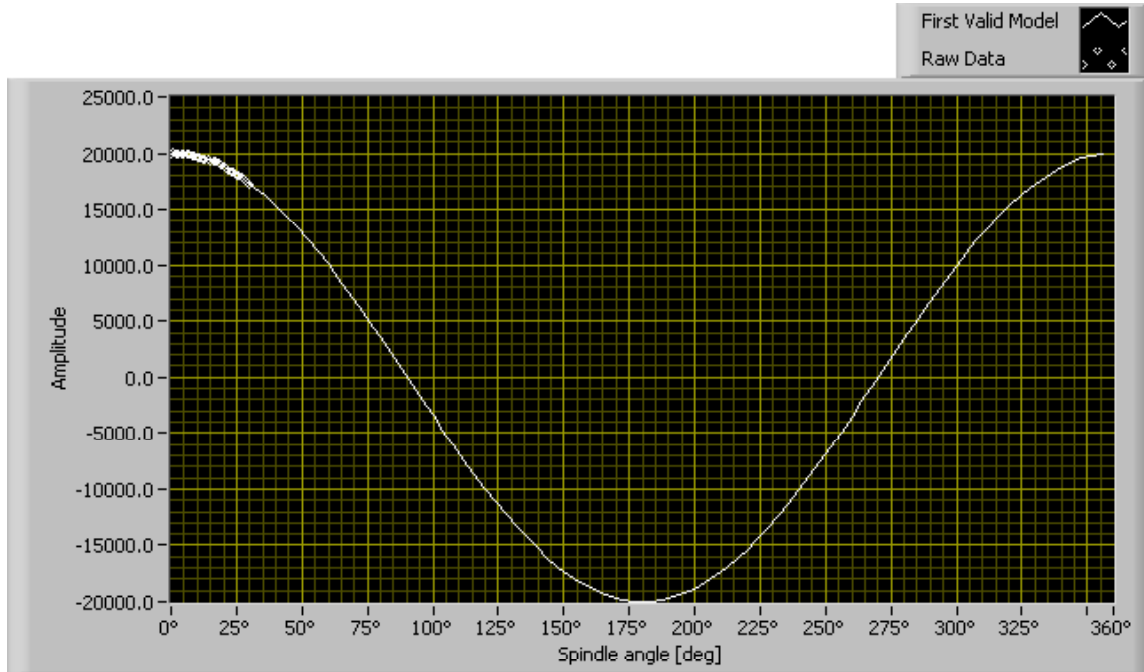


Figure 4.19 - Simulation of Variance-Based Validity, A=20000

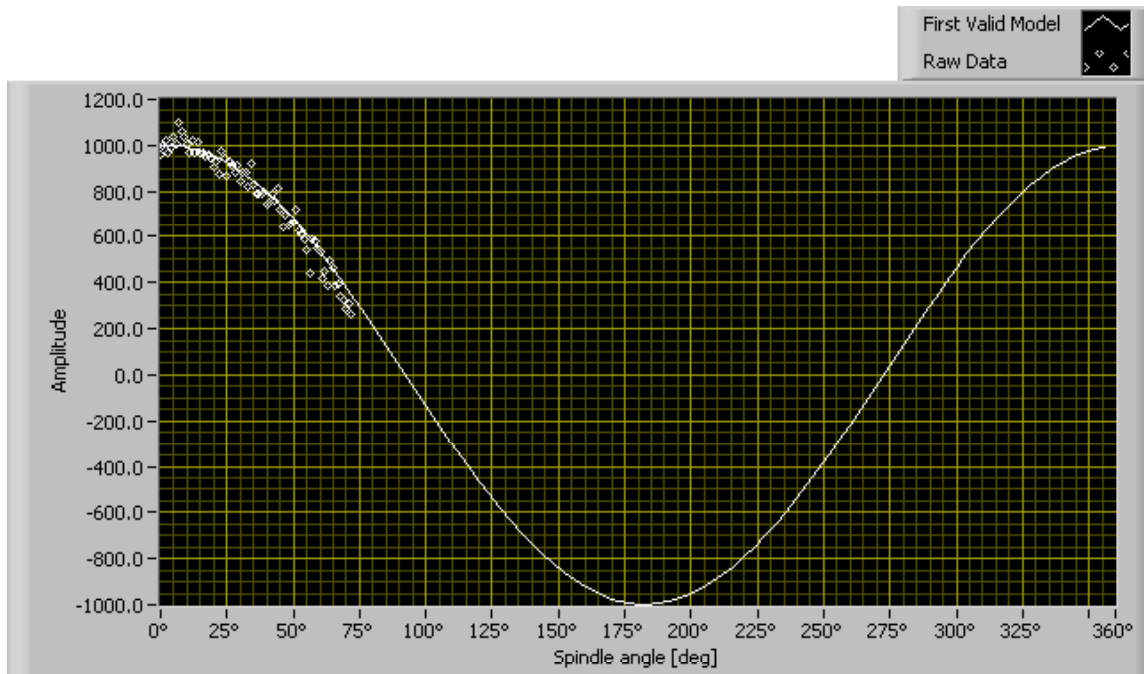


Figure 4.20 - Simulation of Variance-Based Validity, A=1000

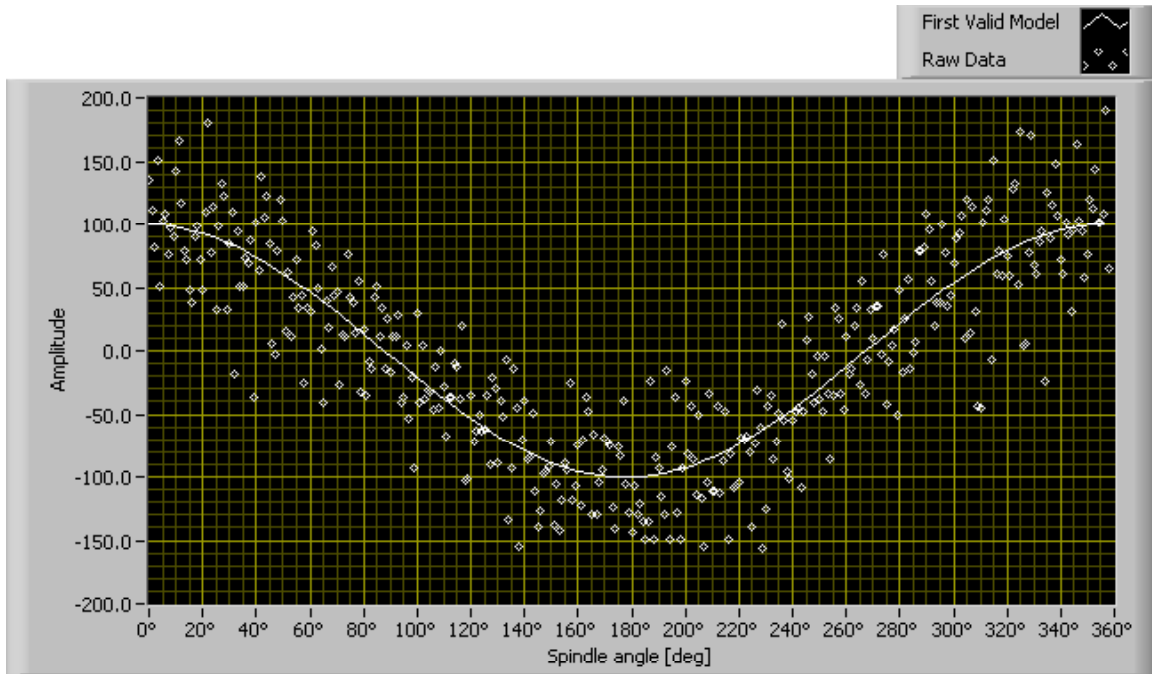


Figure 4.21 - Simulation of Variance-Based Validity, A=100

Accuracy results are summarized in Table 4.6.

Table 4.6 - Simulation Result for Variance-Based Validity

Case	Amplitude [μm]	Spindle Angle Required for Validity [deg]	Resultant Confidence Band of the Mean Estimate [μm]
1	20000	30°	52.7
2	1000	73°	29.7
3	100	360°	13.4

As amplitude is decreased, more data are required to validate the model. As a result, accuracy in the mean estimate is improved as actuation distance decreases. The net tradeoff of increasing cycle time for improvement in modeling accuracy is demonstrated.

Validation Result

A data set for the part of Table 4.3 is measured for the following offset distances:

- Case 1: A=20220
- Case 2: A=1043
- Case 3: A=246

Each case is presented graphically in Figure 4.22 through Figure 4.24 with the accompanying first valid model meeting the criteria

- J=99.9% confidence
- $\varepsilon = 0.01$

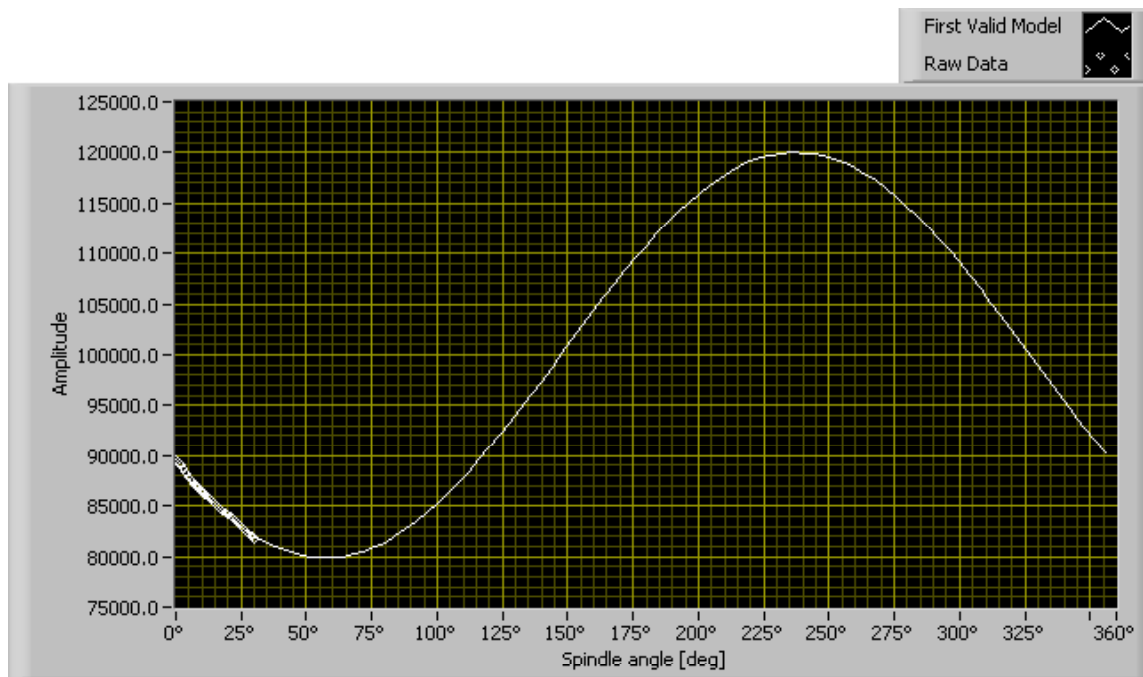


Figure 4.22 - Validation of Variance-Based Validity, A=20220 μm

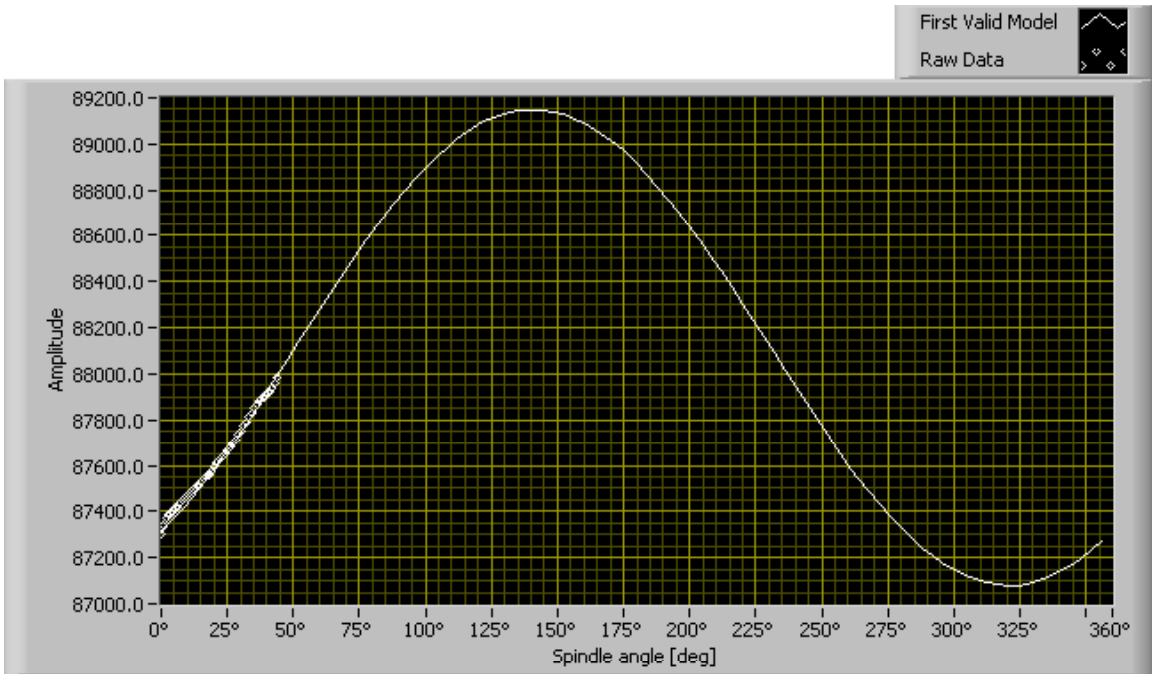


Figure 4.23 - Validation of Variance-Based Validity, A=1043 μm

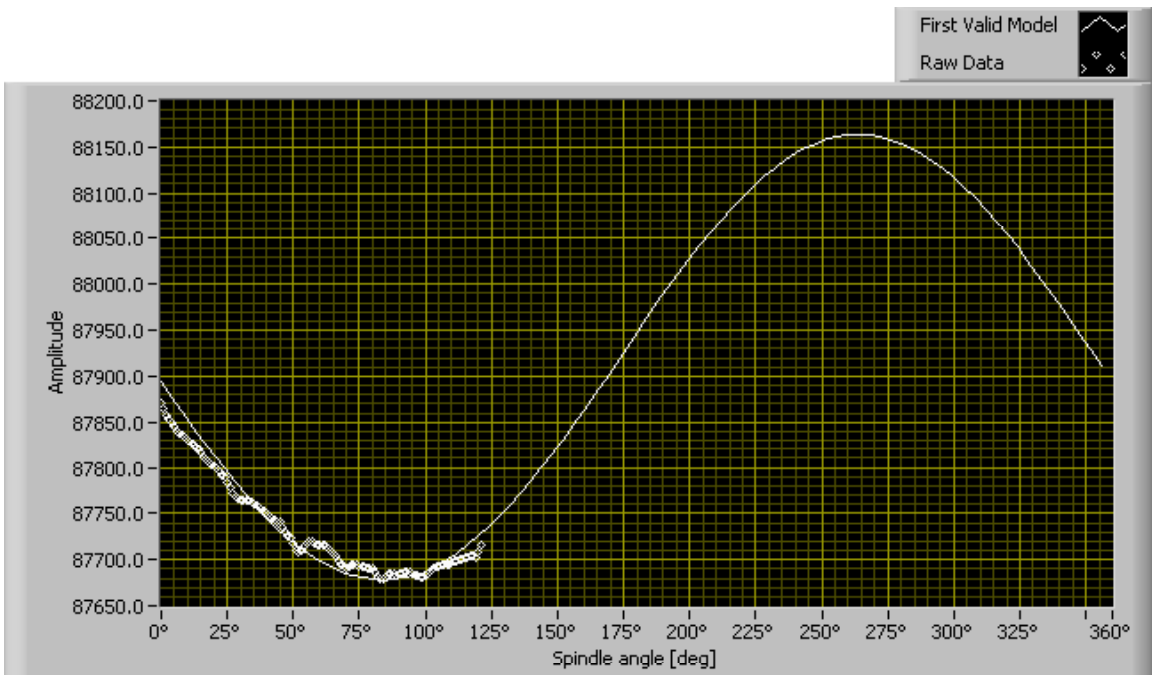


Figure 4.24 - Validation of Variance-Based Validity, A=246 μm

Accuracy results are given in Table 4.7.

Table 4.7 - Validation Result for Variance-Based Validity

Case	Amplitude [μm]	Spindle Angle Required for Validity [deg]	Resultant Confidence Band of the Mean Estimate [μm]
1	20220	30°	153
2	1043	44°	10.3
3	246	121°	2.6

Again, as the amplitude decreases, the method requires more data to meet the validity criterion. Though the system suffers with regard to cycle time due to longer data collection and possible missed actuation opportunities, it delivers better modeling accuracy when needed for more precise actuation at small amplitudes.

CHAPTER 5

TRAJECTORY PLANNING AND LINEAR TIME-INVARIANT CONTROL

Optimal estimation of part geometry made in the previous chapter is used as the basis for actuation path and velocity planning.

Actuation Distance

The push distance is defined as the distance the slide must move toward the part in order to push it from its off-center position to the center of rotation. The push distance is calculated from 3 components:

$$d = d_{gap} + d_{ampl} - d_{lead}$$

$$d_{gap} \equiv \text{distance to close gap between probe and actuator tip}$$

$$d_{ampl} \equiv \text{off-center distance (distance to actuate part)}$$

$$d_{lead} \equiv \text{linear distance to compensate for leading the off-center angle}$$
(5.1)

These distances are graphically represented in Figure 5.1.

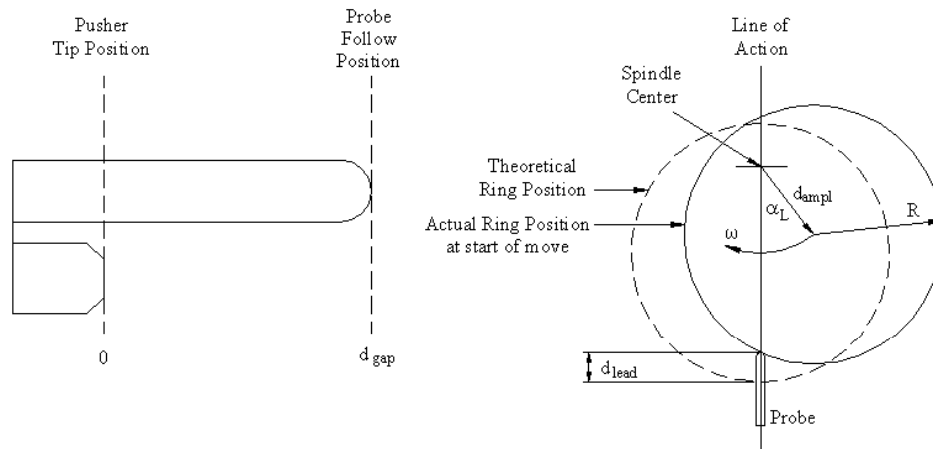


Figure 5.1 - Part Positional Geometry

The distance to close the following gap is calculated directly from the difference between instantaneous probe position and known probe position $d_{probe,pt}$ when the probe is collapsed to the level of the pusher tip:

$$d_{gap} = d_{probe} - d_{probe,pt} \quad (5.2)$$

The distance to move the part is equal to the calculated off-center distance d_{ampl} . The distance to compensate for leading the off-center angle by the angle α_L is determined from the geometry shown in Figure 5.2 as follows:

$$\begin{aligned} d_{lead} &= d_{ampl} + R - x \\ x &\equiv d_{ampl} \cos \alpha_L + R \cos \gamma \\ \alpha_L &\equiv \text{lead angle relative to off-center direction } \phi \\ \gamma &\equiv \sin^{-1} \left(\frac{d_{ampl} \sin \alpha_L}{R} \right) \\ R &\equiv \text{part radius} \end{aligned} \quad (5.3)$$

Substituting,

$$d_{lead} = d_{ampl} + R - d_{ampl} \cos \alpha_L - R \cos \left(\sin^{-1} \left(\frac{d_{ampl} \sin \alpha_L}{R} \right) \right) \quad (5.4)$$

and simplifying

$$d_{lead} = d_{ampl} (1 - \cos(\alpha_L)) + R \left[1 - \cos \left(\sin^{-1} \left(\frac{d_{ampl} \sin(\alpha_L)}{R} \right) \right) \right] \quad (5.5)$$

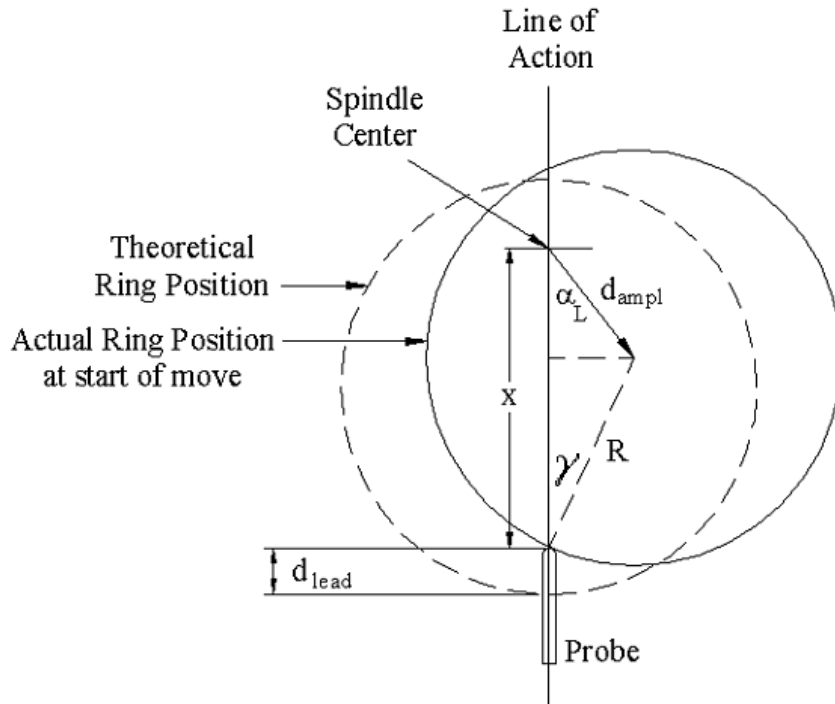


Figure 5.2 - Part Lead Geometry

The final push distance is

$$d = d_{probe} - d_{probe,pt} + d_{ampl} \cos \alpha_L - R + \sqrt{R^2 - d_{ampl}^2 \sin^2 \alpha_L} \quad (5.6)$$

subject to

$$R \geq d_{ampl} \sin \alpha_L \quad (5.7)$$

This is absolutely satisfied independent of rotational velocity when

$$R \geq d_{ampl} \quad (5.8)$$

Simply put, the spindle center must initially be contained within the part outer surface. Otherwise, the line of action of the probe will encounter a “no part” condition at some point during full rotation.

Actuation Input

Once the spindle is in position for the start of the push, servo following is suspended and the slide undergoes a fixed trapezoidal velocity move as shown in Figure 5.3.

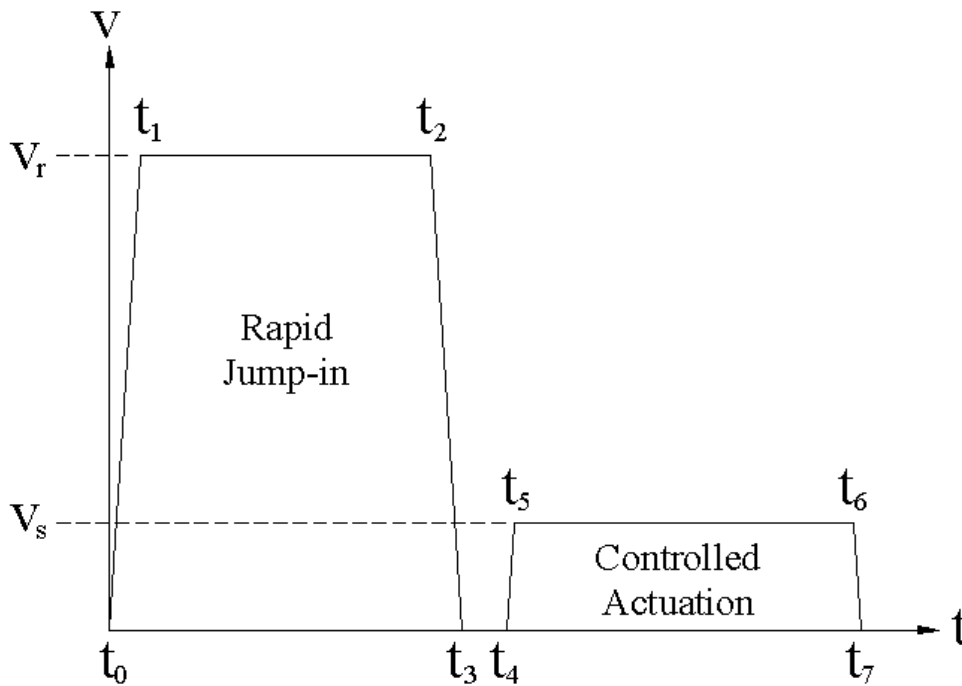


Figure 5.3 - Velocity Idealized Profile of Actuation Move

The slide is accelerated to a rapid velocity of 5000 mm/min, then decelerated to a stop before part contact. After a pause time of 50 ms, the slide is accelerated again to a controlled velocity, then decelerated to arrive at the final push position.

Trajectory Plan

Lead Angle Calculation

To determine the time required to complete the move, the velocity curve is integrated over the total move profile:

$$d = d_{rough} + d_{fine} = \int_{t_0}^{t_3} v \cdot dt = \int_{t_0}^{t_3} v_r \cdot dt + \int_{t_4}^{t_7} v_s \cdot dt \quad (5.9)$$

$$d_{rough} = \int_{t_0}^{t_1} at \cdot dt + \int_{t_1}^{t_2} v_r \cdot dt + \int_{t_2}^{t_3} (at_3 - at) \cdot dt \quad (5.10)$$

$$d_{rough} = \frac{at^2}{2} \Big|_0^{t_1} + v_r t \Big|_{t_1}^{t_2} + \left(at_3 t - \frac{at^2}{2} \right) \Big|_{t_2}^{t_3}$$

The rough distance is typically chosen to allow for rapid approach to the part, stopping with a 500 μm safety gap to prevent contact.

The following relationships are established by inspection:

$$t_1 = \frac{v_r}{a} \quad (5.11)$$

$$t_2 = t_3 - t_1 = t_3 - \frac{v_r}{a}$$

Substituting into (5.10),

$$d_{rough} = \frac{a}{2} t_1^2 + v_r (t_3 - 2t_1) + at_3 (t_3 - t_3 + t_1) - \frac{a}{2} (t_3^2 - t_3^2 + 2t_1 t_3 - t_1^2)$$

$$d_{rough} = \frac{a}{2} \left(\frac{v_r}{a} \right)^2 + v_r \left(t_3 - \frac{2v_r}{a} \right) + at_3 \frac{v_r}{a} - \frac{a}{2} \left(\frac{2v_r}{a} t_3 - \frac{v_r^2}{a^2} \right) \quad (5.12)$$

$$d_{rough} = v_r t_3 - \frac{2v_r^2}{a}$$

This expression is solved for t_3 :

$$t_3 = \frac{d_{rough}}{v_r} + \frac{2v_r}{a} \quad (5.13)$$

The same procedure is carried out for the controlled displacement at velocity v_s , resulting in

$$t_7 - t_4 = \frac{d_{fine}}{v_s} + \frac{2v_s}{a} \quad (5.14)$$

By inspect and substitution of (5.13),

$$\begin{aligned}
t_4 &= t_3 + t_p \\
t_p &\equiv \text{pause time} \\
t_4 &= \frac{d_{rough}}{v_r} + \frac{2v_r}{a} + t_p
\end{aligned} \tag{5.15}$$

Solving for t_7 ,

$$t_7 = \frac{d_{rough}}{v_r} + \frac{d_{fine}}{v_s} + \frac{2v_s}{a} + \frac{2v_r}{a} + t_p \tag{5.16}$$

results in the total time of actuation for the given velocity parameters. This time is used to calculate the angle with which to lead the spindle:

$$\alpha_L = \omega \cdot t_7 \tag{5.17}$$

Note that by (5.6), (5.16) and (5.17), the lead angle and push distance are interdependent, so the solution requires iteration.

Lead Angle Validation

The lead angle is examined for different sample parts, and the residual error of the actual push angle to the desired push angle is examined over a range of off-center distances. Results are shown in Figure 5.4.

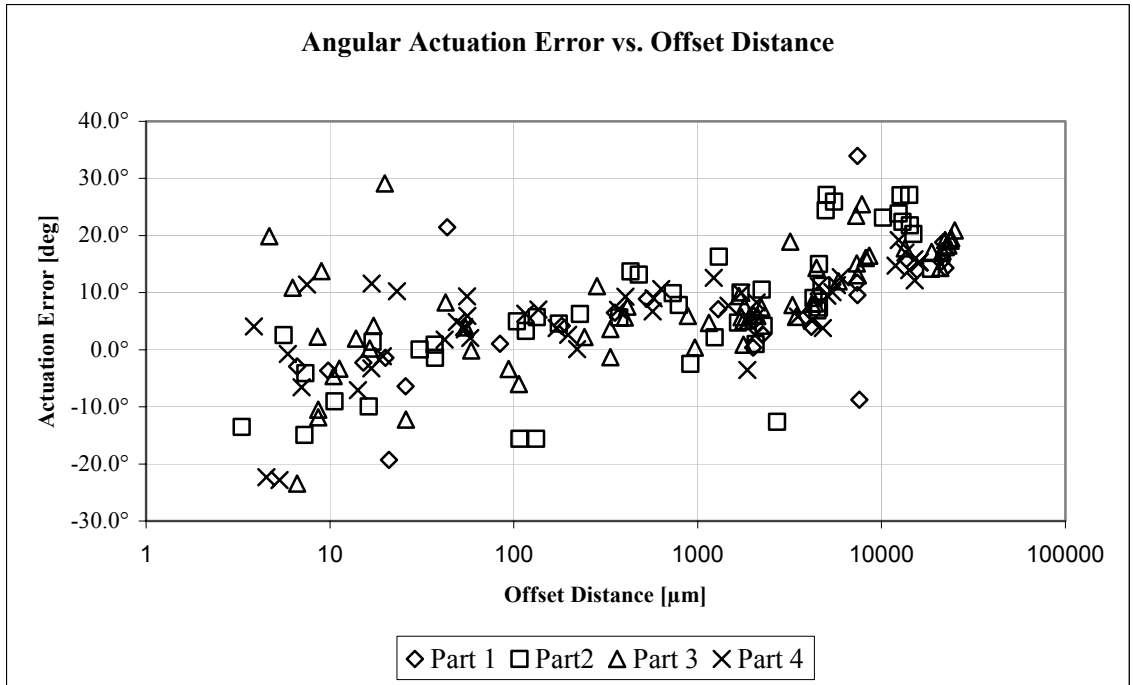


Figure 5.4 - Angular Actuation Error by Offset Distance

Below 1 mm, the average angular error for all parts is 1.4°. The average angular error for all parts over all actuation distances is 4.9°. By Figure 5.4, it is noted that angular error increases with increasing offset distance. This error should be corrected in future work.

Actuation Velocity Energy Balance Model

The prescribed actuation velocity v_s is first explored through the balance of part kinetic energy with the dissipative work of the frictional force. As the analysis will arrive at an initial sliding velocity, a strictly dynamic friction model is employed:

$$\begin{aligned}
E_{kinetic} &= E_{friction} \\
\frac{mv_0^2}{2} &= F_f d \\
d &\equiv \text{sliding distance before rest} \\
F_f &\equiv \text{dynamic friction force} \\
F_f &= \mu_k W = \mu_k mg
\end{aligned}
\tag{5.18}$$

The required initial workpiece velocity to travel a distance d is therefore

$$v_0 = \sqrt{2\mu_k g d} \tag{5.19}$$

To impart such an initial velocity to the part, a slide velocity to strike the part is determined by analysis of free impact. An expression for the slide velocity after impact is determined from Newton's one-dimensional Kinematic Impact Law

$$\begin{aligned}
-\varepsilon(v_{slide,b} - v_{part,b}) &= v_{slide,a} - v_{part,a} \\
\varepsilon &\equiv \text{coefficient of restitution} \\
v_{part,b} &\equiv \text{part velocity before impact} = 0 \\
v_{part,a} &\equiv \text{part velocity after impact} \\
v_{slide,b} &\equiv \text{slide velocity before impact} \\
v_{slide,a} &\equiv \text{slide velocity after impact} \\
v_{slide,a} &= v_{part,a} - \varepsilon v_{slide,b}
\end{aligned}
\tag{5.20}$$

Momentum balance before and after impact is considered to determine a required slide velocity before impact:

$$\begin{aligned}
m_{slide}v_{slide,b} + m_{part}v_{part,b} &= m_{slide}v_{slide,a} + m_{part}v_{part,a} \\
v_{slide,b} &= v_{slide,a} + \frac{m_{part}}{m_{slide}}v_{part,a}
\end{aligned}
\tag{5.21}$$

Substituting from (5.20):

$$\begin{aligned}
v_{slide,b} &= v_{slide,a} + \frac{m_{part}}{m_{slide}} v_{part,a} \\
v_{slide,b} &= v_{part,a} - \varepsilon v_{slide,b} + \frac{m_{part}}{m_{slide}} v_{part,a} \\
v_{slide,b} (1 + \varepsilon) &= v_{part,a} \left(1 + \frac{m_{part}}{m_{slide}} \right) \\
v_{slide,b} &= v_{part,a} \left(\frac{m_{slide} + m_{part}}{m_{slide} (1 + \varepsilon)} \right)
\end{aligned} \tag{5.22}$$

Substituting from (5.19),

$$v_{slide,b} = \left(\frac{m_{slide} + m_{part}}{m_{slide} (1 + \varepsilon)} \right) \sqrt{2\mu_k g d} \tag{5.23}$$

Since free impact is not actually occurring (slide is driven with a constant velocity command), it is assumed that

$$m_{slide} \gg m_{part} \tag{5.24}$$

This assumption reduces (5.23) to

$$v_{slide,b} = \frac{\sqrt{2\mu_k g d}}{1 + \varepsilon} \tag{5.25}$$

This function is used to determine the prescribed slide velocity, given a required actuation distance and assumed kinetic friction coefficient.

Actuation Planning by Energy Balance Model

The previous model is used to generate the constant slide velocity required to actuate a stationary part over a distance d . The assumptions implicit in this model are

- The coefficient of restitution is independent of the contact velocity
- The static friction coefficient is equal to the kinetic friction coefficient (part is assumed to have a negligible presliding velocity)
- The slide undergoes purely free impact during the collision period

An example of application of this rule is given in Figure 5.5. In this case, a small sample part is analyzed and a coefficient of restitution of 0.85 is assumed.

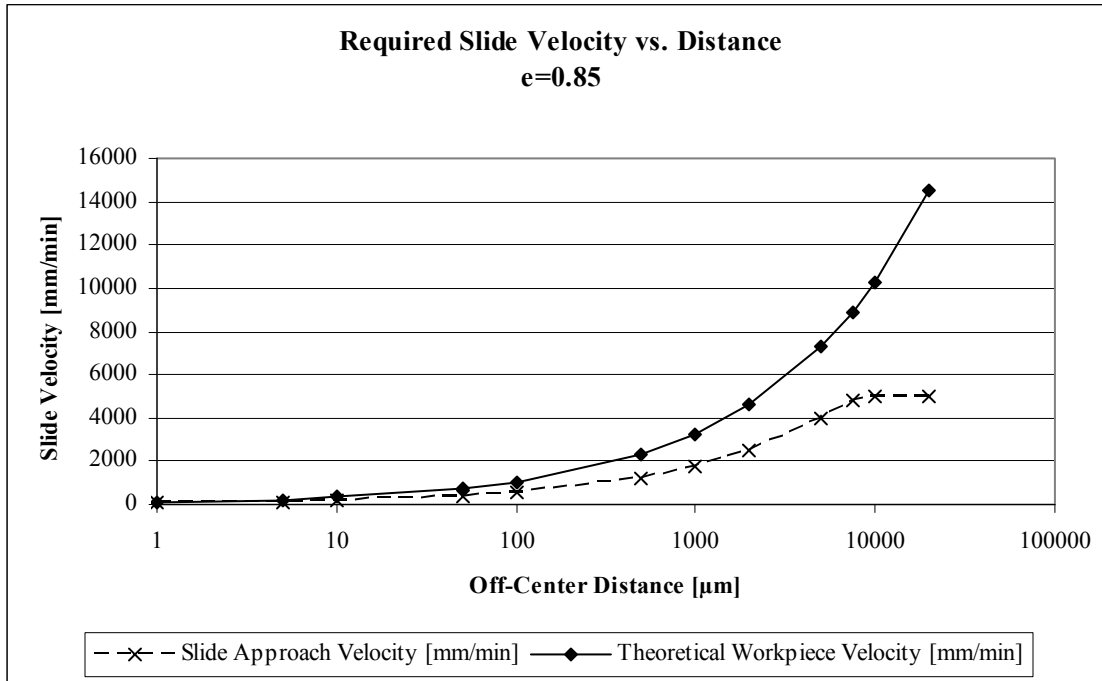


Figure 5.5 - Actuation Velocity Plan, $m=0.8$ kg, $e=0.85$

The slide velocity is limited to 5000 mm/min to prevent following error upon acceleration. The net effect of this limitation is that at large required distances, actuation will take place as a series of impacts rather than a single impact. This calculation is performed in the centering system prior to each actuation to determine the required slide velocity for actuation.

Validation of Actuation Planning by Energy Balance Model

The energy balance calculation is implemented in the centering system to determine the constant slide actuation velocity. This method is compared to constant

velocity actuation independent of desired actuation distance for actuation velocities of 500, 1000 and 2000 mm/min.

Data for a cycle of an 0.8 kg part at an actuation velocity level of 500 mm/min is shown on a logarithmic polar plot as Figure 5.6.

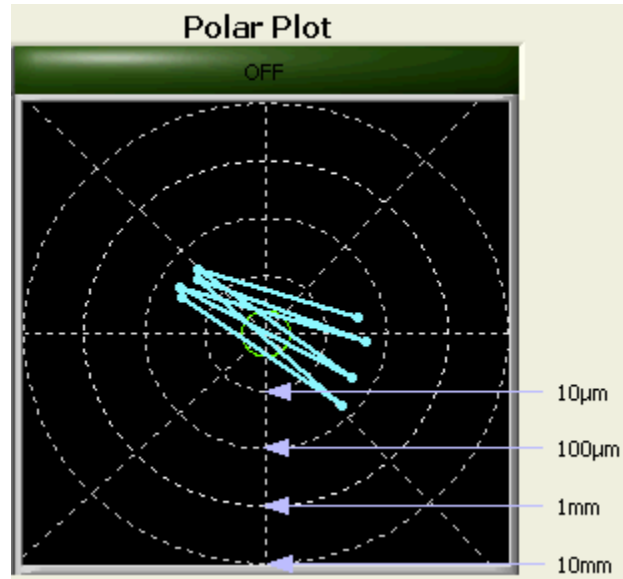


Figure 5.6 - Polar Plot of $v=500$ mm/min Actuation

After approaching center, the off-center distance oscillates steadily across the tolerance zone. As an alternative representation to show more data points, phase data are ignored and only absolute amplitudes are considered as the number of actuations increase. The absolute offset vs. number of actuations is shown in Figure 5.7.

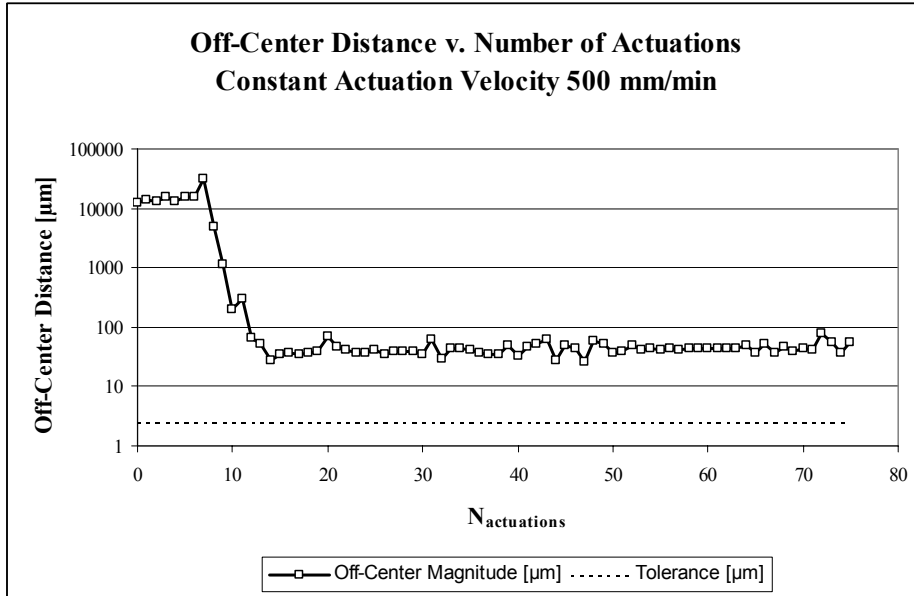


Figure 5.7 - Off-Center Distance over Number of Actuations, v=500 mm/min

The part approaches center, but oscillates around 70 μm off-center distance, and is never able to converge below the tolerance limit.

Magnitude data for the cases of 1000 mm/min and 2000 mm/min are shown as Figure 5.8 and Figure 5.9 respectively.

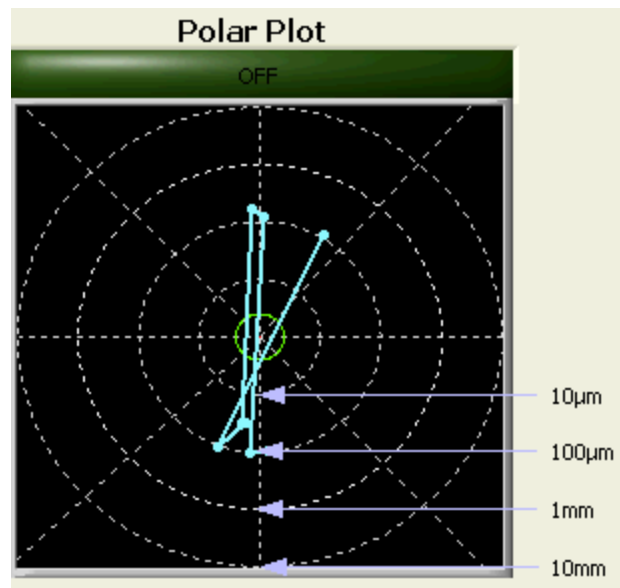


Figure 5.8 - Polar Plot of v=1000 mm/min Actuation

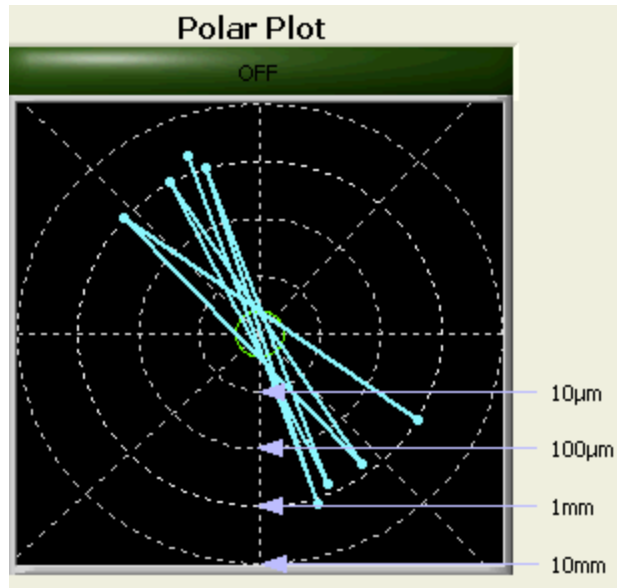


Figure 5.9 - Polar Plot of $v=2000$ mm/min Actuation

The same effect is present as in the case for 500 mm/min, however more pronounced as the constant velocity level increases. For $v=1000$ mm/min, limit cycling is observed around $110 \mu\text{m}$, and for $v=2000$ mm/min, limit cycling is observed around 1 mm. Total cycle magnitude data is shown for $v=1000$ and $v=2000$ mm/min is shown in Figure 5.10 and Figure 5.11 respectively.

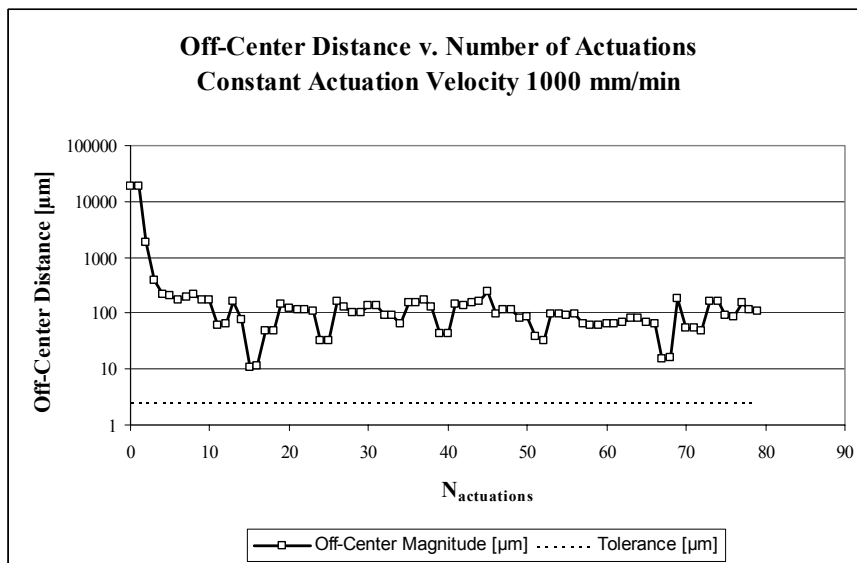


Figure 5.10 - Off-Center Distance over Number of Actuators, $v=1000$ mm/min

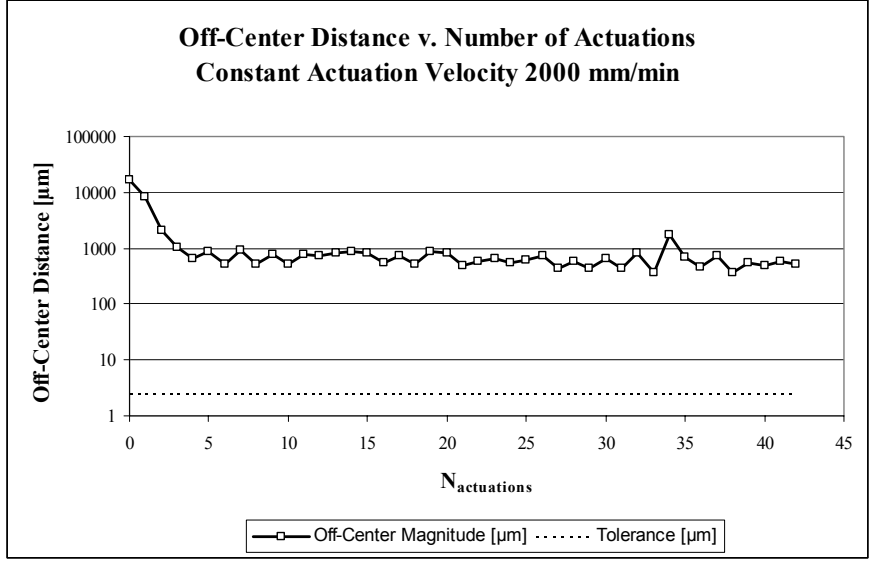


Figure 5.11 - Off-Center Distance over Number of Actuators, $v=2000$ mm/min

Data for a typical cycle using actuation velocity determined by the energy balance model is shown as Figure 5.12.

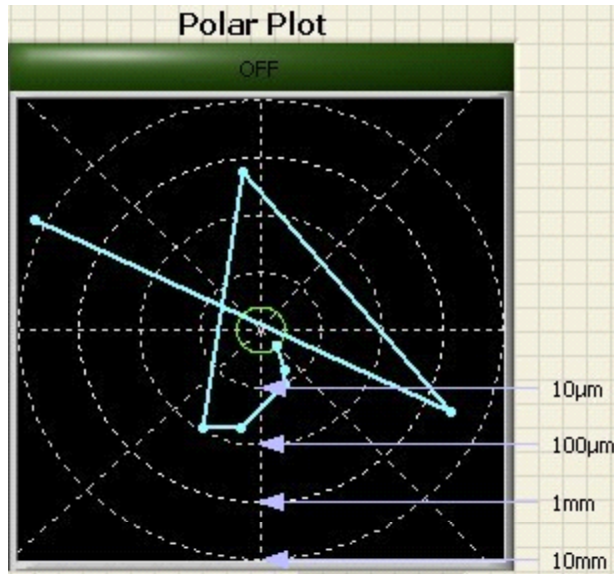


Figure 5.12 - Polar Plot with Actuation Velocity Determined by Energy Balance Method

Absolute offset distance magnitude vs. number of actuators is shown in Figure 5.13.

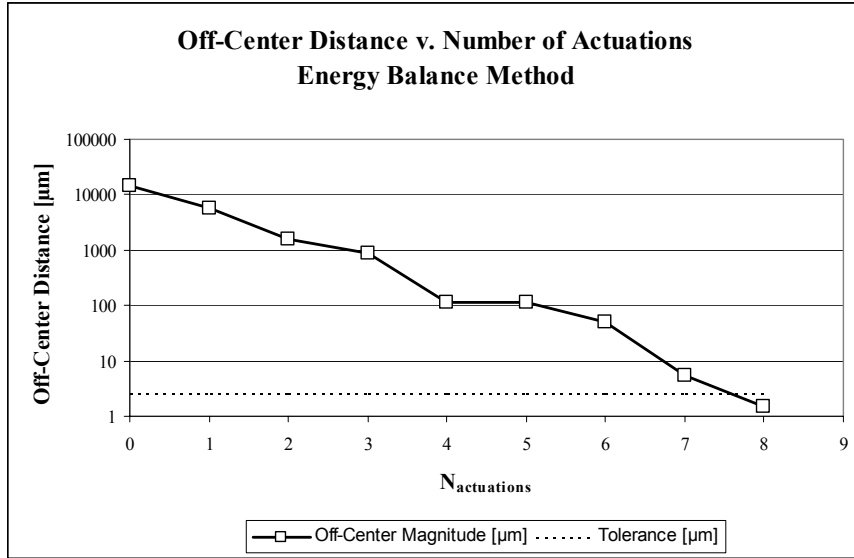


Figure 5.13 - Off-Center Distance over Number of Actuators, v by Energy Balance Method

The velocity is adjusted on a push-by-push basis and decreases as the actuation distance decreases. The net effect is as expected by the simulation results – the actuation distances are on the order of the desired distances, the offset distance steadily approaches zero, and although some overshoot occurs at larger actuation distances, no limit cycling is observed.

Reaction Model

The pushing occurs beginning with zero relative velocity between the part and the top surface of the spindle. Moving the part requires a discontinuous transition between static and kinetic friction as the part starts to move. After breakaway, the required force drops, often causing overshoot of the desired position, and possible return to zero velocity. This stick-slip motion is a common phenomenon occurring in frictional systems. The effect is exemplified by simulation of the system shown in Figure 5.14.

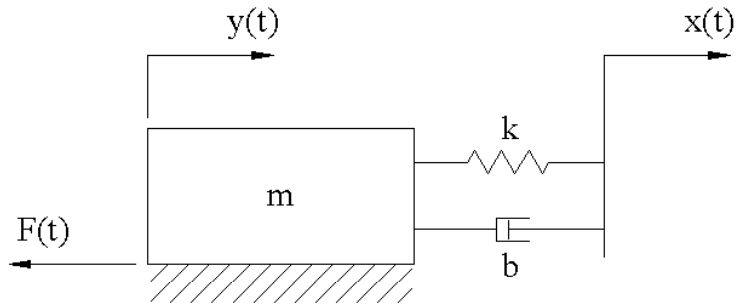


Figure 5.14 - Idealized Relative Motion System

The simulated behavior of this ideal system is shown in Figure 5.15, Figure 5.16 and Figure 5.17 for position, velocity and force respectively.

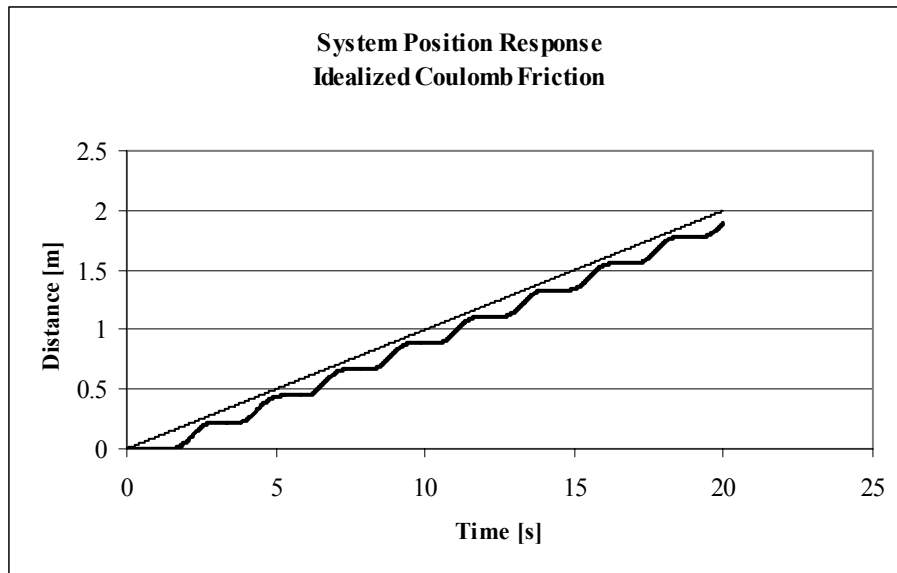


Figure 5.15 - Simulated Idealized System Position Response to Ramp Input

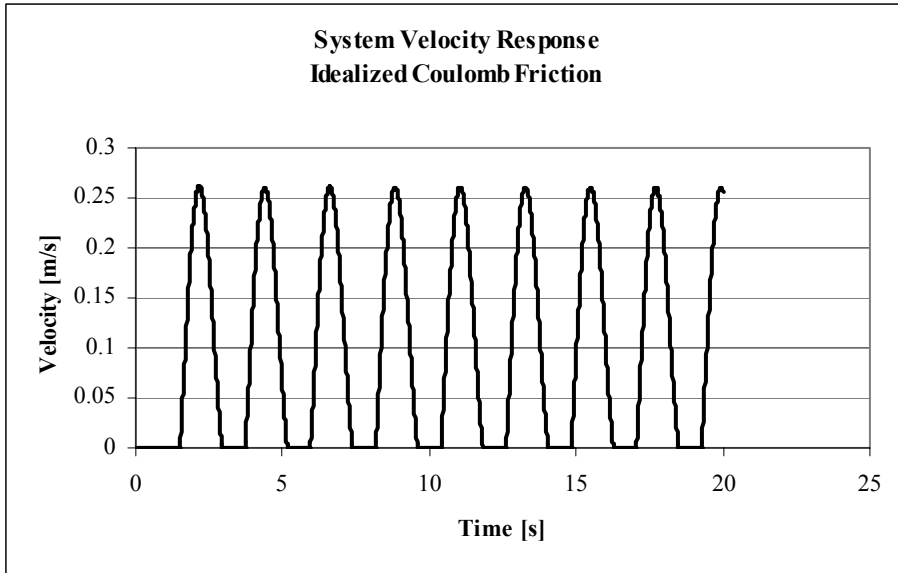


Figure 5.16 - Simulated Idealized System Velocity Response to Ramp Input

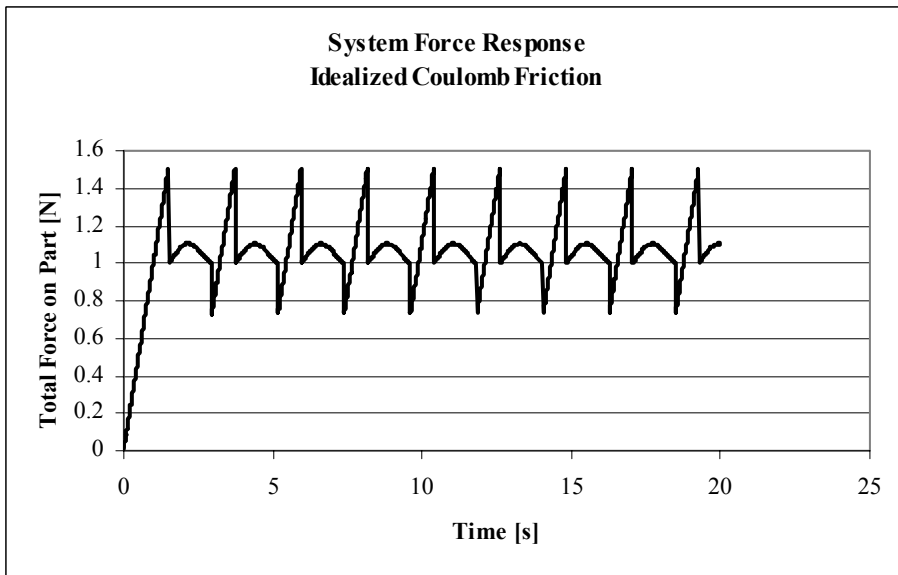


Figure 5.17 - Simulated Idealized System Force Response to Ramp Input

Given a ramp input of the reference position, the velocity of the part starts and stops, inducing a jerky position variation and large fluctuations in the force on the part.

Such large fluctuations tend to create difficulty in real control systems. For instance, the net result of stick-slip in the application is a limit cycling of the position control, causing the part to experience back-and-forth actuation completely across the tolerance zone without convergence. This typically occurs at small required actuation distances (<200 μm) in the centering system, when the amplitude is on the order of one cycle of this stick-slip action. An exaggerated case is presented in Figure 5.18.

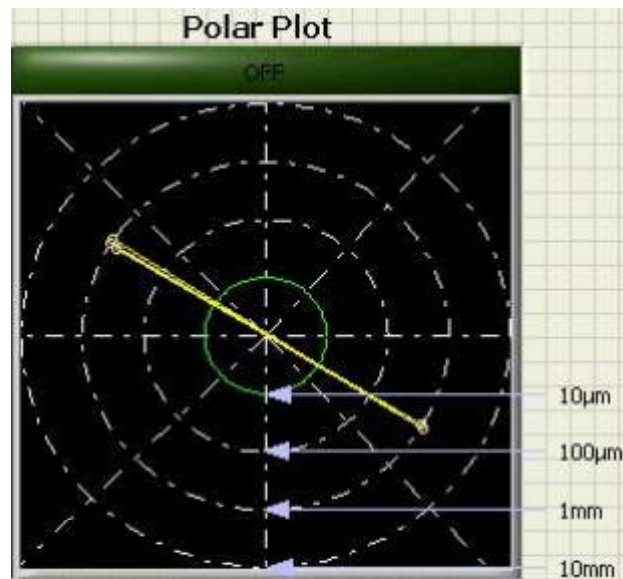


Figure 5.18 - Limit Cycle of Actuation Across Tolerance Zone

To describe the dynamics of the stick-slip phenomenon a second-order model is created for the part dynamic state and forces upon the part due to actuation and friction. Note that the reaction model differs primarily from the energy balance model in its departure from the free impact assumption. In the reaction model, free impact is not assumed and the interaction dynamics of the part-actuator system are modeled explicitly. Recall that the friction of a sliding workpiece can be modeled as

$$F = \begin{cases} F(v), & v \neq 0 \\ F_e & , v = 0 \text{ and } |F_e| < F_s \\ F_s & , \text{ otherwise} \end{cases} \quad (5.26)$$

For a system described as a spring-mass-damper representation with frictional resistance, the model [Luenberger 1979] is

$$m\ddot{x} + b(\dot{y} - \dot{x}) + k(y - x) = -F_f \quad (5.27)$$

The phenomenon of stiction as related to part pushing can therefore be described by the following steps:

- 1) Part is initially at rest
- 2) Actuator makes contact with part
- 3) Part remains at rest as force between actuator and part increases below F_S
- 4) Force exceeds F_S , part accelerates, velocity becomes nonzero
- 5) Movement is resisted by dynamic friction force $F(v)$ until part decelerates to rest
- 6) Process repeats

The sliding object may or may not fully come to rest. In the latter case the frictional force continues to be dynamic and both force from actuator to part and part velocity itself oscillate periodically.

The dynamic model of (5.27) with F_f taken from (5.26) is tuned and validated over a range of trial masses and contact areas. The final model has the following parameters:

- $k = 1200$ N/mm
- $b = 1$ N-s/mm
- $F(v) = \mu_k mg + k_v v$
 - $\mu_k = 0.15$
 - $k_v = 0.1$ N-s/mm

Adaptive modification of these friction parameters is discussed in Chapter 6. The system is solved numerically using a modified Euler scheme. Results in commanded

position, actual position, and predicted force for a case of $m=18.9$ kg, $v=6000$ mm/min are shown in Figure 5.19.

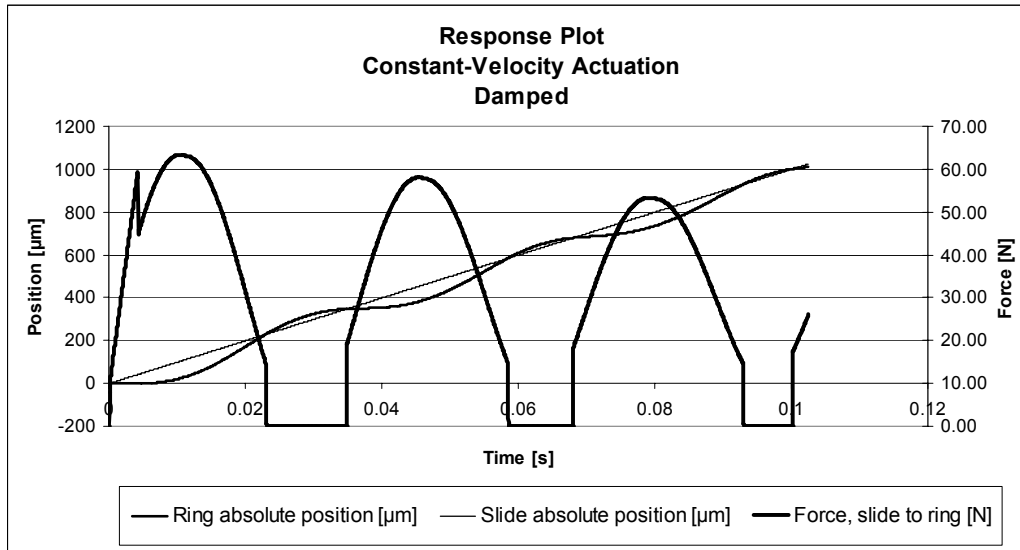


Figure 5.19 - System Response to Constant Velocity Input

Note that the initial force builds linearly against static friction while the part is at rest, then drops sharply as the part begins to move against the resistance of the lower dynamic friction force. The part accelerates highly enough to break contact with the pusher and then comes to rest through deceleration by friction. The process repeats when the actuator contacts again.

Validation of Reaction Model

The reaction model was tested against data taken from a fixed-velocity actuation experiment. The subject part (18.9 kg) was placed on a static table and actuated at constant velocity over a distance of 1 to 5 mm, with enough distance given to capture at least 2 periods of the stick-slip effect. For the case of actuation at 600 mm/min, the experimental data vs. the model for position is shown in Figure 5.20.

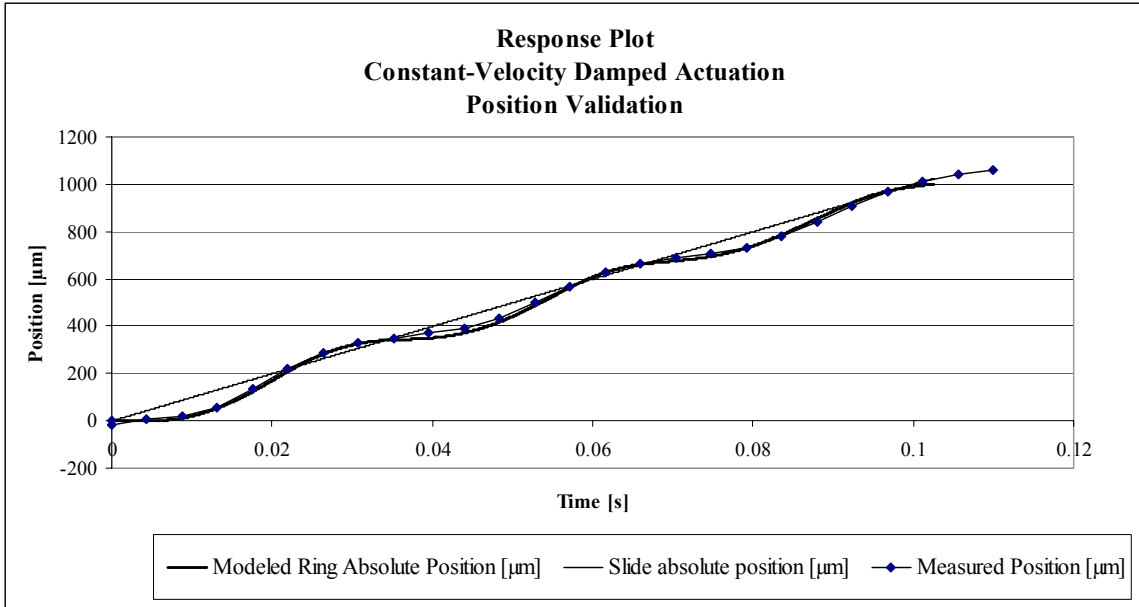


Figure 5.20 - Modeled Position Data vs. Observed for $m=18.9$ kg, $v=600$ mm/min

To improve the resolution of the data scale for position, the data are normalized to the actuator (slide) position in Figure 5.21.

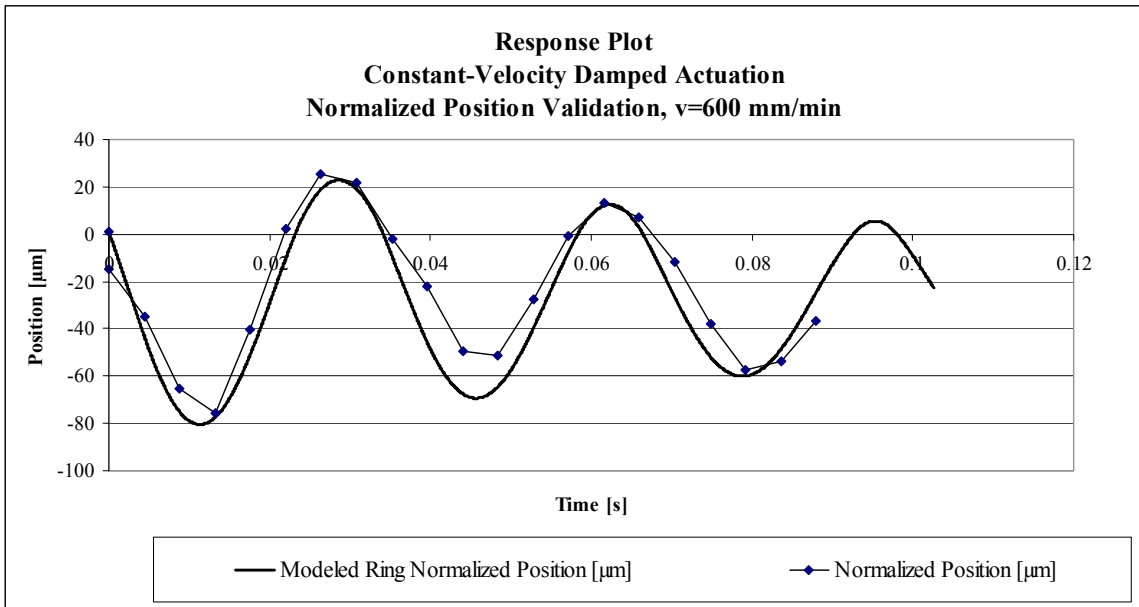


Figure 5.21 - Position Data Normalized to Command Input ($m=18.9$ kg, $v=600$ mm/min)

The maximum free sliding distance estimated by the model is 120 μm , while a free sliding distance of 128 μm was observed in the experiment (-6 % estimation error). The model is a valid predictor of free sliding distance. Results of position modeling for several velocity cases are given in Appendix C.

The position model and experimentally observed results for additional cases are presented in Appendix C. Results of the model error for all cases are summarized in Table 5.1.

Table 5.1 - System Model Validation, m=18.9 kg

Velocity [mm/min]	Modeled Free Sliding Distance [μm]	Measured Free Sliding Distance [μm] (n=1 trial)	Free Distance Error [μm]
100	0	0	0
200	0	0	0
300	13	0	13
400	36	58	-22
500	65	67	-2
600	109	128	-19
700	140	158	-18
800	184	157	27
900	229	192	37
1000	272	279	-7
1200	366	400	-34
1500	494	410	84
2000	948	1089	-141

Applicability of Reaction Model to Actuation

From Figure 5.19, it is seen that the part and pusher lose contact, and then the part undergoes a period of *free sliding*, during which it is under the influence of friction only and cannot be directly controlled by the system input. Furthermore, this free sliding distance can be modeled and predicted based on the part characteristics and planned actuation velocity. It is therefore advantageous to include this information in the path planning stage in order to guarantee that the expected free sliding distance of the part does not exceed the planned actuation distance. Otherwise, the part is consistently actuated beyond the expected distance, and the limit cycling exemplified in Figure 5.18 occurs. It is proposed to augment the previously prescribed actuation in both the distance and velocity domains.

Distance Augmentation

The overall actuation distance is shortened by the expected free sliding distance at the velocity prescribed by the energy balance method. This reduction in the actuation distance below the required movement distance allows for free sliding beyond the end of actuation without overshooting the target. Free sliding distance decreases with decreasing velocity and velocity is reduced by the energy model as the actuation distance drops. Therefore, this distance augmentation will be larger at larger off-center distances and will fall to zero as the part approaches rotational center.

Velocity Augmentation

After the velocity is calculated by the energy balance method, the expected free-sliding distance at this velocity is modeled. If the free-sliding distance is larger than the desired actuation distance, an overshoot condition is guaranteed. The actuation velocity prescribed by the energy balance method is therefore limited to the velocity corresponding to a free sliding distance equal to the desired actuation distance.

For example, given the part tested in Table 5.1, if an actuation distance of 100 μm is desired, the energy balance method prescribes a velocity of 3700 mm/min. However, the actuation velocity will be limited to 600 mm/min (the velocity corresponding to a free sliding distance of 100 μm), preventing an overshoot condition.

Validation of Actuation Planning by Reaction Model

The prototype system program is augmented with the free sliding model and the described actuation planning rules. A cycle run using full actuation distance and velocity planning without compensation for free sliding distance is shown in Figure 5.22 (logarithmic r- θ plot of center position after each actuation).

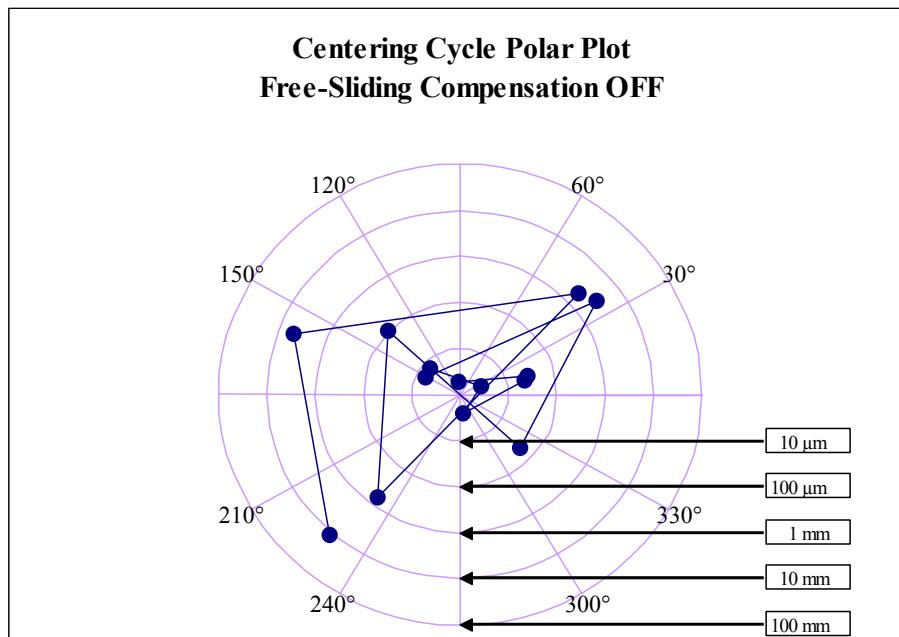


Figure 5.22 - Sample Cycle Push-by-Push Results (Free Sliding Compensation OFF)

The system overshoots the target at each actuation 72% on average, and has a single misactuation of 3 mm (not included in the error average). It takes 14 actuations to center the part, and the entire cycle completes in 30.0 seconds.

Next, a cycle run with the additional rules regarding reduced actuation distance and path planning with respect to free sliding distance is given in Figure 5.23.

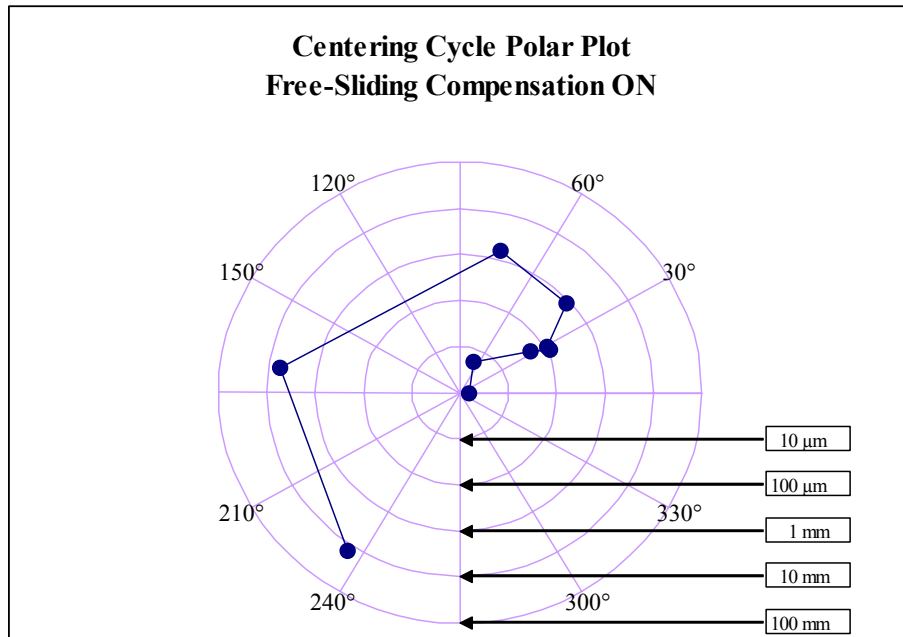


Figure 5.23 - Sample Cycle Push-by-Push Results (Free Sliding Compensation ON)

In this case, there is no system overshoot and a steady progression of part positioning to center. The average error is -16% of desired actuation distance (undershoot), and 9 actuations are required to center the part. The cycle completes in 17.5 seconds.

The validation test was run for 5 cycles with free-sliding distance compensation on and 5 cycles with free-sliding distance compensation off. The results are given in Table 5.2.

Table 5.2 - Validation Results for Free-Sliding Compensation (n=10 trials/level)





Case	Average Push Distance Error [%]	Average No. of Actuations	Average Cycle Time [s]	Average Number of Overshoot / Cycle
No Compensation	22.5%	11.4	24.0	7.1
Free-Sliding Position and Velocity Compensation	-9.1%	9.4	20.2	2.3

Compensation of the free-sliding distance in actuation position and consideration of free sliding distance in velocity planning improves the average positioning error from 22.5% over to 9.1% under, reducing the average number of overshoots by almost 5 per cycle. The number of actuations is reduced by 2 and the cycle time is improved by almost 4 seconds on average with free-sliding position and velocity compensation.

System Performance Results

The system is run for 20 cycles for each of the sample parts tested, and cycle time and number of required actuations recorded. For each trial series, a run chart is created. The parts under test are described in Table 5.3.

Table 5.3 - Descriptions of Parts Under Test

Part No.	Picture	Finish	OD [mm]	Mass [kg]
1		Ground, some heat damage	123.9	0.77
2		Ground and polished	88.9	0.88
3		Ground	170	1.20
4		Rough turned	179	18.9

Run charts for 20 cycles of each part are shown in Figure 5.24 through Figure 5.27.

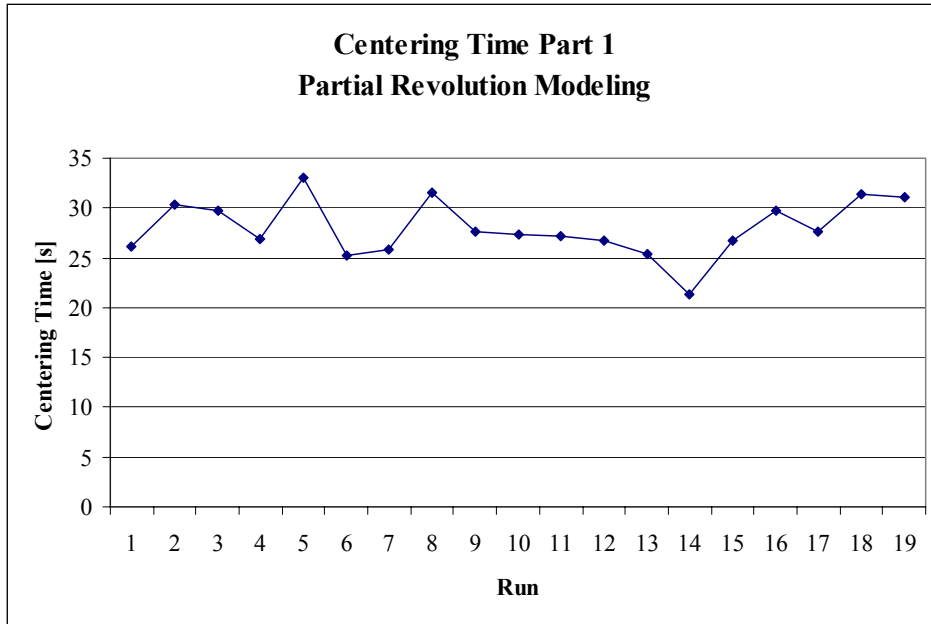


Figure 5.24 - Run Chart for Centering Time and Number of Actuators, Part 1

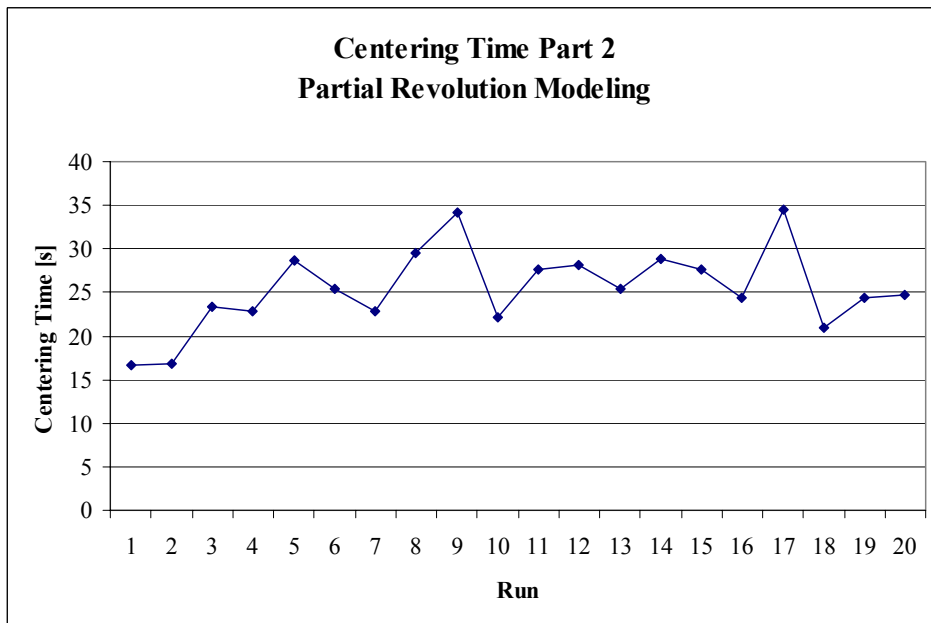


Figure 5.25 - Run Chart for Centering Time and Number of Actuators, Part 2

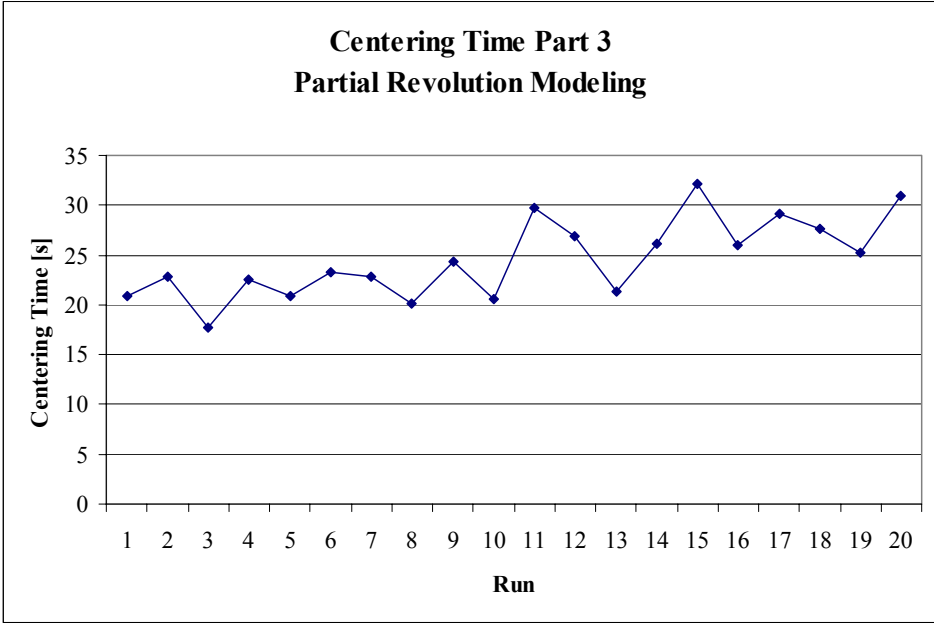


Figure 5.26 - Run Chart for Centering Time and Number of Actuators, Part 3

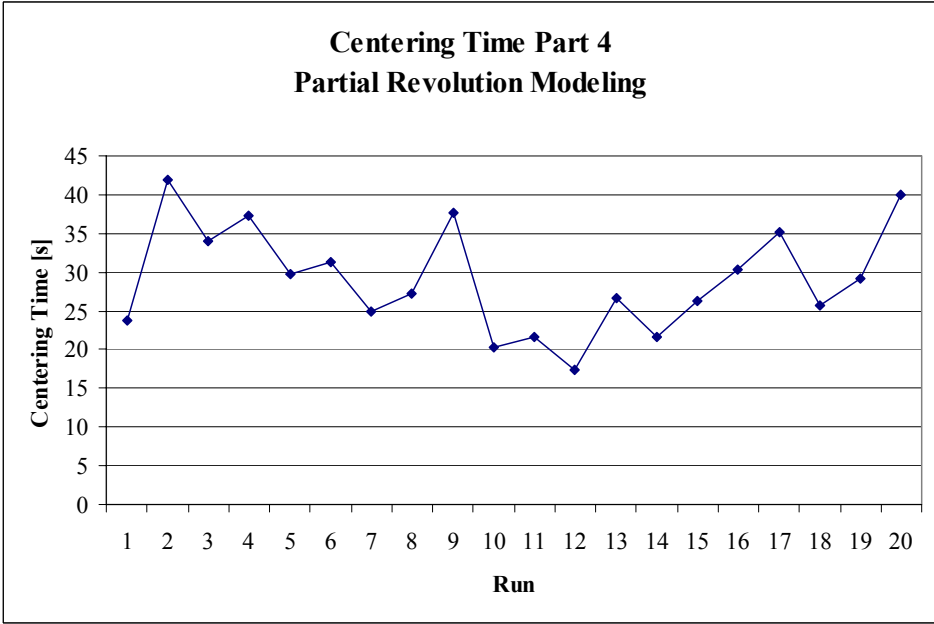


Figure 5.27 - Run Chart for Centering Time and Number of Actuators, Part 4

A summary of the validation trial results is given in Table 5.4.

Table 5.4 - Summary of System Performance Results

Part No.	Average (n=20) Cycle Time [s]	Time Distribution	Average No. of Actuations																												
1	28.0	<table border="1"> <caption>Part 1 Cycle Times [s] Frequency Data</caption> <thead> <tr> <th>Bin</th> <th>Frequency</th> </tr> </thead> <tbody> <tr><td>22</td><td>1</td></tr> <tr><td>24</td><td>0</td></tr> <tr><td>26</td><td>3</td></tr> <tr><td>28</td><td>8</td></tr> <tr><td>30</td><td>3</td></tr> <tr><td>32</td><td>4</td></tr> <tr><td>34</td><td>1</td></tr> <tr><td>More</td><td>0</td></tr> </tbody> </table>	Bin	Frequency	22	1	24	0	26	3	28	8	30	3	32	4	34	1	More	0	10.8										
Bin	Frequency																														
22	1																														
24	0																														
26	3																														
28	8																														
30	3																														
32	4																														
34	1																														
More	0																														
2	25.5	<table border="1"> <caption>Part 2 Cycle Times [s] Frequency Data</caption> <thead> <tr> <th>Bin</th> <th>Frequency</th> </tr> </thead> <tbody> <tr><td>16</td><td>0</td></tr> <tr><td>18</td><td>2</td></tr> <tr><td>20</td><td>0</td></tr> <tr><td>22</td><td>1</td></tr> <tr><td>24</td><td>4</td></tr> <tr><td>26</td><td>5</td></tr> <tr><td>28</td><td>2</td></tr> <tr><td>30</td><td>4</td></tr> <tr><td>32</td><td>0</td></tr> <tr><td>34</td><td>0</td></tr> <tr><td>More</td><td>2</td></tr> </tbody> </table>	Bin	Frequency	16	0	18	2	20	0	22	1	24	4	26	5	28	2	30	4	32	0	34	0	More	2	10.0				
Bin	Frequency																														
16	0																														
18	2																														
20	0																														
22	1																														
24	4																														
26	5																														
28	2																														
30	4																														
32	0																														
34	0																														
More	2																														
3	24.6	<table border="1"> <caption>Part 3 Cycle Times [s] Frequency Data</caption> <thead> <tr> <th>Bin</th> <th>Frequency</th> </tr> </thead> <tbody> <tr><td>18</td><td>1</td></tr> <tr><td>20</td><td>0</td></tr> <tr><td>22</td><td>5</td></tr> <tr><td>24</td><td>4</td></tr> <tr><td>26</td><td>3</td></tr> <tr><td>28</td><td>3</td></tr> <tr><td>30</td><td>2</td></tr> <tr><td>32</td><td>1</td></tr> <tr><td>More</td><td>1</td></tr> </tbody> </table>	Bin	Frequency	18	1	20	0	22	5	24	4	26	3	28	3	30	2	32	1	More	1	9.3								
Bin	Frequency																														
18	1																														
20	0																														
22	5																														
24	4																														
26	3																														
28	3																														
30	2																														
32	1																														
More	1																														
4	29.1	<table border="1"> <caption>Part 4 Cycle Times [s] Frequency Data</caption> <thead> <tr> <th>Bin</th> <th>Frequency</th> </tr> </thead> <tbody> <tr><td>18</td><td>1</td></tr> <tr><td>20</td><td>0</td></tr> <tr><td>22</td><td>3</td></tr> <tr><td>24</td><td>1</td></tr> <tr><td>26</td><td>2</td></tr> <tr><td>28</td><td>3</td></tr> <tr><td>30</td><td>2</td></tr> <tr><td>32</td><td>2</td></tr> <tr><td>34</td><td>1</td></tr> <tr><td>36</td><td>1</td></tr> <tr><td>38</td><td>0</td></tr> <tr><td>40</td><td>2</td></tr> <tr><td>More</td><td>1</td></tr> </tbody> </table>	Bin	Frequency	18	1	20	0	22	3	24	1	26	2	28	3	30	2	32	2	34	1	36	1	38	0	40	2	More	1	8.9
Bin	Frequency																														
18	1																														
20	0																														
22	3																														
24	1																														
26	2																														
28	3																														
30	2																														
32	2																														
34	1																														
36	1																														
38	0																														
40	2																														
More	1																														

The average system cycle time across all parts tested is 26.8 seconds. The average number of actuations is on the order of 9-11 for all parts. Distribution of cycle times is roughly normal to right-skewed, indicating a denser group of lower cycle times with some occasional high times. All run charts are in control with the exception of part 3, which shows a slight upward trending. The system outperforms the cycle time design specification of one minute by a factor of two over all test trials performed.

Assumption of Data Normality

The previous modeling techniques, analyses, comparisons and results are based on a fundamental assumption of normality in the random disturbance variable. This assumption is validated through analysis of the model residuals, *i.e.* deviations of the observed data to the best fit model.

For the four parts in Table 5.3, ranging from ground bearing rings to a rough-turned steel bar, a full revolution of data are collected and a least squares model of the form (4.5) is fit. Deviation of the actual observations from the fit model (*i.e.*, the residual values) are calculated and plotted on normal probability plots in Figure 5.28 through Figure 5.31.

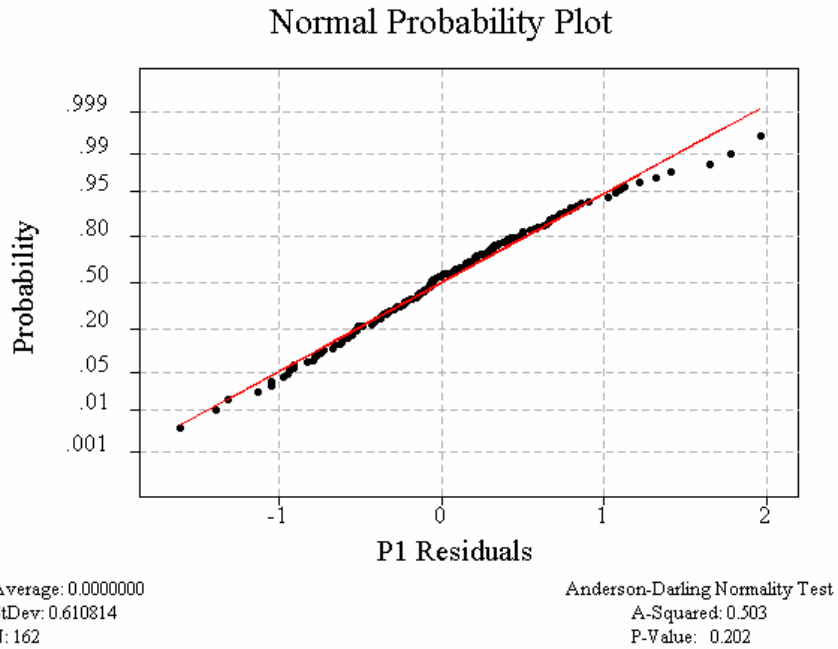


Figure 5.28 - Normal Probability Plot of Ring Model Residual Values, Part 1

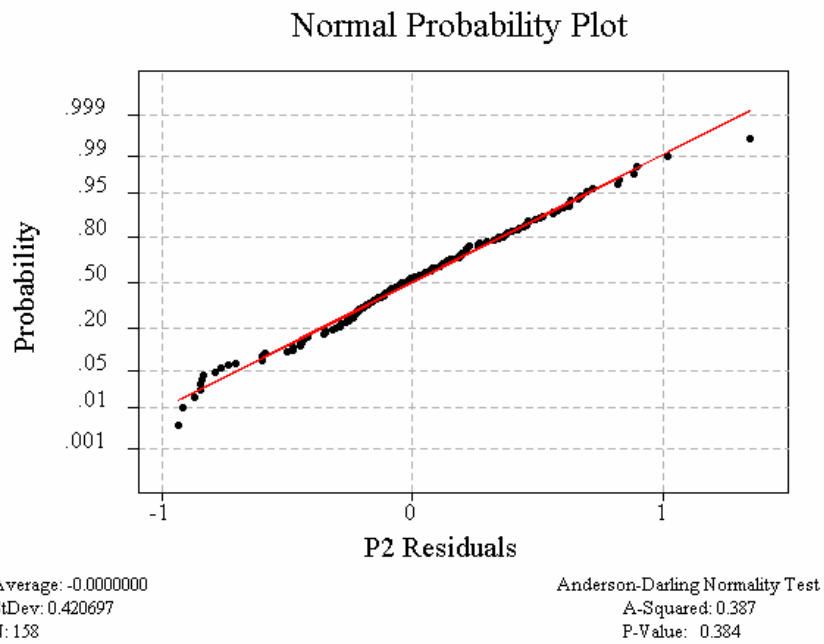


Figure 5.29 - Normal Probability Plot of Ring Model Residual Values, Part 2

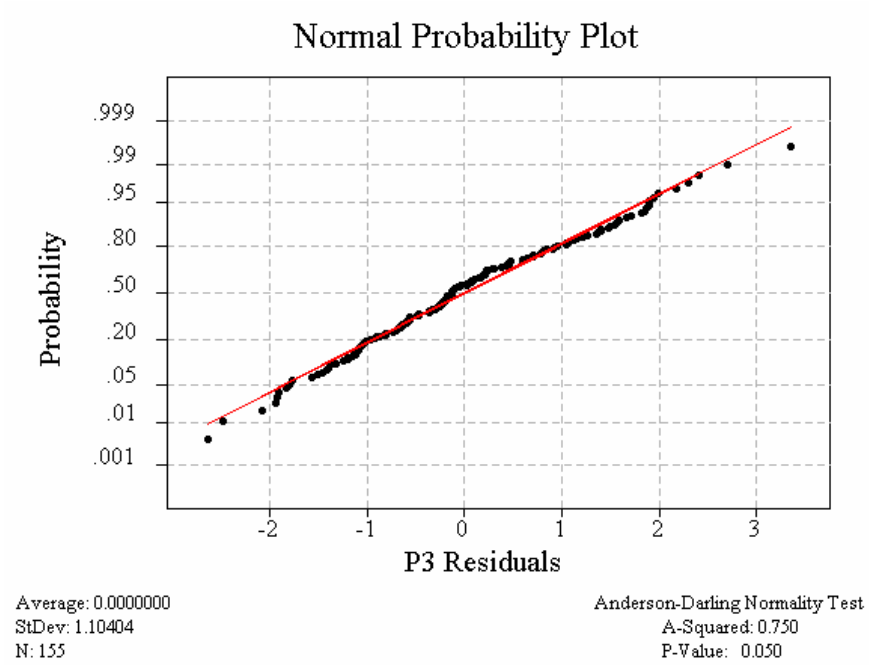


Figure 5.30 - Normal Probability Plot of Ring Model Residual Values, Part 3

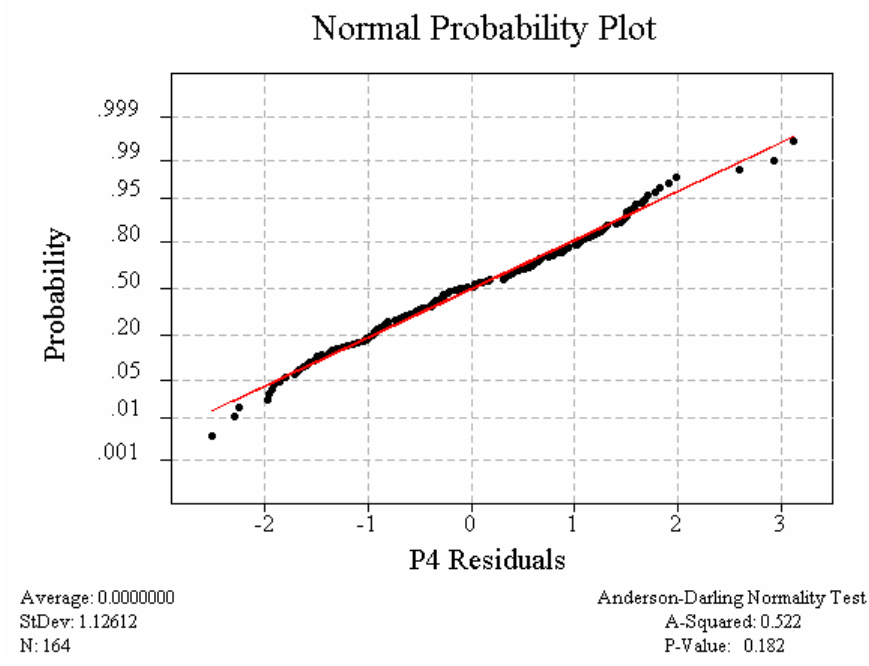


Figure 5.31 - Normal Probability Plot of Ring Model Residual Values, Part 4

The normal probability plot (NPP) indicates normality when the plotted residuals fall along the theoretical normal distribution line. For all parts sampled, this is approximately true. Additionally, the Anderson-Darling A-squared statistic, a measure of the deviation from normality, is calculated. For all parts tested, the statistic is small, indicating good agreement with normal distribution. The normality assumption used in analysis is valid.

For comparison, a NPP of residual data generated randomly on the range [0,1] is shown in Figure 5.32.

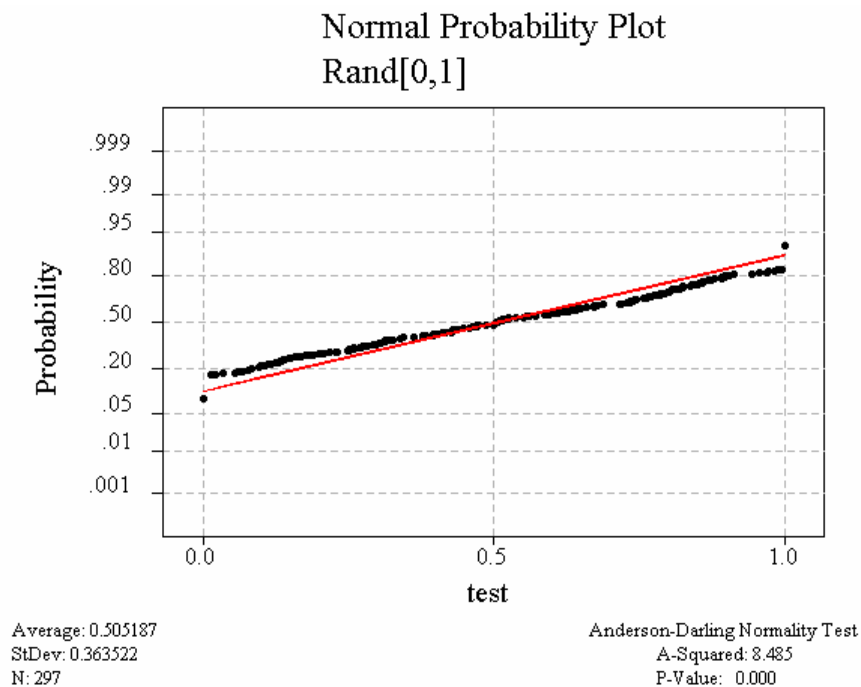


Figure 5.32 – Normal Probability Plot of Randomly-Distributed Data

These data fall away from the theoretical normal line, and the Anderson-Darling statistic is high, indicating departure of the data from a normal distribution. This example validates the previous normality analysis.

Stiction Resonance and Control

The modeling and actuation described and demonstrated in the previous sections is fundamentally based on the assumption that actuation occurs at a fixed velocity after acceleration. Though this simplifies motion control programming, it may not be optimal. A new method of generating the actuation input command is explored, based on analysis of the natural resonant frequency of the stiction effect.

Resonance of Stiction

Fixed-velocity actuation can give rise to the stiction condition described previously, whereby the part whereby upon impact the part accelerates, loses contact with the actuator, and comes to rest. This process is repeated, producing large nonlinear fluctuations in applied force and part velocity. In general, this condition is detrimental to precise and accurate centering.

In the validated model of part actuation by multiple tapping, it is observed not only that the stiction cycle described in previous sections occurs, but also that it occurs at a relatively constant frequency over multiple contacts of the actuator with the part. For the simulated and observed force data in Figure 5.33, the modeled and observed resonance frequencies are 29.9 Hz and 27.8 Hz, respectively.

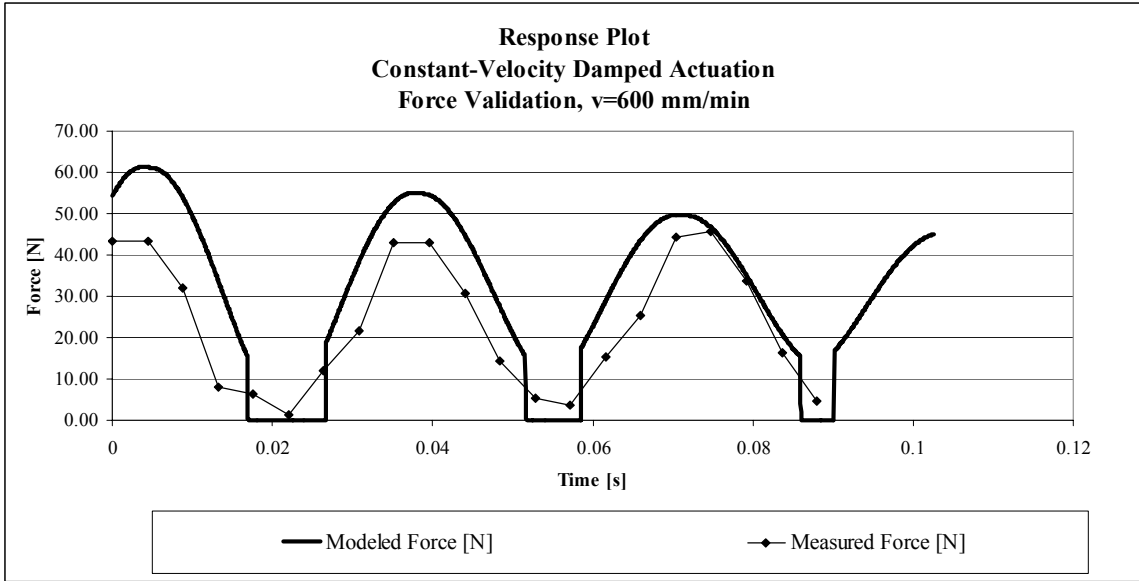


Figure 5.33 - Modeled Force Data vs. Observed for $m=18.9$ kg, $v=600$ mm/min

It is proposed that the input signal be filtered in the frequency domain to remove a band of frequencies around this value in order to avoid excitation of this *stiction resonance frequency*.

Stiction Resonance Frequency Invariance to Velocity

Prior to developing a filtering algorithm, the resonance frequency is analyzed over a range of input velocities. The dominant frequency of the reaction model data is calculated over the range of actuation velocities. Specific results of force modeling for several velocity cases are given in Appendix D. For each case, the modeled and observed resonance is calculated as shown in Figure 5.34.

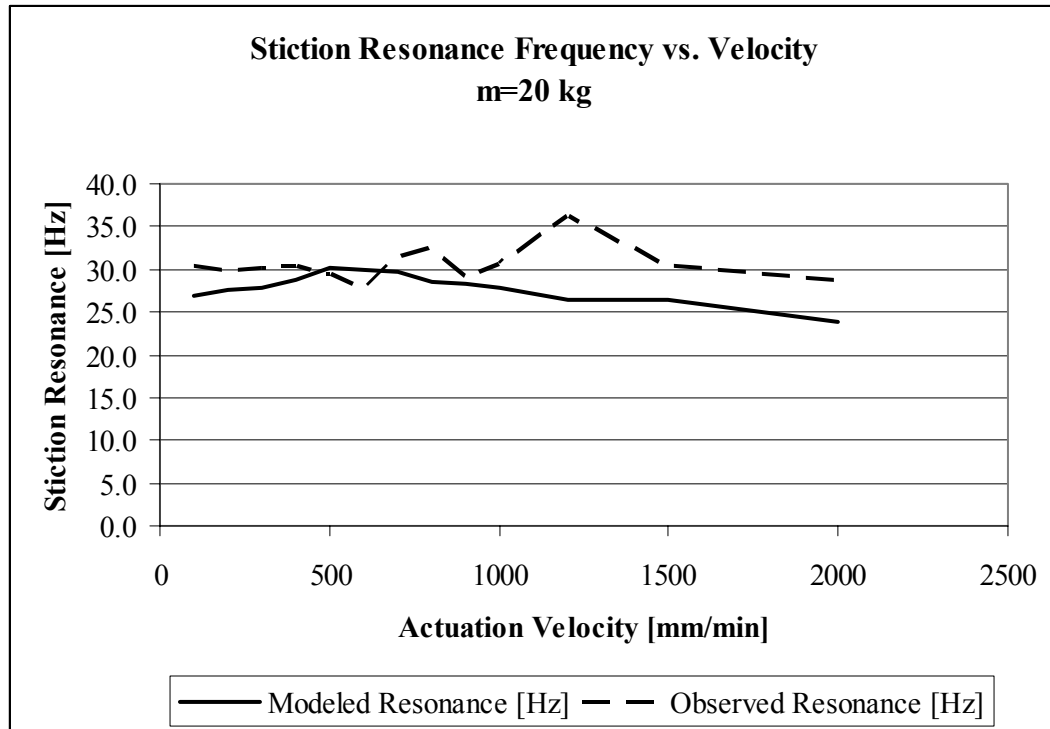


Figure 5.34 - Resonance of Stiction in Constant Velocity Actuation

Two conclusions are drawn from this data:

- 1) Error of the dynamic model with respect to dominant frequency is relatively low across the range of frequencies tested. The maximum absolute error is 9.7 Hz and the average error is 3.1 Hz. The model is validated with respect to stiction resonance frequency prediction.
- 2) The resonance frequency is relatively constant across the domain of actuation velocity. The absolute range of the modeled data is 6.2 Hz and range of the observed data is 8.5 Hz.

Due to the insensitivity of the stiction resonance frequency to changes in velocity over the applicable range of the system, the validated model can be used to predict the stiction resonance of the system for a given part. The system can then apply a fixed limit

bandstop filter to the velocity signal around the resonance frequency rather than using a velocity-specific filtering algorithm.

Input Signal Filtering and Actuation

The data and analyses of previous sections are based on constant-velocity actuation. Once a resonance frequency is identified, the input signal is filtered in the velocity domain to eliminate actuation near resonance.

Using a 3rd order Butterworth filter, the frequency band from 5 Hz to 40 Hz is removed from the constant velocity signal to create the “anti-resonance” signal for this part. The magnitude transfer function for this filter is shown on a linear scale in Figure 5.35.

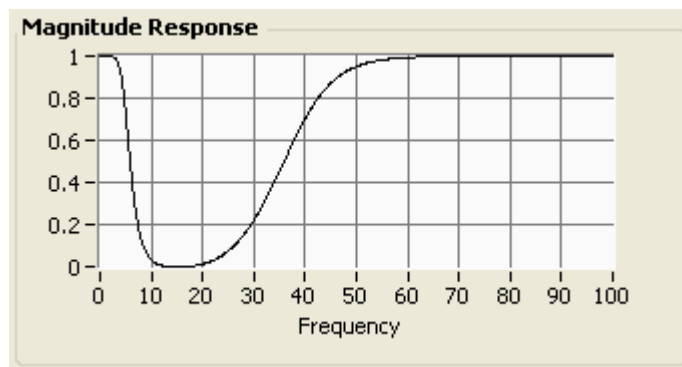


Figure 5.35 - Magnitude Transfer Function of Bandstop Filter

The signal is attenuated in the frequency range around the resonance frequency. The resultant bandlimited filtered velocity command signal is shown in Figure 5.36 with the original constant velocity input for reference.

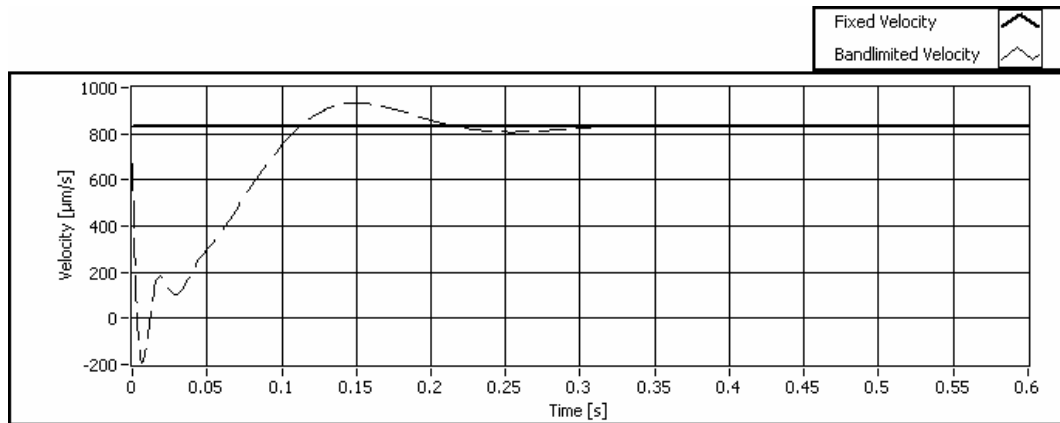


Figure 5.36 - Bandlimited Velocity Signal (20 Hz - 40 Hz removed)

This actuation command results in the slide position contour shown in Figure 5.37.

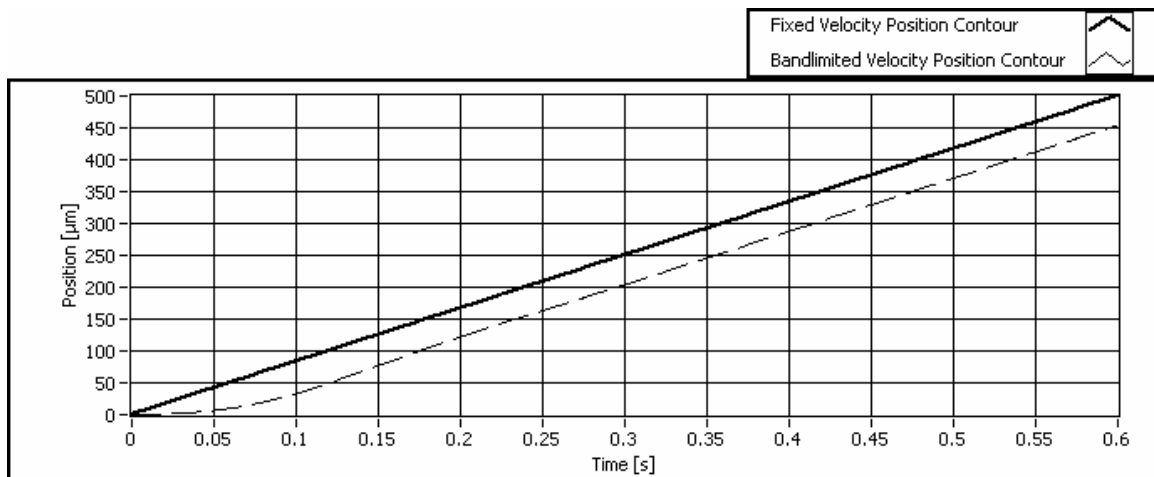


Figure 5.37 - Position Contour of Constant and Bandlimited Velocity Command Profiles

The filtered input command causes a lag in the system. This does not present a problem in the centering application since the trajectory-planning algorithm includes a calculated lead angle variable. This lead can compensate for the expected system lag using the variable rather than constant velocity input.

To better visualize the comparison of these signals, the bandlimited position is normalized to the constant velocity command position. The normalized signal is shown in Figure 5.38.

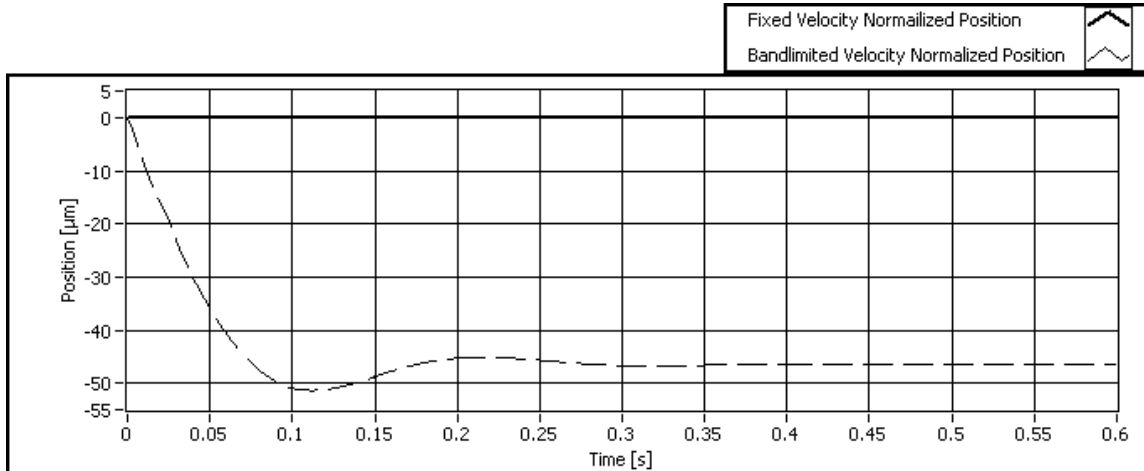


Figure 5.38 - Simulated Command Position Normalized to Constant Velocity Input

The contour falls away from the fixed-velocity contour near the beginning of actuation, then settles to a steady-state actuation that lags the constant-velocity signal by 47 μm. The net effect of this profile is acceleration of the part after contact near the beginning of the actuation, up to the steady-state velocity. This profile dynamically reduces the resonant effect of stiction.

Actuation Simulation Results

The profile of Figure 5.36 is used as the input to the part sliding simulation under the conditions $m=18.9$ kg, $v=600$ mm/min. The modeled force responses for the constant velocity and bandlimited velocity inputs are shown in Figure 5.39.

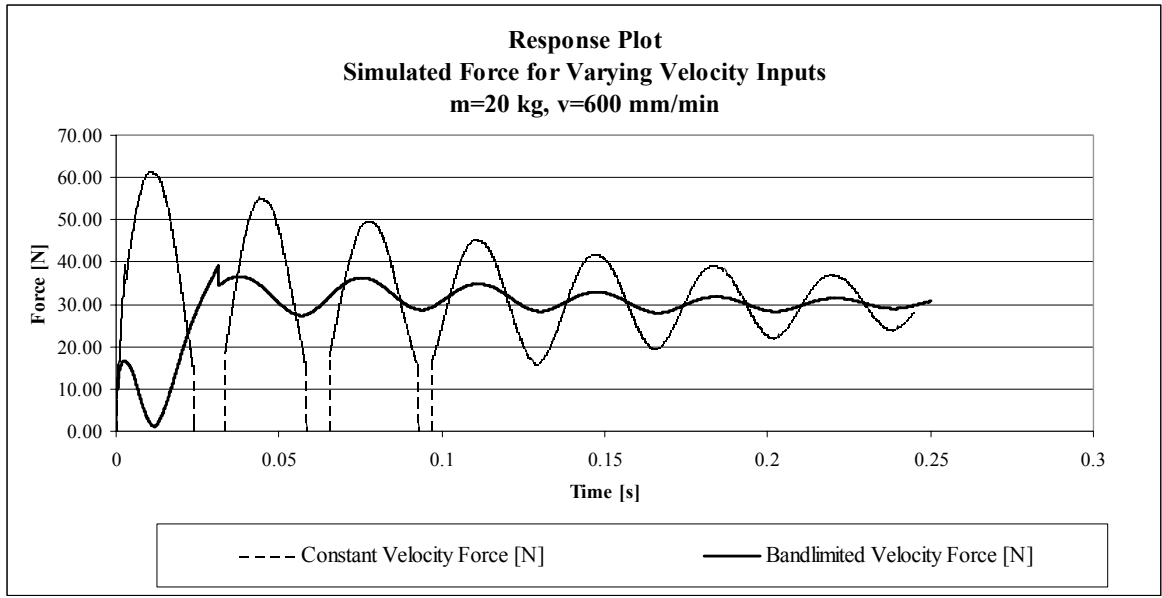


Figure 5.39 - Simulated Force Response with Constant and Bandlimited Velocity Inputs

For actuation at constant velocity, the force fluctuates from a maximum of over 60 N to 0, indicating loss of contact with the part being pushed. The actuator loses contact with the part three times before settling into a slowly decaying resonant pushing mode above 0.1 seconds. When actuated with the bandlimited velocity signal, the force achieves an approximate steady-state level in 0.05 seconds, and fluctuates by a maximum value of only 17 N.

The effect of this improved force response on part positioning is shown in Figure 5.40. The signal is time-shifted to align the final values (accounts for increased lead to compensate for the system lag).

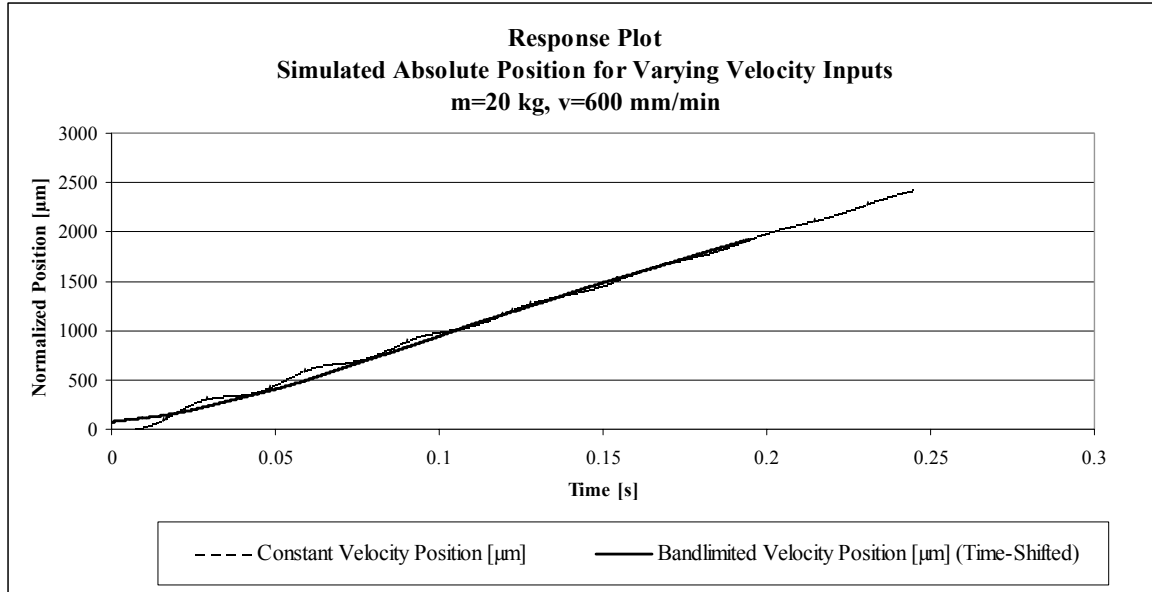


Figure 5.40 – Simulated Position Response with Constant and Bandlimited Velocity Inputs

The fluctuation or resonant effect of sliding is notably reduced. To better quantify this effect, both signals are normalized to the constant velocity input signal in Figure 5.41. Again, the velocity-compensated signal is time-shifted to offset system lag.

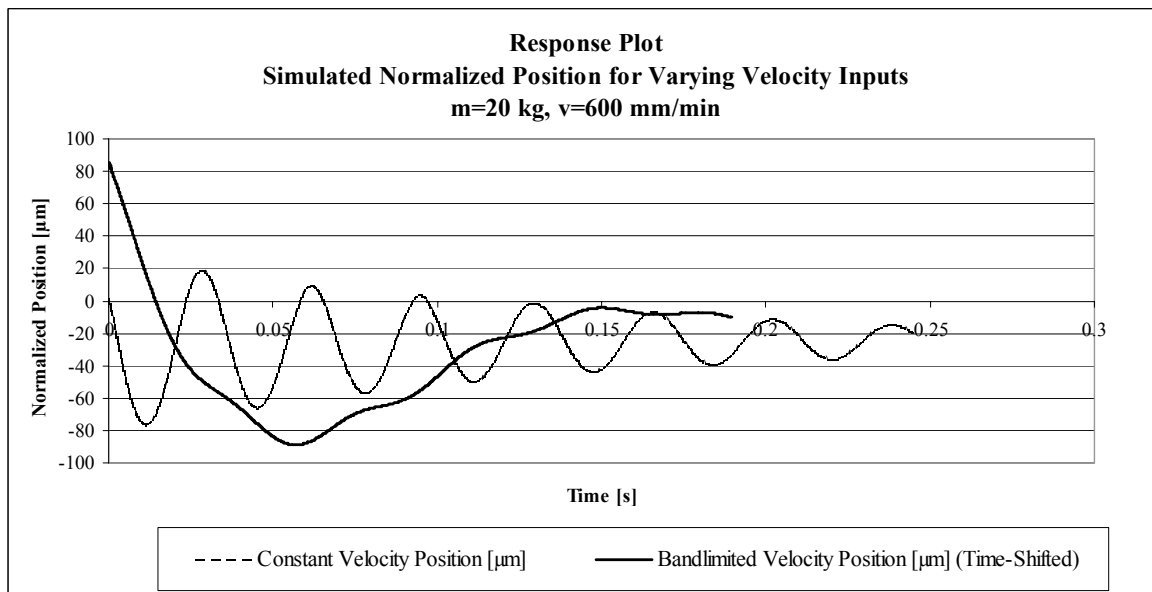


Figure 5.41 - Simulated Normalized Position Response with Constant and Bandlimited Velocity Inputs

Once actuator contact is made with the part, it is maintained, improving controllability of the actuation. Part position fluctuation about the constant velocity command signal is reduced from almost 100 μm using constant velocity input to less than 40 μm using the bandlimited velocity input. The part reaches steady state pushing faster and is less affected by the resonance of stiction.

Validation Results

As shown in simulation, larger parts are more susceptible to actuation problems arising from the large variations in force and expected position caused by stiction. For this reason, the largest part available ($m=18.9\text{ kg}$) is tested using the frequency bandlimiting method. This part is run across a range of velocities, both at constant velocity and frequency-banded velocity command input. The force results of the case for $v=600\text{ mm/min}$ are given in Figure 5.42.

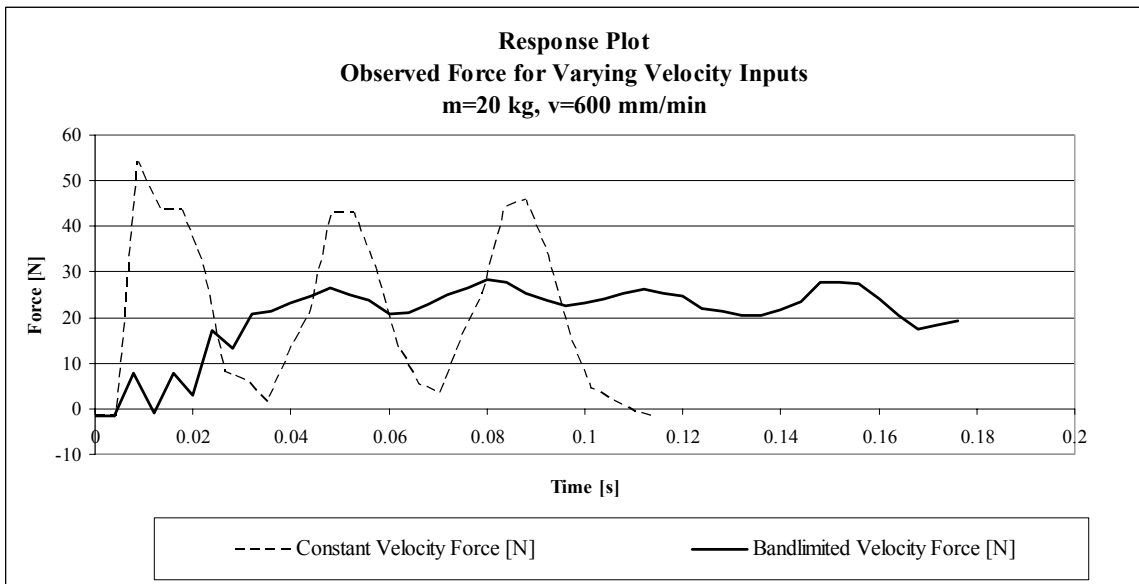


Figure 5.42 - Force Data for Constant Velocity and Bandlimited Velocity Actuation, $m=18.9\text{ kg}$

As predicted by the simulation, the constant velocity input results in a resonant “tapping” of the part, whereby the force periodically drops to zero, indicating loss of contact. Alternatively, the bandlimited velocity profile results in only a single acceleration to steady-state actuation, with less than 10 N of variation at steady state.

Additional experimental result cases for force over a range of base actuation velocities are given in Appendix E. In all cases, the force rises to the average pushing value and exhibits less fluctuation than with constant velocity pushing. In addition, the force is never reduced to zero during the actuation, indicating that contact with the part is never broken.

The position data for this experiment as shown in Figure 5.43 yield similar results when compared with simulation. As in the simulated data, the position response plot for bandlimited data is time shifted to align the endpoints.

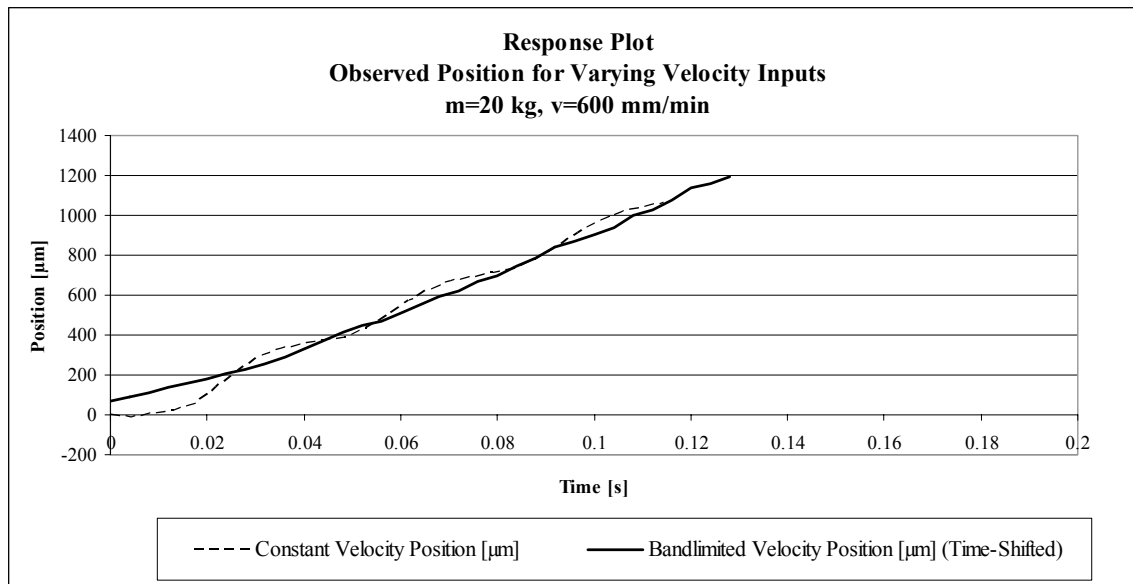


Figure 5.43 – Experimental Position Data for Constant Velocity and Bandlimited Velocity Actuation, m=18.9 kg, v=600 mm/min

The constant-velocity actuation shows a periodic free sliding effect, while the bandlimited-velocity actuation shows a smoother approach to steady state with less

fluctuation. The data are normalized to the constant velocity (straight line) slide position in Figure 5.44.

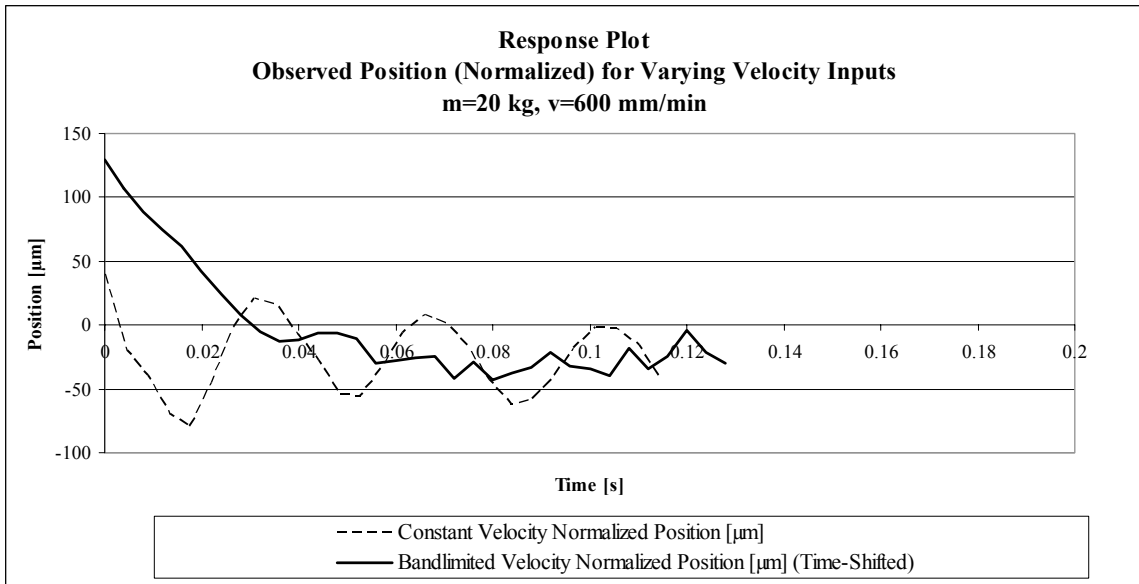


Figure 5.44 – Normalized Experimental Position Data for Constant Velocity and Bandlimited Velocity Actuation, m=18.9 kg, v=600 mm/min

Again, the free sliding condition and larger fluctuation (90 μm overall range) are evident in the constant velocity actuation. Alternatively, the steady state fluctuation range of the bandlimited velocity actuation is 20 μm . This is on the order of the simulated results.

Additional experimental result cases for position of the large subject part over a range of base actuation velocities are given in Appendix F. Position results confirm the force result findings that the part undergoes reduced fluctuation with bandlimited velocity actuation, and contact between actuator and part is maintained.

Validation of Lower Mass Part

The experiment is repeated for a part of m=0.8 kg at 2500 mm/min actuation velocity. In this case, the constant velocity force response is given in Figure 5.45.

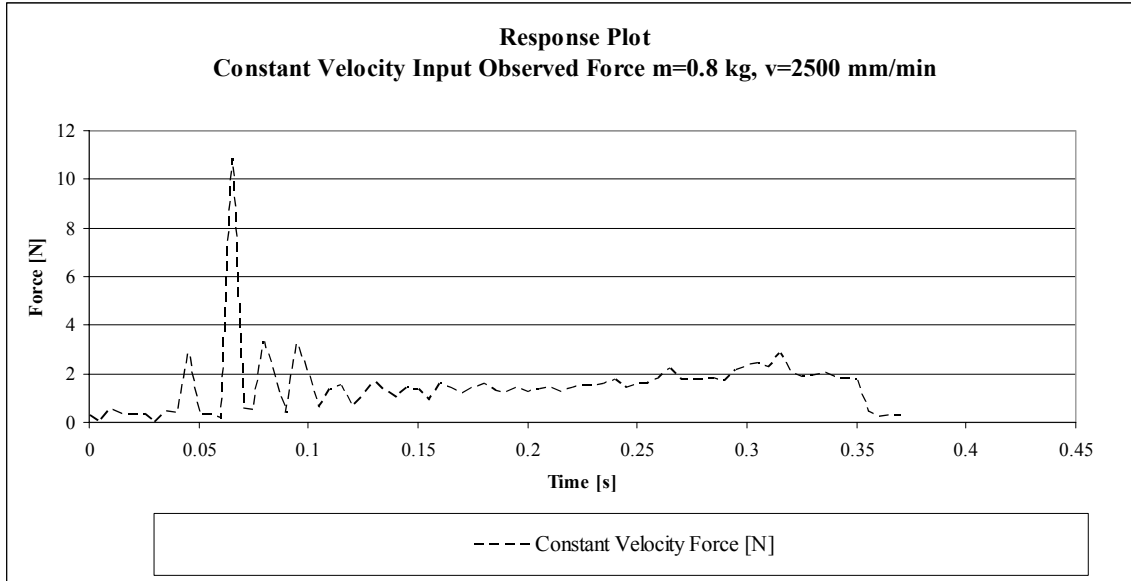


Figure 5.45 - Force Response Data for Constant Velocity Actuation, $m=0.8$ kg

The observed resonance frequency of this part is 51 Hz. The part exhibits little free sliding and does not come completely to rest after initial actuation. A 3rd order Butterworth bandstop filter is applied to the input velocity signal on the frequency range [10, 100]. The resultant velocity command signal is shown in Figure 5.46.

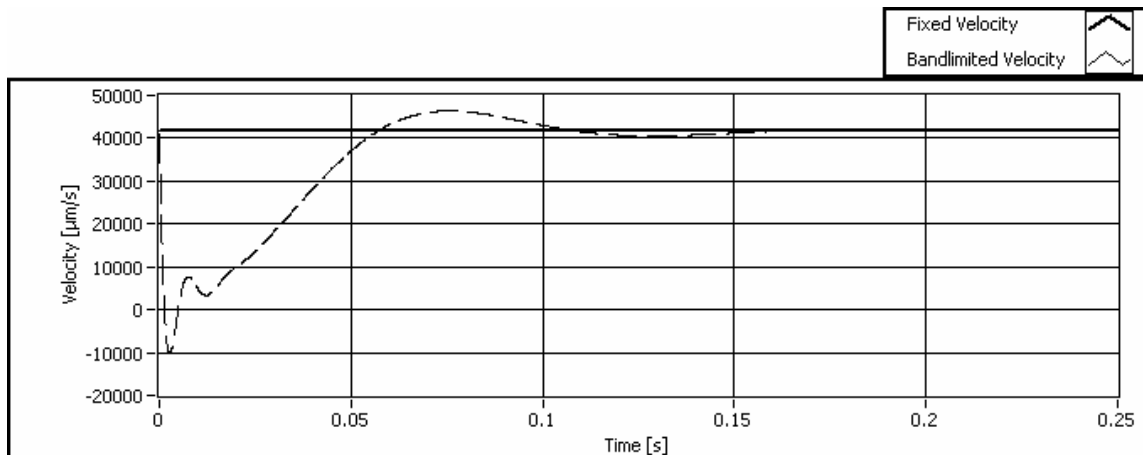


Figure 5.46 - Velocity Command Profile, Constant and [10 Hz, 100 Hz] Filtered, $v=2500$ mm/min

This input command is applied to the $m=0.8$ kg part with position results shown in Figure 5.47 over the constant-velocity actuation results.

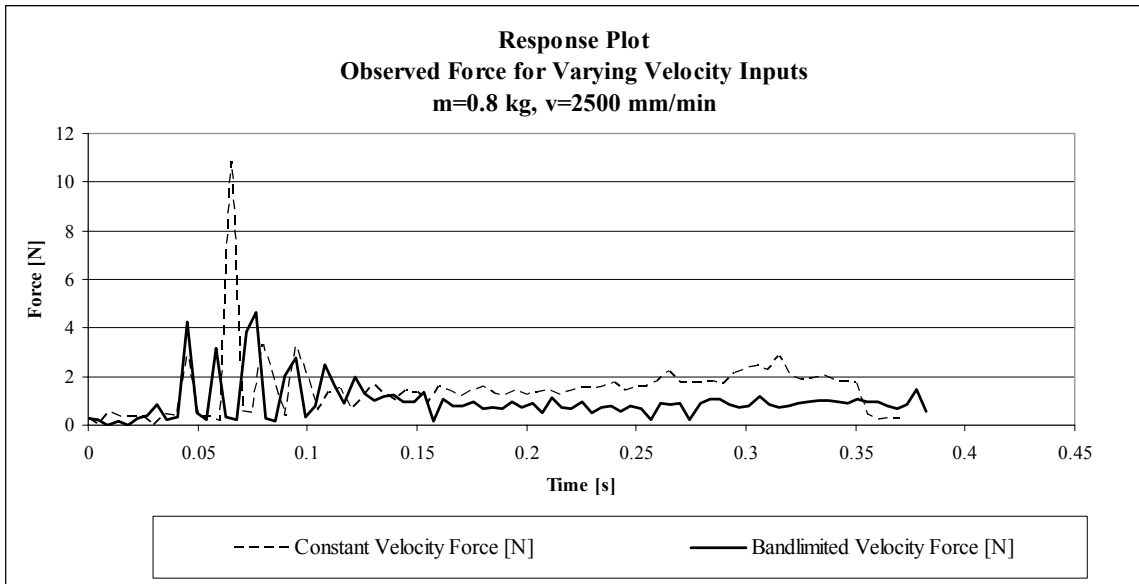


Figure 5.47 - Force Data for Constant Velocity and Bandlimited Velocity Actuation, $m=0.8$ kg

The result of applying bandstop filtering of the velocity signal about the stiction resonance frequency of the lighter part is similar to, though not as profound as the heavier part. For the 0.8 kg part the peak force encountered is reduced 58%, but some resonance actuation is still evident. Resonance in either constant-velocity or bandlimited-velocity actuation of lighter parts damps out quickly, so does not have as appreciable an effect as in actuation of heavier parts.

Applicability of Input Signal Filtering

The stick-slip effect is far more pronounced on the heavier part than on the lighter part. In the case of the heavier part, up to 80% reduction in positional fluctuation was observed, with complete elimination of free sliding in all velocities. In the case of the light part, resonance is only evident in a limited band of input velocities and is attenuated to a far lesser degree through bandlimiting the velocity signal.

This input signal augmentation requires additional calculation time, and should be applied only where significant benefit can be achieved to avoid preemption of higher priority tasks in the real time controller. From the experimental results, it is seen that this benefit is restricted only to heavier part actuation, so a lower mass limit at or below 18.9 kg should be set, above which frequency-bandlimiting velocity actuation is applied.

CHAPTER 6

OPTIMAL ESTIMATION AND SYSTEM ADAPTABILITY

Continuous Real-Time Estimation

Friction Model Parameter Estimation

The foregoing analyses and trajectory planning rules incorporate a friction model that utilizes fixed parameters. These parameters were derived from empirical testing using the prototype setup and subject rings under study. However, it must be realized that in normal use in factory conditions, effects will be present that will change the underlying parameters of the model. Effects can occur acutely such as attempting to center an oily part, or over the long term such as buildup of contaminants on the sliding interface surface.

For this reason, an attempt is made to estimate these underlying parameters during the centering cycle. Such estimation will provide higher accuracy of the underlying model over the initially-determined parameters, and will lead to higher accuracy in centering (a primary design objective). Investigation is made into live parameter estimation using two methods: Direct Force Measurement and Derivation from Sliding Distance.

Direct Force Measurement

The centering prototype machine includes an analog piezoelectric force sensor of range ± 446 N and sensitivity of 11.2 mV/N. During actuation, force is measured in real time (an example is shown in Figure 6.1).

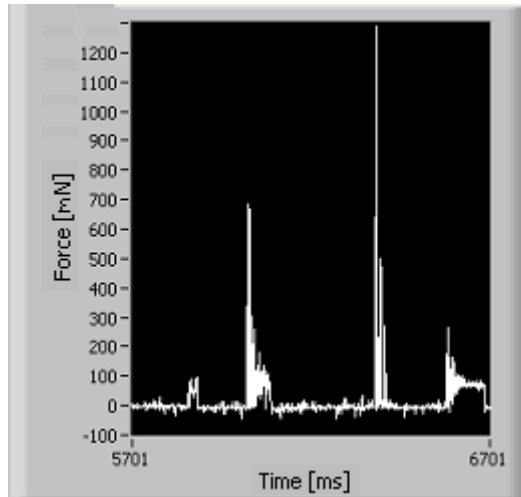


Figure 6.1 - Force Readings from Centering Cycle

If the characteristics of this force curve, specifically peak force per actuation, can be successfully related to underlying friction model parameters, the force input will serve as a friction estimator.

The friction model validated in Chapter 5 for resonance is evaluated with respect to peak force level, hypothetically related to the friction model parameters. The force model vs. experimental data from the case of $m=18.9$ kg, $v=600$ mm/min is repeated in Figure 6.2:

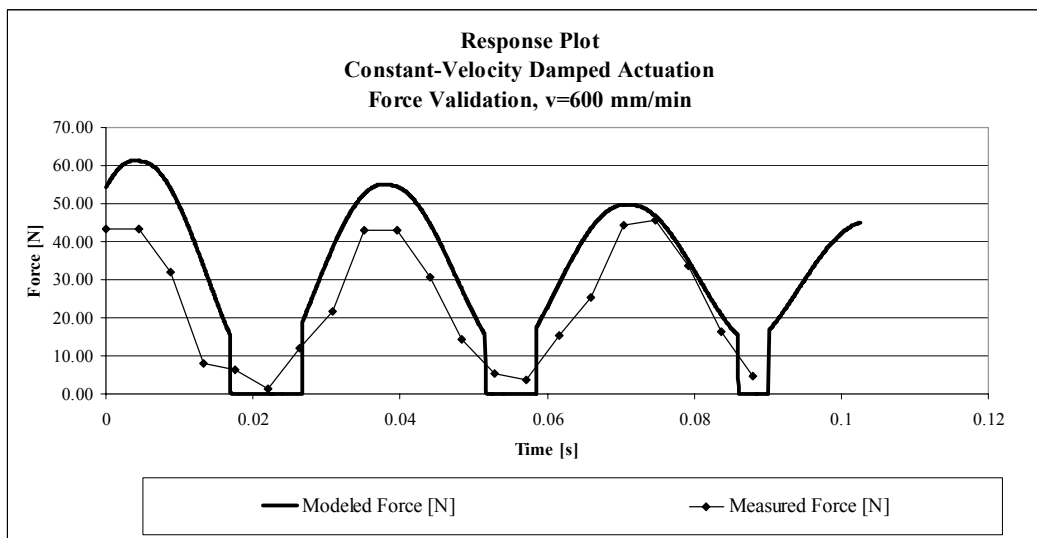


Figure 6.2 - Modeled Force vs. Data, $m=18.9$ kg, $v=600$ mm/min

The modeled peak force level is on the same order as the empirical data, so the model is a feasible estimator. Errors in the peak force estimation using nominal friction parameters for the part described in Table 4.3 across the range of expected actuation velocities are given in Table 6.1:

Table 6.1 - Peak Force Modeling Error

Velocity [mm/min]	Modeled Peak Force [N]	Observed Peak Force [N]	Peak Force Error
100	39.81	35.53	12.0%
200	41.83	30.33	37.9%
300	46.25	33.94	36.3%
400	51.00	37.30	36.7%
500	56.19	40.94	37.3%
600	61.39	54.22	13.2%
700	66.65	47.16	41.3%
800	71.87	50.20	43.2%
900	76.16	57.01	33.6%
1000	79.76	66.71	19.6%
1200	86.95	77.89	11.6%
1500	118.48	107.05	10.7%
2000	123.14	97.58	26.2%

The peak force estimation is high for all velocities by an average of 14.1 N, or 28% of the observed value. This deviation is relatively consistent across actuation velocity and is error-corrected to within 10 N by adding the average error value of all cases:

$$F_{peak,corrected} = F_{peak,observed} + 14.1 \quad (6.1)$$

The force model is evaluated for the small part (m=0.8 kg) over a range of friction parameters, varying μ_s and setting μ_k to 75% of μ_s , on the order of the empirically-observed relationship. These data are presented in Figure 6.3:

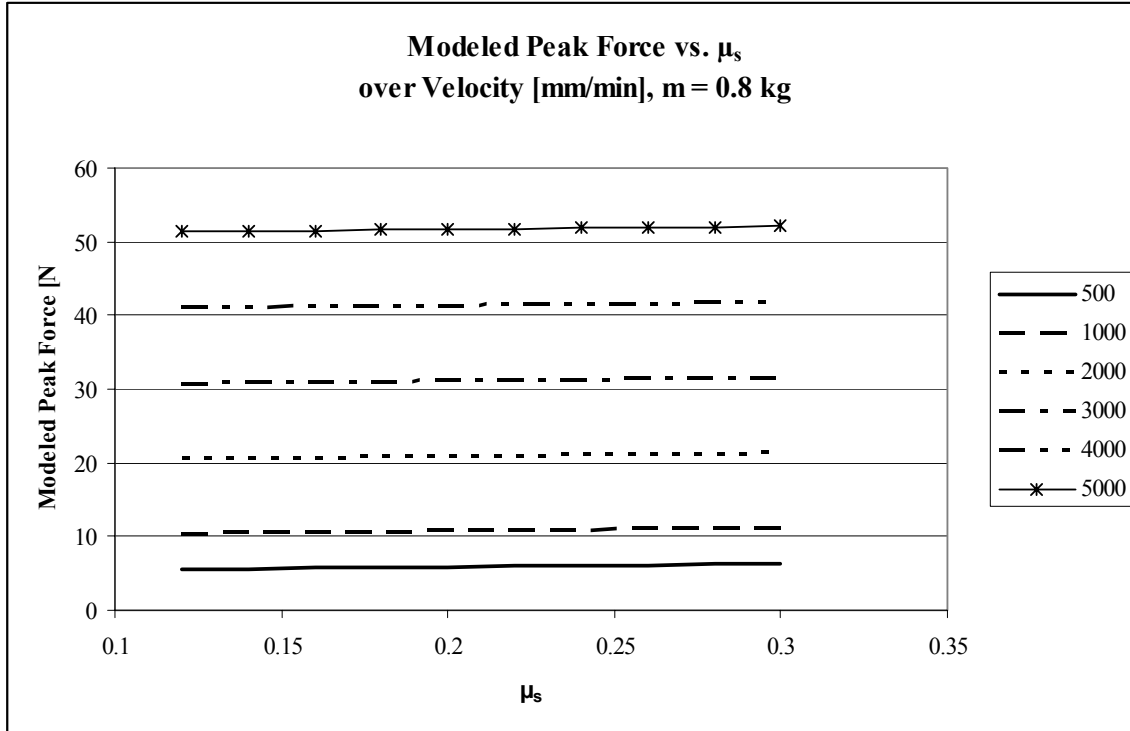


Figure 6.3 – Modeled Force Variation with μ_s over Velocity Range, m=0.8 kg

The figure shows that over a significant range of velocities for the small part, the gradient of the force with respect to the static friction coefficient μ_s is small (maximum of 0.8 N variation, on the order of the sensor resolution):

$$\left. \frac{dF}{d\mu_s} \right|_{m=0.8 \text{ kg}} \approx 0 \quad (6.2)$$

This shows that the force is insensitive to changes in the friction model parameters, so it is not an effective predictor of these parameters.

For the large part, the peak force response to changes in the friction parameter is shown in Figure 6.4.

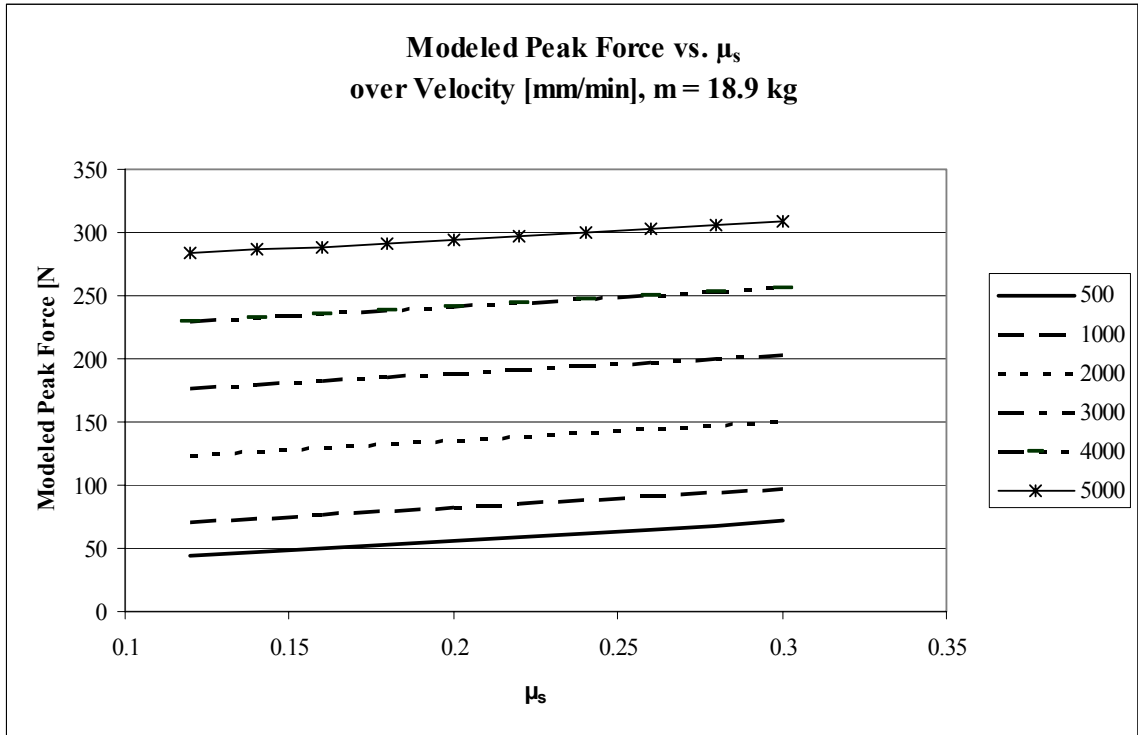


Figure 6.4 - Modeled Force Variation with μ_s over Velocity Range, $m=18.9$ kg

The force gradient in this case is more appreciable (minimum of 25.6 N), and is more readily detected with the force sensor. A linear relationship is established of the form

$$F_p = F_0 + C_\mu \mu_s \quad (6.3)$$

Assuming that the force intercept F_0 is linearly related to velocity,

$$F_p = C_v v + C_\mu \mu_s \quad (6.4)$$

This equation is fit to the model simulation output, with C_v and C_μ plotted relative to input velocity in Figure 6.5:

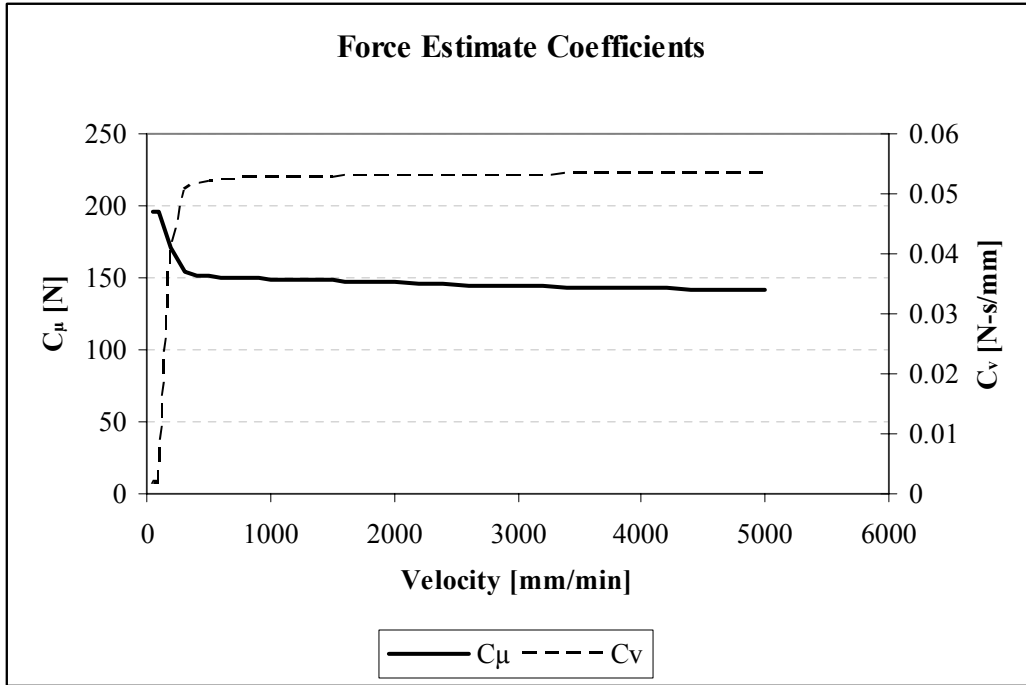


Figure 6.5 - Force Estimate Coefficients vs. Velocity

Over 500 mm/min, the coefficients are stable and the model assumptions are valid. The force model with coefficients at their average values over 500 mm/min is

$$F_p = 0.0529v + 146.2\mu_s \quad (6.5)$$

The friction coefficient can therefore be predicted from the force:

$$\mu_s = \frac{F_p - 0.0529v}{146.2}$$

$$F_p = \text{measured peak force [N]} \quad (6.6)$$

$$v = \text{actuation velocity} \left[\frac{\text{mm}}{\text{min}} \right]$$

The result is an explicit linear approximation to the higher order differential equation (5.27). The approximation is valid for the 18.9 kg subject part, but similar analyses are possible for additional heavy parts.

Friction Parameter Derivation from Sliding Distance

In Chapter 5, the free-sliding distance prediction model was validated for the sample parts. Now this model is explored for sensitivity to friction model parameters, so that the free-sliding distance can be used as a *predictor* of these parameters. The model is again evaluated over a range of friction parameters and velocities for the 0.8 kg part and the 18.9 kg part. The modeled free-sliding distance data for the 0.8 kg part over a range of velocities is given in Figure 6.6:

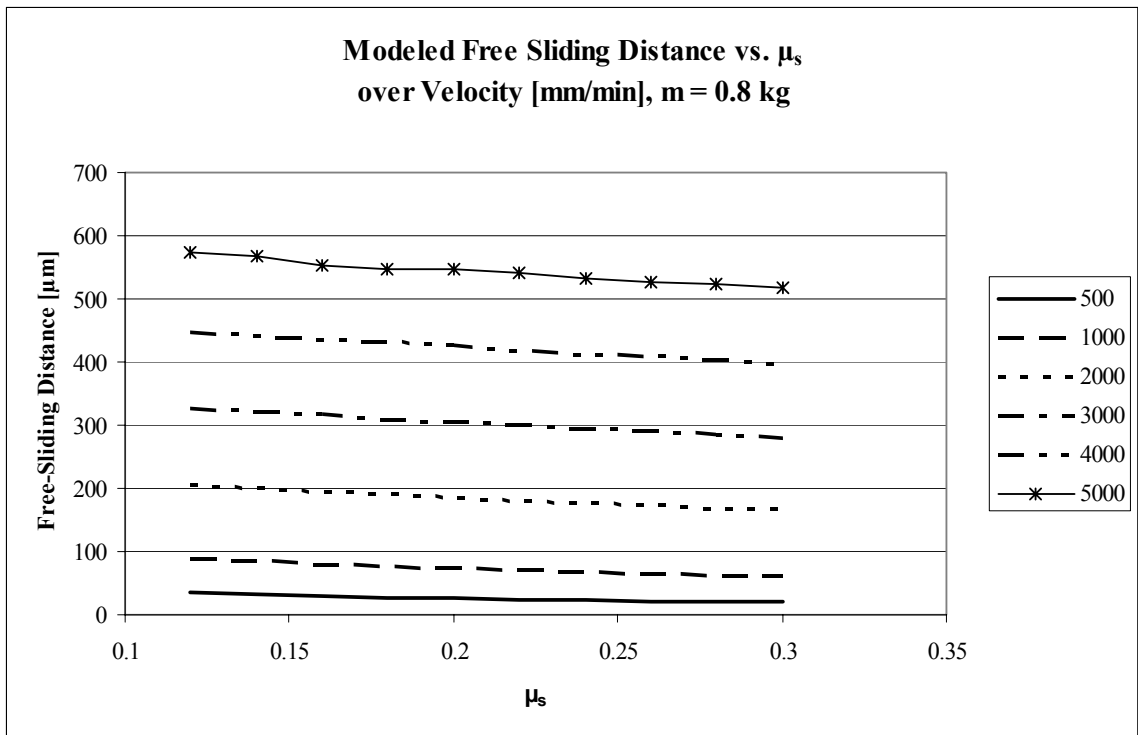


Figure 6.6 - Modeled Free-Sliding Distance vs. Velocity, m=0.8 kg

For the smaller part, the free-sliding distance is a somewhat better predictor of frictional parameters than the peak force. However for this part, the free-sliding distance is still relatively insensitive to changes in μ_s (maximum variation of 58 μm), making it a poor predictor.

For the larger part, free-sliding distance is somewhat more sensitive to friction parameter changes. The modeled free sliding distance vs. friction parameter for this part is shown in Figure 6.7 for a range of velocities:

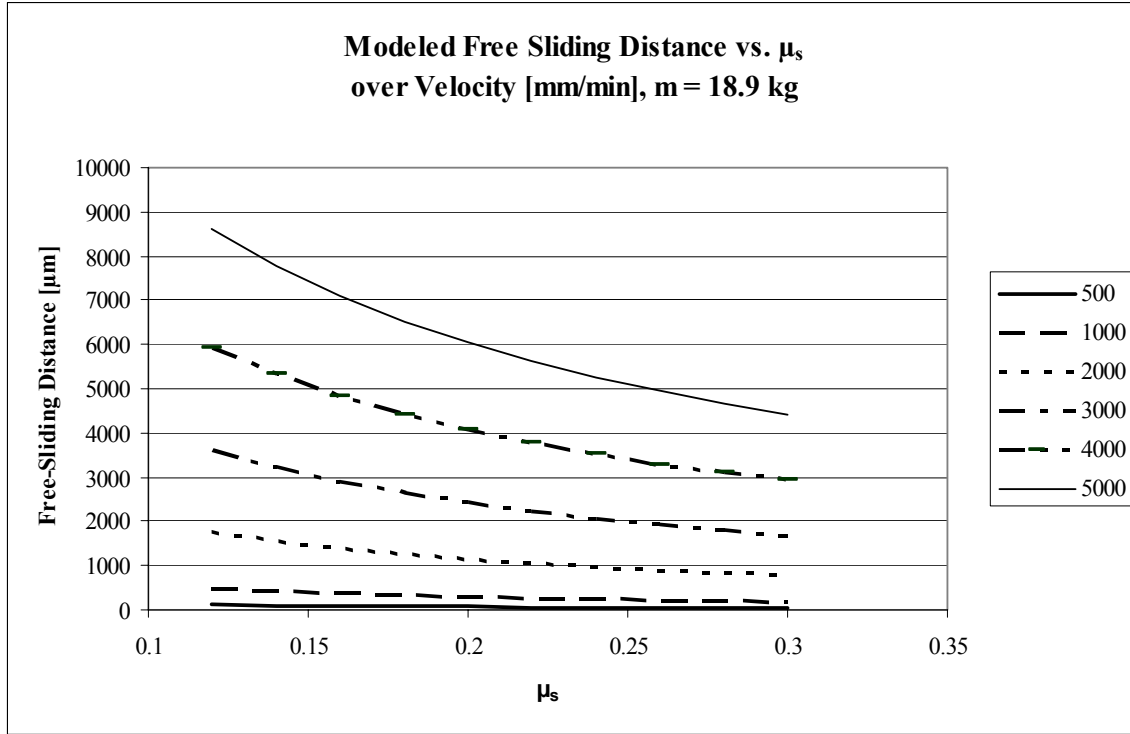


Figure 6.7 - Modeled Free-Sliding Distance vs. Velocity, $m=18.9$ kg

Maximum variation across the friction parameter range is almost 4200 μm , indicating that free sliding distance is a promising predictor of the friction parameter.

A second-order model is assumed of the form

$$d - d_0 = A(\mu - \mu_0)^2 \quad (6.7)$$

Relationships between d_0 , A and v (actuation velocity) are assumed of the power form

$$\begin{aligned} d_0 &= C_1 v^{k_1} \\ A &= C_2 v^{k_2} \end{aligned} \quad (6.8)$$

A nonlinear least squares fitting routine is performed on the data to arrive at the values

$$\begin{aligned}
 \mu_0 &= 0.3415 \\
 C_1 &= 0.00041 \left[\frac{\mu m - \min}{mm} \right]^{1/k_1} \\
 k_1 &= 1.8997 \\
 C_2 &= 0.07379 \left[\frac{\mu m - \min}{mm} \right]^{1/k_2} \\
 k_2 &= 1.6428
 \end{aligned} \tag{6.9}$$

Rearranging (6.7) with μ as the dependent variable and substituting (6.8) gives the relationship

$$\mu = \mu_0 - \sqrt{\frac{d - C_1 v^{k_1}}{C_2 v^{k_2}}} \tag{6.10}$$

Substituting the determined values from (6.9) yields the explicit relationship

$$\begin{aligned}
 \mu &= 0.3415 - \sqrt{\frac{d - 0.00041 v^{1.8997}}{0.07379 v^{1.6428}}} \\
 d &\equiv \text{free sliding distance } [\mu m] \\
 v &\equiv \text{slide velocity } \left[\frac{mm}{min} \right]
 \end{aligned} \tag{6.11}$$

Estimated point values are plotted over the model data in Figure 6.8.

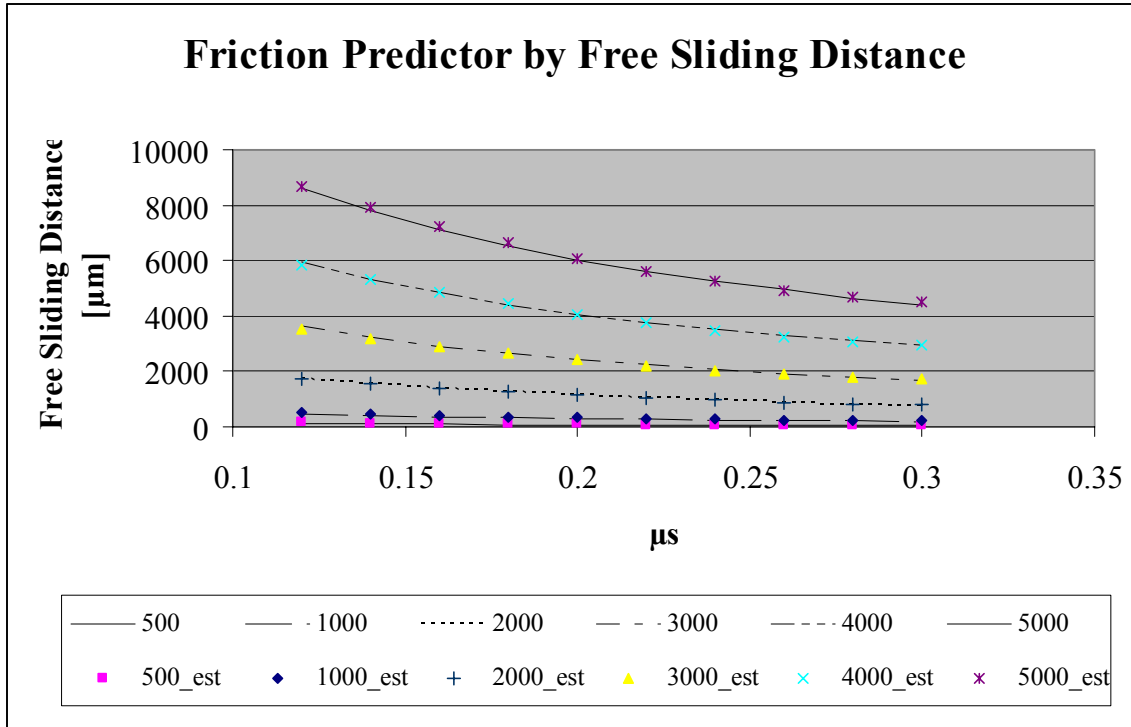


Figure 6.8 - Friction Relationship to Free Sliding Distance

Again, a simple explicit estimator of a higher-order differential equation solution is derived. The approximation is valid for the 18.9 kg subject part, but similar relationships can similarly be derived.

The forgoing friction prediction scheme makes 2 simplifying assumptions:

- $\mu_k = 0.75\mu_s$. This relationship is observed to within 15% over all parts tested.
- k_v is kept constant. In experiments, the value of k_v determined gave only a small contribution to the overall friction force. For example, neglecting the viscous component in experiments with part 4 yielded a difference in the estimated value of μ_k of 0.007, an error of less than 6%. Since k_v is an input to the dynamic model, real-time determination of this value should be possible in future work; however, the additional unknown value in the

model will require an additional data point (i.e., data from two actuations rather than just one).

Predictor Validation

For the validation study, the largest part in the sample set is used, as its predictors were shown to be most sensitive to changes in friction parameters. The part is tested in both a clean, dry environment and a lubricated environment.

Case 1 – Dry

The sliding surfaces of the subject part and table are cleaned using rubbing alcohol. The breakaway friction force is measured using a hand gauge and used to derive the actual frictional parameter as

$$\mu_{s,dry} = 0.141$$

The part is then statically actuated and peak force at 500, 1000, 2000, 3000, 4000 and 5000 mm/min is measured using the piezoelectric force gauge. The resultant peak force is error corrected according to (6.1) and used to predict μ_s . Subsequently, free-sliding distance is measured for each velocity level. This distance is also used to predict μ_s . Results for each case are presented in Table 6.2.

Case 2 – Lubricated

The previous study is repeated for the same part lubricated with DTE Medium industrial oil. The measured μ_s in this case is

$$\mu_{s,wet} = 0.135$$

The same conditions of the previous case are run, and μ_s predicted by both the peak force estimator and the free-sliding estimator. Results of this experiment with prediction errors are summarized in Table 6.2.

Table 6.2 - Results of Friction Prediction Experiment

Surface	Actuation Velocity [mm/min]	Peak Force [N]	μ_s by Force Predictor	Error	Free Sliding Distance [μm]	μ_s by Distance Predictor	Error
dry	N/A	27.6	0.141 (actual)		N/A	N/A	
	500	46.1	0.134	-4.3%	265	0.018	-87.4%
	1000	80.2	0.187	32.8%	613	0.086	-38.6%
	2000	127.3	0.147	4.5%	1240	0.186	32.1%
	3000	181.0	0.152	8.5%	2844	0.165	17.1%
	4000	232.0	0.139	-0.8%	5215	0.145	3.1%
	5000	283.9	0.133	-5.5%	8175	0.133	-5.1%
oily	N/A	26.5	0.135 (actual)		N/A	N/A	
	500	42.1	0.107	-19.9%	267	0.016	-84.3%
	1000	79.7	0.183	34.3%	590	0.193	-29.5%
	2000	136.3	0.209	52.5%	1240	0.186	36.1%
	3000	183.7	0.171	25.7%	2875	0.162	19.5%
	4000	236.8	0.172	26.7%	5475	0.134	-0.4%
	5000	285.9	0.147	8.3%	8620	0.122	-9.5%

The force estimator has a maximum error of 33% in the dry condition and 53% in the oily condition. The free-sliding estimator has a maximum prediction error of 87% in the dry condition and 84% in the wet condition. Both methods at first appear to be poor predictors of friction model parameters. However, prediction error improves with increasing velocity. Except for the force predictor at 4000 mm/min, all predicted values of friction model parameter obtained above 3000 mm/min are within 10% of the experimentally-determined friction value for the given setup. Figure 6.7 and Figure 6.8 support this result. Both figures show a higher sensitivity of the measured quantities to friction parameters at higher velocities, indicating a more accurate predictor.

This situation is beneficial since velocities are typically higher in the first few actuations, so there is better friction prediction ability at the beginning of the cycle to

establish the environmental state, which can then be used to make more accurate actuations when needed toward the end of the cycle.

Considering the model sensitivity to frictional parameters as an indication of the validity of using it as a predictor, each estimator is weighted by its corresponding gradient at the actuation velocity to arrive at an optimal predictor of the form

$$\mu_s^* = \mu_{s,force} \frac{\frac{\partial F}{\partial \mu}}{\frac{\partial F}{\partial \mu} + \frac{\partial d}{\partial \mu} \frac{\Delta F}{\Delta d}} + \mu_{s,dist} \frac{\frac{\partial d}{\partial \mu} \frac{\Delta F}{\Delta d}}{\frac{\partial F}{\partial \mu} + \frac{\partial d}{\partial \mu} \frac{\Delta F}{\Delta d}} \quad (6.12)$$

The slope of the force predictor function is constant according to (6.5) at

$$\frac{dF}{d\mu} = 146.2 \quad (6.13)$$

The slope of the distance predictor function is found by

$$\begin{aligned} d &= A\mu^2 - 2A\mu_0\mu + \mu_0^2 + d_0 \\ \frac{dd}{d\mu} &= 2A(\mu - \mu_0) = 2C_2v^{k_2}(\mu - \mu_0) \end{aligned} \quad (6.14)$$

The absolute value of this slope is used to indicate sensitivity. The distance gradient is normalized to force by scaling over the model range. For an actuation velocity of 5000 mm/min, the scaling factor is found by

$$\frac{\Delta F}{\Delta d} = \frac{(309 - 283)}{(8593 - 4397)} = 0.0062 \quad (6.15)$$

The predicted values of this combined estimator at an actuation velocity of 5000 mm/min are shown with the measured values in Table 6.3.

Table 6.3 - Validation Data of Combined Friction Estimator, $v=5000$ mm/min

Condition	μ_s Measured	μ_s^* Predicted	Error
Dry	0.141	0.133	5.2%
Oily	0.135	0.131	2.9%

The prediction errors are 5.2% (case 1) and 2.9% (case 2). According to Table 6.2 at higher velocity, friction parameters are predicted by this slope-weighted method to within 10% of the actual value. This predictor can be used as both an input to the actuation velocity planning and as a tracking point for detecting changes in the system.

Discrete Adaptability and Estimation

Ideal system performance would result in absolutely quantifying part position, then imparting a single actuation to align the geometric center with the center of rotation within the prescribed tolerance. This single-push centering is not achieved in practice due to a number of possible factors:

- Departure of the empirical velocity model from the “ideal” friction model. As true friction is time- or history-dependent and highly nonlinear in the low-amplitude/low-velocity regime, the simplified model presented cannot account for all effects.
- Compliance in the mechanical system, including compliance of the part, spindle, pusher tip, linear slide, and mounting fixtures.
- Servo system compliance due to the inability of the integral gain control to act quickly enough during very short duration motion trajectories.
- Noise, quantification error, or insufficient filtering of the measurement signal.
- Other physical noise inherent from material transfer (e.g., dust, lubricant) into and out of the system during or between cycles.

Discrete Actuation Error Compensation

To compensate for these effects, a simple computational mechanism is employed in the form of a recursive offset P added to the calculated push distance. The offset function is integral in nature and has two components:

$$\begin{aligned}
 P_{k+1} &= P_k + d_{remain} + d_{stroke} \\
 P_0 &\equiv 0 \\
 d_{remain} &\equiv \text{remaining gap to be closed} \\
 d_{stroke} &\equiv \text{residual dist. error (actual - commanded)}
 \end{aligned}
 \tag{6.16}$$

The remaining gap compensation is calculated when the pusher fails to contact the part (subsequent part models differ by less than 5% of the last desired push distance). This is the difference between the known probe position at full closure and the instantaneous probe position at the end of the push stroke ($d_{probe,pt}$):

$$d_{remain} = d_{probe,pt} - d_{probe,p} \tag{6.17}$$

The stroke compensation is calculated by the difference between the commanded and actual part movement distances:

$$\begin{aligned}
 d_{stroke} &= d_{k-1} - d_{actual} \\
 d_{actual} &= \sqrt{r_{k-1}^2 + r_k^2 - 2r_{k-1}r_k \cos(\theta_k - \theta_{k-1})}
 \end{aligned}
 \tag{6.18}$$

The recursive offset is calculated for the following major events:

- A new cycle is started
- An actuation is ready to be initiated
- A significant model change has occurred (e.g., part has been moved extraneously)

The offset is added to the reference frame just prior to actuation to ensure the latest and most accurate model information is used.

Validation of Discrete Adaptability

The centering system is operated with the discrete adaptation feature disabled. As a result, the error in the initial following gap estimation as well as other unmodeled system variation is not accounted or compensated. A typical operational cycle under these open-loop conditions is shown in Figure 6.9.

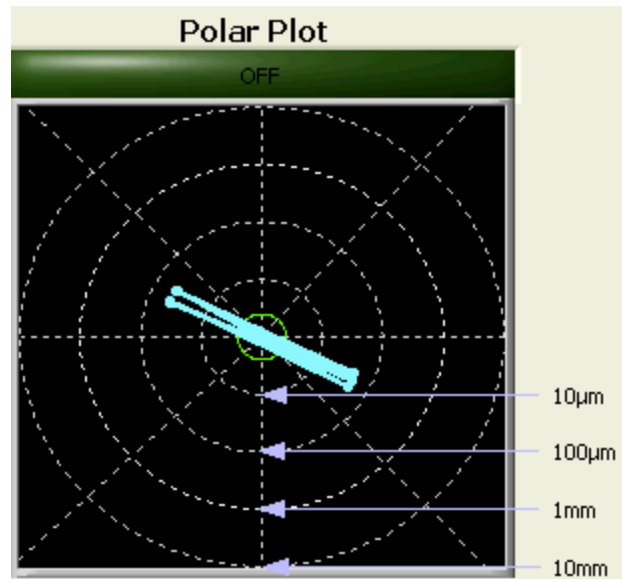


Figure 6.9 - Cycle Operation with Discrete Adaptability OFF

The cycle never converges below the tolerance and exhibits overshoot and limit cycling.

The discrete adaptation feature is then enabled and the same part run again, with a typical cycle is shown in Figure 6.10.

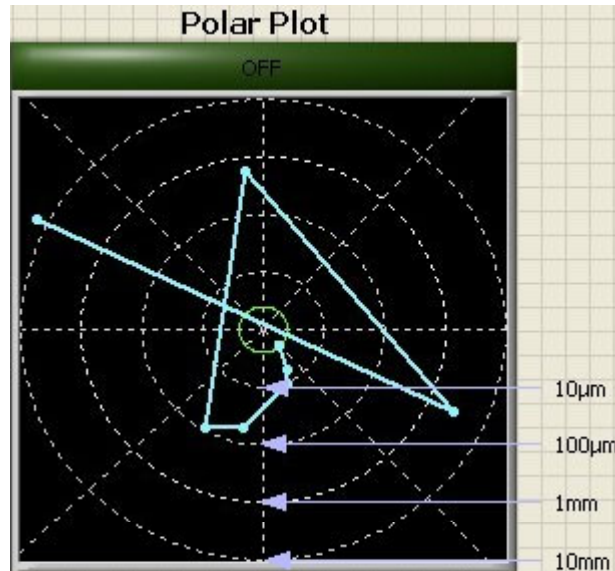


Figure 6.10 - Cycle Operation with Discrete Adaptability ON

The adaptation feature compensates for errors in the following distance with each actuation.

As an additional feature, the compensated following distance can be saved and tracked over time. The optimal estimation of this following distance can be observed through a Kalman filter estimator in the same method described in Chapter 4. Such estimation can be used to optimize the current cycle and to track significant changes over time in order to alert to system environmental changes that might warrant additional events (*e.g.*, alerting operator to clean machine surfaces or to be aware of an unexpected raw material change).

Feedforward Process Information

The centering cycle achieves part position precision relative to the center of rotation prior to processing. In addition, the centering process gathers information and can perform analyses that may be of benefit to the downstream process. Most importantly, information gained by the centering process can be used not only to protect

downstream processes from abnormal input conditions, but also to allow for downstream process improvement or optimization.

Rapid Feed Protection

The typical grinding process feed profile is shown in Figure 6.11.

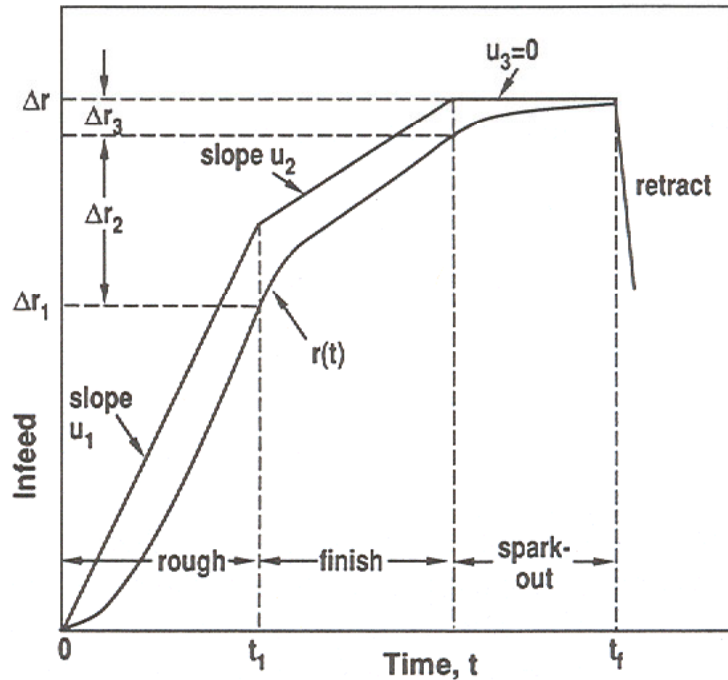


Figure 6.11 - Typical Grinding Cycle with Roughing, Finishing and Sparkout Stages [Malkin 1989]

The grinding slide is retracted at the start of the cycle to allow for part unloading and loading, jumps back into position, then moves in rapid feed to close proximity of the part, and subsequently undergoes controlled feed to remove material. The rapid feed point of changeover to controlled feed (shown at time 0 in Figure 6.11) can be triggered by power sensing (known as *gap elimination*), force sensing, or using a fixed slide position. If the slide rapid feeds into the part, it can cause damage to the grinding wheel, requiring dressing and subsequent loss of production. This can also cause damage to the

part, possibly resulting in a regenerative chatter condition and increased scrap. The fixed slide position is typically set based on allowance of

- Nominal finished part geometry
- Nominal stock removal distance
- Maximum stock removal variation (3σ or 4σ distance)
- Maximum expected out-of-roundness (3σ or 4σ distance)
- Safety gap

where σ represents the population standard deviation of the process.

These values are summed to arrive at the absolute feed changeover position. This position gives high expectation (99.865% for 3σ or 99.997% for 4σ distance) of not making contact with the part on rapid feed. However, for parts with minimal stock and out-of-roundness, such a high changeover point triggers controlled feed long before the grinding wheel contacts the part, resulting in nonproductive “air grinding” and reduced machine utilization.

The centering preprocessing cycle allows for quantification of the true maximum material condition (MMC) of the part rather than using a theoretical value based on the population distribution. This *per-piece intelligence* eliminates the guesswork and inefficiency of basing feed changeover on the worst-case population part. This true MMC can be fed forward to the subsequent machining cycle, and allow for rapid feed directly to a smaller safety gap before the known part maximum. Such information allows for reduction of controlled feed in air and improved machine utilization.

Roundness Estimation

The concept of feed-forward part information can be extended from estimation of the maximum circumscribed circle to angle-specific part roundness information. ISO standard ISO 1492-1985(E) [ISO 1985] defines four methods of centering a given profile:

- Minimum Circumscribed Circle (MCC): The MCC method describes the profile center as equivalent to the center of the smallest circle that contains the measured profile data. This method can be visualized as the smallest rigid ring that will fit over the profile, and is useful for radial external measurements.
- Maximum Inscribed Circle (MIC): The MIC method defines the center of the profile as the center of the largest circle that can be inscribed inside the profile. It can be visualized as the largest plug that will fit inside the profile, and is useful for radial internal measurements.
- Minimum Zone Circle (MZC): The MZC method minimizes the difference between two concentric circles containing the profile data. This is the preferred center measurement method according to the standard, but often requires heuristic or graphical implementation. This method has been extended analytically to the Minimal Area Difference (MAD) measurement, which minimizes the area rather than diametral differences [Le 1991].
- Least Square Center (LSC): The LSC method minimizes the sum of squares of the radial errors between fitted circle and profile data.

The result of each method is shown on a sample data set in Figure 6.12.

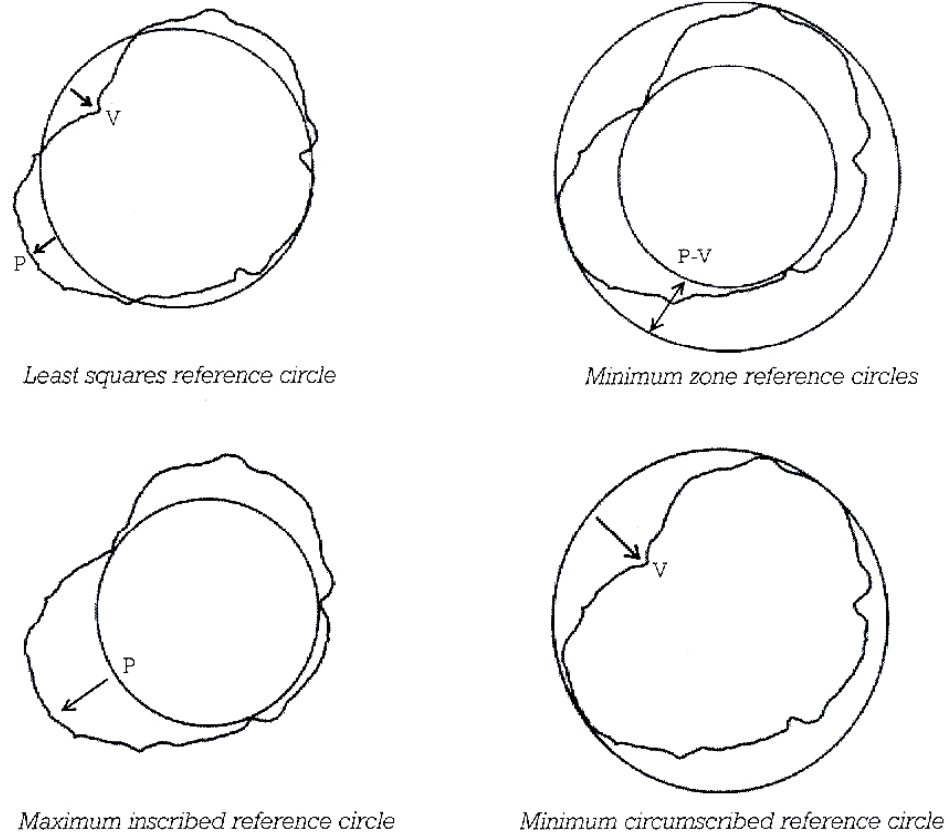


Figure 6.12 - Roundness Measurement Standards based on ISO 4291-1985(E) [Dagnall 1996]

Roundness Representation

The LSC method is considered the most precise quantification of error [Kaiser 1993]. Whether using a recursive estimation algorithm such as RLS or fitting the entire data set with the PRLS algorithm, least squares estimation will result in the most accurate representation of the part. A simplified roundness plot generated by the centering system is shown in Figure 6.13.

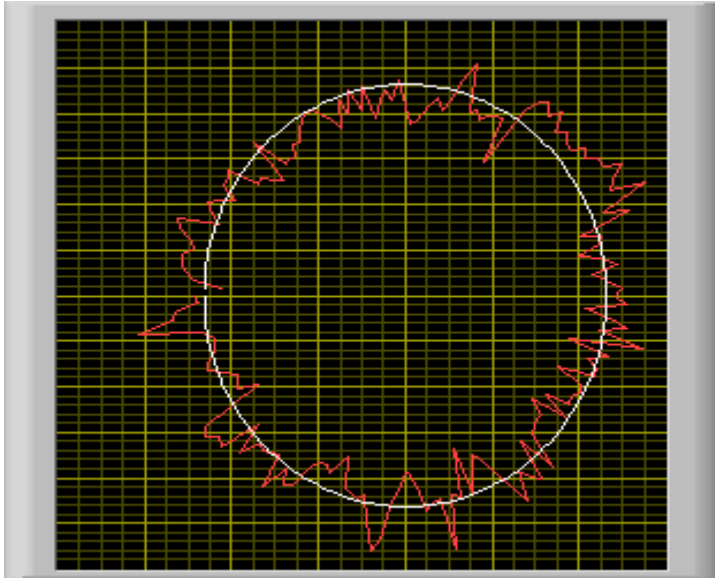


Figure 6.13 - Roundness Plot Generated by Centering System

With this more complete understanding of the part geometry, both downstream material removal and measurement cycles can benefit.

Benefits

The preprocessing system can pass information to material removal cycles such as radial roundness data as well as frequency spectra of the part geometry (see Figure 6.14).

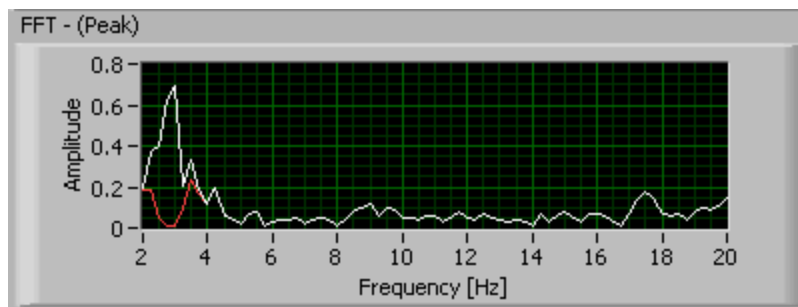


Figure 6.14 - Frequency Spectra of Part Surface

Frequency information allows the process to evaluate if it will excite any existing undulation frequencies, which may result in regenerative chatter and poor finish quality. Such information allows the material removal process to adjust its wheel and/or work rotation speed to operate off of any existing resonance frequencies.

For measurement cycles, foreknowledge of part geometry can provide path planning for approach of the measurement probe and automatic scaling to the known geometry range.

Limitations

Due to the sampling rate of the part geometry and the probe roller tip, only limited frequency information is available and some signal processing is required.

Required Geometry Signal Processing

The data are gathered using a bearing-style roller tip as shown in Figure 6.15.

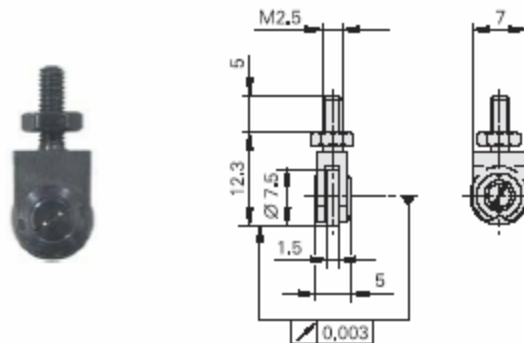


Figure 6.15 - Measuring Probe Roller Tip [Heidenhain 2005]

By design, the roller has runout of up to 3 μm that appears in the measurement data. This unwanted disturbance becomes more evident as the part becomes centered and the single undulation per revolution frequency component drops. The spindle trace

shown in Figure 6.16 of a part offset by 5 μm from center shows a distinct periodic signal at 2.8 Hz.

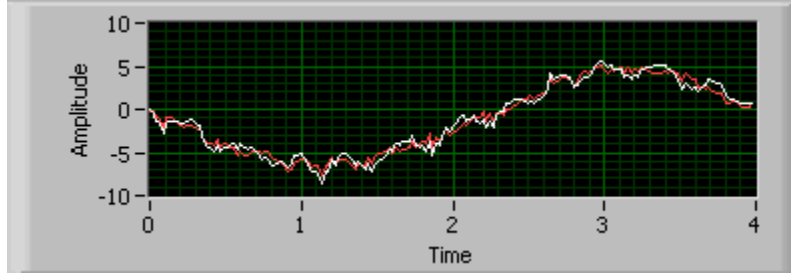


Figure 6.16 - Part Geometry at 5 μm Offset Amplitude

To more accurately represent the part geometry, this frequency component is first identified then removed. The identification is performed in the time domain with knowledge of the system geometry.

$$f_{tip} = f_{part} \cdot \frac{C_{part}}{C_{tip}}$$

$$f_{tip} \equiv \text{roller tip frequency [Hz]}$$

$$f_{part} \equiv \text{part rotational frequency [Hz]}$$

$$C_{part} \equiv \text{part circumference} = \pi d_{part} = 2\pi R$$

$$C_{tip} \equiv \text{tip circumference} = 2\pi R_{tip} \quad (6.19)$$

$$f_{tip} = f_{part} \cdot \frac{R}{R_{tip}}$$

$$f_{part} [\text{Hz}] = \frac{f_{part} [\text{rpm}]}{60} = \frac{SS}{60}$$

$$SS \equiv \text{spindle speed [rpm]}$$

$$R_{tip} = 3.75 \text{ mm}$$

$$f_{tip} = \frac{SS \cdot R}{225} \quad (6.20)$$

This identification is verified through Fast Fourier Transform (FFT) peak frequency identification.

The signal is bandstop filtered to remove the identified frequency component. The original and filtered frequency spectra are shown in Figure 6.14 and the time domain data in Figure 6.16. This filtered time signal is transformed to polar data, resulting in the roundness information available to downstream processes such as Figure 6.13.

Loss of High-Frequency Information

The roller tip itself acts as a mechanical low-pass signal filter by bridging close-proximity peaks in the part geometry. This is shown in the comparison of measurement tip size effect in Figure 6.17.

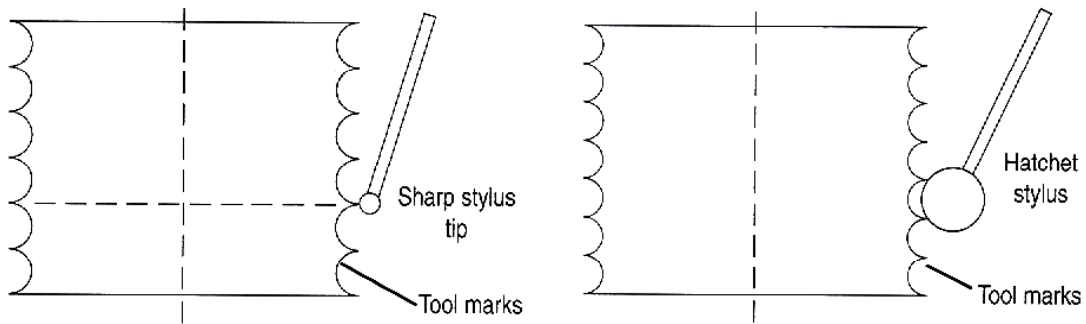


Figure 6.17 - Small vs. Large Measurement Tip, Bridging Effect [Dagnall 1996]

This bridging effect limits accurate high-frequency information. An additional loss of information comes from sampling frequency, as the system data sampling occurs at a lower rate than the typical roundness machine measurement. The centering system typically takes 1 point per degree of rotation (360 ppr), while a typical roundness machine samples at 4096 ppr. Due to the reduced sampling on a single rotation, the frequency content of the FFT is reduced accordingly. The Nyquist criterion states that

$$f_{\max} - f_{\min} \leq \frac{f_s}{2} \tag{6.21}$$

That is, the sampling frequency must be at least twice the desired resolution bandwidth to prevent unwanted aliasing of nonexistent higher-order frequencies. As an example, for a subject part rotating at 20 rpm, the bandwidth is limited to

$$\begin{aligned}
 f_{\max} - f_{\min} &\leq \frac{f_s}{2} \\
 f_{\min} &= 0 \\
 f_{\max} &= \frac{360}{2} \left[\frac{\text{points}}{\text{rev}} \right] \left[20 \frac{\text{rev}}{\text{min}} \right] \left[\frac{\text{min}}{60 \text{ s}} \right] \\
 f_{\max} &= 60 \text{ Hz}
 \end{aligned}
 \tag{6.22}$$

This is analogous to a radial frequency of 180 upr, regardless of rotational speed.

Validation

The roundness result obtained on the ring centering prototype equipment is compared with results of the same ring on an offline roundness measurement gauge. The subject part characteristics are given in Table 6.4.

Table 6.4 - Roundness Validation Part Information

Material	52100 bearing steel
Diameter [mm]	123.88
Finish type	Ground, some surface defects
Roundness deviation, peak to peak [μm]	1.3 μm T.I.R.

The part is first tested on a TSK Rondcom 30C roundness measuring machine. Sampling is 4096 points per rotation using 500 upr cutoff filter for plotting and a 60 upr cutoff filter for frequency analysis. The resulting roundness plot is given in Figure 6.18.

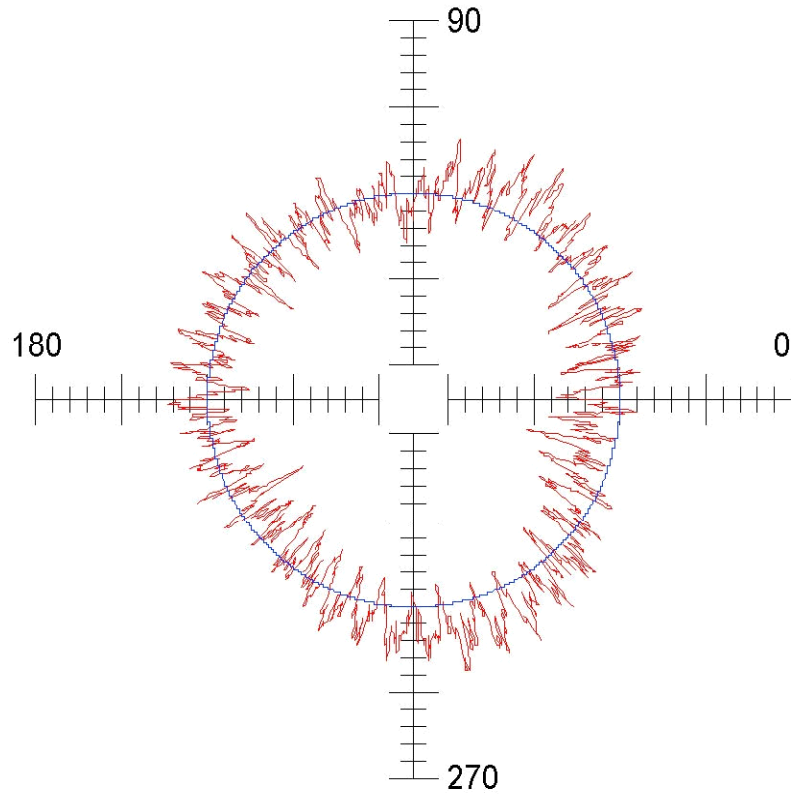


Figure 6.18 - Roundness Plot Obtained by Rondcom 30C Measuring Machine (0.2 $\mu\text{m}/\text{div}$)

The part form is analyzed in the frequency domain, with the resulting FFT magnitude plot given in Figure 6.19.

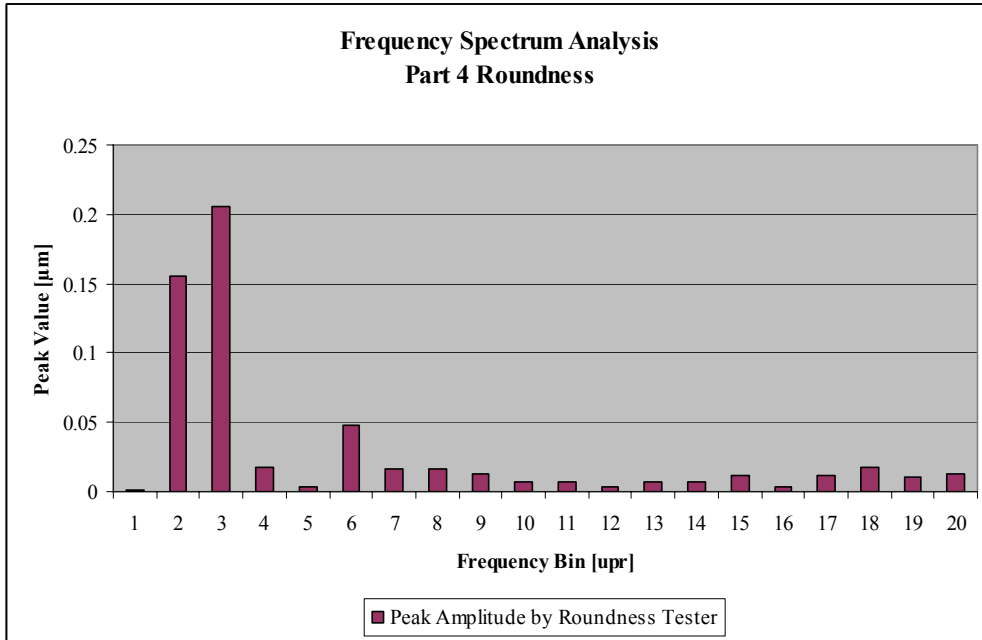


Figure 6.19 - Frequency Magnitude Plot Obtained by Rondcom 30C

The peak readings sorted by decreasing magnitude are given in Table 6.5.

Table 6.5 - Peak Magnitude Reading Obtained by Rondcom 30C

Frequency [μpr]	Magnitude [μm]
43	0.235
3	0.206
2	0.155
6	0.048
44	0.040
21	0.038
22	0.036
42	0.029
4	0.018
18	0.018

The roundness measurement is repeated using the centering prototype machine. The resulting polar plot is shown in Figure 6.20.

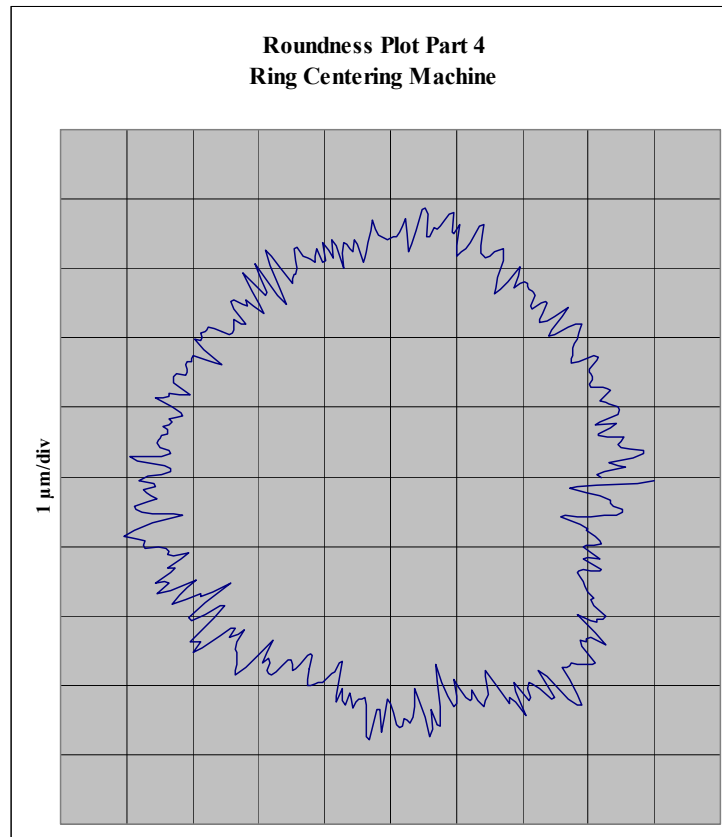


Figure 6.20 - Roundness Plot of Subject Part on Centering Machine

The total indicated runout (T.I.R.) of the profile is the measure of the peak-to-peak variation around the total data set. The T.I.R. measured on the centering prototype equipment is 3.4 μm, compared to 1.3 μm T.I.R. measured on the roundness machine.

The profile is filtered in the frequency domain to arrive at the FFT magnitude plot shown in Figure 6.21. Roundness data from the Rondcom 30C is shown on the same plot for comparison.

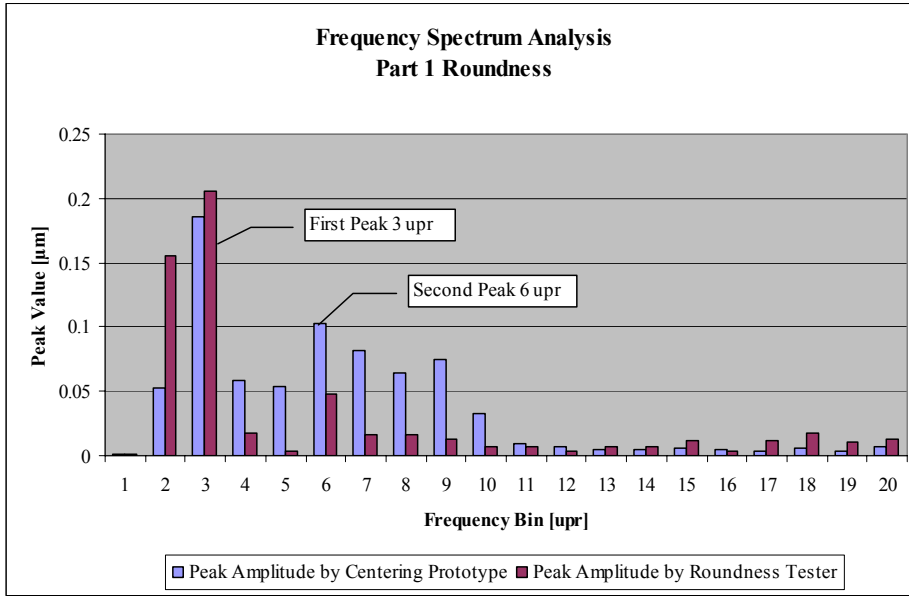


Figure 6.21 - Frequency Magnitude Plot of Subject Part on Centering Machine

The centering equipment is able to identify the modes and relative magnitudes at 3 upr and 6 upr that were identified on the roundness machine. The 43 upr peak is reduced on the centering equipment measurement due to mechanical lowpass filtering at the roller tip. The 2 upr peak is apparent, but identified at a lower magnitude than on the roundness machine, possibly due to removal of the roller tip frequency.

Validation data is taken and analyzed for 2 additional parts:

- 1) Rough turned bar stock (representing poor surface finish)
- 2) Bearing ring compressed in gross 2-point out of round (representing poor low-frequency quality)

The frequency plot for rough-turned stock is shown in Figure 6.22.

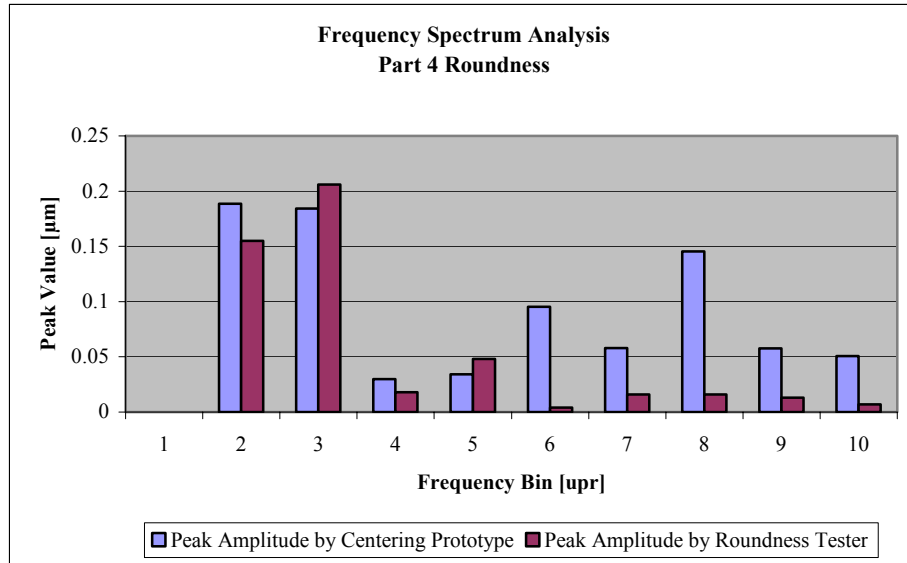


Figure 6.22 - Frequency Magnitude Chart of Rough-Turned Part

Maximum peaks as measured on the ring-centering prototype align well with peaks measured on the off-line roundness machine.

The result of the analysis carried out on the part with severe out-of-roundness is shown in Figure 6.23.

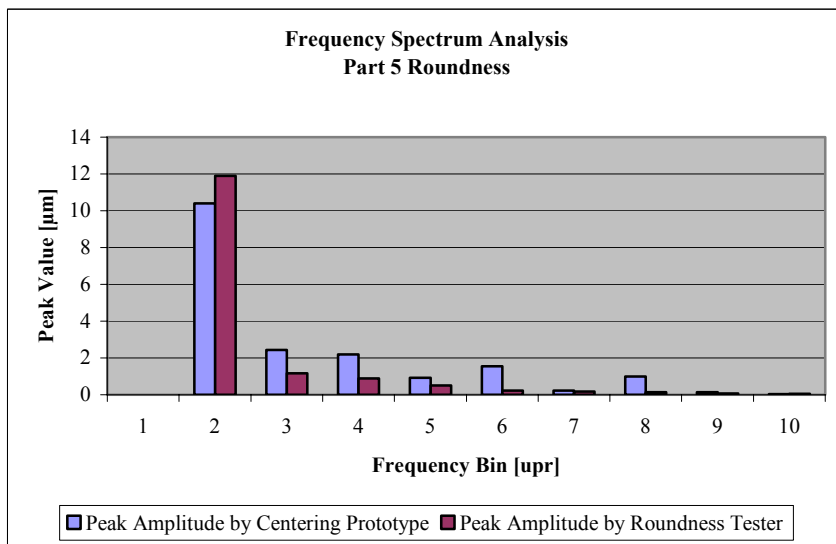


Figure 6.23 - Frequency Magnitude Chart of 2-Point Out of Round Part

For this part, the magnitudes measured on the ring centering equipment is comparable with more accurate off-line roundness measuring. Additionally, the known defect of the ring (2-point out of round) is readily identifiable.

This validation shows that the live roundness estimation performed on the centering equipment is a reasonably accurate representation of the true part condition, and can be used to pass roundness information to subsequent processes for better per-piece intelligent processing.

CHAPTER 7

CONCLUSIONS AND FUTURE WORK

Conclusions

This dissertation presents a flexible tooling system as a successful alternative to existing hard tooling or manual methods for centering rotationally symmetric workpieces in machining and metrology applications. The proposed system avoids the errors, inconsistencies, and safety concerns inherent with the manual centering process and is designed for ready integration into existing manufacturing and metrology equipment.

The system as a demonstration platform is made possible by research into related fundamental technologies, specifically:

- Optimal state identification and geometry characterization optimized for accuracy and computational effectiveness;
- Development of a multitasking distributed control architecture utilizing a real-time dedicated controller networked via TCP with a nondeterministic data processing system;
- Confidence-based data validity and application of a validity rule to motion path planning;
- Development of a motion model incorporating frictional effects, which is used to augment an energy-based path planning algorithm;

Additionally, use of the centering system as a test platform has given rise to additional research areas, most notably

- Live friction parameter prediction from a derivative-based optimal combination of estimators using measured force and free sliding distance;

- Open-loop compensation of the actuation input signal through a bandstop filtering scheme based on stiction motion frequency.

Each of the described research areas has extended possible applications not only within metrology and manufacturing processes outside of centering, but also within extended areas of product and system design.

In the following sections, the original research objectives and questions are addressed, followed by a description of specific contributions and related areas of future work.

Research Objectives

The original research objectives are addressed below:

1. *Generation of a parametric system model that accurately incorporates frictional effects and required actuation input based on part geometry and operating conditions.*

This model was generated according to (5.27), and subsequently used to drive the velocity and actuation distance determination calculations. The model was also used to develop the described initial real-time friction identification scheme. Additionally, successful trajectory planning models were developed based on part geometry and operating parameters.

2. *Development of a control algorithm, including workpiece position detection and feedback position control law. This includes an initial push with feedback and subsequent iterative actuations, as well as model refinement (adaptation) based on the system response to an input.*

This objective was met through:

- Development and tuning of the following controller
- Position detection and treatment of optimal state estimation

- Heuristic adaptation through a recursive error compensation scheme, and
 - Fundamental work in real-time friction model identification
3. *Development of an overall system architecture for characterizing an unknown workpiece and actuating it to center, including prioritization levels applied to parallel processes.*

The architecture was developed using parallel threaded processes with prioritization. The implementation was used to measure and optimally characterize a given part geometry, derive actuation parameters from this model, and use these parameters as input to a motion control scheme that actuates the part to the center of rotation. The architecture is implemented on a 2-node distributed network utilizing data transfer by TCP.

Important Research Questions

The original research questions are addressed:

1. *What is an appropriate cost function of performance for the centering problem and what is its response over ranges of design variables?*

The metric of success defined for the project is minimization of cost, achieved through minimization of cycle time. The accuracy requirement was held constant at the tolerance level of the manual process for the purposes of this work. However, the optimal estimation concepts described lend themselves toward improvement in accuracy, which leads to overall improvement in quality of processing, which ultimately reduces total cost.

2. *Can a single adaptive control algorithm be parameterized to account for a family of similar parts?*

The described control algorithm has been applied to a range of test part masses from 0.5 kg to 20 kg using the same control architecture, estimation routines and adaptation scheme. The domain of applicability is restricted to roughly circular

parts. however, this is only a rough restriction due to the effectiveness of the optimal geometry estimation routine.

3. *How robust is the system response over a variation of part and environment characteristics?*

The system response is consistent over a wide range of part masses, face finishes and diametral finishes.

4. *What is the economic viability of automated part centering as compared with the existing manual operation?*

The prototype system hardware cost is less than \$10,000 and maintenance costs are anticipated to be low (*e.g.*, no daily maintenance requirement, all electronic components are sealed). If an operator cost is assumed as \$50,000 per year and the operator spends 10% of his time at the centering process, the system should return its investment in 2 years if implemented on a single machine. This return on investment will decrease with multiple implementations. The system is a viable alternative.

5. *How can the resulting control methodology be extrapolated or enhanced to encompass different and larger part families?*

The control methodology is applicable to a wide range of parts in this application. The applicability range can be extended by changing machine component sizing (*i.e.*, a bigger hammer for bigger parts). However, more fundamentally the described state estimation routines can be adapted for different types of parts (*e.g.*, changing estimation basis functions in order to center elliptical parts). Additionally, the underlying friction model, though accurate and effective, is simple. Inclusion of more sophisticated friction modeling may help extend the range of applicability of this and similar systems. Finally, the motion control schemes used in this architecture are classical linear. Advanced and nonlinear

controller designs may lend to applicability in a wider domain. Some of these concepts are treated in the section on Future Work.

Contribution List

The following intellectual academic contributions are presented as a result of this project:

- 1) Design of an automated centering system for round artifacts that surpasses performance of manual processing and reduces overall implementation cost;
- 2) Development of a distributed multitasking control hierarchy, including prioritization and task preemption, as well as distributed real-time control system features such as intersystem data sharing using simplified Transmission Control Protocol (TCP) data structures;
- 3) Quantification and selection validation of an optimal state estimation algorithm through the criteria of accuracy, theoretical computational requirement, computation time and applicability to the part centering problem;
- 4) A method for estimating roundness and maximum part material condition during centering, to be passed to downstream metrology and material removal processes to provide per-piece intelligence of incoming part condition;
- 5) A method for validating a curve fit data model based on a confidence estimate of the standard error of the mean, normalized to a motion control parameter (off-center distance in this case) and compared to a threshold error value;
- 6) A correction function for estimation of circular part geometry using the limaçon approximation to the circle, most beneficial when a large offset of part center from rotational center exists;
- 7) Application of an energy balance and kinematic impact method for sliding distance input to centering;
- 8) A method to account for consideration of free-sliding distance in path planning through augmentation of actuation distance and restriction of

- velocity level to limit free sliding below the desired actuation distance to prevent uncontrolled target overshoot;
- 9) A method for real-time friction parameter estimation for use in actuation planning, a derivative-based optimal combination of modeled friction estimators from peak force and sliding distance;
 - 10) A frequency-filtered actuation method whereby the stick-slip friction effect is characterized by frequency and the constant-velocity signal is bandstop filtered to remove a band around this value, resulting in smoother actuation motion and better control of final actuation distance.

Contribution Details

1 Automated Centering System

An automated centering system has been described and designed for estimating a rotating part's center of geometry, then actuating the part to align this center of geometry with the center of rotation. A prototype system was built and tested to demonstrate the design effectiveness. The main design objective is minimization of overall cycle time while aligning the centers within a specified tolerance, currently 2.5 μm . Performance of the system was compared to the current method of centering, namely manual tapping by a human operator. The prototype system consistently outperforms the standard manual method.

2 Distributed Control Hierarchy

A control hierarchy has been described and implemented on a dedicated real-time processing system whereby multiple parallel task threads are carried out using a prioritization schedule. Higher priority threads have the ability to preempt and suspend lower priority activities to gain processor control and then return control when the higher priority task is complete.

Distributed processing has also been implemented in the hierarchy so that non-time-critical activities such as user input and system display are accomplished using a nondeterministic (Windows[®]-based) system, reserving deterministic system processing power for time-critical tasks such as motion control and synchronization of data collection.

Communication between the two systems was accomplished by an efficient data formatting algorithm implemented over a TCP (*i.e.*, Ethernet) protocol line. Such a distributed communication structure can be expanded to a multi-node network.

3 Optimal State Estimation Algorithm Validation

A method specific to part quantification was described as Partial Revolution Least Squares (PRLS), whereby a general least squares curve fit algorithm is applied to the entire data set at the collection of each new data point. This method is compared to the inherently recursive Kalman state estimator and Recursive Least Squares estimator using the criteria of

- Achievable accuracy in quantifying circular part geometry
- Required computation time per data step
- Applicability of the method to the centering problem, particularly convergence of the state estimation to the true part geometry

The RLS method is found to be superior in this application, as it converges the most quickly, has the smallest absolute error, and executes in less than 10 μ s per time step on the tested real-time system.

Optimal geometric state estimation in this application accounts for both measurement and process disturbances, and provides the best estimate of the measured part surface geometry. Computational efficiency is considered and benchmarked. Also considered is inclusion of a known basis function, which provides knowledge of the underlying state function and enhances algorithm convergence and estimation error.

4 Roundness Information Derivation

A method was described for providing an explicit estimation of part roundness in both time and frequency domains, and for providing a peak expected offset. As the measuring tip disturbance signal is deterministic and known, this method incorporates complete removal of that signal from the part geometry estimate.

The information gained from this process is available to upstream processes as a form of control chart feedback, and to downstream processes for cycle optimization and jump-in damage protection through more specific advanced part geometry knowledge.

5 Confidence-Based Data Modeling

A method was described whereby data collected from a circular part is analyzed for validity to allow modeling using the data. The validity criterion is based on a user-specified confidence level and accuracy requirement. This uncertainty-based data validity criterion prevents modeling and subsequent decision processes from a data set without enough information to be accurate. The method also allows a model to be generated at the first point where accuracy requirements are met so actuation is initiated as soon as possible using a valid model. This method is successfully implemented in the centering system in such a way that actuation is only allowed when data accuracy is

considered valid, preventing errant actuation and longer cycle times arising from inaccurate modeling of part geometry.

6 Correction Function for Geometry Estimation

As the center of geometry departs from the center of rotation, use of the limaçon approximation to the circular fit results in greater error in the estimation of part diameter.

A function determining the size correction factor was developed, giving an expression for

$\frac{\text{actual size}}{\text{limaçon estimated size}}$ as a function of $\frac{\text{offset distance}}{\text{limaçon estimated size}}$. The correction reduces

the maximum ideal error in size estimation at maximum offset from 34.5% to 0.2%.

7 Energy Balance Method for Free-Sliding Control

A method was presented for determination of the required constant-velocity striker speed to impart a desired sliding distance of the actuated part. This method is based upon the kinetic friction coefficient and coefficient of restitution of the impulsive actuation. The method is directly applied to the ring centering problem.

8 Free-Sliding Distance Augmentation to Impulsive Actuation

A model was described to predict free sliding distance resulting from constant-velocity impulsive actuation. The model was implemented in a motion control planning algorithm to accomplish two goals:

- Improve actuation distance planning. The impulsive actuation distance is reduced by the modeled free sliding distance in order to reduce overshoot in positioning. This accounts for additional free sliding at the end of the actuation stroke.
- Improve actuation velocity planning. The prescribed constant actuation velocity is checked against the modeled free-sliding distance at that

velocity. If the free sliding distance is larger than the desired actuation distance, the actuation velocity is reduced. This prevents actuation at a velocity that would result in positional overshoot by free sliding.

Both the model of free-sliding distance and use of the model to augment constant-velocity actuation planning have been validated in experiment.

9 Real-Time Iterative Friction Model Parameter Estimation

The previously-described free-sliding distance model and velocity planning method are based on a time- and environment-invariant friction model with fixed model parameters taken from experimental testing.

A new method was described to estimate in real-time the underlying friction model parameters from two input sources:

- Force-based friction modeling. The measured force during actuation was compared to a part-specific force model to determine the closest approximation to the underlying friction model parameters.
- Distance-based friction modeling. The free sliding distance model was compared with the actuated part sliding distance to determine an approximation to the underlying friction model parameters.

These methods have been optimally combined through a weighting scheme where weights are proportional to the model surface derivative with respect to friction coefficient. The underlying assumption in this weighting is that a higher slope is equivalent to greater sensitivity to the friction parameter at the given conditions, and is therefore a more accurate estimator than a similar function with lower sensitivity.

The described estimation scheme is applicable to higher mass parts (>15 kg in the prototype application), and was validated with less than 10% error on the prototype machine.

10 Frequency-Based Anti-Resonance Actuation

A study was made of stick-slip friction in constant-velocity sliding actuation from the standpoint of dominant frequency component. *Stiction resonance* has been defined as the dominant frequency component in the velocity of a part actuated at constant actuator velocity.

The stiction resonance frequency was used to design a frequency domain bandstop filter for the input signal for actuation. The constant velocity signal is thereby transformed to a *bandlimited velocity* signal for actuating the subject part. This augmented input reduces the stiction effect and eliminates free sliding in impulsive actuation.

This method has been validated as reducing fluctuation in force through experiments on a nonrotating part of 18.9 kg across a wide range on nominal actuation velocities.

Recommendations for Future Work

The presented research and contributions lead to a number of areas that warrant further study.

Trajectory Planning

The residual angular error of the actuation is positively correlated to the off-center distance (see Figure 5.4). Presently, trajectory planning is undertaken to provide *initial* contact along the desired line of action. Future work should include modification of trajectory planning to relate average part actuation direction to desired direction to eliminate dependence of the angular error on actuation distance. Additional research can be undertaken to reduce the variation in observed angular error.

Controller Design

The controller in the described application is a PID controller with gain scheduling depending on part type. The controller performs well in the application, however there is some undesirable oscillatory behavior in the system during actuation (see Figure 3.12). Future research in this area will be directed to advanced controller designs readily adaptable to varying part and environmental conditions. As the system is applied to heavier parts, system compliance is expected to be appreciable and to reduce the effectiveness of a linear controller. Schemes such as sliding mode control and nonlinear controllers better able to react to high force gradients and more readily adaptable to changing environmental conditions should be investigated in the actuation application.

Multivariable Control

The described application uses the maximum likelihood estimator (MLE) of a single position input. Force input is used to validate models and to estimate friction model parameters, but is excluded from the controller scheme. Another area of research is inclusion of force feedback to the centering actuation problem as an additional input variable.

Environment Estimation Tracking

Force used in estimation of friction parameters can also be researched as a time-domain or part-domain process. The forces encountered in actuation can be observed over time and across part families to detect changes in either part or machine state. Optimal estimation routines described and used in this work such as Kalman filtering can be applied to this running environmental state estimation. The same state estimation can be applied to the friction predictor directly, through force prediction, sliding distance prediction, and the described optimal combination of these estimation methods.

This tracking of changes can also be extended to tracking of the running offset by the adaptive compensation scheme described in Chapter 6. Optimal estimation of the state of the system over time using this variable can also lead to tracking of systemic changes in the face of process noise. The running offset obtained by the compensation mechanism can be optimally estimated via a Kalman filtering scheme.

The optimal estimation of each of these parameters can be tracked in both part flow and time domains to detect significant systemic changes either in environment (*e.g.*, machine condition) or incoming material condition. Results from this analysis can be used to alert operators to potentially abnormal conditions, or to automatically adjust the downstream process for optimal operation.

Distributed Network Information Sharing

The described system demonstrates a data system structure for passing information efficiently and bidirectionally via Transmission Control Protocol from a user PC to a dedicated deterministic operating system. This data distribution architecture can be expanded to include multiple nodes and layers, as well as a management system for directing and handling information. Such a system would need to include measures for each node or process of:

- Information that can be generated by the process,
- Information required by the process,
- Information that can improve the process, either through reduction of process time, improvement in accuracy, improvement in subsequent information generated by the process in quality or quantity,
- A metric of usefulness of information available to each process

This research in distributed information sharing and process augmentation is applicable in a variety of domains, most obviously manufacturing systems, but also to service, product and design systems.

Final Comments

The work culminating in this dissertation has produced a prototype ring centering system used as a demonstration platform for a number of fundamental research areas, encompassing optimal state estimation, distributed communication and control, friction modeling, friction estimation, and alternative motion path planning.

A vision is also created for future work not only in the described areas, but also in the areas of advanced controller design incorporating multiple variables, derived machine diagnostic information, and application of the distributed communication architecture to information flow throughout the manufacturing organization. These research lines are important not only to reduce manufacturing costs in the face of global competition, but also to continue improving the national technical base in manufacturing understanding, development and optimization.

APPENDIX A

HOST CODE AND DESCRIPTION

Front Panel

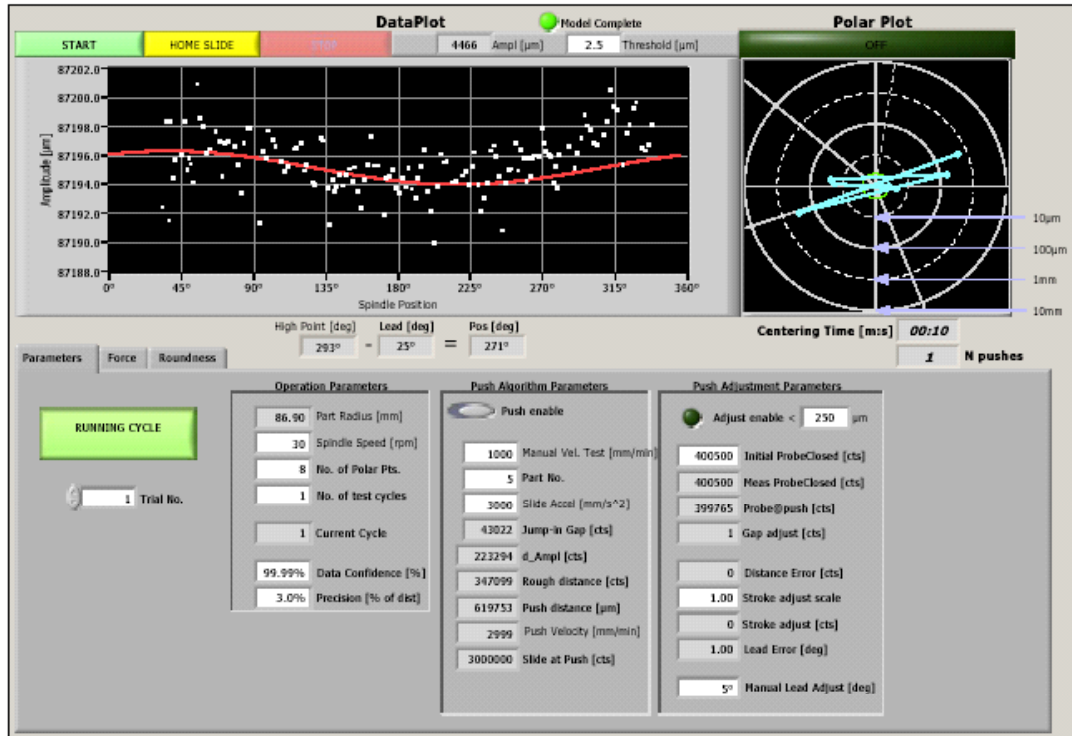


Figure A-1 - User Interface Front Panel

Controls and Indicators

Push enable	Data Confidence [%]	Part Radius [mm]	
stop	Precision [% of dist]	Gap adjust [cts]	
Threshold [μm]	vel,dt,F	Stroke adjust [cts]	
No. of Polar Pts.	Point	Probe@push [cts]	y
Spindle Speed [rpm]	Log Force?	Adjust enable <	ModelPlot
Manual Vel. Test [mm/min]	Log Roundness Data?	Spind@push	Test Model SubVI
Part No.	Tab Control	Model Complete	y
Initial ProbeClosed [cts]	DataPlot	Rough distance [cts]	Debug Registers
No. of test cycles	High Point [deg]	Slide at Push [cts]	y
Home	Ampl [μm]	Lead Error [deg]	ForceChart
Start	Push distance [μm]	Distance Error [cts]	countdown
Slide Accel [mm/s ²]	Push Velocity [mm/min]	Current Cycle	MaxForce
Stroke adjust scale	Lead [deg]	Jump-in Gap [cts]	Y out
AdjLimUp	Pos [deg]	Results	Point
Manual Lead Adjust [deg]	CentOK	Meas ProbeClosed [cts]	Waveform Graph
Trial No.	Polar Plot	d_Ampl [cts]	Roller tip freq [Hz]
Pause	Centering Time [m:s]	Polar Plot_X	FFT - (Peak)
	N pushes	y	Roundness Plot
	Force dt [μs]	Polar Plot_Y	Max Deviation [μm]

Figure A-2 - Host Program Controls and Indicators

List of SubVIs and Express VIs with Configuration Information











	Simple Error Handler.vi D:\Program Files\National Instruments\LabVIEW 7.1\vi.lib\Utility\error.lib\Simple Error Handler.vi
	Boolean Crossing PtByPt.vi D:\Program Files\National Instruments\LabVIEW 7.1\vi.lib\ptbypt\Other Functions.lib\Boolean Crossing PtByPt.vi
	Find Home.vi F:\SKOO\!PHD\!Project\MotionControl\Find Home.vi
	TCP Msg Write.vi F:\SKOO\!PHD\!Project\MotionControl\TCPMsgProtocol2.lib\TCP Msg Write.vi
	Meta Element.ctl F:\SKOO\!PHD\!Project\MotionControl\TCPMsgProtocol2.lib\Meta Element.ctl
	MM2CTS.vi F:\SKOO\!PHD\!Project\MotionControl\MM2CTS.vi
	TCP Msg Read.vi F:\SKOO\!PHD\!Project\MotionControl\TCPMsgProtocol2.lib\TCP Msg Read.vi
	Start Spindle.vi F:\SKOO\!PHD\!Project\MotionControl\Start Spindle.vi
	Tick Count Tick Count Returns the value of the free running counter in the units specified. The output and internal counter are both of the configured width.
	Reset Position.flx D:\Program Files\National Instruments\LabVIEW 7.1\vi.lib\Motion\FlexMotion\FunctionsVIs\Trajectory\Trajectory.lib\Reset Position.flx
	Axis To Control.flx D:\Program Files\National Instruments\LabVIEW 7.1\vi.lib\Motion\FlexMotion\CustomControls\FlexCtls.lib\Axis To Control.flx
	Board Id D:\Program Files\National Instruments\LabVIEW 7.1\vi.lib\Motion\FlexMotion\CustomControls\FlexCtls.lib\Board Id
	Load Constant to Variable.flx D:\Program Files\National Instruments\LabVIEW 7.1\vi.lib\Motion\FlexMotion\FunctionsVIs\On-board Programming\Data Operations.lib\Load Constant to Variable.flx
	Var D:\Program Files\National Instruments\LabVIEW 7.1\vi.lib\Motion\FlexMotion\CustomControls\FlexCtls.lib\Var
	Set Operation Mode.flx D:\Program Files\National Instruments\LabVIEW 7.1\vi.lib\Motion\FlexMotion\FunctionsVIs\Trajectory\Trajectory.lib\Set Operation Mode.flx
	AxisOrVectorSpace To Control.flx D:\Program Files\National Instruments\LabVIEW 7.1\vi.lib\Motion\FlexMotion\CustomControls\FlexCtls.lib\AxisOrVectorSpace To Control.flx
	Load Accel/Decel in RPS/sec.flx D:\Program Files\National Instruments\LabVIEW 7.1\vi.lib\Motion\FlexMotion\FunctionsVIs\Trajectory\Trajectory.lib\Load Accel/Decel in RPS/sec.flx
	Tick Count2 Tick Count Returns the value of the free running counter in the units specified. The output and internal counter are both of the configured width.



Figure A-3 - Host Subprogram Listing

-  **Open/Create/Replace File.vi**
D:\Program Files\National Instruments\LabVIEW 7.1\vi.lib\Utility\file.llb\Open/Create/Replace File.vi
-  **Mean.vi**
D:\Program Files\National Instruments\LabVIEW 7.1\vi.lib\analysis\baseanly.llb\Mean.vi
-  **Polar Plot 3_log.vi**
F:\SKOO\!PhD\!Project\MotionControl\Polar Plot 3_log.vi
-  **Tick Count3**
Tick Count
Returns the value of the free running counter in the units specified. The output and internal counter are both of the configured width.
-  **Tick Count4**
Tick Count
Returns the value of the free running counter in the units specified. The output and internal counter are both of the configured width.
-  **Data Queue PtByPt.vi**
D:\Program Files\National Instruments\LabVIEW 7.1\vi.lib\ptbypt\Other Functions.llb\Data Queue PtByPt.vi
-  **RAD2DEG.vi**
F:\SKOO\!PhD\!Project\MotionControl\RAD2DEG.vi
-  **Convert to Dynamic Data3**
Convert to Dynamic Data
Converts numeric, Boolean, waveform and array data types to the dynamic data type for use with Express VIs.
-  **Convert to Dynamic Data4**
Convert to Dynamic Data
Converts numeric, Boolean, waveform and array data types to the dynamic data type for use with Express VIs.
-  **Build XY Graph2**
Build XY Graph
formats the data displayed on an X-Y Graph.
-  **Array subset single rotation2.vi**
F:\SKOO\!PhD\!Project\MotionControl\Array subset single rotation2.vi
-  **Value Has Changed PtByPt.vi**
D:\Program Files\National Instruments\LabVIEW 7.1\vi.lib\ptbypt\Other Functions.llb\Value Has Changed PtByPt.vi
-  **CreateModel.vi**
F:\SKOO\!PhD\!Project\MotionControl\CreateModel.vi
-  **Write To Spreadsheet File.vi**
D:\Program Files\National Instruments\LabVIEW 7.1\vi.lib\Utility\file.llb\Write To Spreadsheet File.vi
-  **Convert to Dynamic Data**
Convert to Dynamic Data
Converts numeric, Boolean, waveform and array data types to the dynamic data type for use with Express VIs.
-  **Spectral Measurements**
Spectral Measurements
Performs spectral measurements, such as peak spectrum and auto-power spectrum, on a signal.

This Express VI is configured as follows:

Selected Measurements: Magnitude (RMS)
View Phase: Wrapped and in Radians
Windowing: Hanning
Averaging: None

Figure A-3 continued

-  **Convert to Dynamic Data5**
 Convert to Dynamic Data
 Converts numeric, Boolean, waveform and array data types to the dynamic data type for use with Express VIs.
-  **Spectral Measurements2**
 Spectral Measurements
 Performs spectral measurements, such as peak spectrum and auto-power spectrum, on a signal.

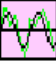




- This Express VI is configured as follows:
- Selected Measurements: Magnitude (RMS)
 View Phase: Wrapped and in Radians
 Windowing: Hanning
 Averaging: None
-  **Acausal Filter2_notch.vi**
 F:\SKOO\!PhD\!Project\MotionControl\Acausal Filter2_notch.vi
-  **Convert to Dynamic Data2**
 Convert to Dynamic Data
 Converts numeric, Boolean, waveform and array data types to the dynamic data type for use with Express VIs.
-  **Convert to Dynamic Data8**
 Convert to Dynamic Data
 Converts numeric, Boolean, waveform and array data types to the dynamic data type for use with Express VIs.
-  **Roundness Plot.vi**
 F:\SKOO\!PhD\!Project\MotionControl\Roundness Plot.vi
-  **Part Lookup.vi**
 F:\SKOO\!PhD\!Project\MotionControl\Part Lookup.vi

Figure A-3 continued

APPENDIX B

REAL-TIME CODE AND DESCRIPTION

Controls and Indicators

 **stop**



warning out

The `error out` cluster passes error or warning information out of a VI to be used by other VIs.

The pop-up option `Explain Error` (or Explain Warning) gives more information about the error displayed.



status

The `status` boolean is either TRUE (X) for an error, or FALSE (checkmark) for no error or a warning.

The pop-up option `Explain Error` (or Explain Warning) gives more information about the error



code

The `code` input identifies the error or warning.

The pop-up option `Explain Error` (or Explain Warning) gives more information about the error



source

The `source` string describes the origin of the error or warning.

The pop-up option `Explain Error` (or Explain Warning) gives more information about the error

Figure B-1 - Real-Time Program Controls and Indicators

List of SubVIs and Express VIs with Configuration Information




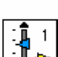









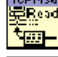


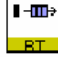



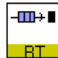
	Stop Timed Loop.vi D:\Program Files\National Instruments\LabVIEW 7.1\vi.lib\Platform\TimedLoop\scheduler\LVUserAPI\Stop Timed
	RTFIFOCreate.vi D:\Program Files\National Instruments\LabVIEW 7.1\vi.lib\addons\rt\RTFIFO.lib\RTFIFOCreate.vi
	AlarmRef__NATIONAL_INSTRUMENTS_lvalarm.cti D:\Program Files\National Instruments\LabVIEW 7.1\vi.lib\Platform\TimedLoop\utilities.lib\AlarmRef__NATIONAL_INSTRUMENTS_lvalarm.cti
	timing.cti D:\Program Files\National Instruments\LabVIEW 7.1\vi.lib\Platform\TimedLoop\utilities.lib\timing.cti
	loadIvalarms.vi D:\Program Files\National Instruments\LabVIEW 7.1\vi.lib\Platform\TimedLoop\ConfigExtNode.lib\loadIvalarms.vi
	RTFIFOCreate DBLA.vi D:\Program Files\National Instruments\LabVIEW 7.1\vi.lib\addons\rt\RTFIFO.lib\RTFIFOCreate DBLA.vi
	Time to Push_RT.vi F:\SKOO\!PhD\!Project\MotionControl\Time to Push_RT.vi
	Follow MT2581.vi F:\SKOO\!PhD\!Project\MotionControl\Follow MT2581.vi
	Model Main 9_SEM.vi F:\SKOO\!PhD\!Project\MotionControl\Model Main 9_SEM.vi
	RTFIFORead.vi D:\Program Files\National Instruments\LabVIEW 7.1\vi.lib\addons\rt\RTFIFO.lib\RTFIFORead.vi
	TCP Listen.vi D:\Program Files\National Instruments\LabVIEW 7.1\vi.lib\Utility\tcp.lib\TCP Listen.vi
	Error to Warning.vi F:\SKOO\!PhD\!Project\MotionControl\TCPMsgProtocol2.lib>Error to Warning.vi
	TCP Msg Read.vi F:\SKOO\!PhD\!Project\MotionControl\TCPMsgProtocol2.lib\TCP Msg Read.vi
	TCP Msg Write.vi F:\SKOO\!PhD\!Project\MotionControl\TCPMsgProtocol2.lib\TCP Msg Write.vi
	InitFIFOs_RT.vi F:\SKOO\!PhD\!Project\MotionControl\InitFIFOs_RT.vi
	RTFIFOWrite.vi D:\Program Files\National Instruments\LabVIEW 7.1\vi.lib\addons\rt\RTFIFO.lib\RTFIFOWrite.vi
	RTFIFOWrite DBL.vi D:\Program Files\National Instruments\LabVIEW 7.1\vi.lib\addons\rt\RTFIFO.lib\RTFIFOWrite DBL.vi
	RTFIFOWrite I32.vi D:\Program Files\National Instruments\LabVIEW 7.1\vi.lib\addons\rt\RTFIFO.lib\RTFIFOWrite I32.vi
	RTFIFOWrite BOOL.vi D:\Program Files\National Instruments\LabVIEW 7.1\vi.lib\addons\rt\RTFIFO.lib\RTFIFOWrite BOOL.vi
	RTFIFORead DBL.vi D:\Program Files\National Instruments\LabVIEW 7.1\vi.lib\addons\rt\RTFIFO.lib\RTFIFORead DBL.vi
	RTFIFORead BOOL.vi D:\Program Files\National Instruments\LabVIEW 7.1\vi.lib\addons\rt\RTFIFO.lib\RTFIFORead BOOL.vi

Figure B-2 - Real-Time Subprogram Listing


















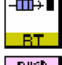
	RTFIFO Write DBLA.vi D:\Program Files\National Instruments\LabVIEW 7.1\vi.lib\addons\rt\RTFIFO.lib\RTFIFO Write DBLA.vi
	Meta Element.cti F:\SKOO\!PhD\!Project\MotionControl\TCPMsgProtocol2.lib\Meta Element.cti
	Read Data Point 4_test.vi F:\SKOO\!PhD\!Project\MotionControl\Read Data Point 4_test.vi
	Calculate Lag Angle 7_RT.vi F:\SKOO\!PhD\!Project\MotionControl\Calculate Lag Angle 7_RT.vi
	Multiple of.vi F:\SKOO\!PhD\!Project\MotionControl\Multiple of.vi
	Push Algorithm9_RT.vi F:\SKOO\!PhD\!Project\MotionControl\Push Algorithm9_RT.vi
	Update Var Stream_Model.vi F:\SKOO\!PhD\!Project\MotionControl\Update Var Stream_Model.vi
	Update Var Stream_Data.vi F:\SKOO\!PhD\!Project\MotionControl\Update Var Stream_Data.vi
	Wait Until Next Multiple Wait Until Next Multiple Waits until the value of the timer becomes a multiple of Count. Use this function to synchronize activities. You can call this function in a loop to control the loop execution rate.
	Back off slide absolute.vi F:\SKOO\!PhD\!Project\MotionControl\Back off slide absolute.vi
	Stop Spindle.vi F:\SKOO\!PhD\!Project\MotionControl\Stop Spindle.vi
	Board Id D:\Program Files\National Instruments\LabVIEW 7.1\vi.lib\Motion\FlexMotion\CustomControls\FlexCtrls.lib\Board Id
	ADC.flx D:\Program Files\National Instruments\LabVIEW 7.1\vi.lib\Motion\FlexMotion\CustomControls\FlexCtrls.lib\ADC.flx
	Read ADC.vi D:\Program Files\National Instruments\LabVIEW 7.1\vi.lib\Motion\FlexMotion\FunctionsVIs\Analog & Digital IO\Analog & Digital IO.lib\Read ADC.vi
	RTFIFO Read DBLA.vi D:\Program Files\National Instruments\LabVIEW 7.1\vi.lib\addons\rt\RTFIFO.lib\RTFIFO Read DBLA.vi
	RTFIFO Read I32.vi D:\Program Files\National Instruments\LabVIEW 7.1\vi.lib\addons\rt\RTFIFO.lib\RTFIFO Read I32.vi
	Update Var Stream_Push.vi F:\SKOO\!PhD\!Project\MotionControl\Update Var Stream_Push.vi
	Tick Count Tick Count Returns the value of the free running counter in the units specified. The output and internal counter are both of the configured width.

Figure B-2 continued

APPENDIX C

POSITION SIMULATION RESULTS

The position model and experimentally observed results for additional velocity cases of a 18.9 kg part are presented in Figure C-1 through Figure C-12.

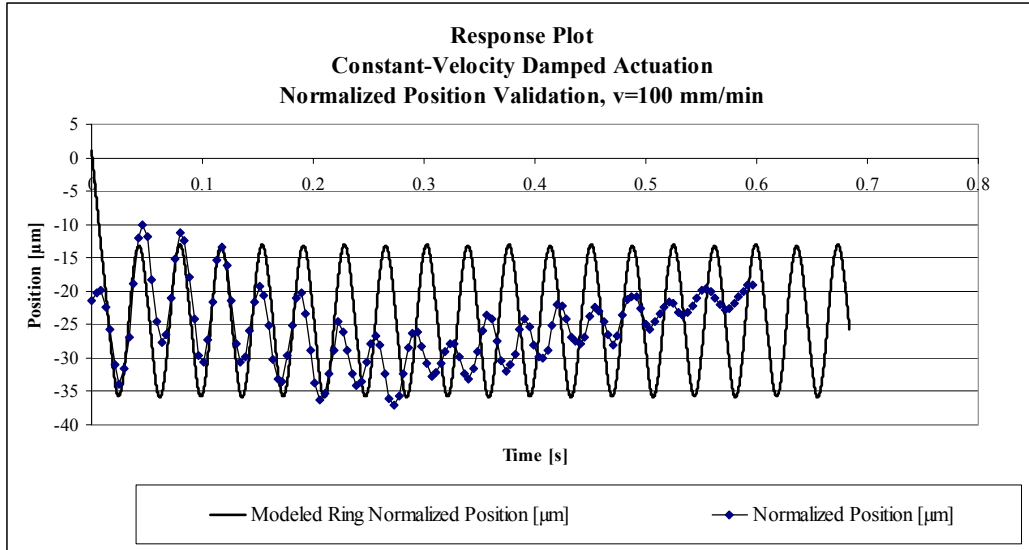


Figure C-1 - Normalized Position Response Plots with Model Values (v=100 mm/min)

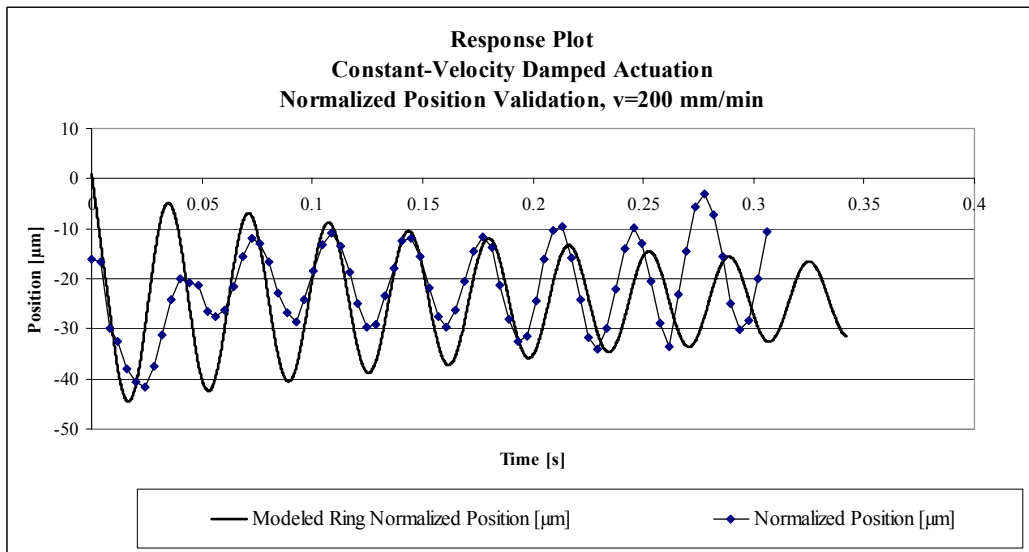


Figure C-2 - Normalized Position Response Plots with Model Values (v=200 mm/min)

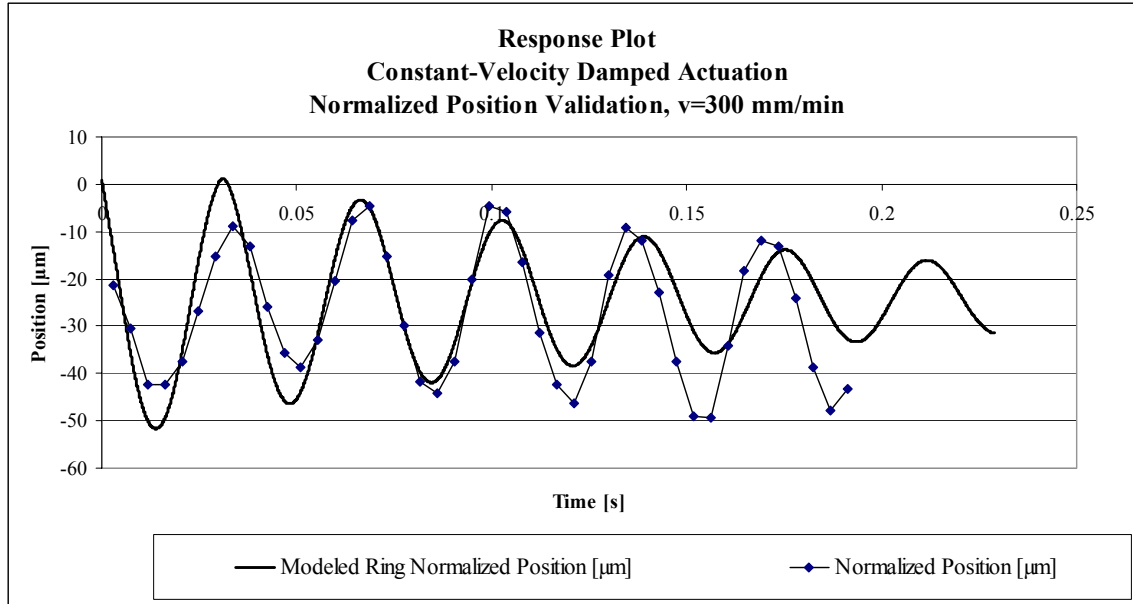


Figure C-3 - Normalized Position Response Plots with Model Values (v=300 mm/min)

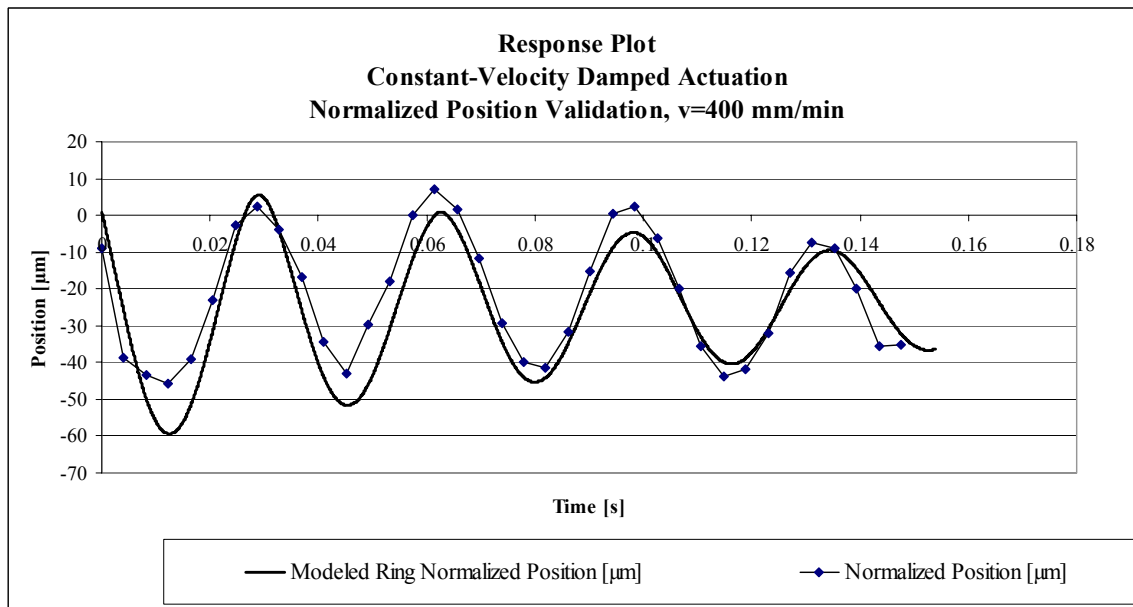


Figure C-4 - Normalized Position Response Plots with Model Values (v=400 mm/min)

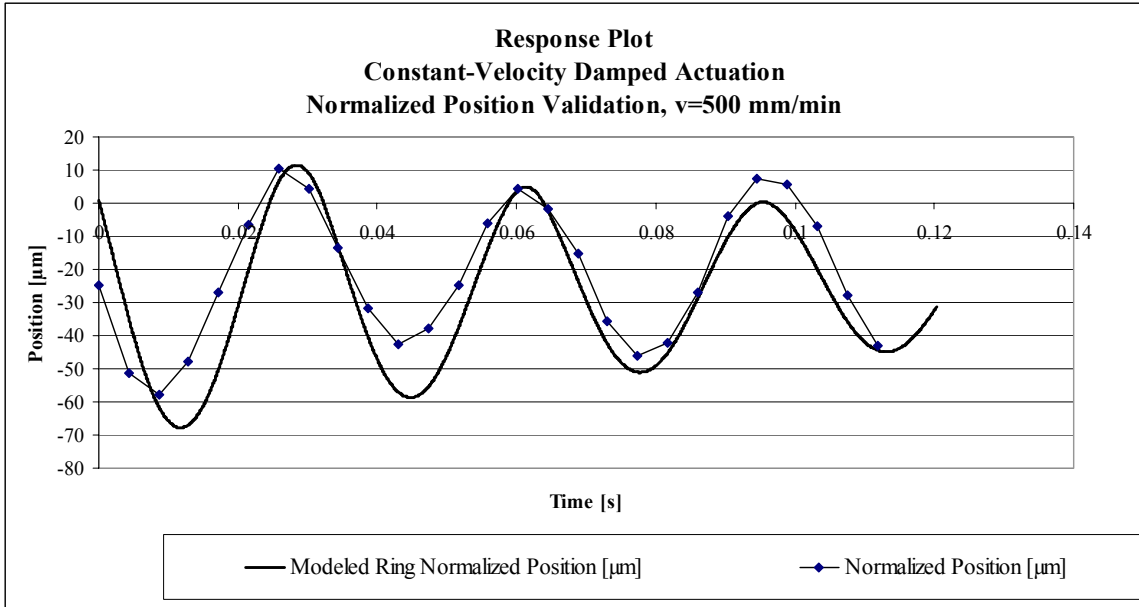


Figure C-5 - Normalized Position Response Plots with Model Values (v=500 mm/min)

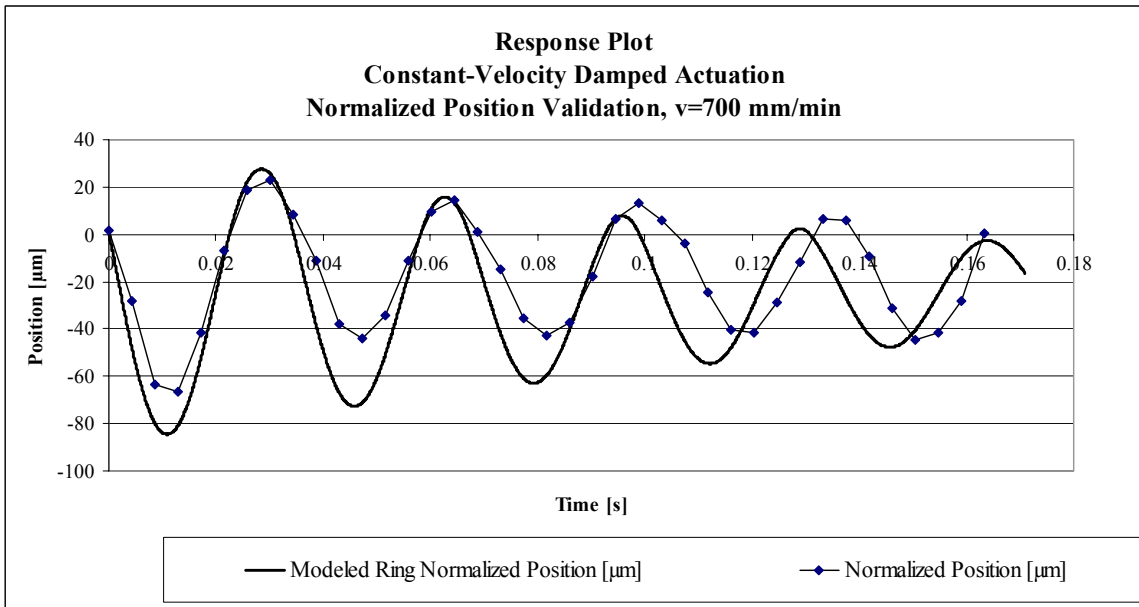


Figure C-6 - Normalized Position Response Plots with Model Values (v=700 mm/min)

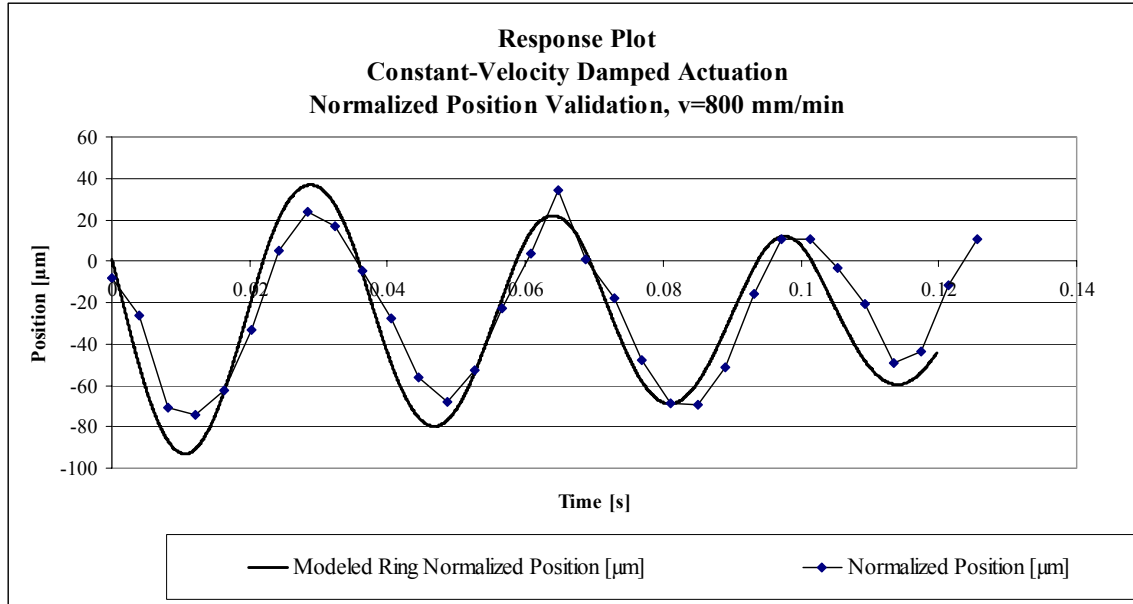


Figure C-7 - Normalized Position Response Plots with Model Values (v=800 mm/min)

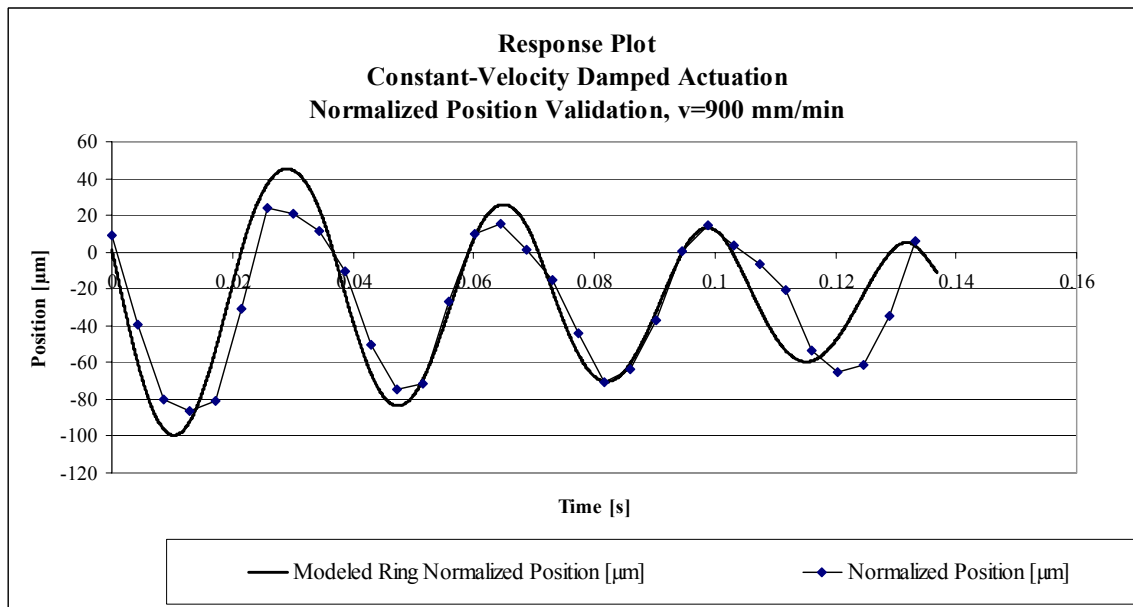


Figure C-8 - Normalized Position Response Plots with Model Values (v=900 mm/min)

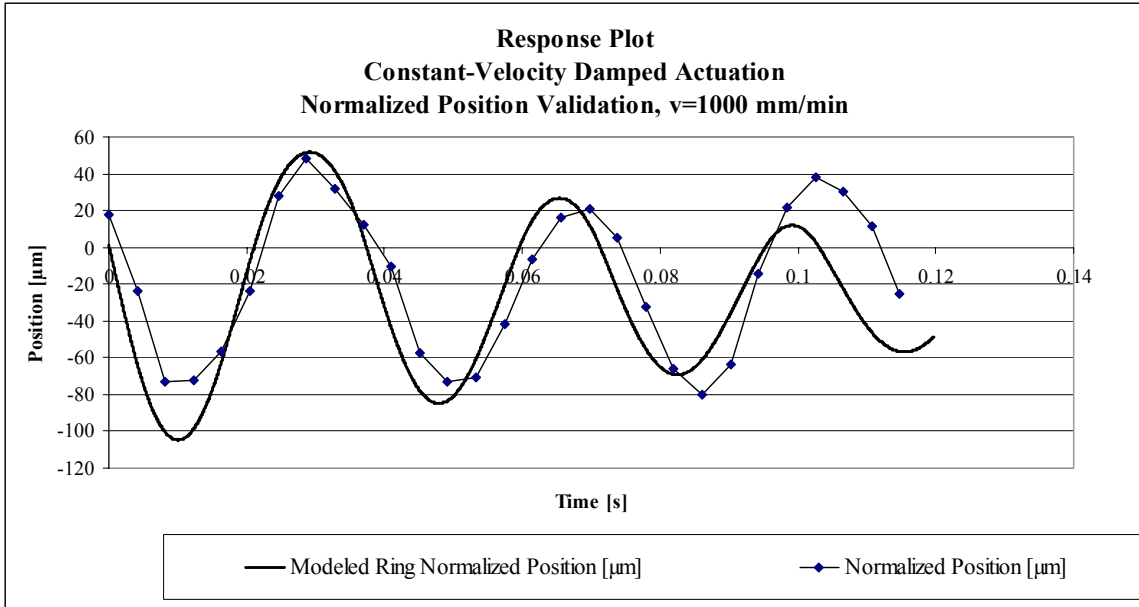


Figure C-9 - Normalized Position Response Plots with Model Values (v=1000 mm/min)

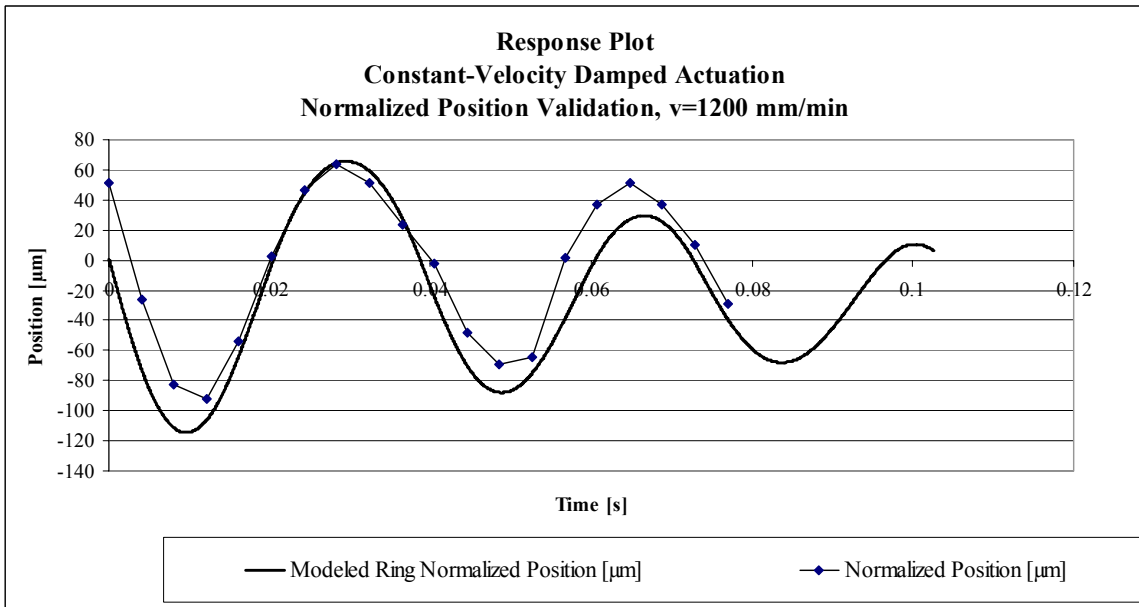


Figure C-10 - Normalized Position Response Plots with Model Values (v=1200 mm/min)

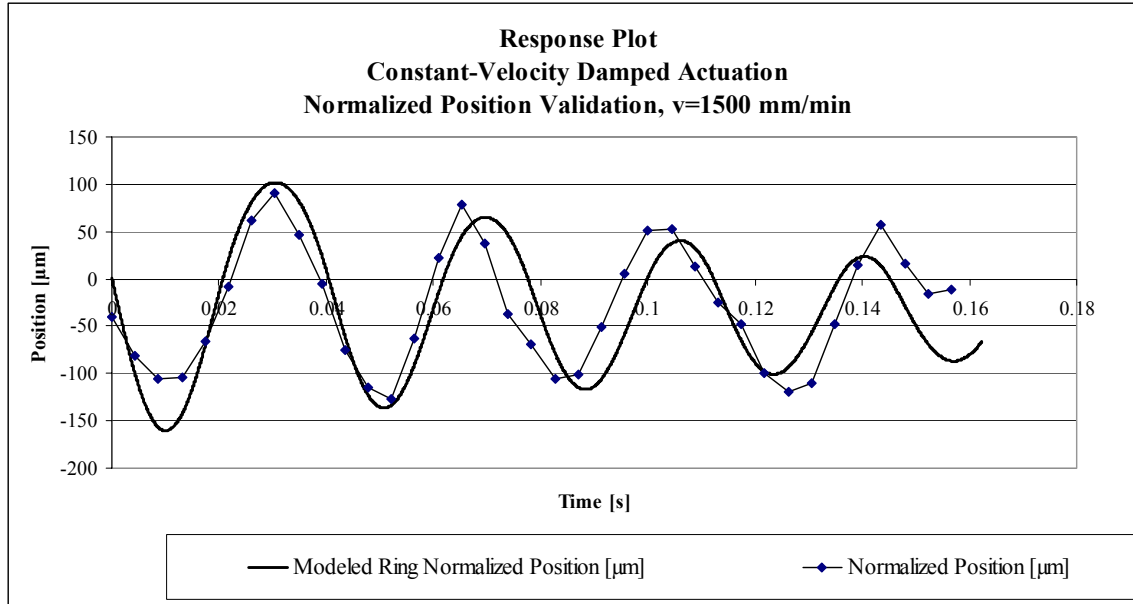


Figure C-11 - Normalized Position Response Plots with Model Values (v=1500 mm/min)

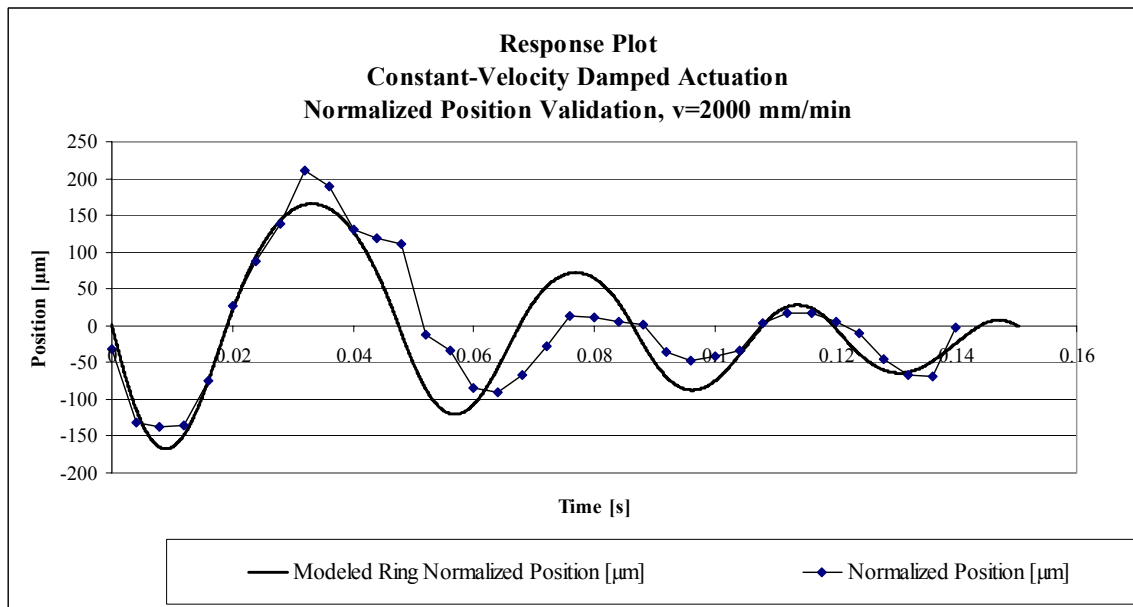


Figure C-12 - Normalized Position Response Plots with Model Values (v=2000 mm/min)

APPENDIX D

FORCE SIMULATION RESULTS

The force model and experimentally observed results for additional cases are presented in Figure D-1 through Figure D-12 (differing actuation velocities).

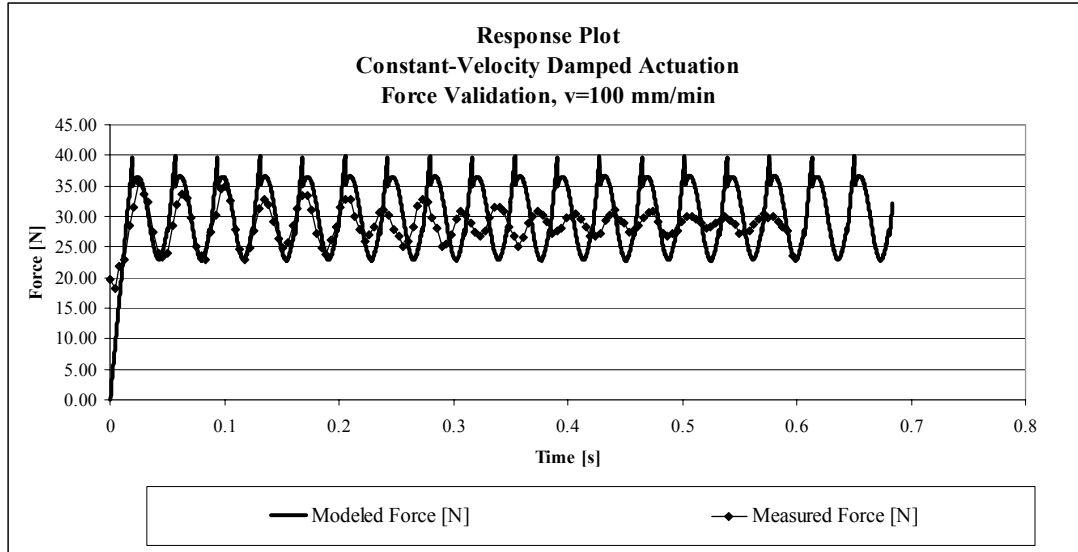


Figure D-1 – Force Response Plots with Model Values ($v=100$ mm/min)

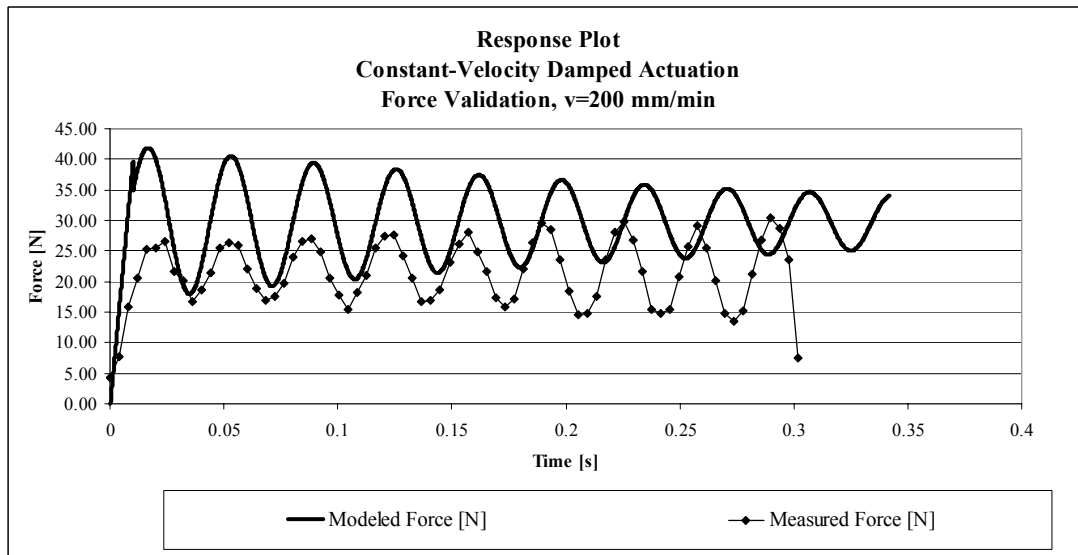


Figure D-2 – Force Response Plots with Model Values ($v=200$ mm/min)

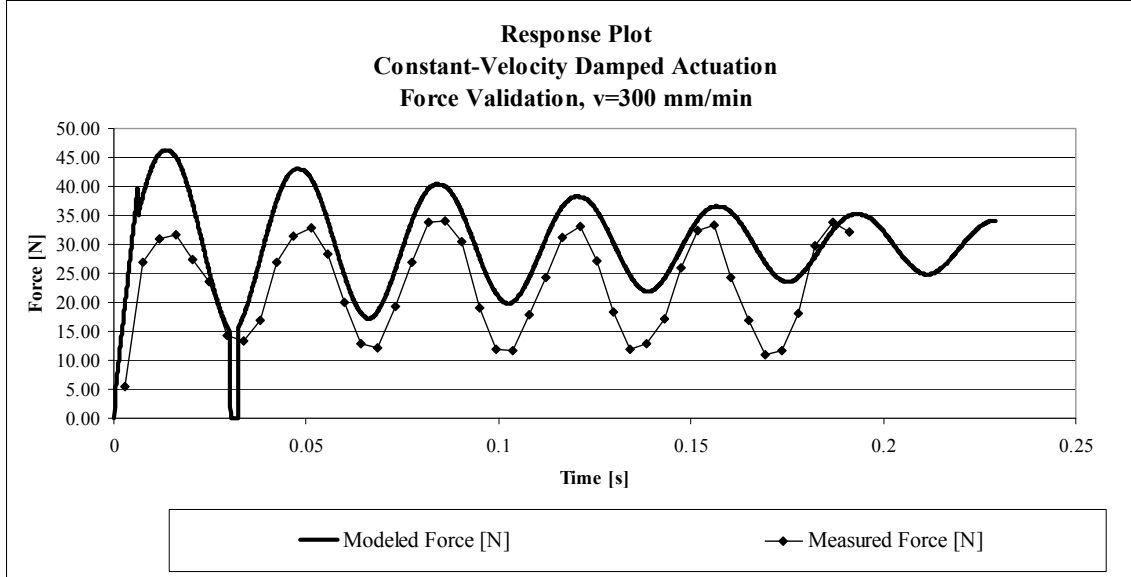


Figure D-3 – Force Response Plots with Model Values ($v=300$ mm/min)

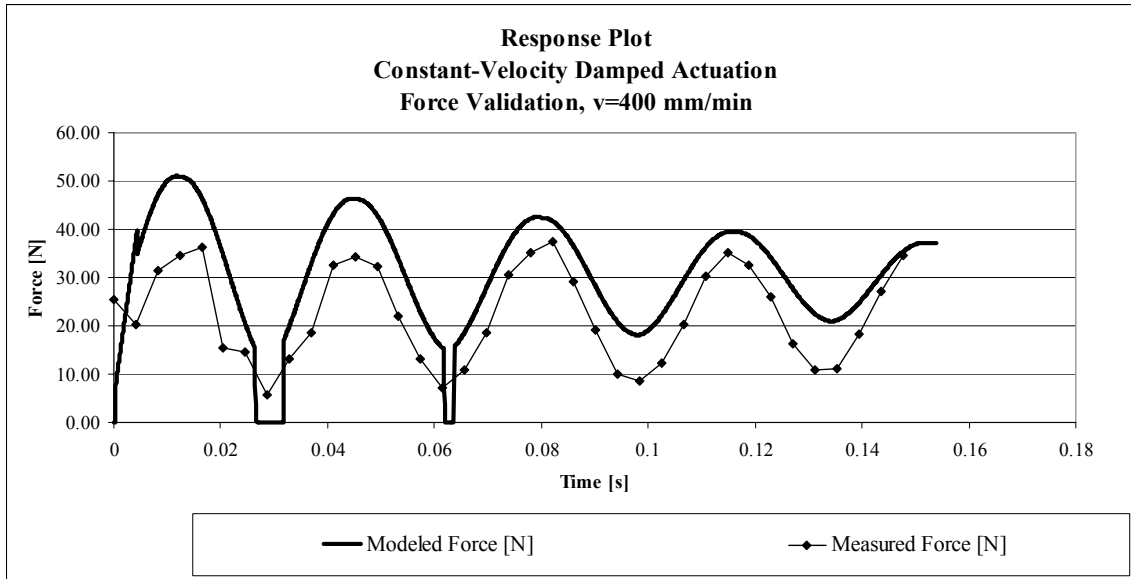


Figure D-4 – Force Response Plots with Model Values ($v=400$ mm/min)

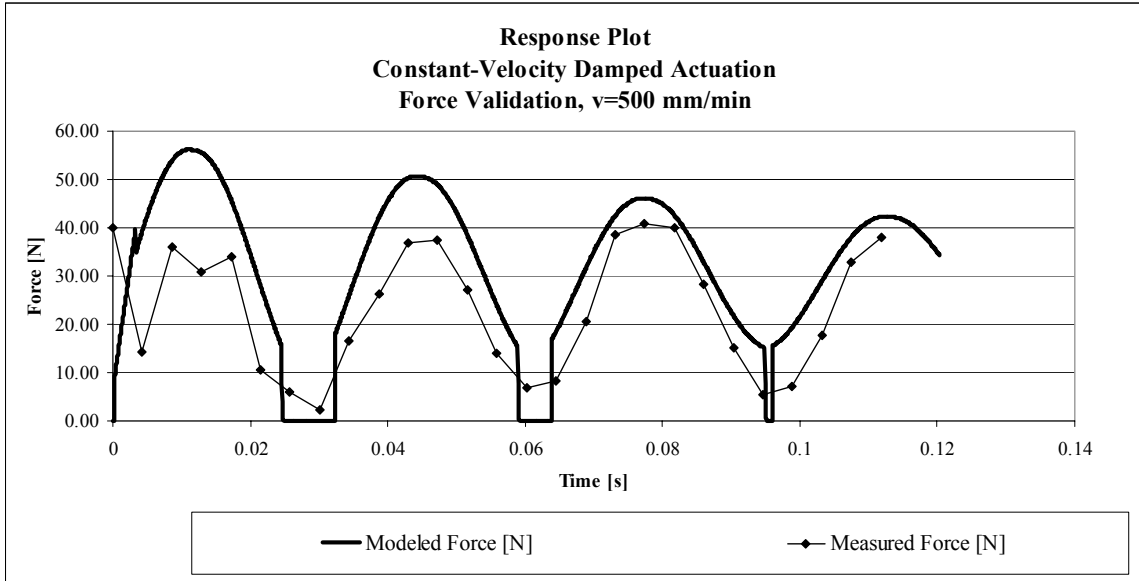


Figure D-5 – Force Response Plots with Model Values ($v=500$ mm/min)

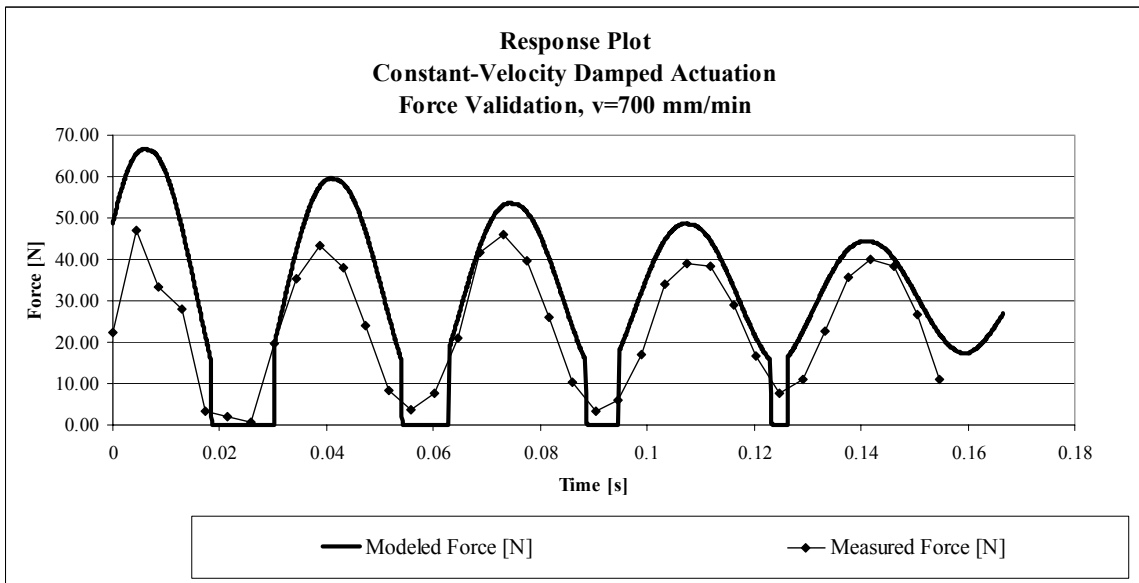


Figure D-6 – Force Response Plots with Model Values ($v=700$ mm/min)

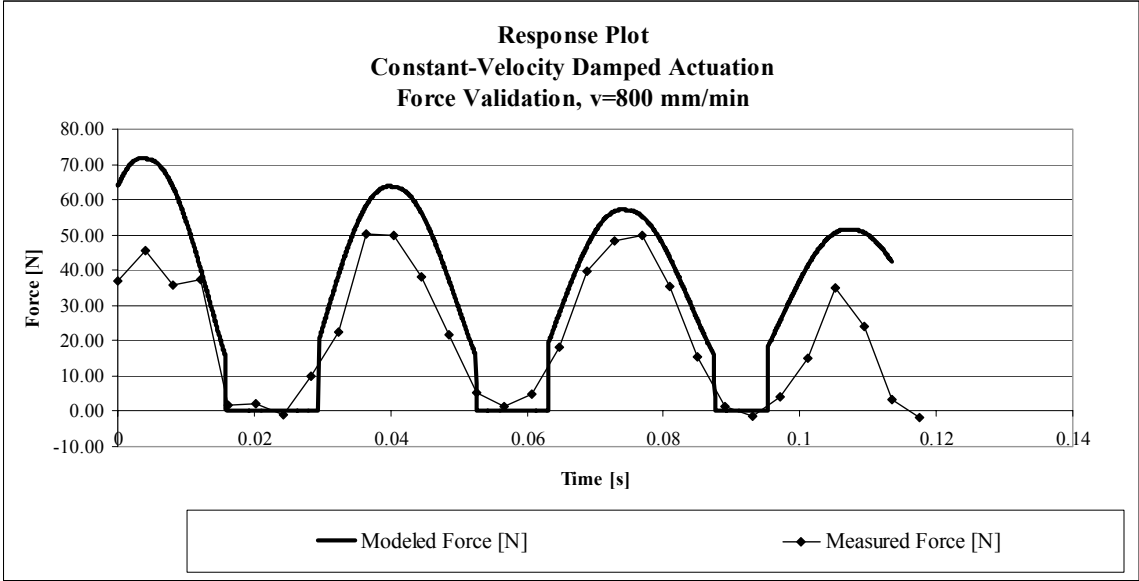


Figure D-7 – Force Response Plots with Model Values (v=800 mm/min)

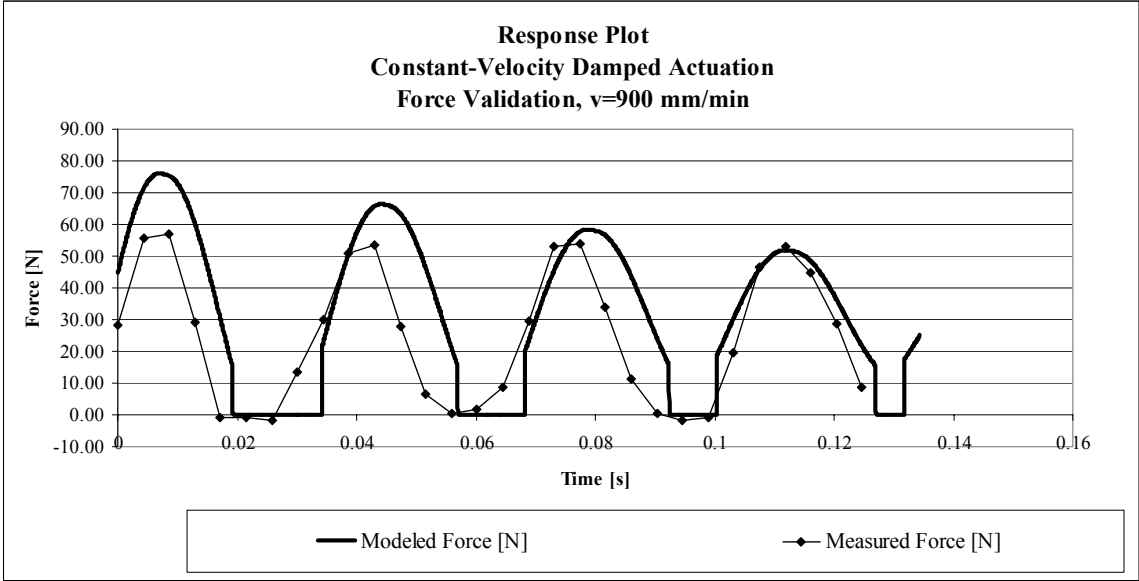


Figure D-8 – Force Response Plots with Model Values (v=900 mm/min)

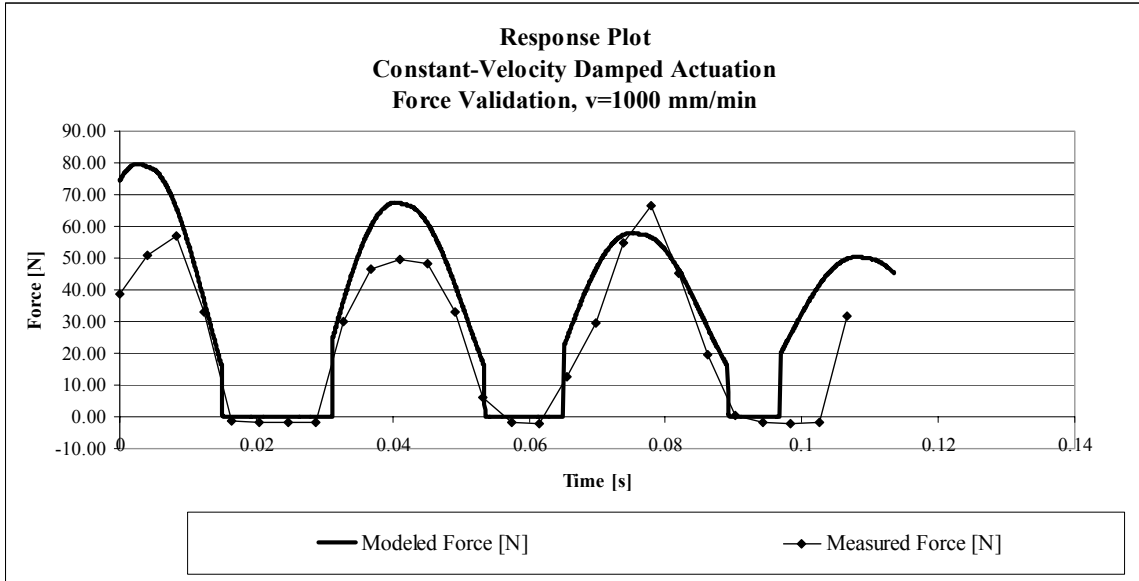


Figure D-9 – Force Response Plots with Model Values (v=1000 mm/min)

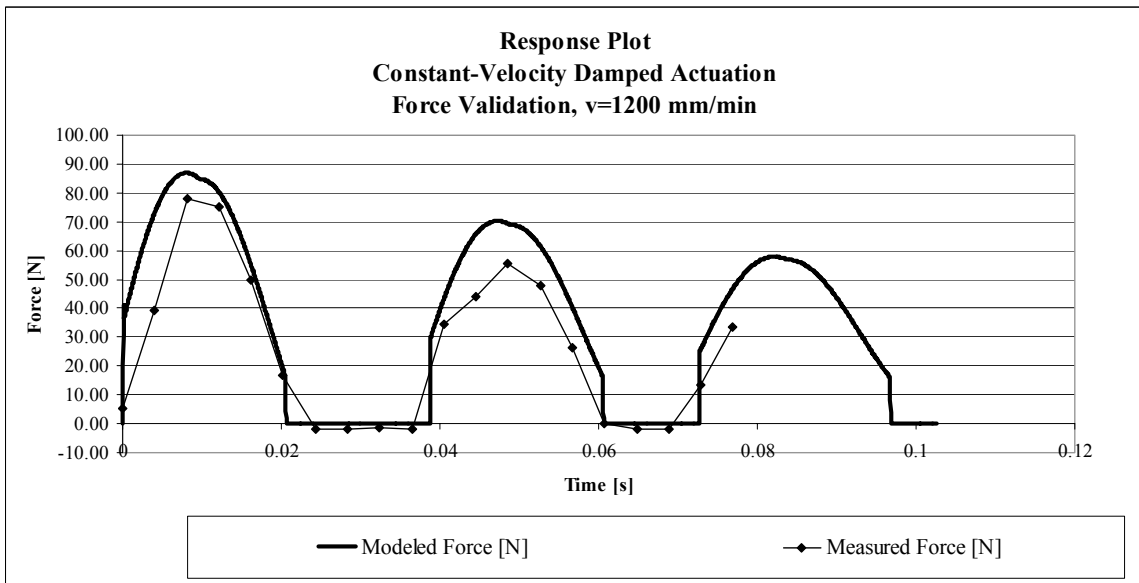


Figure D-10 – Force Response Plots with Model Values (v=1200 mm/min)

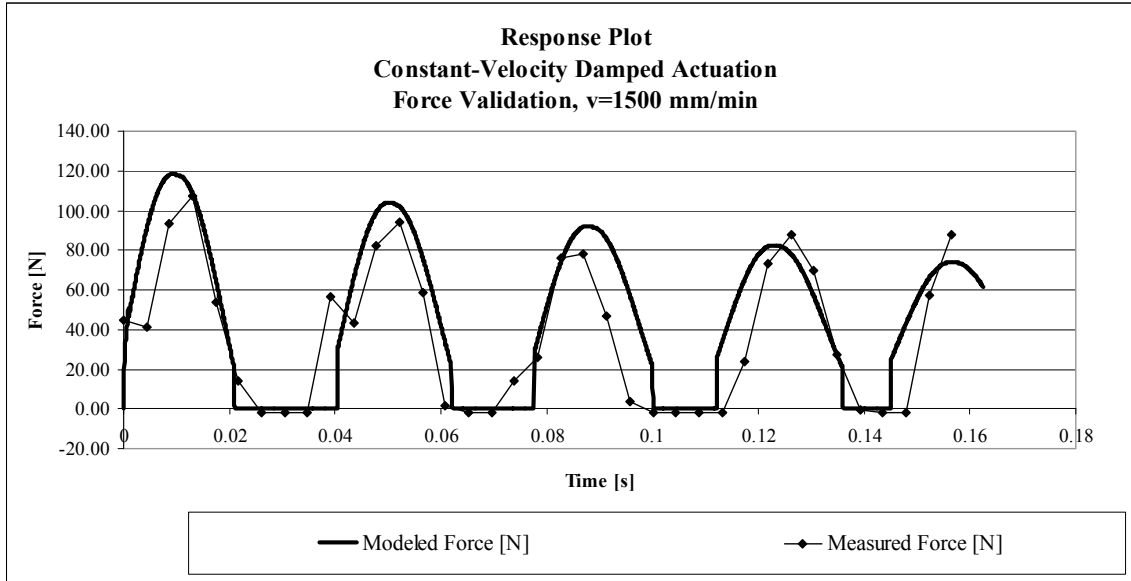


Figure D-11 – Force Response Plots with Model Values (v=1500 mm/min)

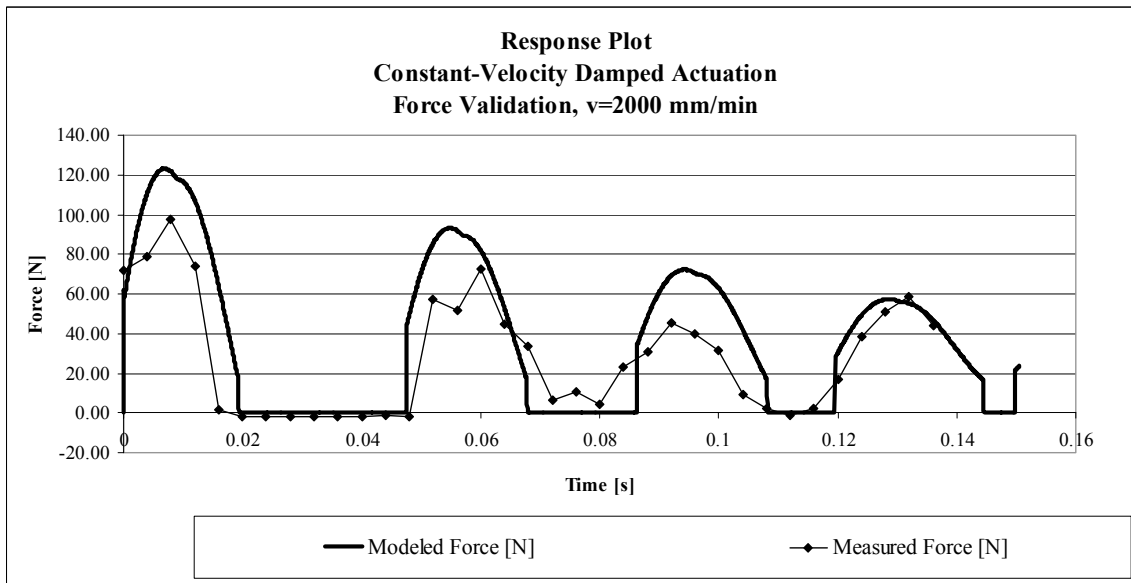


Figure D-12 – Force Response Plots with Model Values (v=2000 mm/min)

APPENDIX E

BANDLIMITED VELOCITY ACTUATION FORCE

The observed force traces for pushing by constant and by frequency-bandlimited velocity are presented for a range of base actuation velocities in Figure E-1 through Figure E-12.

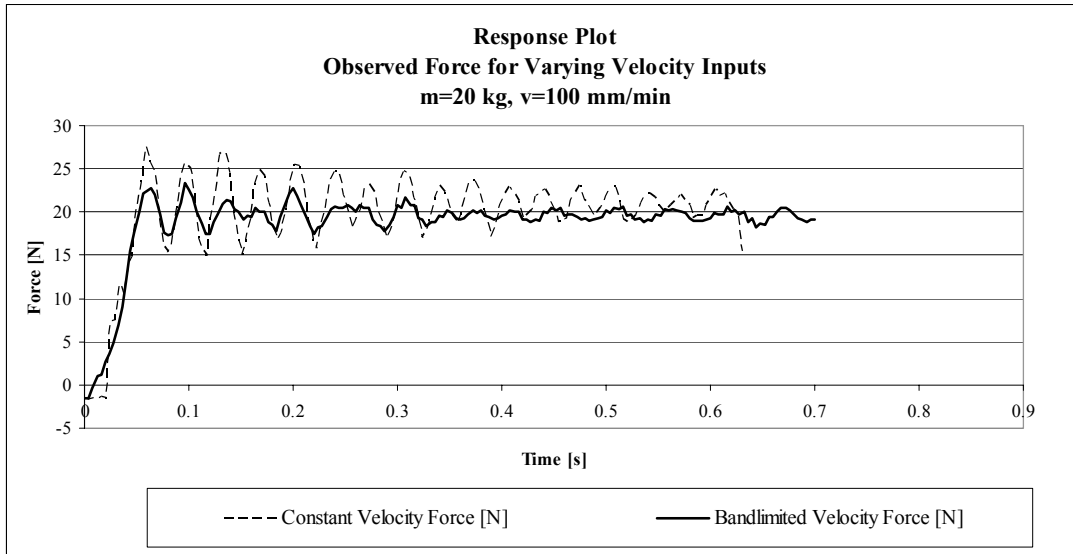


Figure E-1 - Constant Velocity Pushing vs. Bandlimited Pushing Force, $m=18.9$ kg, $v=100$ mm/min

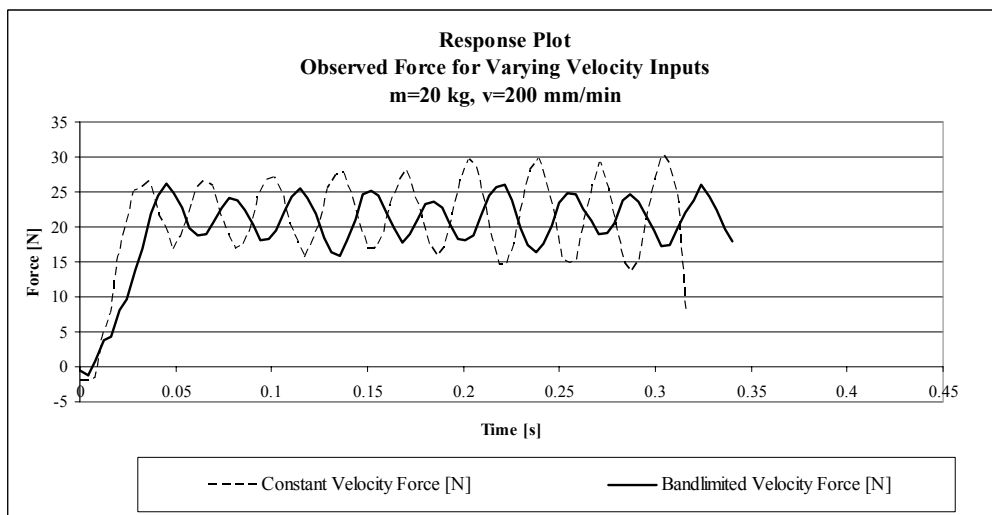


Figure E-2 - Constant Velocity Pushing vs. Bandlimited Pushing Force, $m=18.9$ kg, $v=200$ mm/min

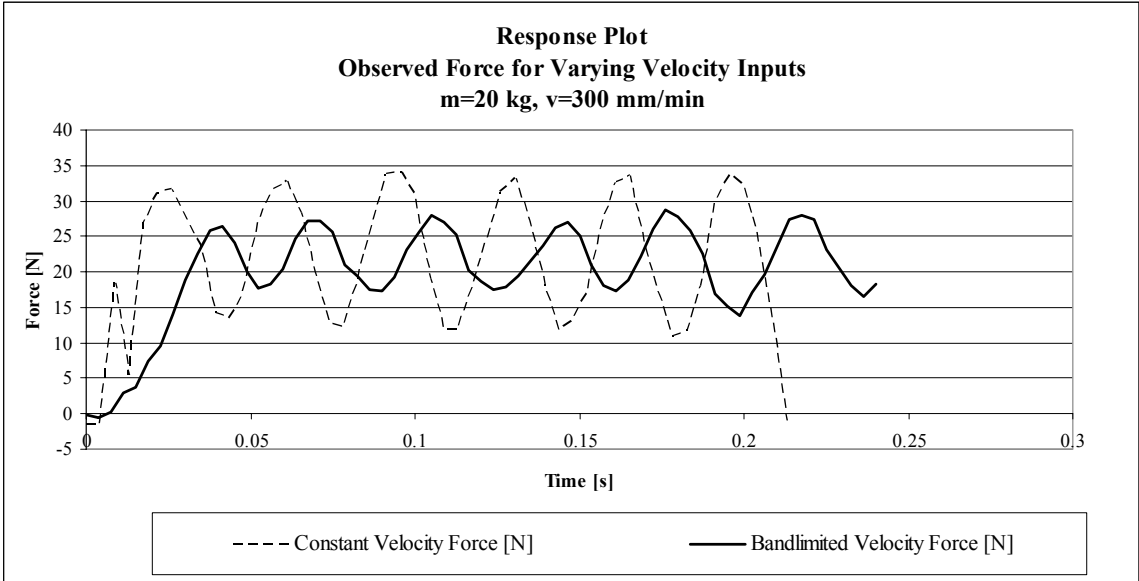


Figure E-3 - Constant Velocity Pushing vs. Bandlimited Pushing Force, m=18.9 kg, v=300 mm/min

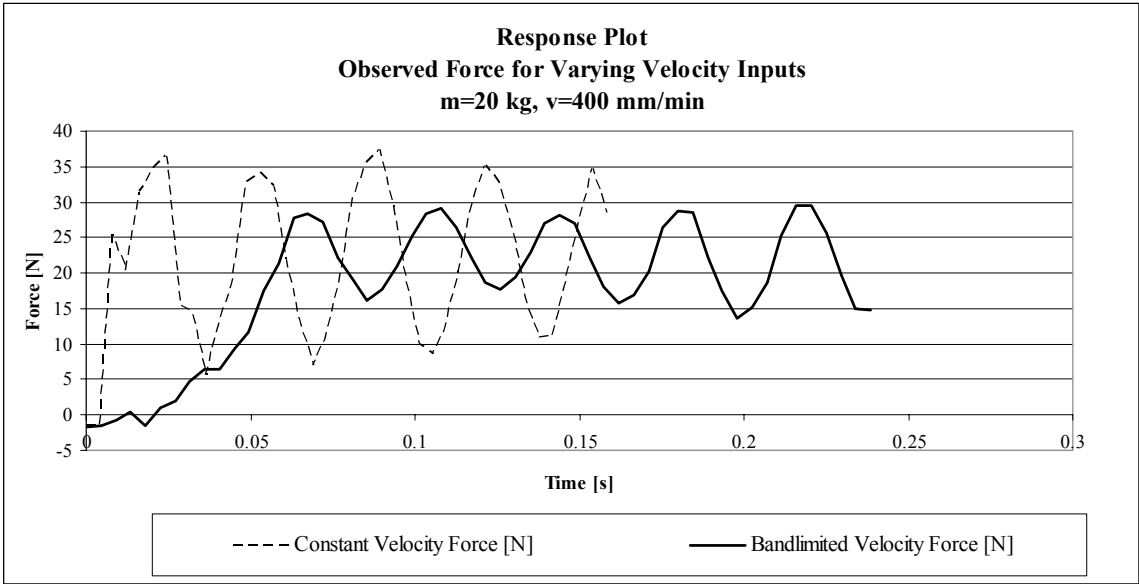


Figure E-4 - Constant Velocity Pushing vs. Bandlimited Pushing Force, m=18.9 kg, v=400 mm/min

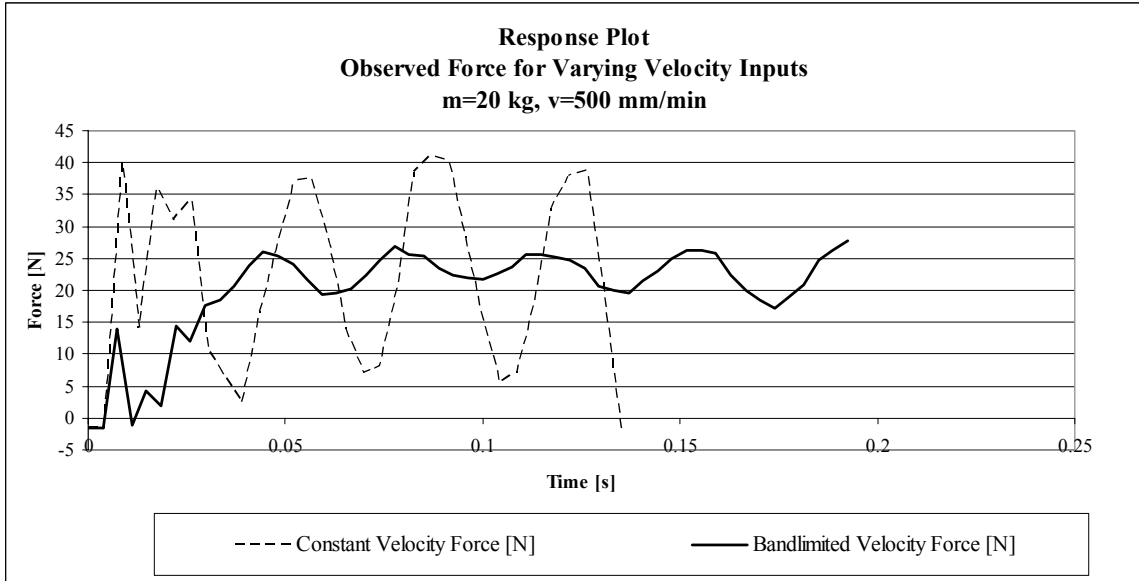


Figure E-5 - Constant Velocity Pushing vs. Bandlimited Pushing Force, m=18.9 kg, v=500 mm/min

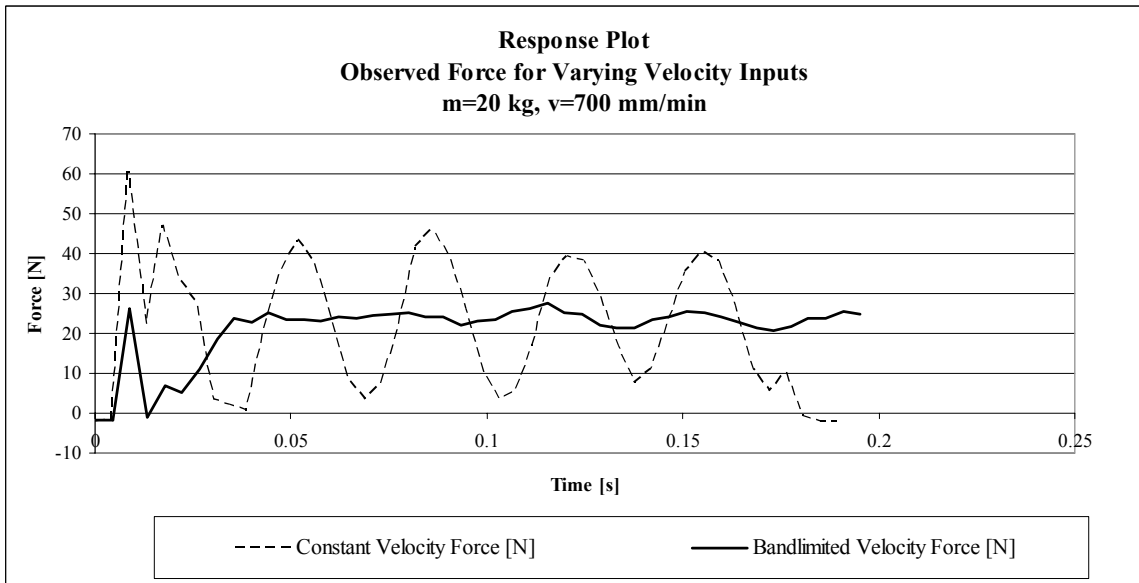


Figure E-6 - Constant Velocity Pushing vs. Bandlimited Pushing Force, m=18.9 kg, v=700 mm/min

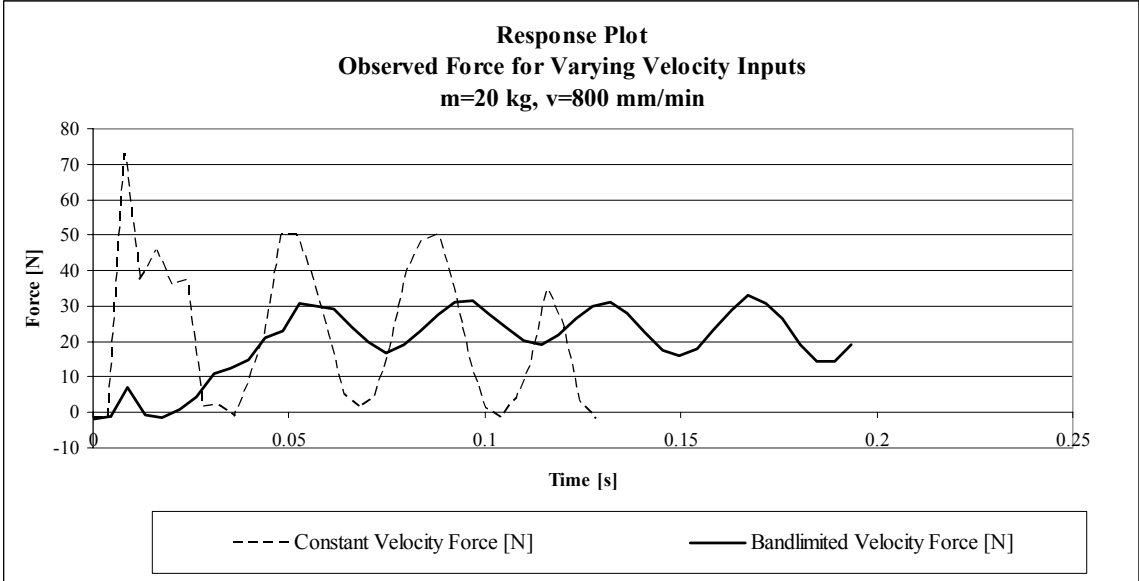


Figure E-7 - Constant Velocity Pushing vs. Bandlimited Pushing Force, m=18.9 kg, v=800 mm/min

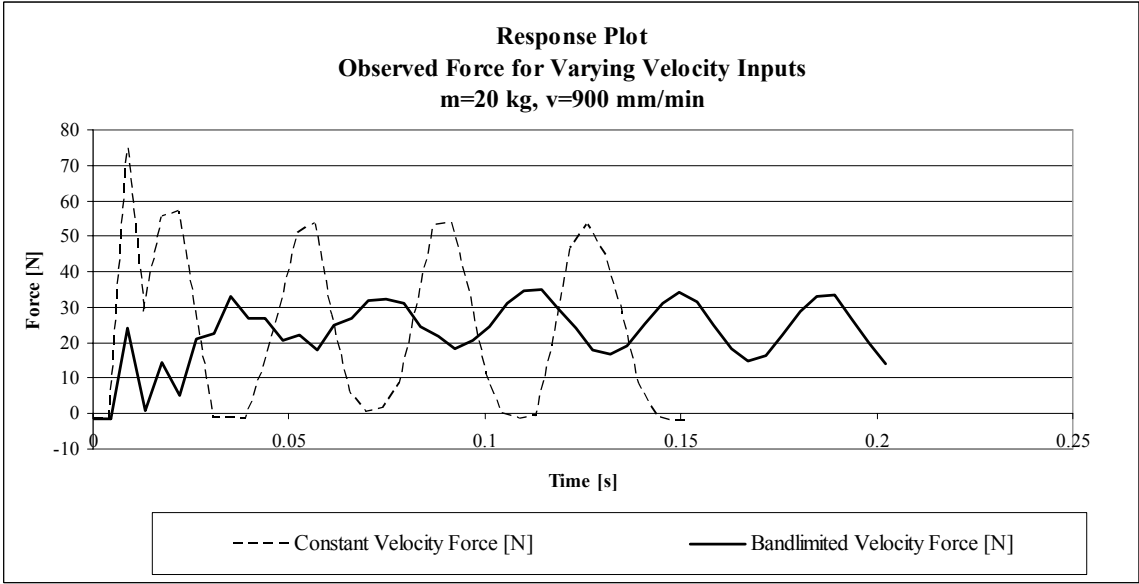


Figure E-8 - Constant Velocity Pushing vs. Bandlimited Pushing Force, m=18.9 kg, v=900 mm/min

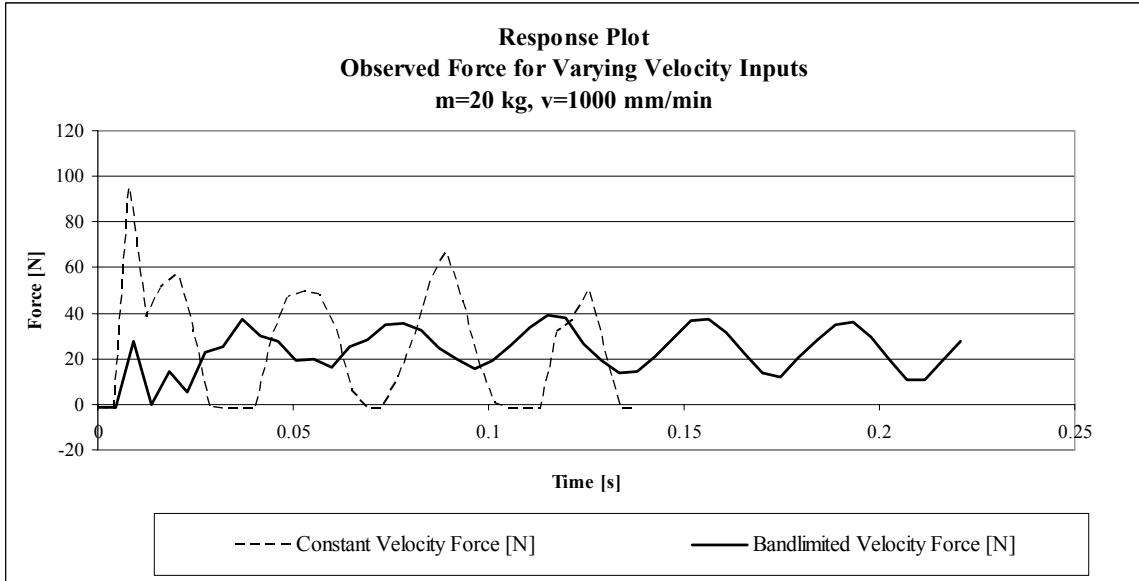


Figure E-9 - Constant Velocity Pushing vs. Bandlimited Pushing Force, m=18.9 kg, v=1000 mm/min

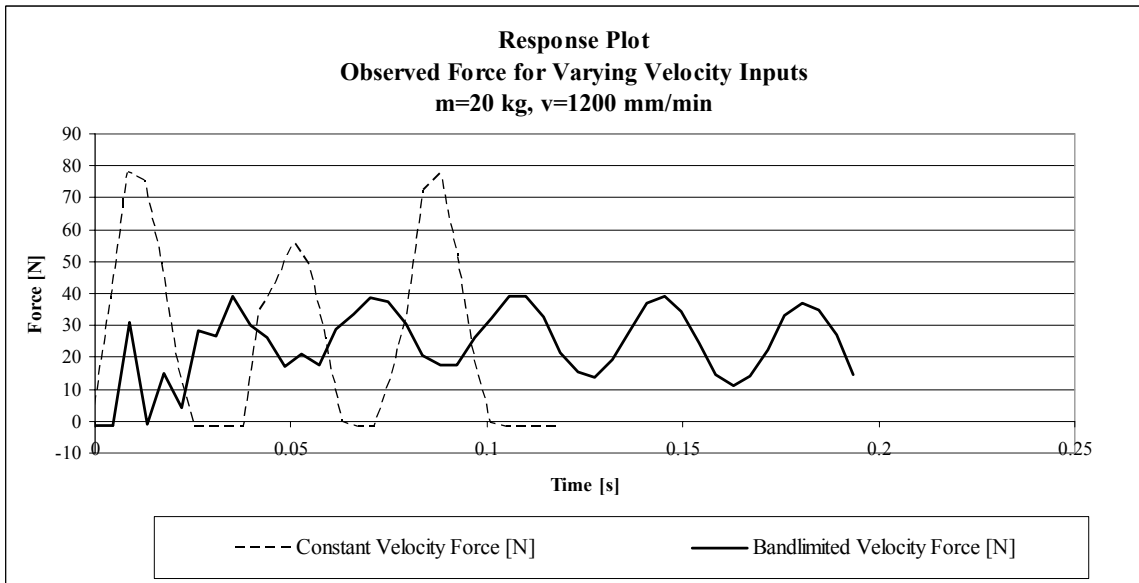


Figure E-10 - Constant Velocity Pushing vs. Bandlimited Pushing Force, m=18.9 kg, v=1200 mm/min

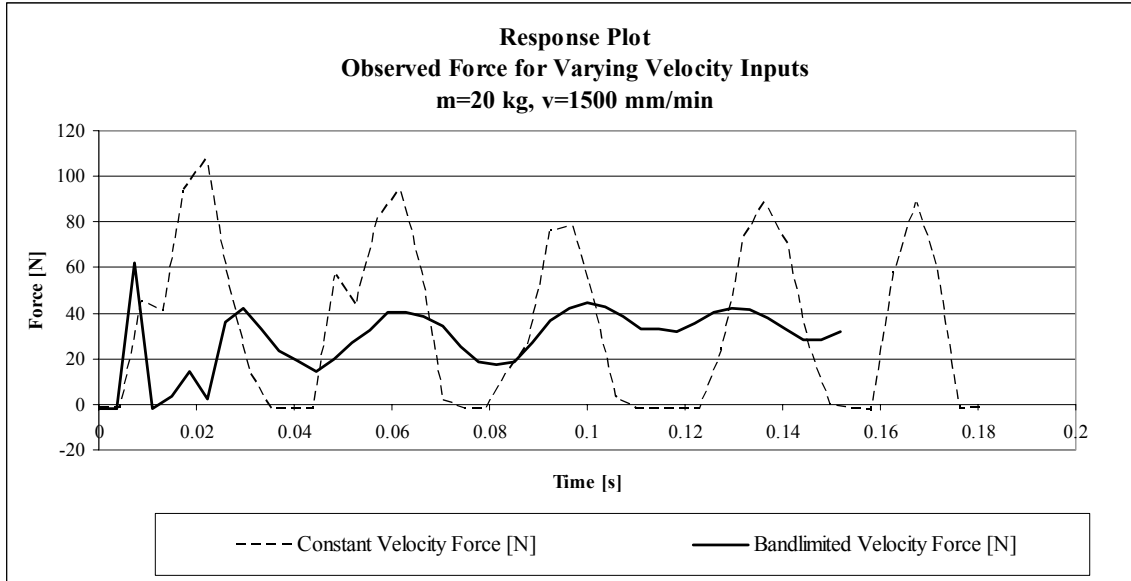


Figure E-11 - Constant Velocity Pushing vs. Bandlimited Pushing Force, m=18.9 kg, v=1500 mm/min

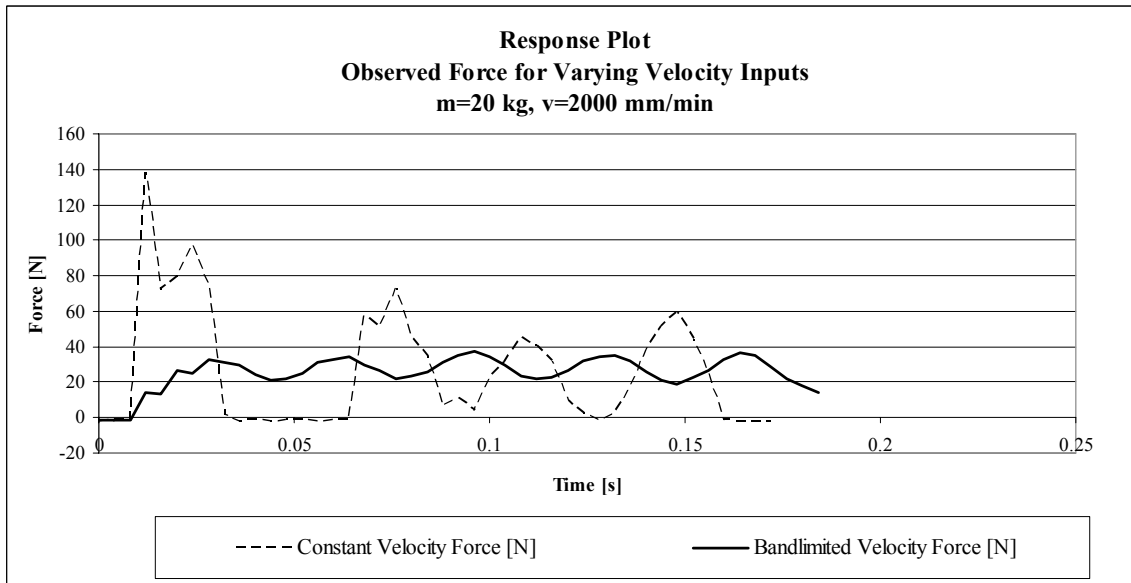


Figure E-12 - Constant Velocity Pushing vs. Bandlimited Pushing Force, m=18.9 kg, v=2000 mm/min

APPENDIX F

BANDLIMITED VELOCITY ACTUATION POSITION

The observed position traces for pushing by constant and by frequency-bandlimited velocity are presented for a range of base actuation velocities in Figure F-1 through Figure F-12. For better resolution, positions are normalized to the constant velocity ramp signal, and the bandlimited actuation is time shifted to align the end positions.

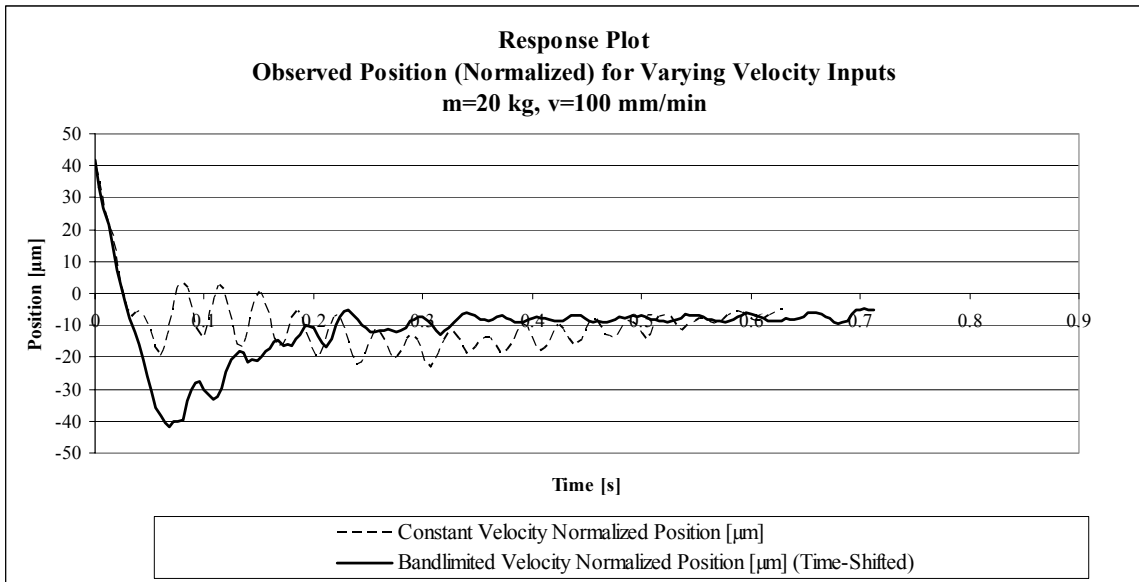


Figure F-1 - Constant Velocity Pushing vs. Bandlimited Pushing Position, m=18.9 kg, v=100 mm/min

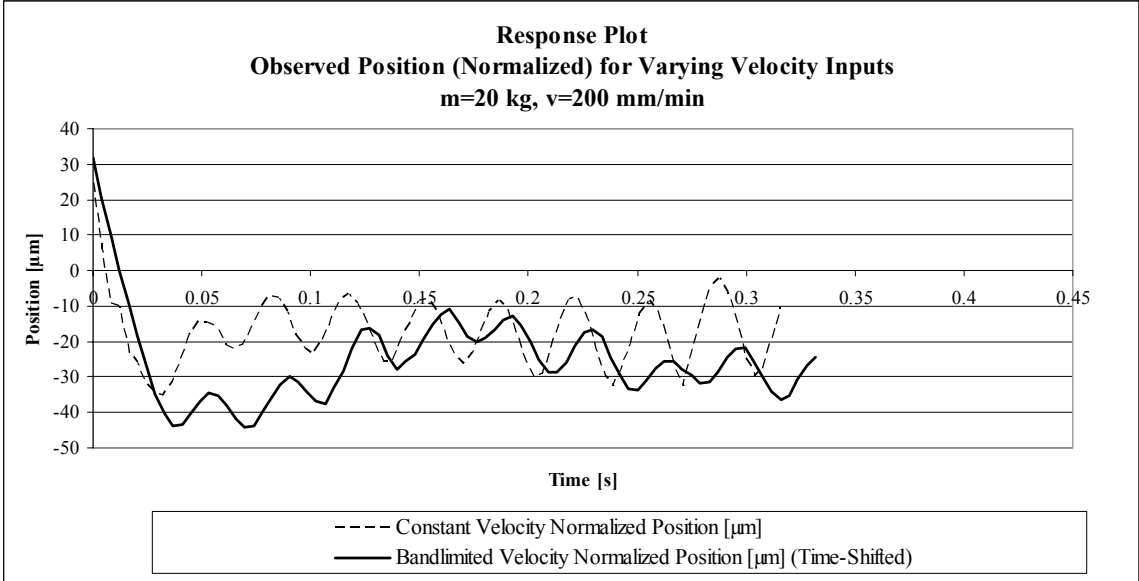


Figure F-2 - Constant Velocity Pushing vs. Bandlimited Pushing Position, m=18.9 kg, v=200 mm/min

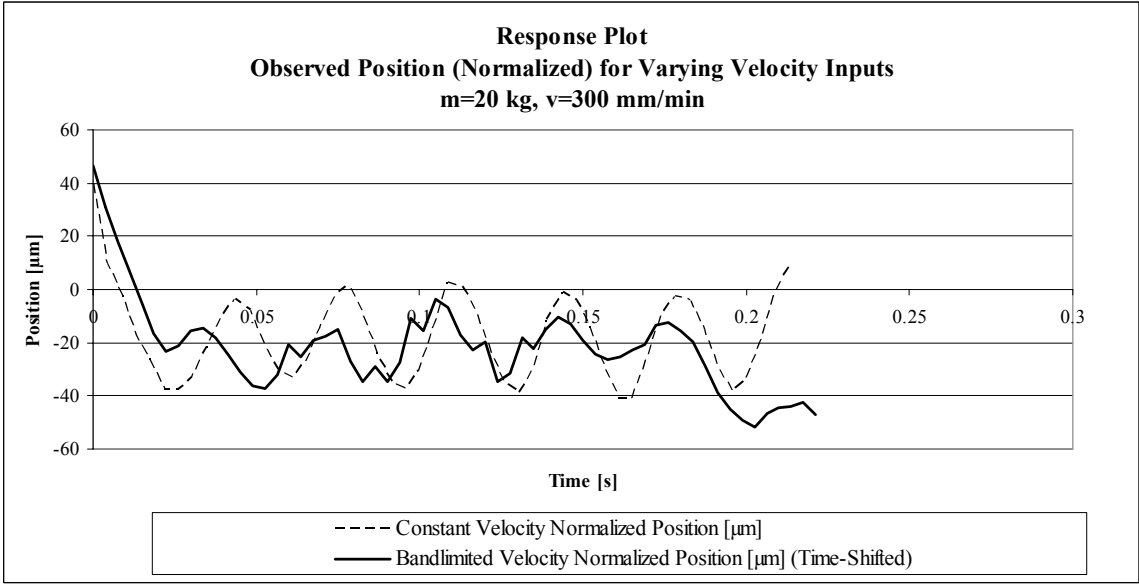


Figure F-3 - Constant Velocity Pushing vs. Bandlimited Pushing Position, m=18.9 kg, v=300 mm/min

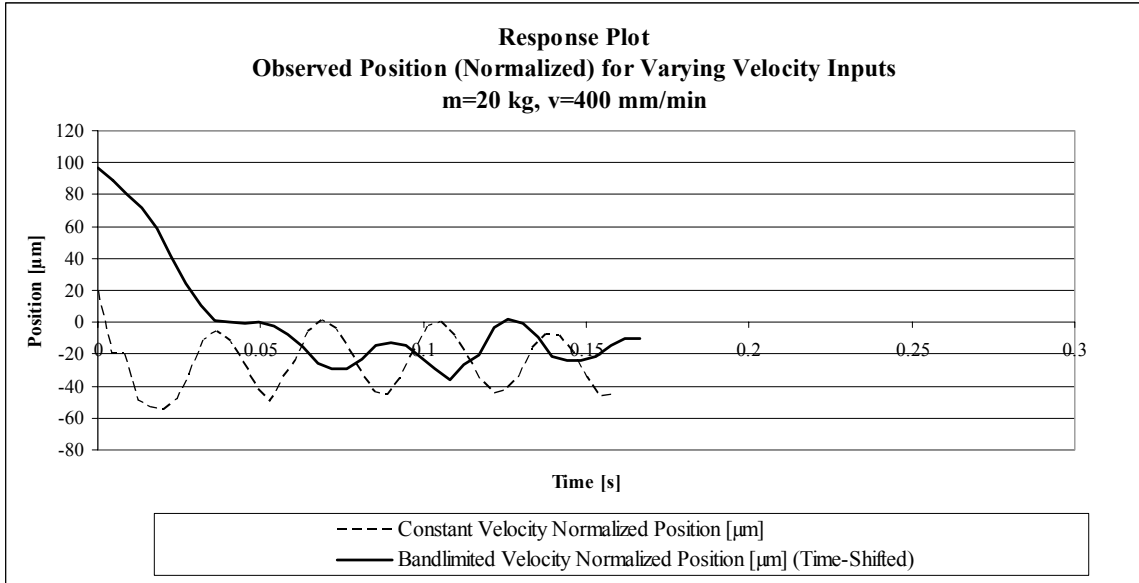


Figure F-4 - Constant Velocity Pushing vs. Bandlimited Pushing Position, m=18.9 kg, v=400 mm/min

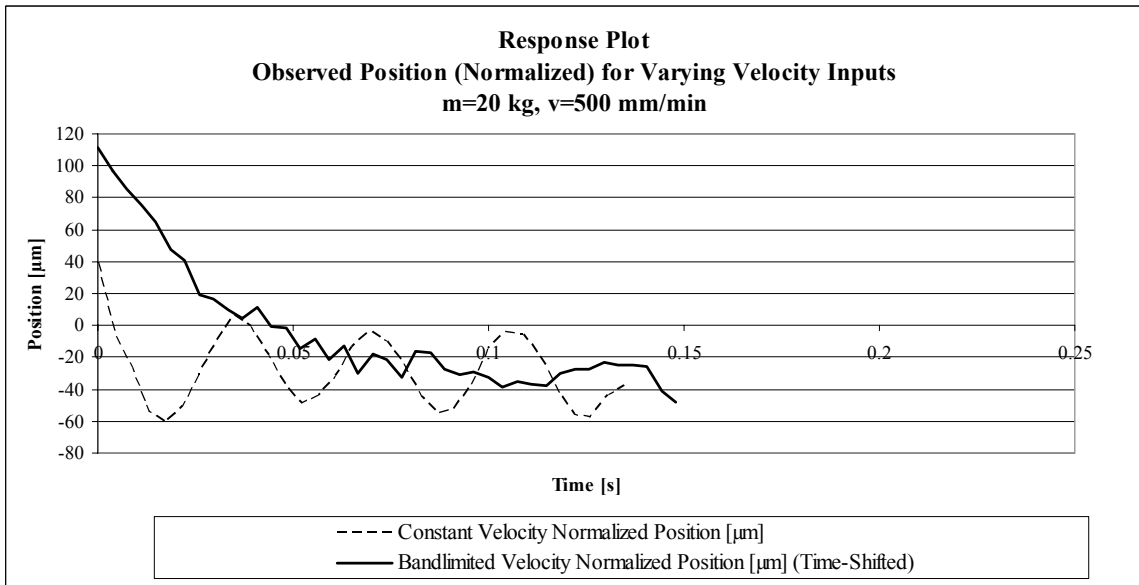


Figure F-5 - Constant Velocity Pushing vs. Bandlimited Pushing Position, m=18.9 kg, v=500 mm/min

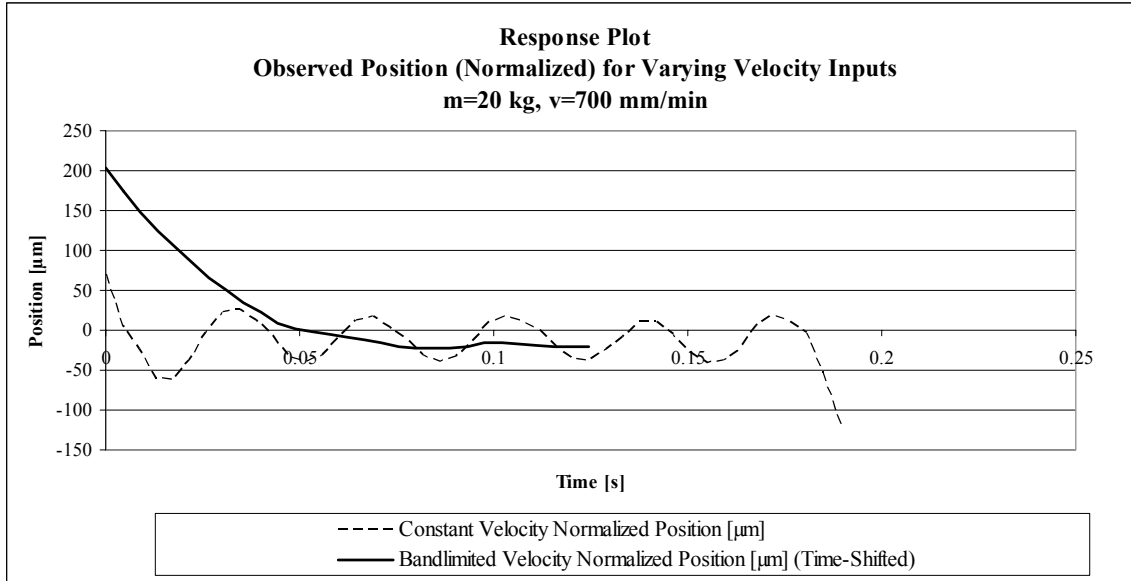


Figure F-6 - Constant Velocity Pushing vs. Bandlimited Pushing Position, m=18.9 kg, v=700 mm/min

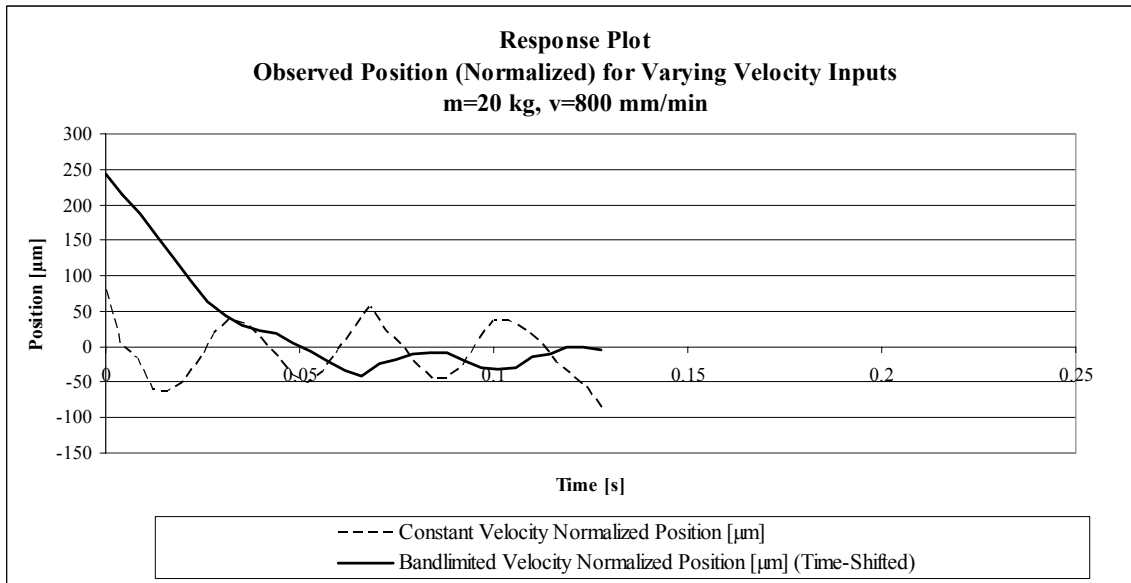


Figure F-7 - Constant Velocity Pushing vs. Bandlimited Pushing Position, m=18.9 kg, v=800 mm/min

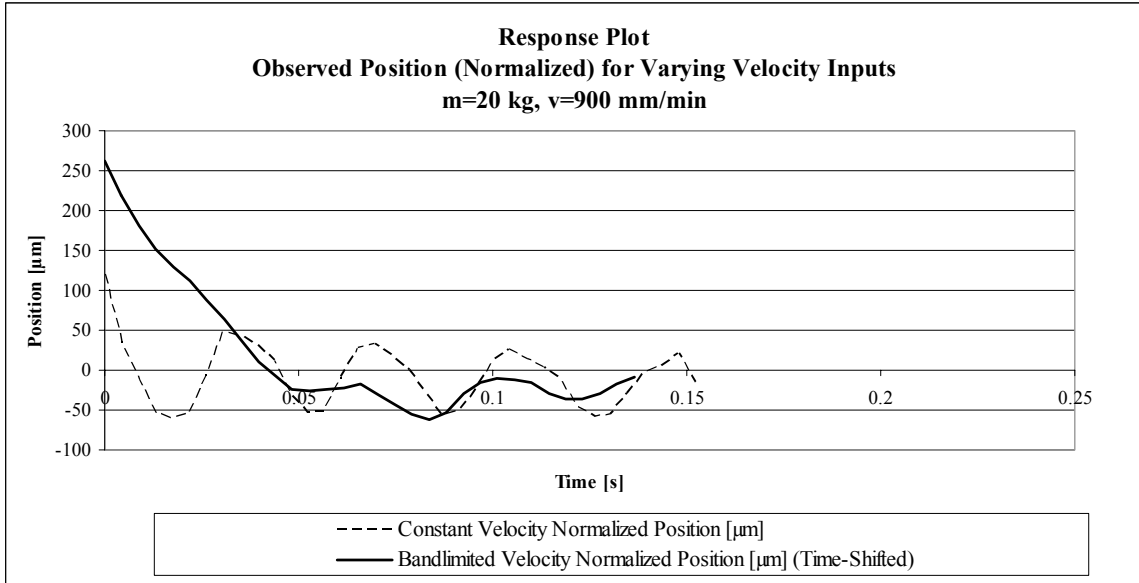


Figure F-8 - Constant Velocity Pushing vs. Bandlimited Pushing Position, m=18.9 kg, v=900 mm/min

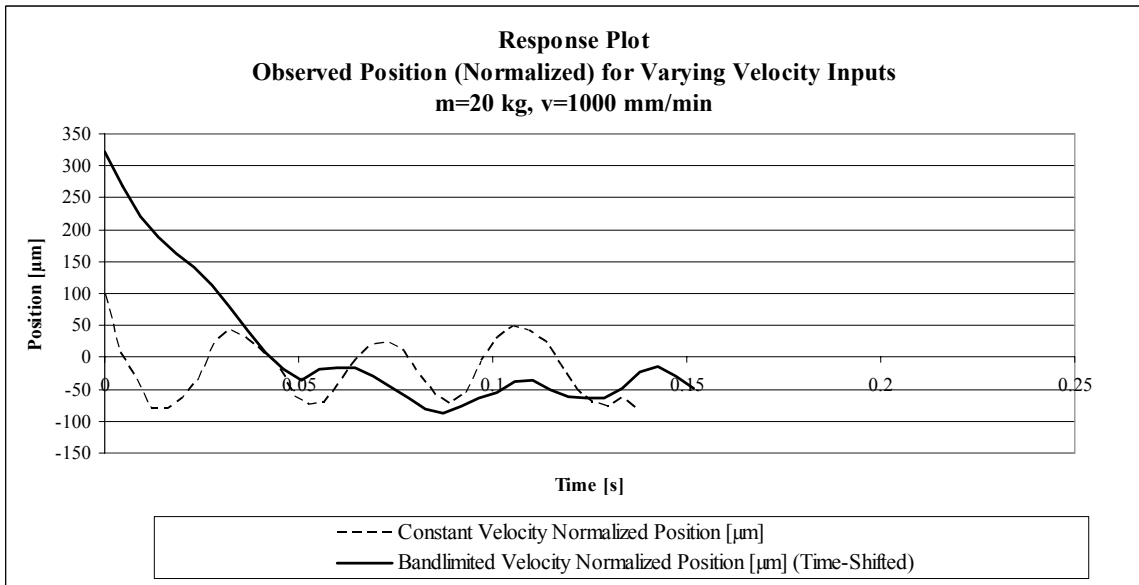


Figure F-9 - Constant Velocity Pushing vs. Bandlimited Pushing Position, m=18.9 kg, v=1000 mm/min

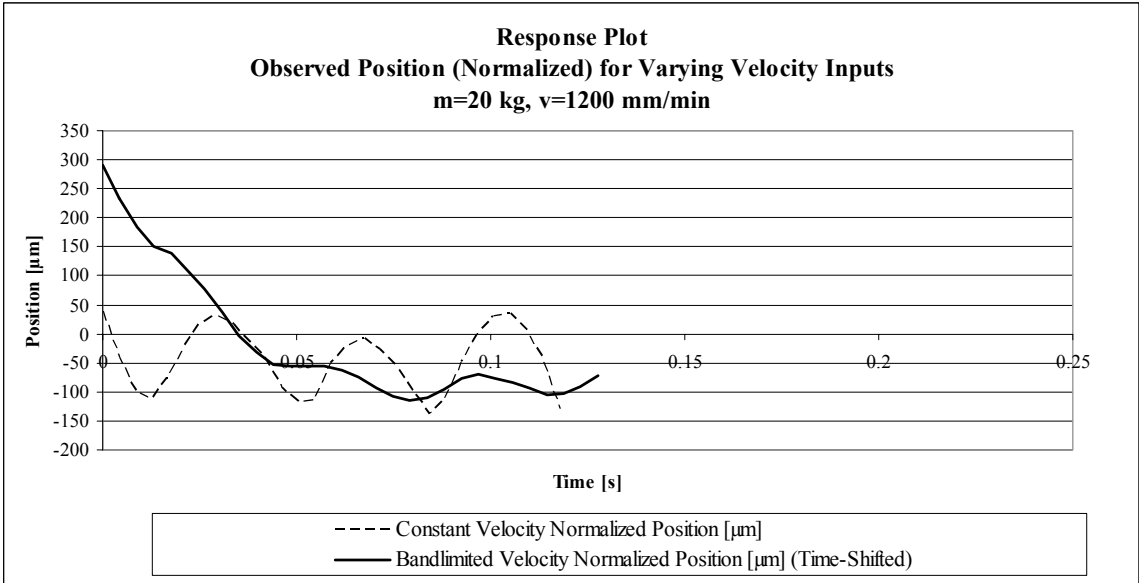


Figure F-10 - Constant Velocity Pushing vs. Bandlimited Pushing Position, m=18.9 kg, v=1200 mm/min

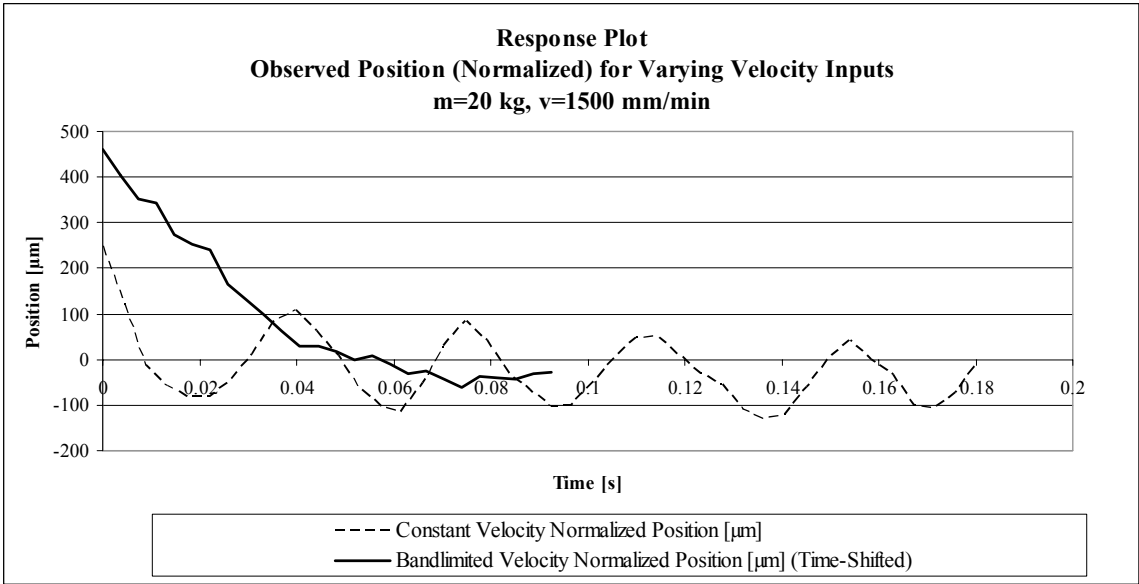


Figure F-11 - Constant Velocity Pushing vs. Bandlimited Pushing Position, m=18.9 kg, v=1500 mm/min

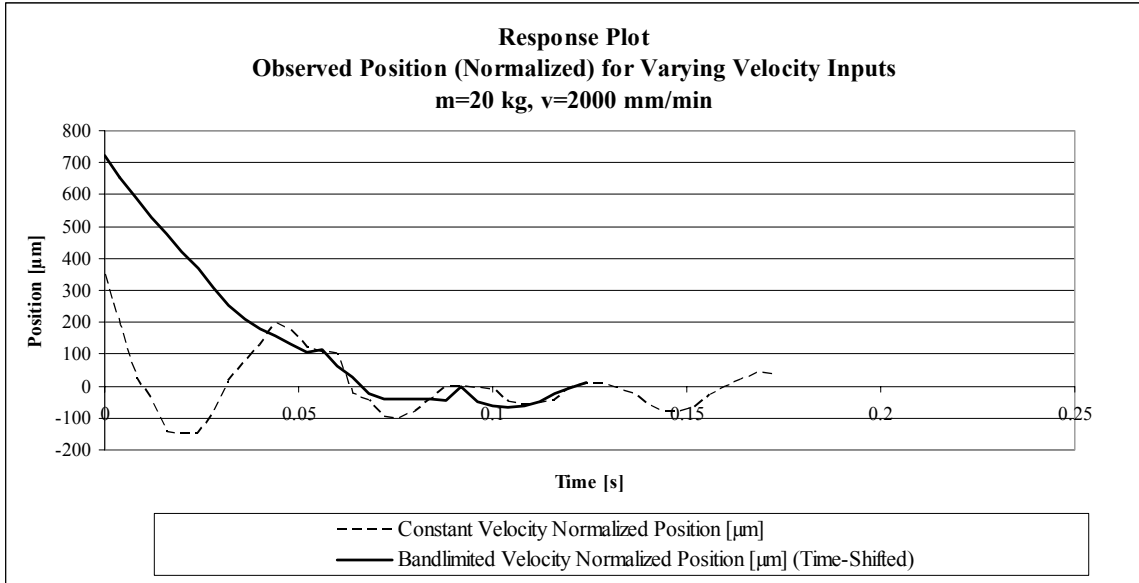


Figure F-12 - Constant Velocity Pushing vs. Bandlimited Pushing Position, m=18.9 kg, v=2000 mm/min

REFERENCES

- Adams, J. and S. Payandeh. "On Methods for Low Velocity Friction Compensation: Theory and Experimental Study." *Journal of Robotic Systems*, v13, n6, Jun, 1996: 391-404.
- Alvarez-Ramírez, J, R. Garrido and R. Femat. "Control of systems with friction." *Physical Review E (Statistical Physics, Plasmas, Fluids, and Related Interdisciplinary Topics)*, v51, n6, pt.B, June 1995: 6235-8.
- Åström, K. "Control of Systems with Friction." Technical paper. Department of Automatic Control, Lund Institute of Technology, 1998.
- Avanzini, F., S. Serafin and D. Rochesso. "Modeling Interactions Between Rubbed Dry Surfaces Using an Elasto-Plastic Friction Model." *Proceeds of the 5th International Conference on Digital Audio Effects (DAFx-02)*, Hamburg, Germany, September 26-28, 2002.
- Canudas de Wit, C., H. Olsson, K.J. Åström and P. Lischinsky. "New model for control of systems with friction." *IEEE Transactions on Automatic Control*, v40, n3, Mar, 1995: 419-425.
- Chernov, N. and C. Lesort. "Least squares fitting of circles." *Journal of Mathematical Imaging and Vision*, v23, n3, November, 2005: 239-252.
- Deng, H. and S.N. Melkote. "Analysis of fixturing dynamic stability in machining." *IEEE/ASME International Conference on Advanced Intelligent Mechatronics, AIM*, v2, 2005: 869-874.
- Destefani, J. "Answers to tough workholding challenges." *Manufacturing Engineering*, v134, n2, Feb., 2005: 71-79.
- Dupont, P.E. "Avoiding stick-slip in position and force control through feedback." *Proceedings. 1991 IEEE International Conference on Robotics and Automation (Cat. No.91CH2969-4)*, 1991: 1470-1475.
- Dupont, P., B. Armstrong and V. Hayward. "Elasto-plastic friction model: contact compliance and stiction." *Proceedings of the American Control Conference*, v2, 2000: 1072-1077.

- Dupont, P., V. Hayward and B. Armstrong. "Single State Elasto-Plastic Friction Models." *IEEE Transactions on Automatic Control*, v47, n5, May, 2002: 787-792.
- Feeny, B. and J. Liang. "A Decrement Method for the Simultaneous Estimation of Coulomb and Viscous Friction." *Journal of Sound and Vibration*, v195, n1, Aug, 1996: 149-154.
- Ferrero, J.F. and J.J. Barrau. "Study of dry friction under small displacements and near-zero sliding velocity ." *Wear*, v209, n1-2, Aug, 1997: 322-327.
- Hirschorn, R.M. and G. Miller. 1998, "Control of Nonlinear Systems with Friction." *IEEE Transactions on Control Systems Technology*, v7, n5, Sep, 1999: 588-595.
- Heidenhain Corporation. "Length Gauge Catalog." Date accessed: Mar. 2005 <http://www.heidenhain.com/wcmsshow.php?filepath=wcmsmimefiles/208_945_26_15179.pdf&&mimetype=application/pdf&WCMSMimeFileUID=13961>.
- Huang, W., E. Krotkov and M. Mason. "Impulsive Manipulation." *Proceedings - IEEE International Conference on Robotics and Automation*, v1, 1995: 120-125.
- Huang, W. and M. Mason. "Experiments in Impulsive Manipulation." *Proceedings - IEEE International Conference on Robotics and Automation*, v2, 1998: 1077-1082.
- Huang, W. and M. Mason. 1996, "Limiting Cases of Impulsive Manipulation." *Technical Report CMU--RI-- TR--96--24*, The Robotics Institute, Carnegie Mellon University, Sep., 1996.
- Huang, W. and M. Mason. "Mechanics, Planning, and Control for Tapping." *International Journal of Robotics Research*, v19, n10, Oct, 2000: 883-894.
- International Standards Organization (ISO). "Methods for the assessment of departure from roundness – Measurement of variations in radius." *ISO Standard 4291-1985(E)*, 1985.
- Jin Jiang and Youmin Zhang. "A novel variable-length sliding window blockwise least-squares algorithm for on-line estimation of time-varying parameters." *International Journal of Adaptive Control and Signal Processing*, v18, n6, Aug, 2004: 505-21.
- Kaiser, M. J. and T. L. Morin. "Centers, out-of-roundness measures, and mathematical programming." *Computers & Industrial Engineering*, v26, n1, 1994: 35-54.

- Kalman, R.E. "New approach to linear filtering and prediction problems." *American Society of Mechanical Engineers Transactions of Journal of Basic Engineering Series D*, v82, n1, Mar, 1960, 59-IRD-11: 35-45.
- Kraus, P., V. Kumar and P. Dupont. "Analysis of Frictional Contact Models for Dynamic Simulation." *Proceedings - IEEE International Conference on Robotics and Automation*, v2, 1998: 976-981.
- Le, Van-Ban and D. T. Lee. "Out-of-roundness problem revisited." *IEEE Transactions on Pattern Analysis and Machine Intelligence*, v13, n3, Mar, 1991: 217-223.
- Li, B. and S.N. Melkote. "Fixture clamping force optimisation and its impact on workpiece location accuracy." *International Journal of Advanced Manufacturing Technology*, v17, n2, 2001: 104-113.
- Liu, Yung-Tien, T. Higuchi and Rong-Fong Fung. "A novel precision positioning table utilizing impact force of spring-mounted piezoelectric actuator - Part I: Experimental design and results." *Precision Engineering*, v27, n1, Jan., 2003: 14-21.
- Luenberger, D. *Introduction to Dynamic Systems: Theory, Models, & Applications*. New York: John Wiley & Sons, 1979.
- Lynch, K. "The Mechanics of Fine Manipulation by Pushing." *Proceedings - IEEE International Conference on Robotics and Automation*, v3, 1992: 2269-2276.
- Lynch, K. "Estimating the Friction Parameters of Pushed Objects." *1993 International Conference on Intelligent Robots and Systems*, 1993: 186-193.
- Lynch, K.M. "Locally controllable manipulation by stable pushing." *IEEE Transactions on Robotics and Automation*, v15, n2, April 1999: 318-27.
- Lynch, K. and M. Mason. "Pulling by Pushing, Slip with Infinite Friction, and Perfectly Rough Surfaces." *Proceedings - IEEE International Conference on Robotics and Automation*, v1, 1993: 745-751.
- Lynch, K.M. and M.T. Mason. "Controllability of Pushing." *Proceedings - IEEE International Conference on Robotics and Automation*, v1, 1995: 112-119.
- Lynch, K. and M. Mason. "Stable Pushing: Mechanics, Controllability, and Planning." *The International Journal of Robotics Research*, v15, n6, Dec., 1996: 533-556.

- Malluck, J.A. and S.N. Melkote. "Modeling of deformation of ring shaped workpieces due to chucking and cutting forces." *Transactions of the ASME. Journal of Manufacturing Science and Engineering*, v126, n1, Feb., 2004: 141-147.
- Malkin, S. *Grinding Technology: Theory and Applications of Machining with Abrasives*. Dearborn, MI: Society of Manufacturing Engineers, 1989.
- Mears, L., F. Kolarits, M. Thompson and T.R. Kurfess. "Design of a Flexible Centering Tooling System." *International Journal of Computer Applications in Technology, Special Issue "Advanced Manufacturing Tooling"*, 2006 (in publication).
- Mears, L. and T.R. Kurfess. "Design of a Flexible and Agile Centering Preprocessing System." *Proceedings of International Conference on Agility (ICAM2005)*, Helsinki, Finland, July 27-28, 2005: 307-313.
- Mendes, J., M. Nishimura, K. Tomizawa, Y. Yamagata and T. Higuchi. "Printed board positioning system using impact drive mechanism." *Proceedings of the SICE Annual Conference*, 1996: 1123-1128.
- Mirtich, B. and J. Canny. "Impulse-based Simulation of Rigid Bodies." *Proceedings of the Symposium on Interactive 3D Graphics*, 1995: 181-188.
- Mishra, B. "Workholding Analysis and planning." *Proceedings of 1991 IEEE RSJ International Workshop on Intelligent Robots and Systems (IROS 91)*, Osaka, Japan, Nov 3-5 1991: 53-57.
- Mitutoyo America Corporation. "Roundtest RA-1400/1500." Technical Bulletin 1731, 2005 <<http://www.mitutoyo.com/pdf/4198-211.pdf>>.
- Mitutoyo America Corporation. "Roundtest RA-100." Catalog US4145-211, 2006 <<http://www.mitutoyo.com/pdf/4145-211.pdf>>.
- Ogata, K. *System Dynamics (4th ed.)*. Upper Saddle River, NJ: Prentice-Hall, 2004.
- Olsson, H. and K.J. Åström. "Friction generated limit cycles." *IEEE Transactions on Control Systems Technology*, v9, n4, July, 2001: 629-36.
- Olsson, H., K.J. Åström, C. Canudas de Wit, M. Gafvert and P. Lischinsky. "Friction models and friction compensation." *European Journal of Control*, v4, n3, 1998: 176-195.
- Peshkin, M.A. and A.C. Sanderson. "The Motion of a Pushed, Sliding Workpiece." *IEEE Journal of Robotics and Automation*, v4, n6, Dec., 1988: 569.

- Raghu, A. and S.N. Melkote. "Modeling of workpiece location error due to fixture geometric error and fixture-workpiece compliance." *Transactions of the ASME. Journal of Manufacturing Science and Engineering*, v127, n1, Feb., 2005: 75-83.
- Rathbun, D., M. Berg and K. Buffington. "Pulse Width Control for Precise Positioning of Structurally Flexible Systems Subject to Stiction and Coulomb Friction." *Journal of Dynamic Systems, Measurement and Control, Transactions of the ASME*, v126, n1, 2004: 131-138.
- Rathbun, D., M. Berg and K. Buffington. "Piecewise-Linear-Gain Pulse Width Control for Precise Positioning of Structurally Flexible Systems Subject to Stiction and Coulomb Friction." *Journal of Dynamic Systems, Measurement and Control, Transactions of the ASME*, v126, n1, 2004: 139-143.
- Salisbury, E. J. and F.E. Peters. "Impact of surface errors on fixtured workpiece location and orientation." *Society of Manufacturing Engineers Technical Paper MS98-262*, 1998: 1-6.
- Siebenaler, S.P. and S.N. Melkote. "Prediction of workpiece deformation in a fixture system using the finite element method." *International Journal of Machine Tools and Manufacture*, v46, n1, Jan., 2006: 51-58.
- Siebenhaar, C. "Precise adjustment method using stroke impulse and friction." *Precision Engineering*, v28, n2, April, 2004: 194-203.
- Song, P., P. Kraus and V. Kumar. "Analysis of Rigid Body Dynamic Models for Simulation of Systems with Frictional Contacts." *Transactions of the ASME. Journal of Applied Mechanics*, v68, n1, Jan., 2001: 118-28.
- Stewart, D., "Time-Stepping Methods and the Mathematics of Rigid Body Dynamics." *Impact and Friction of Solids, Structures and Machines*. Burkhäuser, 2000. Ch. 9.
- Taylor-Hobson Precision Corporation. "Talyrond 290/265." Catalog TR290/265 6ESCP, Aug., 2003.
- Wallace, A. "Design of a Piezoelectric Impact Mechanism for Tap Centering." Master's Thesis. Massachusetts Institute of Technology. 2003.
- Waurzyniak, P. "Workholding Essentials." *Manufacturing Engineering*, v123, n1, Jul, 1999: 72-78.

- Waurzyniak, P. "Chuck speeds rising." *Manufacturing Engineering*, v123, n3, Sep, 1999: 70-80.
- Welch, G. and G. Bishop. "An Introduction to the Kalman Filter." *SIGGRAPH Conference Proceedings*, 2001.
- Xu, L. and B. Yao. "Adaptive Robust Control of Mechanical Systems with Nonlinear Dynamic Friction Compensation." *Proceedings of the American Control Conference*, v4, 2000: 2595-2599.
- Yamagata, Y., T. Higuchi, H. Saeki and H. Ishimaru. "Ultrahigh vacuum precise positioning device utilizing rapid deformations of piezoelectric elements." *Journal of Vacuum Science & Technology A (Vacuum, Surfaces, and Films)*, v8, n6, 1990: 4098-4100.
- Yamagata, Y. and T. Higuchi. "Micropositioning device for precision automatic assembly using impact force of piezoelectric elements." *Proceedings - IEEE International Conference on Robotics and Automation*, v1, 1995: 666-671.
- Yao, W.; B. Chen and C. Liu. "Energetic coefficient of restitution for planar impact in multi-rigid-body systems with friction." *International Journal of Impact Engineering*, v31, n3, March, 2005: 255-265.
- Zelniker, E. E., B.C. Appleton and I.V.L. Clarkson. "Optimal Circle Fitting Via Branch and Bound." *2005 IEEE International Conference on Acoustics, Speech, and Signal Processing (IEEE Cat. No.05CH37625)*, v4, 2005: 709-712.
- Zesch, W. and R. Fearing. "Alignment of Microparts Using Force Controlled Pushing." *Proceedings of SPIE - The International Society for Optical Engineering*, v3519, 1998: 148-156.

VITA

M. LAINE MEARS

MEARS was born in Jacksonville, Florida in 1970. He attended public schools in Florida and Virginia, received a BS degree in Mechanical Engineering from Virginia Polytechnic Institute and State University in 1993 and a MS degree in Mechanical Engineering from Georgia Institute of Technology in 2001. He worked in the Manufacturing industry for over ten years in the areas of bearings and automotive engine components before coming to Georgia Tech full time to pursue a doctorate in Mechanical Engineering. He is a registered Professional Engineer in Georgia and enjoys exercise, 20th century fiction and brainteasers related to logic, programming and number theory.